Elastic LADAR Modeling for Synthetic Imaging Applications

by

Robin R. Burton

B.A., Physics, University of Colorado at Boulder, Colorado, 1994

A dissertation submitted in partial fulfillment of the
requirements for the degree of Doctor of Philosophy
in the Chester F. Carlson Center for Imaging Science
Rochester Institute of Technology

2002

Signature of the Author _____

Accepted by _____
Coordinator, Ph.D. Degree Program Date

CHESTER F. CARLSON CENTER FOR IMAGING SCIENCE
ROCHESTER INSTITUTE OF TECHNOLOGY
ROCHESTER, NEW YORK

CERTIFICATE OF APPROVAL

Ph.D. DEGREE DISSERTATION

The Ph.D. Degree Dissertation of Robin R. Burton
has been examined and approved by the
dissertation committee as satisfactory for the
dissertation required for the
Ph.D. degree in Imaging Science

John Schott, Ph.D., Dissertation Advisor

Roger Easton, Ph.D.

Elliott Horch, Ph.D.

Frank Sciremammano, Ph.D.

Date

DISSERTATION RELEASE PERMISSION

ROCHESTER INSTITUTE OF TECHNOLOGY

CHESTER F. CARLSON CENTER FOR IMAGING SCIENCE

Title of Dissertation:

Elastic LADAR Modeling for Synthetic Imaging Applications

I, Robin R. Burton, hereby grant permission to Wallace Memorial Library of R.I.T. to reproduce my thesis in whole or in part. Any reproduction will not be for commercial use or profit.

Signature _____

Date

Elastic LADAR Modeling for Synthetic Imaging Applications

by

Robin R. Burton

Submitted to the
Chester F. Carlson Center for Imaging Science
in partial fulfillment of the requirements
for the Doctor of Philosophy Degree
at the Rochester Institute of Technology

Abstract

The Digital Imaging and Remote Sensing Image Generation (DIRSIG) model was developed to create synthetic images of remotely sensed scenes (Schott et al. 1999). It is a quantitative model based on first principles that calculates the radiance reaching the sensor from the visible region of the spectrum through to the long-wave. DIRSIG generates a very accurate representation of what a sensor would see by modeling all processes involved in the imaging chain. Currently, DIRSIG only models light from passive sources such as the sun, blackbody radiation due to the temperature of an object, and local incoherent illuminants. Active systems allow the user to tailor the illumination source for specific applications. Remote sensing Laser Detection and Ranging (LADAR) systems that use a laser as the active source have existed for almost 40 years (Fiocco and Smullin 1963). LADAR systems are used to locate the position of an object. Light Detection and Ranging (LIDAR) systems are used to derive the properties of an object, such as density or chemical composition. Recently, advances in tunable lasers and infrared detectors have allowed much more sophisticated and accurate work to be done, but a comprehensive spectral LADAR/LIDAR model

has yet to be developed.

To provide a tool to assist in LADAR/LIDAR development, this research incorporates a first-principle-based elastic LADAR/LIDAR model into DIRSIG. It calculates the spectral irradiance at the focal plane for both the atmospheric and topographic return, based on the system characteristics and the assumed atmosphere. The model accounts for the geometrical form factor, a measure of the overlap between the sensor and receiver field of view, in both the monostatic and bistatic cases. The model includes the effect of multiple bounces from topographical targets. Currently, only direct detection systems are modeled. Several sources of noise are extensively modeled, such as speckle from rough surfaces and atmospheric turbulence phase effects.

Acknowledgements

First and foremost I need to thank Mr. Scott Brown. This work would not have been possible without his coding expertise and the many phenomenology discussions he endured. Second, I would like to thank Dr. John Schott for his unwavering support that allowed me to become a Ph.D. candidate in the first place. Next, I would like to thank the members of my committee for their advise and the time they took out of their schedules to work with me. Fourth, I would like to thank Dr. Jaime Zapata for his proofreading and advise. Finally, I'd like to thank the following individuals for their general support and friendship: Sue Chan, Carolyn Kitchen, Andy and Piper Fordham, Joe and Diane Kloiber, Margaret's House, Jason Meyers, Dr. Harvey Rhody, and Cindy Schultz.

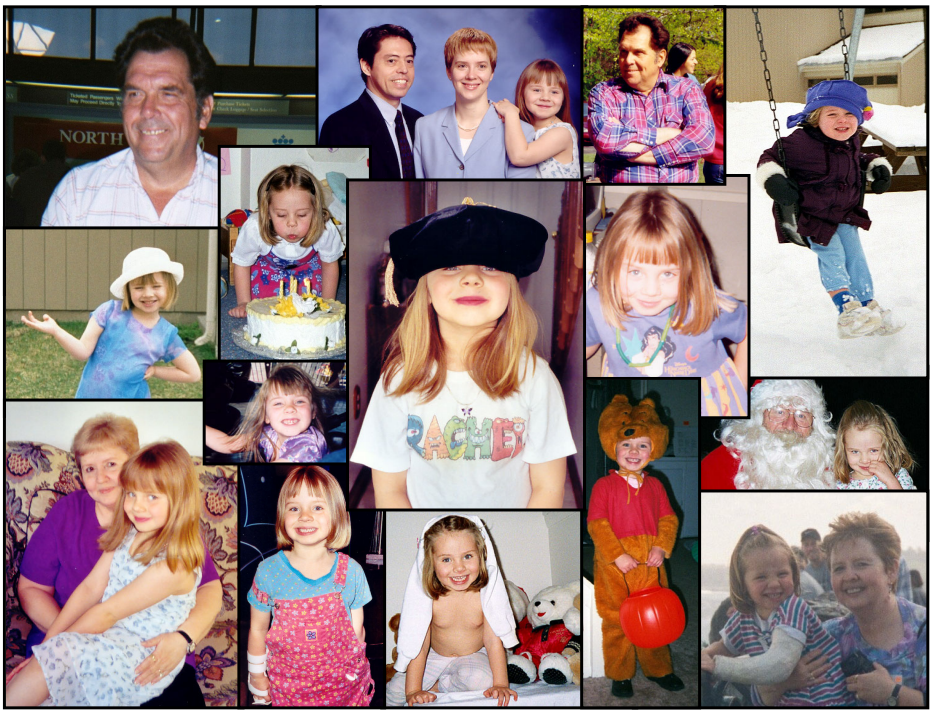

This work is dedicated

To my daughter - who sacrificed the most.

To my husband - who brings me joy.

To my parents - who are always there.

To my grandmother - who is the foundation.

Disclaimer

The views expressed in this dissertation are those of the author and do not reflect the official policy or position of the United States Air Force, Department of Defense, or the U.S. Government.

Contents

List of Figures

List of Tables

Nomenclature

Symbol	Definition
A	Value of C_n^2 one meter above the ground
A	Amplitude of the initial field
A_0	Area of the objective lens or mirror
A_0	On-axis amplitude of a plane wave
$A\left\{r_T\left(R\right), W\left(R\right)\right\}$	Area overlap function
$A\left(r_{op}, r_0\right)$	Integration area
$A\left(x_{od}, y_{od}, r_b\right)$	Area excluded in the integration
$a\left(R\right)$	Distance between the receiver and laser axis in the object plane
$a_f\left(R\right)$	Amount the irradiance is shifted off-axis in the focal plane
a_0	On-axis amplitude of a Gaussian beam
$B_x\left(\mathbf{R}_1, \mathbf{R}_2\right)$	Covariance
$B_\chi\left(0\right)$	Log amplitude covariance evaluated at zero
C	Contrast
C_n^2	Index of refraction structure constant
c	Speed of light
D	Diameter of the aperture
D_{corr}	Speckle correlation diameter in the receiver plane
D_{rec}	Receiver diameter
D_{tar}	Diameter of the beam in the target plane at range R
$D_x\left(\mathbf{R}_1, \mathbf{R}_2\right)$	Structure function
d	Separation between the receiver and laser axes in the target plane
d	Length of the semiconductor crystal
d_0	Separation between the receiver and laser axes at the LADAR
$E\left(t\right)$	Electric field

Symbol	Definition
E	Spectral irradiance
E_L	Total energy in the laser pulse
$E\left(\lambda_L, R\right)$	Total energy measured by the detector
$E_f\left(r_f, R\right)$	Irradiance on the focal plane
$\overrightarrow{E}(\overrightarrow{R})$	Vector amplitude of the electric field
$e\left(t\right)$	Combined field on the focal plane in a heterodyne detection system
F_0	Phase front radius of curvature of beam at transmitter
$F\left(R, r, \psi\right)$	Distribution of laser power over the target plane
f	Focal length of the system
h	Height above the ground
$h\left(\lambda - \lambda^{'}, R\right)$	Normalized spectral distribution after scattering
I	Irradiance
I	Intensity
I	Signal current
$I\left(\xi, \eta\right)$	Spatial intensity profile across the target
I_0	Modified Bessel function of the first kind
$i\left(t\right)$	Current through the sample
J_1	First order Bessel function of the first kind
$\mathbf{K}$	Spatial wavenumber
k	Wavenumber
L_0	Outer scale of turbulence
L	Spectral radiance
$L\left(l, \theta_0, \phi_0, \lambda\right)$	Spectral radiance reaching the sensor
ℓ_0	Inner scale of turbulence
l	Slant range
$l\left(\lambda\right)$	Normalized spectral distribution
$MCF\left(\rho\right)$	Aperture mutual coherence function
$m\left(\mathbf{R}\right)$	Overall mean
$N\left(R\right)$	Number density of the species of interest
N_c	Number of excited carriers
$n(\overrightarrow{R})$	Index of refraction
n Number of range steps	
P_L	Average power in the laser pulse
$P\left(\lambda_L, R\right)$	Total scattered laser power
p_I	Probability density function for intensity
p_Θ	Probability density function for phase

Symbol	Definition
$p_{I,\Theta}$	Joint probability density function
$p(\theta, \phi)$	Scattering phase function
$Q_b^N(\lambda)$	Background-radiation noise
R, L	Distance of the scattering volume from the transmitter-receiver
R	Distance from the center of a spherical wave
R	Scalar distance between two position vectors
$\mathbf{R}$	Difference between two position vectors
R_{ref}	Reference range
$R_I(\Delta x, \Delta y)$	Speckle intensity autocorrelation
$R_S(\Delta x, \Delta y)$	Aperture autocorrelation function
R_T	Range to the topographical target
dR	Size of a range step
$\mathbf{r}$	Position in the target plane
r_0	Effective radius of the telescope lens
r_0	Fried's coherence length
r_b	Radius of the central obscuration
r_f	Position on the focal plane
r_{op}	Object point in the target plane
$r_T(R)$	Radius of the receiver field of view in the object plane
S	Area of the aperture
$S(R)$	Range-normalized signal variable
s_b	Distance between the central obscuration and the mirror
$U(\overrightarrow{R})$	Scalar component of the electric field in the plane transverse to the direction of propagation
$V(t)$	Analytic signal
W	Root-mean-square wind speed
W_0	Laser output aperture radius, i.e. beam radius
$W(R)$	Radius of the laser pulse in the target plane
$x_1(\mathbf{R})$	Fluctuating part of a random process with zero mean
x_f	x position on the focal plane
x_{od}	Obscuration point x position in the target plane
x_{op}	Object point x position in the target plane
Δx	Difference in position in the x direction
y_f	y position on the focal plane
y_{od}	Obscuration point y position in the target plane
y_{op}	Object point y position in the target plane

Symbol	Definition
Δy	Difference in position in the y direction
z	Altitude above mean sea level
α	Absorptance
$\beta\left(\lambda_L, R\right)$	Volume backscatter coefficient
χ	Gaussian distributed random variable
δ	Inclination angle between the receiver and laser axes
$< \delta^2 >$	Mean-square displacement in the focal plane
$\delta\left(\nu_X, \nu_Y\right)$	Dirac delta function
η	y distance variable in the target plane
η	Quantum efficiency
γ	Radius of curvature of the beam
κ	Scalar spatial wavenumber
$\kappa\left(\lambda_L, r\right)$	Total atmospheric extinction
$\overline{\kappa}\left(\lambda_L, r\right)$	Atmospheric extinction without the species of interest
λ_L	Wavelength of the transmitted light
$\lambda^{'}$	Wavelength after inelastic scattering
$\mu_A\left(\Delta x, \Delta y\right)$	Complex coherence factor
ν	Spatial wavenumber in focal plane
ν	Spatial frequency
$\overline{\nu}$	Drift velocity
ν_L	Frequency of the laser
ν_X	Spatial frequency in the x direction
Ω_0	Acceptance solid angle of the receiver system
ω_0	Angular frequency of the light
ν_Y	Spatial frequency in the y direction
$\Phi_n\left(\kappa\right)$	Kolmogorov spectrum
$\Phi_x\left(\kappa\right)$	Spatial power spectral density
ϕ	Receiver-optics half opening angle
ϕ	Phase of the electric field
ϕ_0	Constant phase of a plane wave
ϕ_0	Azimuthal angle
ρ	Position in the receiver aperture plane
ρ	Spatial frequency
ρ	Reflectance
ρ_c	Short term beam centroid
ρ_L	Long term beam radius
ρ_s	Short term beam radius

Symbol	Definition
ρ^s	Topographical target's scattering efficiency
ρ_0	Long term transverse coherence length
ρ_{0s}	Short term transverse coherence length
σ	Standard deviation
σ^2	Variance
σ_I^2	Normalized intensity variance
σ_χ^2	Variance of the log amplitude χ
$\sigma^A(\lambda_L)$	Absorption cross section of the species of interest
τ	Multipath time
τ	Transmission
τ_d	Integration period of the detector
τ_d	Drift time of a carrier across the length of a semiconductor crystal
τ_L	Effective pulse duration
τ_0	Average lifetime of an excited carrier
τ_0	Time constant of the atmosphere
τ_d	Drift time for a carrier across d
θ	Phase
θ	Laser's half divergence angle
θ_0	View angle
φ	Zenith angle
φ	Power spectral Density
ξ	x distance variable in the target plane
$\xi(R)$	Geometrical form factor
$\xi(R, r, \psi)$	Geometrical probability factor
$\xi(\lambda_L)$	Receiver's spectral transmission factor
$\zeta(x, y)$	Receiver aperture function

Chapter 1

Introduction

Optical remote sensing can be divided into passive and active categories based on the source of the light. Passive systems detect natural sources, such as the sun or blackbody radiation due to the temperature of an object. Active systems use a light source, such as a laser, that can be controlled by the user and tailored for specific applications. Several types of active systems are used. Laser Detection and Ranging (LADAR) systems are analogous to Radio Detection and Ranging (RADAR) systems, but use light instead of radio waves. LADAR systems have existed for almost 40 years, but have been hampered by complexity and high costs (Fiocco and Smullin 1963). LADAR systems are used to locate the position of an object. Light Detection and Ranging (LIDAR) systems are used to derive the properties of an object, such as density or chemical composition. Various types of LIDAR systems exist, each based on a different scattering process and operate in different spectral regions from the ultraviolet through the infrared. These systems have been used for a variety of commercial and military applications such as pollution monitoring and tracing, forest fire detection, and agriculture monitoring.

Advances in tunable lasers and infrared detectors have recently allowed much more sophisticated and accurate work to be done, especially in the infrared spectral region, but a comprehensive spectral LADAR/LIDAR model has yet to be developed. The infrared portion of the spectrum is significant because the narrow absorption lines in the $3-5$ and $8-12$ micron regions due to roto-vibrational molecular transitions allow trace species to be uniquely distinguished, although water vapor and carbon dioxide absorption can limit the practical measurement range. The near infrared (NIR) range, $0.7-2.5$ microns, contains overtone and combination vibrational bands that are suitable for long-range measurements of concentrated gases such as carbon dioxide, water vapor, carbon monoxide, and oxygen. Infrared Differential Absorption Ladar (DIAL) measurements in the NIR are capable of detecting small concentrations of gases at long distances and are used to perform meteorological measurements such as water vapor concentration and temperature and pressure profiles. Rapidly tunable infrared lasers allow the simultaneous detection of molecules with absorption lines in the $3-5$ and $9-12$ micron regions.

The Digital Imaging and Remote Sensing Image Generation (DIRSIG) model was developed at the Chester F. Carlson Center for Imaging Science (CIS) (Schott et al. 1999). It is a quantitative model based on first principles that calculates the spectral radiance reaching the sensor from the visible through to the long-wave infrared. DIRSIG generates an accurate representation of what a sensor would see by modeling all processes involved in the imaging chain. Currently DIRSIG only models passive sources. The model is an integrated collection of independent submodels that are combined to produce radiance field images with high radiometric fidelity in the $0.3-30.0$ micron region.

To provide a tool to assist in LADAR/LIDAR development, this research is the first stage of a multipart effort to incorporate a LADAR/LIDAR model into DIRSIG. To allow for future growth, the model and coding are modular and anticipate the inclusion of ad-

vanced sensor models and inelastic scattering. The model at this point considers only elastic scattering processes. It calculates the irradiance onto the focal plane based on the system characteristics and the assumed atmosphere. The model accounts for the geometrical form factor (a measure of the overlap between the sensor and receiver field of view) in both the monostatic and bistatic cases. The model includes the effect of multiple bounces from topographical targets. Currently, only direct detection systems are modeled. Several sources of noise are extensively modeled, such as speckle from rough surfaces and atmospheric turbulence phase effects.

The DIRSIG LADAR/LIDAR model is unique in several aspects. It is the first synthetic image LADAR/LIDAR model to model a bistatic system and atmospheric turbulence and to include the aerosol return and the effects of multiple bounce. Additionally, DIRSIG is inherently a spectral model and multiple runs are not necessary to model the return at multiple wavelengths.

Since this effort is only the first stage of a multipart effort, Chapter 2 contains a general overview of the various types of LADAR/LIDAR systems and their uses. Chapter 3 contains not only the basic LADAR/LIDAR theory implemented, but also includes the basic inversion techniques, reviews several detection methods, and summarizes the major sources of noise. Chapter 4 reviews current LADAR simulation programs, their approach, and their limitations. Chapter 5 summarizes the DIRSIG integration. Finally, Chapter 6 shows actual results from the DIRSIG LADAR/LIDAR model. The DIRSIG LADAR/LIDAR model has yet to be validated. Where applicable, parts of the code were used to reproduce published results.

Chapter 2

Overview

This chapter begins with an overview of the various types of LIDAR systems, their underlying physical processes, and applicable wavelength ranges. Following the LIDAR discussion, the concept of LADAR is reviewed along with examples of its use. Section 2.2 contains a review of the variety of laser sources and the methods to do wavelength conversion. The chapter ends with an introduction to DIRSIG and its various components.

2.1 Types of LADAR/LIDAR

Each type of LIDAR is based on an interaction of light with matter through the mechanism of absorption, fluorescence, scattering, or a combination (Measures 1984). Absorption occurs when the incident light has the same frequency as a specific molecular transition and is absorbed and not re-emitted, resulting in attenuation of the incident light. Fluorescence occurs when the incident light has the same frequency as a specific atomic or molecular transition and is absorbed and then re-emitted at a lower frequency. There are four basic types of scattering: Rayleigh, Mie, Raman, and resonance. Rayleigh scattering occurs

when the scatterers are much smaller than the wavelength of the incident light. The light scatters elastically, i.e., with no change in wavelength. Mie or "aerosol" scattering occurs when the size of the scatterers is approximately equal to the wavelength of the incident light. Again, the light scatters elastically with no change in wavelength. Raman scattering is an inelastic mechanism so that the wavelength of the scattered light differs from that of the incident light. The wavelength shift is characteristic of the molecule. Resonance scattering or "atomic fluorescence" occurs when the incident light has the same frequency as a specific atomic transition and is scattered by a large cross section with no change in frequency. Differential absorption and scattering (DAS) (as the name implies) is a combination of absorption and scattering and is more a "technique" than a physical "process". The absorption features of molecules are broadened due to a combination of natural, collision, and Doppler broadening. In DAS the backscattered signals at two frequencies of light are compared: one tuned to the peak of an absorption feature and the other to the wing of the same feature. Of all the phenomena reviewed, Mie scattering has the largest cross section (10^{-8} $\frac{cm^2}{sr}$), followed by resonance scattering (10^{-14} $\frac{cm^2}{sr}$), DAS (10^{-18} $\frac{cm^2}{sr}$), molecular fluorescence (10^{-20} $\frac{cm^2}{sr}$), Rayleigh scattering (10^{-25} $\frac{cm^2}{sr}$), and at the lowest end Raman scattering (10^{-28} $\frac{cm^2}{sr}$). In general, the larger the cross section the smaller the concentration that can be detected. The benefit of a large cross section can be offset by large atmospheric absorption.

Often, the division between the many different types of LIDAR is arbitrary. Several types are reviewed in Section 2.1.1 through Section 2.1.10. This is not an exhaustive list, but highlights some of the differences, various uses, advantages, and disadvantages. Figure 2.1 contains a snapshot of the various LIDAR/LADAR systems that will be covered.

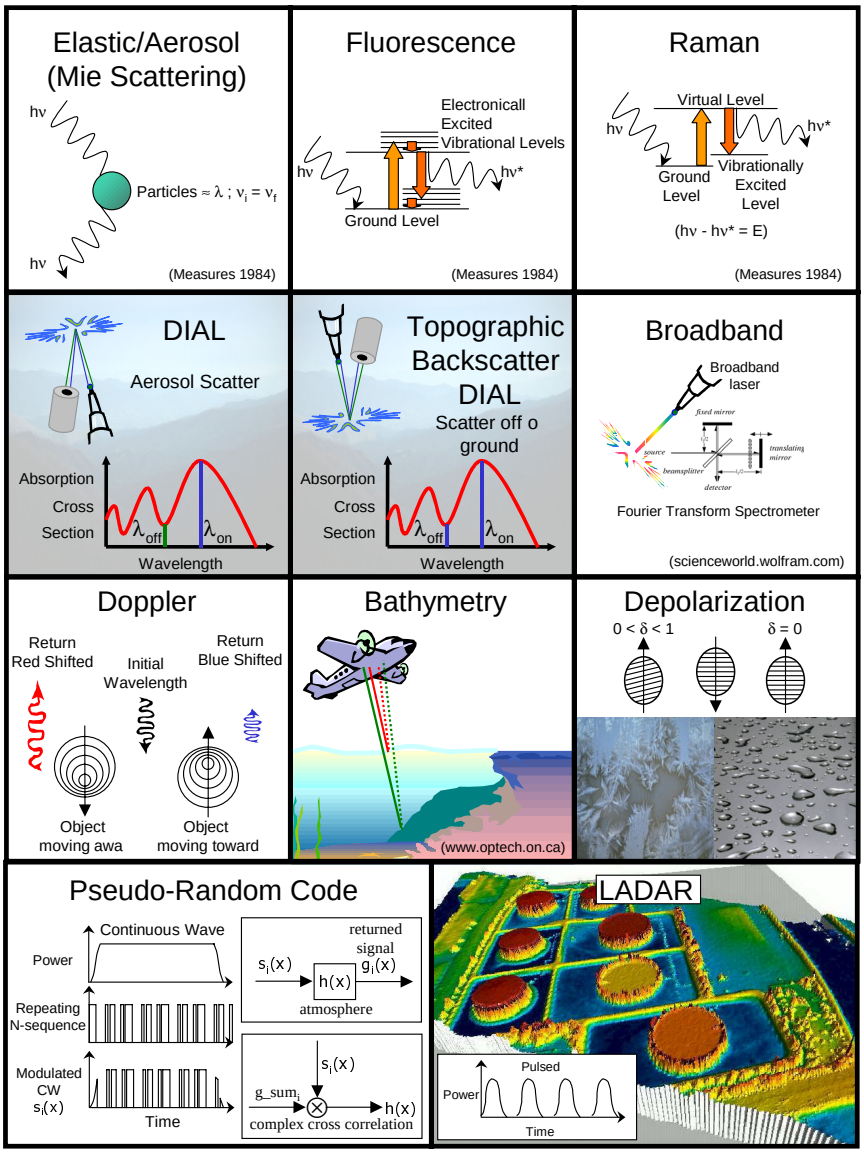

Figure 2.1: The various types of LIDAR/LADAR systems are summarized above. Each type of LIDAR is based on an interaction of light with matter through the mechanism of absorption, fluorescence, scattering, or a combination. Often, the division between the many different types of LIDAR is arbitrary. This is not an exhaustive list. DIRSIG has the capability of modeling Elastic Scattering, DIAL, Topographic Backscatter DIAL, Broadband, Bathymetry, and LADAR.

2.1.1 Backscatter / Elastic / Aerosol Lidar

Elastic LIDAR, often called "backscatter or aerosol" LIDAR, is based on Mie scattering. Since Mie scattering has the largest cross section and a narrow bandwidth, this technique is the most sensitive and thus has the longest detection range. Elastic LIDAR uses optical filters to remove the background illumination that can make the returning light hard to detect. Shorter wavelengths are more effectively scattered, but also experience more atmospheric attenuation. Three-dimensional maps of aerosol concentration can be obtained by scanning of laser beam and by gating the detection time. Time-gating uses a pulsed laser which sends out discrete pulses of light. The light then elastically scatters from the atmosphere and returns to the detector. The time delay is related by the speed of light to the total distance the light travelled. By measuring the return signal at various times, the aerosol volume backscattering coefficient at varying distances from the detector is measured. The aerosol concentration is derived by using measured data that equates a certain aerosol volume backscatter to a certain aerosol concentration or by using a model based upon an assumed size distribution and aerosol type. Elastic LIDARs have employed Nd:YAG lasers at 1.06 micron and eye safe lasers at 1.5 micron. Unlike fluorescence, Raman, DIAL, and broadband LIDARs, elastic LIDAR can neither detect molecules nor determine the composition of a scattering material. Elastic LIDARs can be used to measure the height of cloud bases and track plumes. One of the more well-known elastic LIDARs is the Lidar In-space Technology Experiment (LITE) instrument developed by NASA. This instrument was used to measure various quantities including the vertical distribution of clouds, planetary boundary layer height, tropospheric and stratospheric aerosols, and surface reflectance. Figure 2.2 shows a map of multilayer cloud structures produced from LITE data.

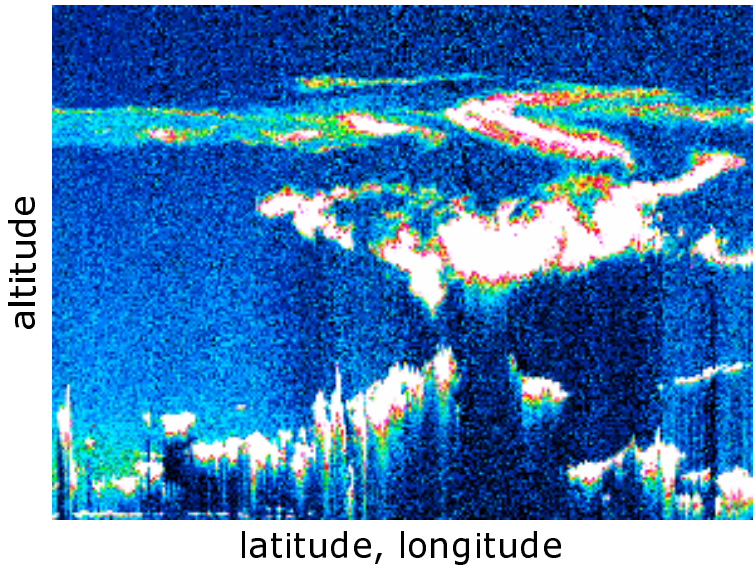

Figure 2.2: Map of Multilayer Cloud Structures Produced by LITE (obtained from http://www-lite.larc.nasa.gov/)

2.1.2 Fluorescence LIDAR

Fluorescence LIDAR can identify scattering constituents. Like Raman LIDAR, the wavelength difference in the returned signal allows species to be identified. For most atmospheric work, the molecules of interest are organic and have broad-band UV absorptions. Fluorescence LIDARs are limited because they use ultraviolet (UV) wavelengths to ensure effective absorption. The resulting fluorescence is also in the UV spectral range and is severely attenuated by the atmosphere. The wide bandwidth of the fluorescence signal requires that the detectors have a wide bandwidth, which results in lower sensitivity and allows background illumination to enter the detector. As a result, many fluorescence measurements are made at night. The necessary wavelengths are generated by either UV excimer lasers or from solid-state lasers often doubling, tripling, or even quadrupling the

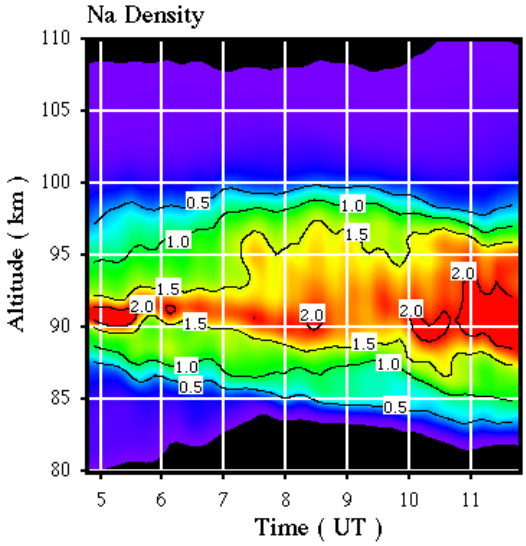

Figure 2.3: Graph of Na Density Produced by GALE (obtained from http://conrad.ece.uiuc.edu/Research/SOR/Observed/950404/)

frequency with nonlinear optical techniques to the desired wavelength. An example of a fluorescence LIDAR is the Na Wind/Temperature LIDAR developed by the Electro-Optic Systems Laboratory (EOSL) at the University of Illinois (Gardner and Papan 1995). Data from this instrument has been used to measure both wind speed and temperature. During the Giant Aperture Lidar Experiment (GALE), the Na Wind/Temperature LIDAR was coupled to a 3.5-meter telescope at Starfire Optical Range. Figure 2.3 shows a graph of Na density produced from GALE data.

2.1.3 Raman LIDAR

As already mentioned, Raman scattering has the lowest cross section. The returning light has a predictable narrow wavelength if scattered from certain molecules. The narrow wavelength allows Raman scattering to be employed to detect molecules with high con-

centrations, such as water vapor. Since Raman LIDAR systems do not use tunable lasers, powerful lasers are available. The low scattering cross section is actually useful in certain cases because it allows the light to penetrate farther into areas of high concentration, such as clouds. Like fluorescence LIDAR, Raman LIDAR is employed in the ultraviolet (UV) region of the spectrum because its cross section strongly depends on wavelength. The significant atmospheric attenuation in the UV region limits the range of Raman LIDAR systems. An example of a Raman LIDAR is the CART Raman Lidar used by the Atmospheric Radiation Measurement Program, which is studying global changes under the sponsorship of the Department of Energy (DOE). The CART instrument is used to measure the vertical profile of the water-vapor mixing ratio, aerosol scattering ratio, and backscatter depolarization ratio. Figure 2.4 shows a graph of the water vapor mixing ratio.

2.1.4 DAS / Differential Absorption LIDAR (DIAL)

Since DAS, often called DIAL, systems are based on gaseous absorption, they can be used in the UV, visible, and infrared regions. Thus many different molecules such as ozone and carbon monoxide can be detected. DIAL systems usually employ line-tunable molecular lasers and can discriminate among specific molecules. CO_2 DIAL systems operate in the $8 - 12$ micron window, which spectroscopists call the 'fingerprint' region because so many narrow absorption features exist there that allow molecules to be uniquely distinguished.

Traditional DIAL is similar to aerosol LIDAR in that the returned signal is elastically scattered. Two different wavelengths are chosen, one with and one without significant molecular absorption. By evaluating the ratio of powers in the two time-gated returns, three-dimensional concentration maps of a specific molecule can be generated, as shown in Figure 2.5.

Each absorption feature has three characteristics: peak position, absorption cross sec-

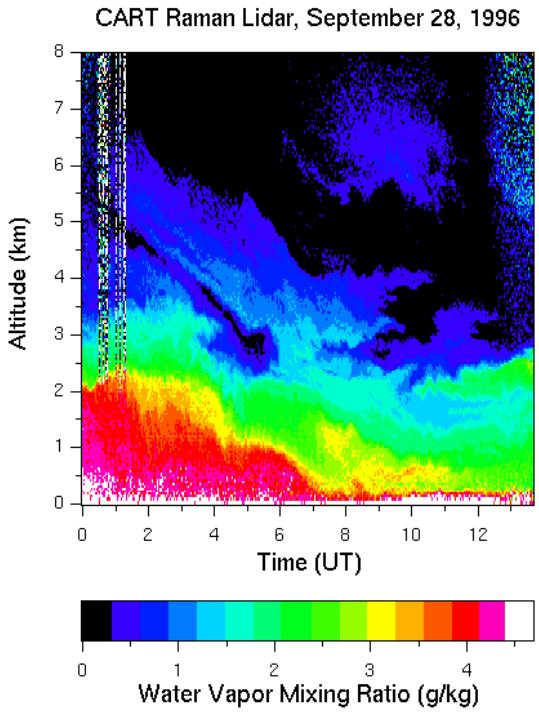

Figure 2.4: Graph of Water Vapor Mixing Ratio Produced by CART (obtained from http://www.arm.gov/docs/instruments/static/rl.html#Primary_Quantities_Measured_with_System)

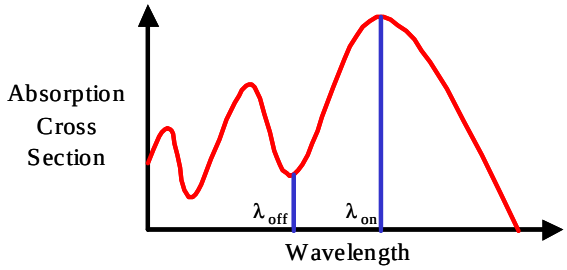

Figure 2.5: DIAL systems calculate the ratio of the power in the returned on-line laser pulse to the power in the off-line laser pulse.

tion, and linewidth that depend on such variables as density, pressure, and temperature. When the dominant broadening mechanism is molecular collisions, the absorption cross section is assumed to be Lorentzian; when due to the Doppler effect, the cross section is assumed to be Gaussian. When neither of these broadening mechanisms are dominant, the convolution of the Lorentzian and Gaussian profiles is used. This is called the Voigt profile. Another factor to consider is that the peak position of the absorption feature is pressure dependent. These spectral parameters for various gases are included in the high-resolution transmission molecular absorption (HITRAN) database developed by the Air Force Cambridge Research Laboratories (AFCRL). If some of these parameters are known, the others can be calculated. For example, gases of known concentrations that are both globally and locally well mixed can be used to determine the atmospheric temperature. This stability allows DIAL systems to use oxygen absorption in the near-infrared region to determine temperature and pressure profiles.

Traditional DIAL measurements are based on several assumptions (Fastig et al. 1996). First, the atmospheric transmission and the Rayleigh backscatter at the two wavelengths are assumed equal. This is not always the case. For example, the backscatter depends significantly on wavelength at $\lambda \approx 9.5$ microns. Second, the pulse separation time between

the on-line and off-line pulses is less than the time constant of atmospheric turbulence. Under strong turbulence conditions or with an airborne system, the return signals can differ due to beam wandering, changes in the scattering composition, etc. The resulting error in the calculated concentrations can be reduced by averaging many shots. Finally, the spectral width of the laser pulses must be less than the width of the absorption feature. Fastig demonstrated that a laser pulse with a spectral width up to a few times wider than the absorption feature can be used in combination with a gas-filter correlation technique without significantly reducing sensitivity (1996). Bosenberg lists some additional standard assumptions (1998). The backscattered light is assumed to be incoherent. Single scattering is dominant. The scattering time constant is much less than the length of the laser pulse. The source is monochromatic. Finally, the wavelength remains unchanged throughout the process.

A standard DIAL system uses the ratio of the returns at each wavelength or the derivative of the natural logarithm of the ratio. By averaging many shots, the resulting noise should decrease as $N^{-\frac{1}{2}}$, where N is the number of pulses averaged. This assumes that the noise is uncorrelated.

Finally, DIAL systems need to be rapidly tunable between many laser wavelengths to distinguish between many different chemicals. Lasers capable of being rapidly tuned have only recently become available.

2.1.5 Topographic Backscatter DIAL

In topographic DIAL, the signal is scattered from a solid target, such as a retroreflector. This technique evaluates the integrated concentration-absorption cross section over the pathlength, therefore, range information is unavailable. By scanning the system, angles may be determined accurately. Topographic DIAL has more sensitivity than traditional

DIAL, but its use depends on the availability of a target and assumes that the reflectivity of the topographical reflector remains constant. This is not true in airborne systems that use the earth as the topographical reflector and can result in large systematic errors.

2.1.6 Broadband LIDAR

Broadband LIDAR systems use broadband lasers as sources and make spectral discriminations on the receiver end. Broadband lasers emit a range of wavelengths. Broadband lasers can be pulsed or emit a continuous beam. The first continuous broadband laser was developed at Bell Laboratories (Gmachl et al. 2002). It is based on semiconductors and produces an output from $6-8$ microns. A Fourier transform spectrometer is a typical receiver. Unlike the typical DIAL system, "broadband" LIDAR has the advantage of being able to measure the concentration of many gases simultaneously. Some additional advantages of broadband LIDAR include: the ability to use narrow absorption features without a narrow bandwidth source; suppression of Doppler error; decreased requirement for laser calibration and linewidth stability; reduced error if several absorption features are available for the same gas; ability to measure spectral broadening and thus obtain pressure and temperature information; and corrections for overlapping absorption features that can be made without more measurements or assumptions (Douard et al. 1996). This last feature is especially advantageous in the infrared spectral region where the features of numerous gases overlap. The main disadvantage of broadband LIDAR is the inability to use this technique over large distances due to the spreading of the energy over a wide spectral range.

2.1.7 Coherent Doppler LIDAR

Doppler LIDAR also uses the signal from aerosol scattering, but it is the Doppler shift of the return signal that is measured. The velocity and direction of wind can be determined

from this measurement. Coherent detection is used to measure the Doppler shift. Since the measurement depends on the difference in frequency between the laser and the scattered signal caused by the motion of the source, the laser frequency must be pure, highly stable, and precisely determined. Applications of coherent Doppler LIDAR include measurement of wind velocity, direction, shear, and wake vortices for aircraft safety and improved weather prediction.

2.1.8 LIDAR Bathymetry

LIDAR Bathymetry is based on the property that green light penetrates water. LIDAR bathymetry systems use pulses of green and red light to measure water depth. The red light reflects from the surface of the water while some of the green light penetrates the water and reflects from the bottom. The difference in return times between the two pulses gives the depth of the water.

2.1.9 Depolarization LIDAR

Depolarization LIDAR is used for studying cirrus clouds. Spherical water droplets do not modify the polarization of the beam while nonspherical ice crystals cause the reflected beam to be slightly depolarized. The transmitted laser beam is polarized and the receiver is polarization sensitive. By evaluating the ratio of the depolarized component to the original polarization, the quantity and size of ice crystals can be determined. As mentioned previously, the CART instrument is polarization sensitive and is used to make measurements of the backscatter depolarization ratio, as shown in Figure 2.6.

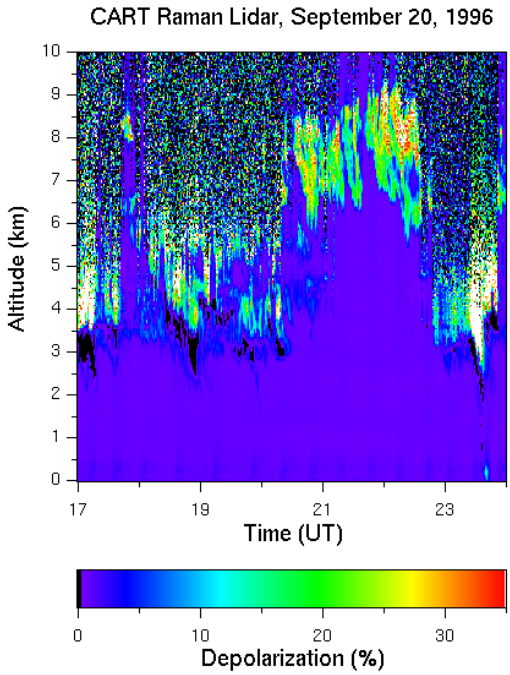

Figure 2.6: Graph of the Backscatter Depolarization Ratio Produced by CART (obtained from http://www.arm.gov/docs/instruments/static/rl.html#Primary_Quantities_Measured_with_System)

2.1.10 Pseudo-Random Code Modulation

LIDAR systems use both pulsed (short pulse) and continuous wave (long pulse) beams. Continuous lasers are smaller, lighter in weight, and cheaper. Pseudo-random code modulation systems use a continuous wave laser and modulate the power amplitude using a repeating N-sequence as shown in Figure 2.7. The N-sequence resembles a random sequence, but has a specific autocorrelation function. The return signal is the convolution of the repeating N-sequence with the impulse response of the atmosphere. To increase the signal-to-noise, the return is divided into each N-sequence and then summed. Since the cross correlation of the signal with itself approximates a delta function, the atmospheric impulse response is generated by performing a complex cross correlation with the original signal. These systems tend to have a lower signal-to-noise ratio than equivalent direct-detection pulsed systems. Machol's (1997) comparison of the two techniques contains more information on the differences between the two types of systems.

2.1.11 LADAR

LADAR systems are used to detect the positions of topographical targets in three dimensions. Since solid targets scatter much more light than the scattering off of the atmosphere, LADAR systems have a greater range than LIDAR systems. LADAR systems that have both precise position and pointing information can provide both in-scene and absolute geospatial accuracy. Therefore, high-resolution LADAR data is a source of digital terrain elevation data (DTED). In recent years, many commercial airborne LADARs have become available that can provide high-resolution geospatial data over large areas. Currently, there are over forty-six LADAR firms worldwide.

LADAR systems are not just a source of DTED. Many LADAR systems not only

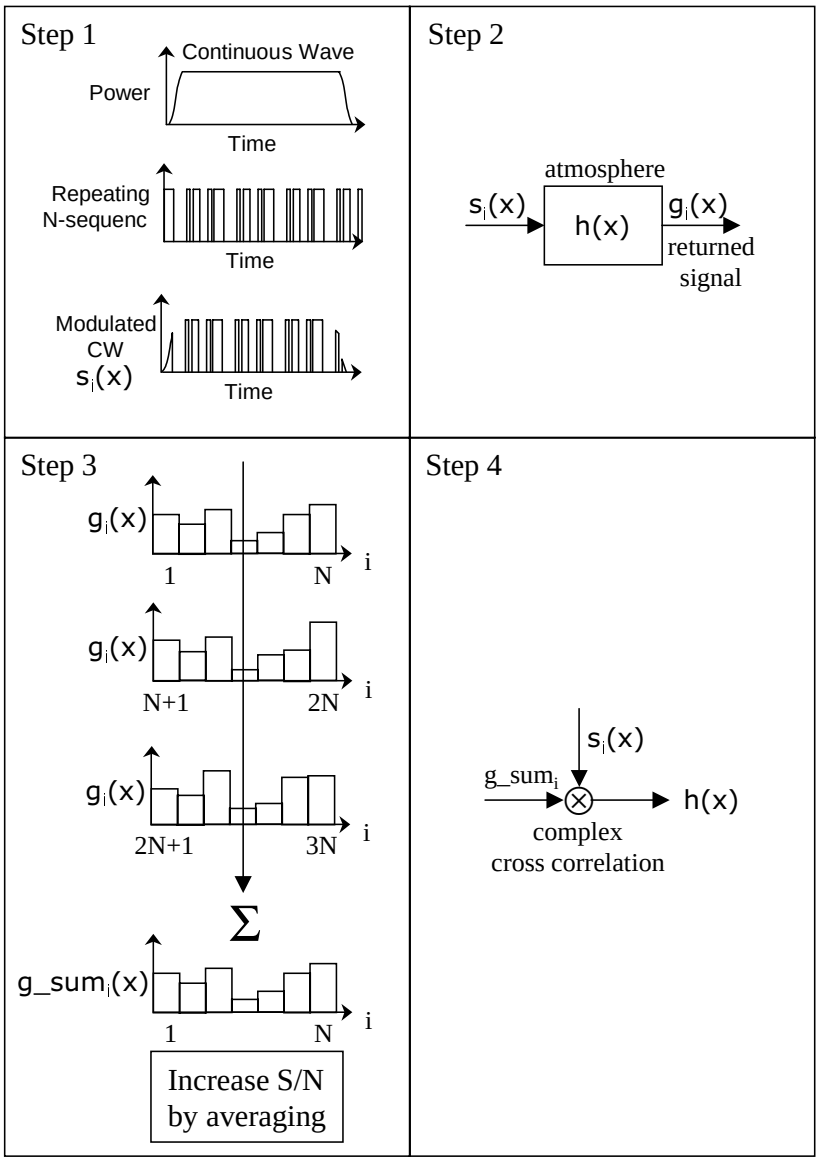

Figure 2.7: A pseudo-random code modulation LIDAR works by first modulating a continuous wave laser (long pulse) with a repeating N-sequence. The return signal is the convolution of the repeating N-sequence with the impulse response of the atmosphere. To increase the signal-to-noise, the return is divided into each N-sequence and then summed. Finally, the atmospheric impulse response is recovered by performing a complex cross correlation.

calculate the range to the target (Figure 2.8), but also record the intensity of the returned light. The fusion of the intensity information with the DTED data creates high-resolution three-dimensional imagery. Since LADAR systems do not rely on passive illumination, they can also image at night. If the LADAR system records all returns then the resulting image can be processed to allow partially obscured objects to detected. This "poke-thru" capability can be used to see beneath foliage to create bare-earth DTED maps (Figure 2.9). LADAR can also be used to detect objects hidden under camouflage. Objects that are often difficult to see in regular imagery, such as telephone wires, can be enhanced in LADAR imagery as shown in Figure 2.10. Finally, for LADAR data with high absolute accuracy, subsequent data sets can be compared to detect geometric changes.

The review of the various types of LIDAR/LADAR is complete. DIRSIG models elastic LIDAR, DIAL, topographic backscatter DIAL, broadband (without speckle), bathymetry, and LADAR. To model fluorescence and Raman LIDAR, fluorescence and Raman models would need to be integrated into DIRSIG. These models would need to calculate the change in wavelength of the scattered light, the direction of the scattered light, and the time delay between absorption and emission. To improve the broadband LIDAR model, DIRSIG would need to account for the wavelength dependence of speckle across the waveband of the transmitter. To model Doppler LIDAR, DIRSIG would need to add movement as a material characteristic to each surface. At each time, the position and instantaneous velocity of each moving surface would need to be calculated and the corresponding frequency shift of the scattered light. To model polarization, DIRSIG would need to calculate the polarization of the source. Since DIRSIG already incorporates polarization in the passive calculation, the polarized LIDAR return could be calculated. To incorporate pseudo-random code modulation, DIRSIG would have to be modified to accept a temporal pulse distribution other than Gaussian. The next section reviews the different types of sources and typical

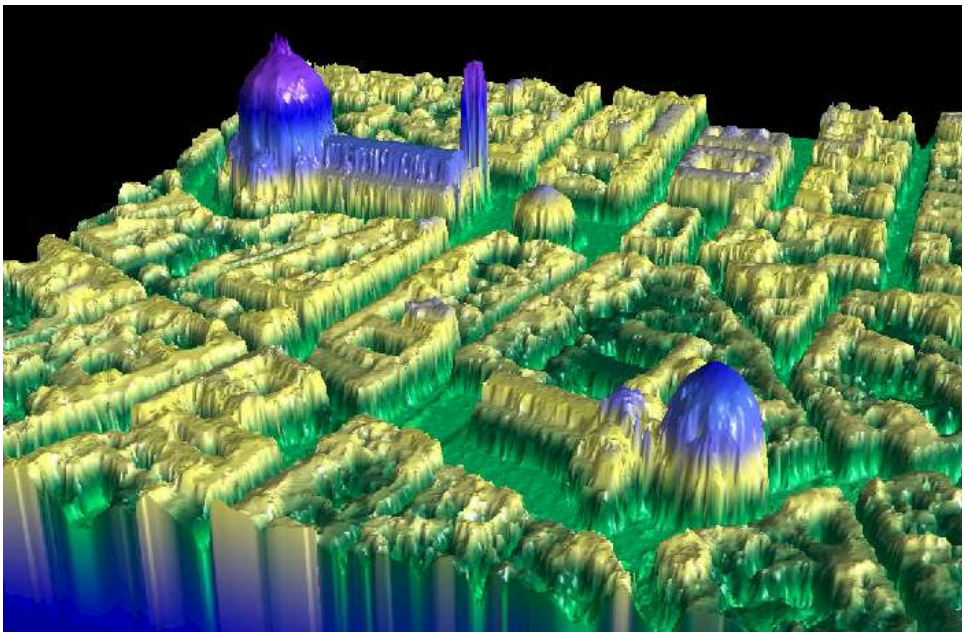

Figure 2.8: LADAR data can be processed to create high resolution DTED of complex scenes. (Image obtained from http://www.optech.on.cal)

systems parameters.

2.2 Types of Sources

Table 2.1 lists some of the different types of lasers used in LIDAR systems and their wavelength ranges. This is not an exhaustive list, but includes the major types. Most of these types are familiar, except perhaps for the optical parametric oscillator (OPO). The OPO is a nonlinear optical device that derives two beams (the signal and the idler) from the original laser "pump" (Milton et al. 1992). The frequencies of the idler and the signal sum to the frequency of the pump, and they can be tuned to various frequencies by adjusting the OPO or by varying the frequency of the pump. OPOs can even be used in tandem to

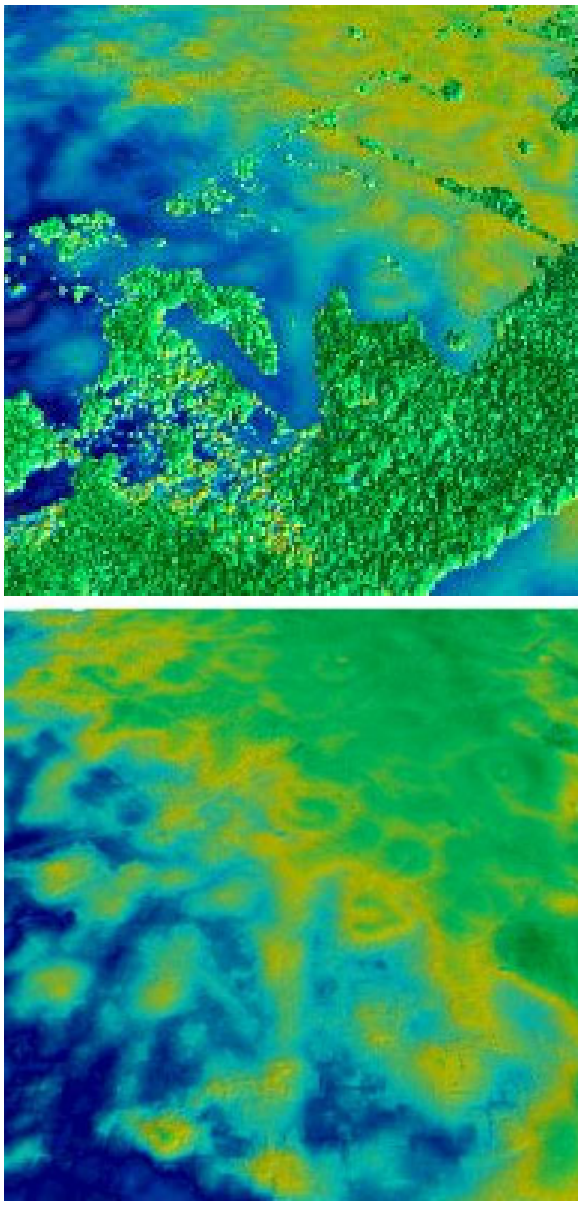

Figure 2.9: LADAR data can be processed to remove vegetation and create bare earth DTED. The top image was created using the first peak return and shows the bare ground and the top of any vegetation. The bottom image was created using the last return, consequently all vegetation has been removed. (Images obtained from http://www.optech.on.cal)

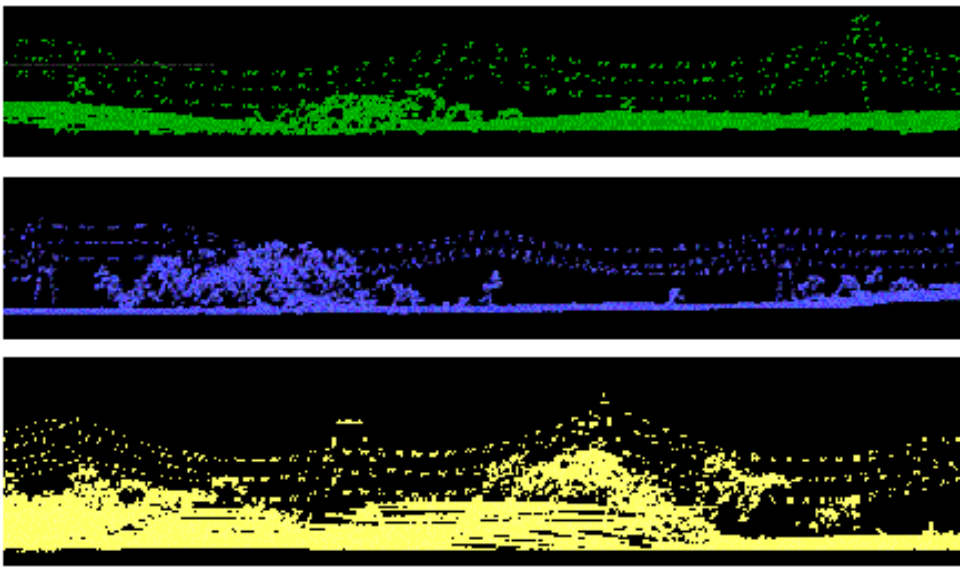

Figure 2.10: LADAR data can be used to detect objects that are often difficult to see in regular imagery. The ability to place the points in three dimensions allows the image to be rotated and separates the hits from the telephone wires from the rest of the image. This separation, along with the ability of the brain to connect disjoint points, allows easy identification of the wires. (Image obtained from http://www.optech.on.cal)

Type of Lasers	**Wavelengths**
Dye Lasers	0.2-1 μm
Excimer Lasers	0.19-0.35 μm
Solid-state Lasers	Ruby - 0.694 μm Nd:YAG – 1.06 μm
Tunable Solid-state Lasers	Alexandrite 0.71-0.8 μm Ti:Al_2O_3 0.65-1 μm Co:MgF_2 1.5-2.3 μm
Gas Lasers	CO_2 9-11 μm CO 5-6 μm HF 2.7-3 μm DF 3.7-4 μm N_2O 10-11 μm CS_2 11-12 μm
Color-Center Lasers	0.4-2 μm
Wavelength Converters	Shift emission or tunable range to longer or shorter wavelengths by use of Raman shifting, harmonic generators, or mixing crystals. For doubling, tripling, and mixing CO_2 wavelengths, crystals such as $AgGaS_2$ or AgGaSe are used.
OPOs	Wide range continuously tunable low power output. Uses crystals such as $LiNbO_3$ tunable from 1.5-4 μm or urea and BBO both tunable from UV to NIR when pumped by Nd:YAG or its harmonics.
GaAs Diode Lasers	Gallium Aluminium Arsenide 0.75-0.9 μm Indium Gallium Arsenide Phosphide 1.2-1.5 μm Gallium Indium Phosfide 0.65-0.69 μm

Table 2.1: Types of Sources (Zanzottera 1990)

System Parameter	Typical Values
Pulse Energy	0.3-1 J
Repetition Rate	10-20 pulses per second
Pulse Duration	10 nsec for Nd:YAG and excimers lasers 100-200 nsec Alexandrite 300 nsec Co:MgF_2 0.1-1 μsec CO_2
Beam Quality	Heterodyne - diffraction limited All others - beam divergence lower than telescope field of view
Spectral purity	Greater than 99%

Table 2.2: Typical Source Parameters (Zanzottera 1990)

create even wider frequency ranges.

Until recently, the use of DIAL in the mid-infrared spectral region has been limited by the absence of suitable sources (Gardiner et al. 1996) (Vezin et al. 1996). The mid-infrared band ($3-4$ microns) is important because it contains the fundamental carbon-hydrogen stretch absorption associated with gases such as methane, petroleum vapor, ethene, and hydrogen chloride (Gardiner et al. 1996). Most molecules of interest to organic chemists have spectral features in the $2.5-15$ micron region. There is less Rayleigh backscatter in the infrared region and interference between gases is increased. These conditions necessitate the use of the DIAL technique. For a DIAL system, a source must meet three criteria. The source must be able to tune to the peak of an absorption feature of the target gas. The laser linewidth must be less than the width of the absorption feature. Finally, the source must be able to switch rapidly from the on-line and off-line wavelengths. The second criterion can be addressed by the use of "injection seeding," which is used to create narrow linewidths. In injection seeding, a low-power, narrow-linewidth laser is injected into the resonant cavity of a high-power laser or OPO. In materials with a broad emission spectrum many wavelengths are often competing to lase. If the low power beam is injected before any wavelength becomes dominant, then the high powered laser will lase at the wavelength of the low powered one. The third criterion is addressed by recent advances in rapidly tunable lasers. To give the reader a feel for an average source, Table 2.2 gives typical values for various system parameters.

This section reviewed the different types of sources and typical system parameters. The different types of sources included dye, excimer, solid-state, tunable solid-state, gas, color-center, wavelength converters, OPOs, and GaAs diode lasers. Advances in laser development are rapidly occurring. Depending on the purpose of the system, the parameters of a LIDAR/LADAR system vary. In general, work is being done to improve the quality of

the laser source, in decreasing the pulse duration, and in creating more sensitive detectors. The final section of this chapter reviews the DIRSIG model.

2.3 DIRSIG

DIRSIG is a synthetic imagery generation model developed at the Center for Imaging Science (CIS) at the Rochester Institute of Technology (RIT) (Schott et al. 1999). It is a quantitative first principles based model that calculates the sensor reaching radiance from the visible region through to the long-wave infrared region on a spectral basis. DIRSIG generates a very accurate representation of what a sensor would see by modeling all the processes involved in the imaging chain. A sample image is shown in Figure 2.11.

DIRSIG is an integrated collection of independent submodels based on first principles that work in conjunction to produce radiance field images with high radiometric fidelity in the $0.3 - 30.0$ μm region. Some of these links are illustrated in Figure 2.12. The geometric database contains the faceted surfaces in the scene that make up the various objects. Wire-frame objects are constructed with AutoCAD, a computer-aided design program from Autodesk. Each faceted surface is assigned a material type. The material database associates the optical and thermodynamic properties to each material type. The properties of the sensor, such as field of view, sampling pattern, sampling density, focal point location, and modulation transfer functions of the various system components, are contained in the sensor model. The raytracer uses the information in the sensor model to cast a ray from the focal point of the sensor through each pixel in the effective focal plane to a point on the ground. Additional rays are then cast from this point to determine current sun-shadow conditions, sun-shadow history, the downwelled skylight and atmospheric emission reflected from the target back to the sensor. These values, together with information contained in

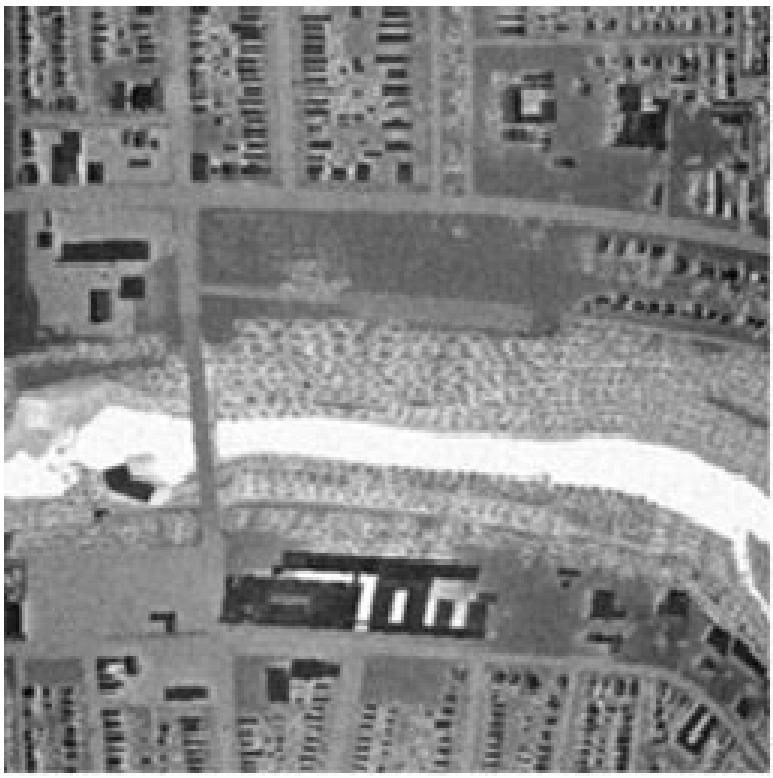

Figure 2.11: A DIRSIG simulation of downtown Rochester, NY with a Bendix infrared line scanner

the site and meteorological databases, are passed to the thermal model that calculates the temperature of the facet to determine its thermal self-emission. MODTRAN, a model of atmospheric transmission, radiance, and flux developed jointly by Spectral Sciences, Inc. and the Air Force Research Laboratory, is used to create atmospheric data profiles that contain atmospheric transmission, self-emission, and scattered sunlight. The radiation propagation model uses these profiles, along with the target, path, and background data, to account for all sources of radiation reaching the sensor at each wavelength. Radiance images are produced by numerically integrating the spectral radiance reaching the sensor with the peak normalized spectral response of the sensor in each band and then convolving with the point spread function of the sensor to produce the final image.

Elastic LIDAR is the most prevalent type. Therefore as a first step in the development of a comprehensive first-principle-based LADAR/LIDAR model, an elastic LADAR/LIDAR model will be incorporated into DIRSIG. The next chapter contains the actual theory necessary to implement the model.

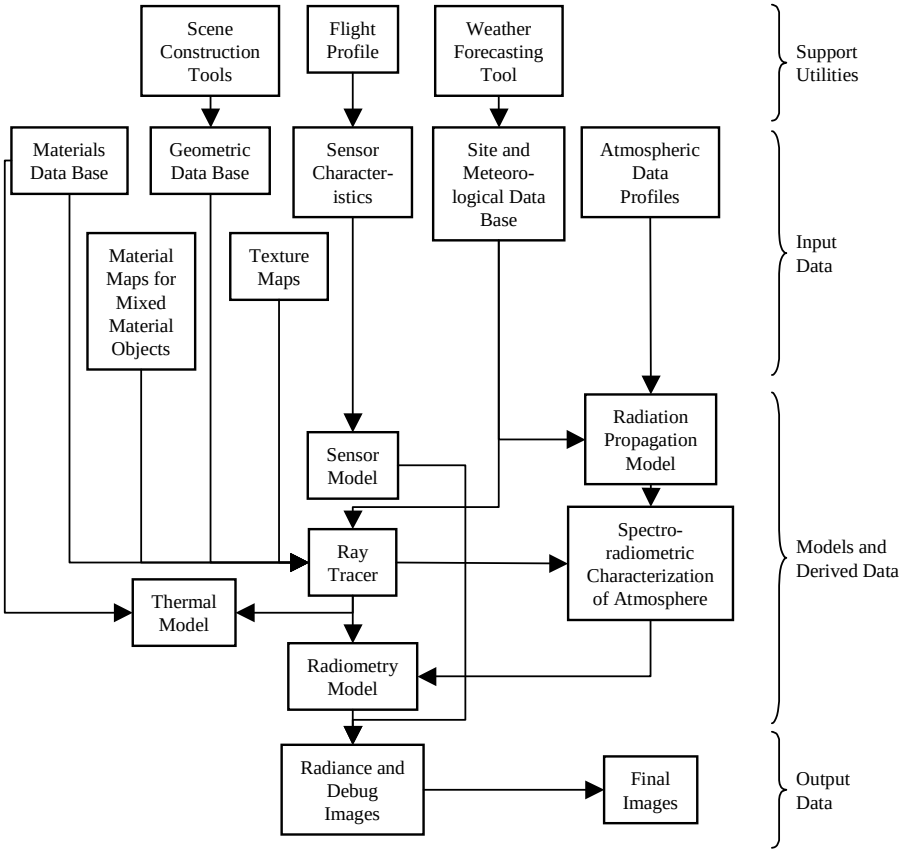

Figure 2.12: Simplified DIRSIG flowchart (Schott)

Chapter 3

Theory

The first section of this chapter motivates the resulting theory by presenting the overall problem and what physical processes will be accounted for. Some processes will also be reviewed to understand the difficulties involved in their implementation and how their absence affects the accuracy of the overall result. Section 3.2 begins with the basic LADAR/LIDAR theory for both the aerosol and topographical return. It briefly describes the basic techniques used to calculate the quantity of interest from the sensed return. It then reviews the geometrical form factor for both monostatic and bistatic systems with and without a central obscuration. The geometrical form factor accounts for the overlap of the transmitted beam and receiver as a function of distance. Next, the compression effect at short-to-intermediate distances due to unfocused returns is reviewed. The section ends with a description of how to calculate the return on a spectral basis. The next section describes the propagation of a laser beam through the atmosphere. It begins with a review of Maxwell's wave equation and the basic types of beams. A major portion of this section describes the effects on the return due to propagation through atmospheric turbulence including scintillation, beam

spread, beam wander, image blurring, and image dancing. The scintillation discussion begins with the formulation of the index-of-refraction structure constant, which shows up in many of the subsequent equations. The scintillation discussion ends with a description of the enhanced backscatter effect, which occurs when a beam travels twice through the same turbulent atmosphere. The formulation presented is based upon weak turbulence theory and the Kolmogorov spectrum. The final two subsections of this section contain a review of atmospheric transmission and a brief introduction to thermal blooming. The second major source of noise, speckle, is reviewed in Section 3.4. Section 3.5 contains a mathematical description of the basic detector types: direct and coherent detection. The calculation of the passive return within the spectral range of the detector in reviewed in Section 3.6. The chapter ends with a discussion of the multiple bounce of photons from topographical targets.

3.1 Relevant Physical Processes

Figure 3.1 illustrates the ensemble of physical processes that the model will take into account. The pulse begins at some arbitrary point in the atmosphere at certain height above the ground and pointing in a certain direction. The pulse itself is spread over space, time, and wavelength. The pulse propagates through the atmosphere and is attenuated by molecular absorption and Mie and Rayleigh scattering. The atmosphere also introduces additional effects because of turbulence, including broadening of the pulse both spatially and temporally. Additionally, the beam will be randomly deflected from its initial propagation direction. This deflection will cause the position of the beam centroid to vary from one pulse to the next. Atmospheric turbulence also causes random spatial and temporal fluctuations in the beam intensity. The fluctuations superimpose a speckle-type pattern onto the beam. Some of the scattered energy will make it back to the receiver and create an atmospheric

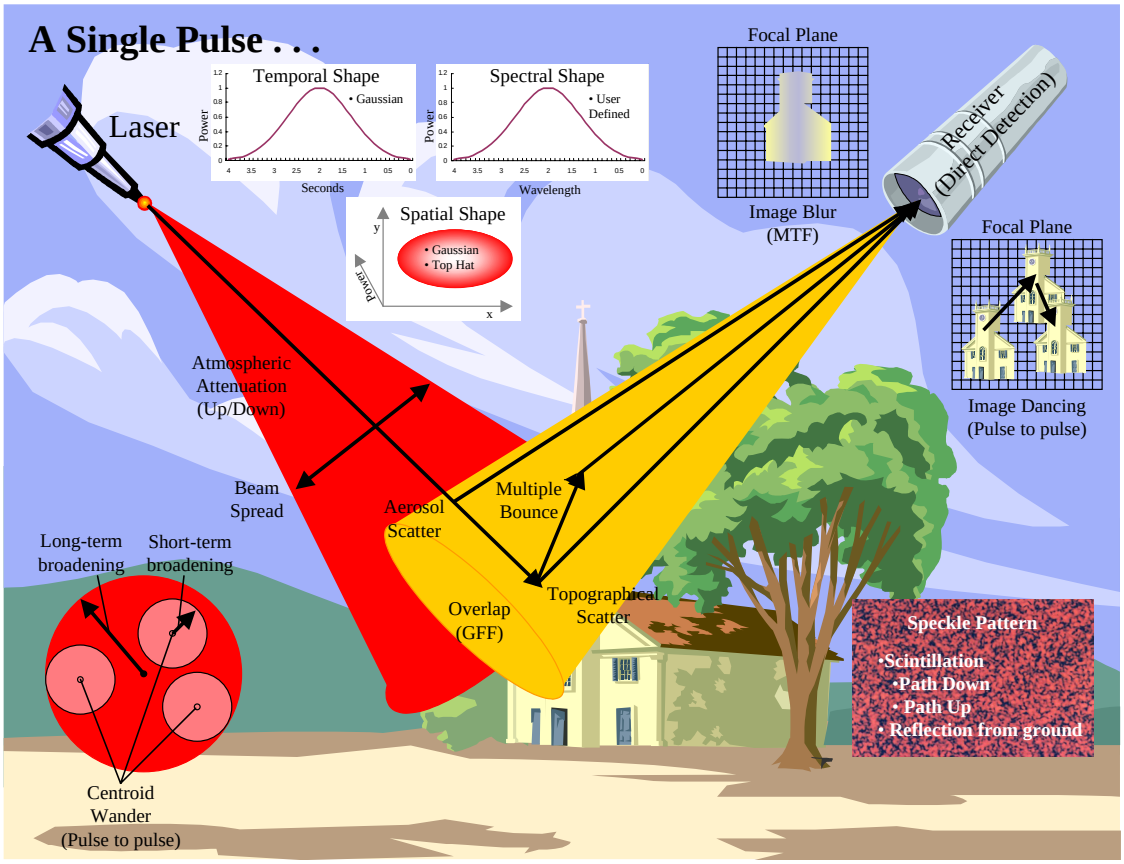

Figure 3.1: This overview illustrates the physical processes included in the model: atmospheric attenuation, atmospheric turbulence, speckle, and multiple bounce off of topographical targets. The atmosphere and topographical returns are modeled spatially, temporally, and spectrally.

return, referred to as the aerosol return. How much energy makes it back to the receiver depends upon the volume backscatter coefficient and the overlap of the beam and the receiver field of view. Part of the energy that reaches the ground will reflect in the direction of the receiver and create the topographical return. If the scene is complicated, parts of the beam may reflect from several surfaces before it is reflected back in the direction of the receiver. Reflection by a topographical surface also imposes a speckle pattern onto the beam due to the surface roughness. As the beam propagates to the receiver, it experiences the same atmospheric effects as before. The broadening of the beam results in a blur in the focal plane and the varying deflection of the beam from pulse to pulse causes the image to move about the focal plane. The receiver, as currently implemented, uses direct detection and is only sensitive to the intensity of the beam.

Figure 3.2 shows some additional physical processes that occur in an actual LADAR/LIDAR system that either will not be modeled or will be modeled at a future date. These additional processes, in no particular order, include coherent detection, the enhanced backscatter effect, multiple scattering, partially developed speckle, Raman scattering, and strong turbulence. Some LADAR/LIDAR systems use coherent detection, where the return signal is mixed with a local oscillator, to increase the signal-to-noise ratio. It is recommended that the model be expanded to model coherent detection in the future, which would require tracking relative phase. The enhanced backscatter effect occurs only in coaxial LADAR/LIDAR systems and causes an increase in the return near the optical axis. This effect will not be incorporated into the model. Multiple scattering within clouds, fog, and dust will not be included in the model and is mentioned only to distinguish it from the topographical multiplebounce. Raman scattering is not included in the model, but should be included at a future date to model Raman LIDAR systems. Finally, the turbulence effects included in the model are valid only under weak turbulence conditions and expansion of the model to

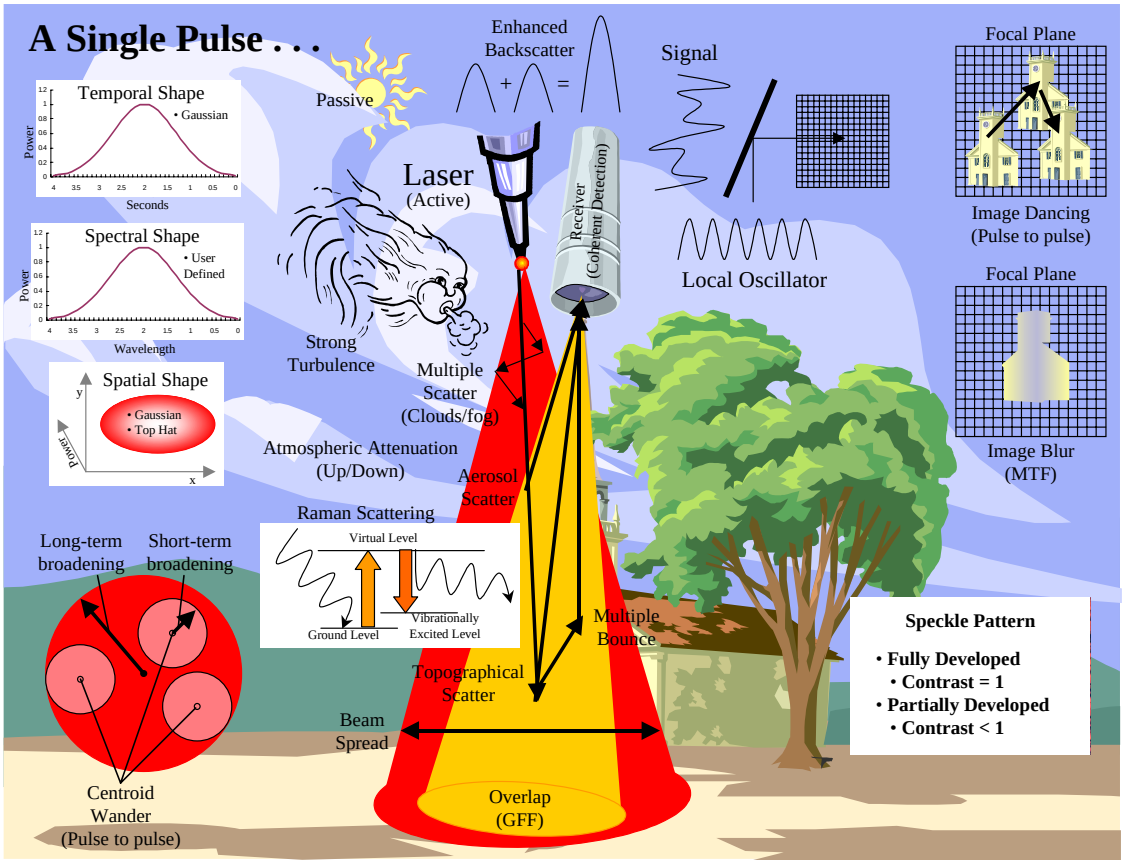

Figure 3.2: The physical processes that affect the recovered signal whether modeled or not. The processes that are not modeled include coherent detection, enhanced backscatter, multiple scattering, partially developed speckle, Raman scattering, and strong turbulence.

include strong turbulence conditions is not anticipated.

3.2 LADAR/LIDAR Basics

The foundation of the model is the basic LIDAR equation formulated by Measures (1984)

$$P\left(\lambda_L, R\right) = P_L \frac{c\tau_L}{2} \frac{A_0}{R^2} \xi\left(\lambda_L\right) \xi\left(R\right) \beta\left(\lambda_L, R\right) \exp\left[-2 \int_0^R \kappa(\lambda_L, r) dr\right], \tag{3.1}$$

where $P\left(\lambda_L, R\right)$ is the total scattered laser power received in watts at a time corresponding to the leading edge of the laser pulse propagating to a range R and returning to the LIDAR/LADAR system, λ_L is the wavelength of the transmitted light in meters, R is the distance of the scattering volume from the transmitter-receiver in meters, P_L is the average power in the laser pulse in watts, c is the speed of light in meters per second, τ_L is the effective pulse duration in seconds, $c\tau_L$ is the effective laser pulse length in meters, A_0 is the area of the objective lens or mirror (i.e., the active area of the receiver telescope) in meters squared, and $\xi\left(\lambda_L\right)$ (unitless) is the receiver's spectral transmission factor at wavelength λ_L. The geometrical form factor (unitless) $\xi\left(R\right)$ is a function of the geometrical probability factor $\xi\left(R, \mathbf{r}\right)$. The geometrical form factor is discussed in more detail in Section 3.2.1. The geometrical probability factor or overlap is the probability that radiation from position $\mathbf{r}$ in the target plane at range R will reach the detector based on geometrical considerations. In this equation, the overlap is assumed to be unity where the field of view of the receiver optics overlaps the laser beam and zero elsewhere. The volume backscatter coefficient $\beta\left(\lambda_L, R\right)$ in inverse meters inverse steradians is obtained from MODTRAN at distance R and $\kappa\left(\lambda_L, R\right)$ is the total atmospheric extinction in inverse meters including molecular absorption and Mie and Rayleigh scattering. The term $\frac{A_0}{R^2}$ is a solid angle and

has units of inverse steradians. The quantities used in the basic equations are illustrated in Figure 3.3. The quantity $c\tau_L$ is divided by two because time is referenced to the leading edge of the pulse. The leading edge of the pulse makes it back to the receiver at a time $t = \frac{2R}{c}$. To integrate over the entire effective pulse duration, the integration starts at t and goes to $t + \tau_L$. Since $2R = ct$, this corresponding to integrating over range from $\frac{ct}{2}$ to $\frac{c(t+\tau_L)}{2}$. The integration over range results in $\frac{c\tau_L}{2}$, as shown in Figure 3.4. The basic LIDAR equation assumes either a monostatic system or that the transmitter and receiver are close to each other.

By integrating the basic LIDAR equation over the integration period of the detector τ_d in seconds, the total energy measured by the detector in joules at wavelength λ_L during its integration period is:

$$E(\lambda_L, R) = E_L \frac{c\tau_d}{2} \frac{A_0}{R^2} \xi(\lambda_L) \xi(R) \beta(\lambda_L, R) \exp\left[-2 \int_0^R \kappa(\lambda_L, r) dr\right], \tag{3.2}$$

where E_L is the total energy in the laser pulse in joules. This equation must be solved to obtain the optical parameters $\kappa(\lambda_L, R)$ or $\beta(\lambda_L, R)$. Some type of assumption or model must be used, such as assuming $\kappa(\lambda_L, R) \approx 1$, using a model to specify $\kappa(\lambda_L, R)$, or assuming a relationship between $\kappa(\lambda_L, R)$ and $\beta(\lambda_L, R)$. The most common inversion technique is the slope method, which is valid for a homogeneous atmosphere and good visibility. The slope method uses a range-normalized signal variable:

$$S(\lambda_L, R) = \ln\left\{E(\lambda_L, R) R^2\right\}. \tag{3.3}$$

If $\xi(R) \approx 1$ Measures shows that

$$\frac{dS(\lambda_L, R)}{dR} = \frac{1}{\beta(\lambda_L, R)} \frac{d\beta(\lambda_L, R)}{dR} - 2\kappa(\lambda_L, R). \tag{3.4}$$

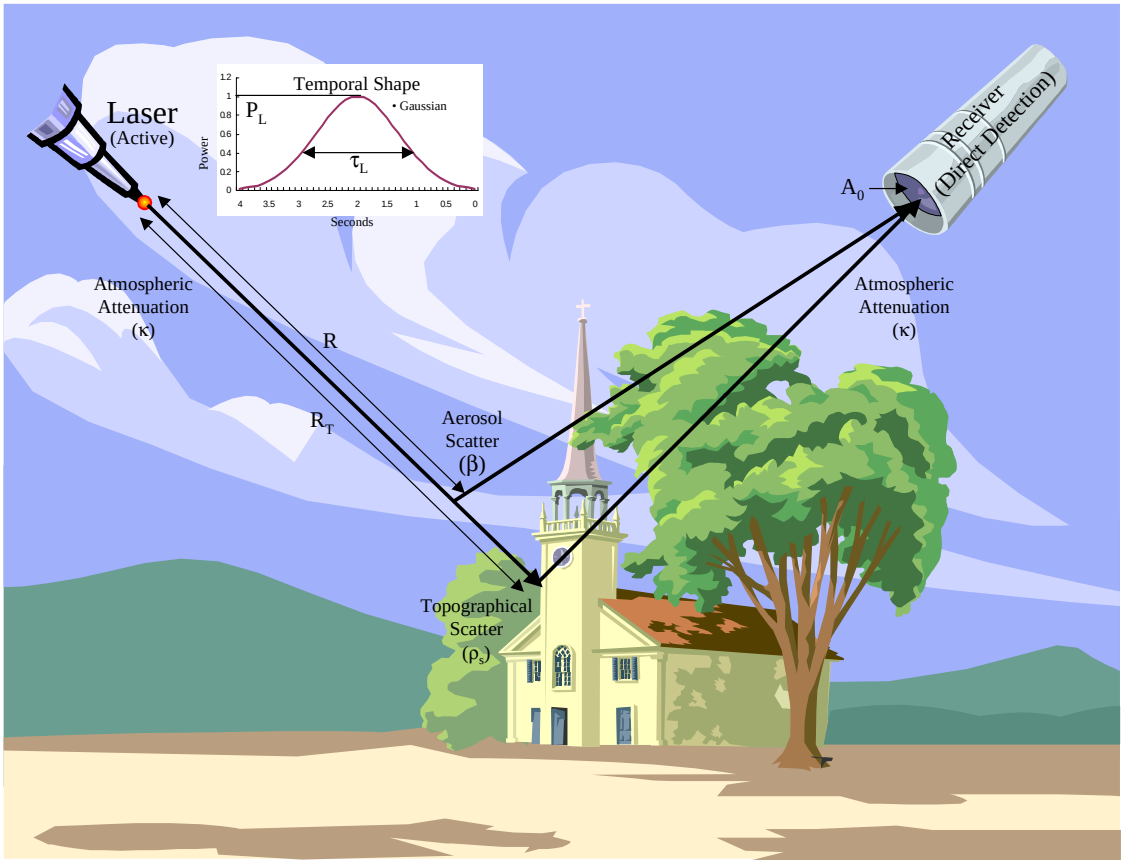

Figure 3.3: The quantities included in the basic aerosol and topographical equations are: P_L - the average power in the laser pulse, τ_L - the effective pulse duration, A_0 - the area of the objective lens or mirror, R - the distance of the scattering volume from the transmitter-receiver, R_T - the range to the topographical target, $\beta(\lambda_L, R)$ - the volume backscatter coefficient, $\kappa(\lambda_L, R)$ - the total atmospheric extinction, and ρ^s - the topographical target's scattering efficiency.

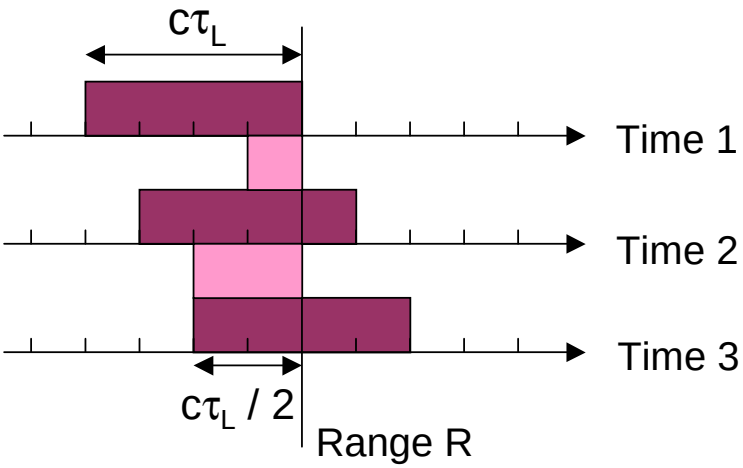

Figure 3.4: The quantity $c\tau_L$ is divided by two because the basic LIDAR equation accounts for pulse propagation to R and back. The return from range R folds back on itself. Integration over the time τ_L corresponds to integration over the range interval equal to $\frac{c\tau_L}{2}$.

By assuming $\frac{d\beta(\lambda_L,R)}{dR} \approx 0$ for a homogenous atmosphere, equation 3.4 can be solved

$$2\kappa_{hom} = -\frac{dS\left(\lambda_L, R\right)}{dR}. \tag{3.5}$$

A more general result can be obtained for elastic scattering by assuming that the relationship between $\kappa\left(\lambda_L, R\right)$ and $\beta\left(\lambda_L, R\right)$ is

$$\beta\left(\lambda_L, R\right) = C\kappa^g\left(\lambda_L, R\right), \tag{3.6}$$

where C is a constant and κ is raised to the power g. The value of g depends on the wavelength of the laser and the molecule being detected. Substitution of this relationship into equation 3.4 results in a nonlinear ordinary differential equation with the solution (Measures 1984)

$$\kappa_L(\lambda_L, R) = \frac{\exp^{-\frac{\left[S\left(\lambda_L, R_{Ref}\right) - S(\lambda_L, R)\right]}{g}}}{\frac{1}{\kappa_L\left(\lambda_L, R_{Ref}\right)} + \frac{2}{g}\int_R^{R_{Ref}} \exp^{-\frac{\left[S\left(\lambda_L, R_{Ref}\right) - S(\lambda_L, R^*)\right]}{g}} dR^*}, \tag{3.7}$$

where R_{Ref} is the reference range. Equation 3.7 is not satisified under multiple scattering conditions.

Several assumptions must be made to obtain the number density of the species of interest in a DIAL system using a distributed reflector. The average power in the laser pulse is assumed the same for both wavelengths. The total atmospheric extinction is assumed to be of the form

$$\kappa_L(\lambda_L, R) = \overline{\kappa}(\lambda_L, R) + N(R)\,\sigma^A(\lambda_L), \tag{3.8}$$

where $N(R)$ is the number density of the species of interest at range R, $\sigma^A(\lambda_L)$ is the absorption cross section of the species of interest at the laser wavelength, and $\overline{\kappa}(\lambda_L, R)$ is the atmospheric extinction that results if the species of interest is not present. The absorption cross section is a function of both temperature and pressure. Therefore, the atmospheric conditions must be considered when evaluating this parameter. Finally, the spectral transmission factors of the receiver at both wavelengths are assumed approximately equal. The differential of the natural log of the ratio of the total scattered laser power at λ_1 to the total scattered laser power at λ_2 results in an equation for the number density of the species of interest:

$$N(R) = \frac{\left[\frac{d}{dR}\left\{\ln\left[\frac{P(\lambda_2,R)}{P(\lambda_1,R)}\right] - \ln\left[\frac{\beta(\lambda_2,R)}{\beta(\lambda_1,R)}\right]\right\} + \overline{\kappa}(\lambda_2, R) - \overline{\kappa}(\lambda_1, R)\right]}{2\left(\sigma^A(\lambda_1) - \sigma^A(\lambda_2)\right)}. \tag{3.9}$$

When simulating a DIAL system, DIRSIG will calculate the total scattered laser power at both wavelengths. The number density of the species of interest can then be calculated using Equation 3.9.

When working with a topographical reflector, the basic LADAR equation is

$$P\left(\lambda_L, t\right) = P_L \frac{A_0}{R_T^2} \xi\left(\lambda_L\right) \xi\left(R_T\right) \frac{\rho^s}{\pi} \exp\left[-2 \int_0^{R_T} \kappa(\lambda_L, r) dr\right], \tag{3.10}$$

where R_T is the range to the topographical target and ρ^s is its scattering efficiency (Measures 1984). The total energy received by the detector is obtained by multiplying the total scattered laser power by the integration time of the detector τ_d in seconds. In a DIAL system the logarithm of the ratio of the total scattered laser energy at λ_1 to the total scattered laser energy at λ_2 is used to calculate

$$\int_0^{R_T} N\left(r\right) dr = \frac{\left[\ln\left\{\frac{E(\lambda_2, R_T)}{E(\lambda_1, R_T)}\right\} + \overline{\kappa}\left(\lambda_2, R_T\right) - \overline{\kappa}\left(\lambda_1, R_T\right)\right]}{2\left(\sigma^A\left(\lambda_1\right) - \sigma^A\left(\lambda_2\right)\right)}, \tag{3.11}$$

where N is the number density of the species of interest, $\overline{\kappa}$ is the atmospheric extinction without the species of interest, σ^A is the absorption cross-section of the species of interest, E is the total energy received by the detector, and R_T is the range to the topographical target. This equation gives the integrated concentration of the species of interest along the path. Topographical DIALs gain signal-to-noise at the expense of range information. When simulating a topographical DIAL system, DIRSIG will calculate the total scattered laser power at both wavelengths. The integrated concentration of the species of interest can then be calculated using Equation 3.11.

3.2.1 Geometrical Form Factor

The geometrical form factor is defined as

$$\xi\left(R\right) = \frac{1}{\pi W^2\left(R\right)} \int_{r=0}^{r_T} \int_{\psi=0}^{2\pi} \xi\left(R, r, \psi\right) F\left(R, r, \psi\right) r d\psi dr, \tag{3.12}$$

where $F(R, r, \psi)$ [unitless] is the distribution of laser power over the target plane, $\xi(R, r, \psi)$ [unitless] is probability that light scattered from position (r, ψ) at range R reaches the detector due to geometry, $W(R) = \sqrt{W_0^2 + \theta^2 R^2}$ is the radius of the laser pulse in the target plane in meters, R is the range of the scattering volume from the receiver in meters, r_T is the radius of the receiver field of view in the object plane in meters, W_0 is the laser output aperture radius in meters, θ is half of the laser divergence angle, r is the radial distance in the object plane from the receiver optical axis in meters, d is the distance between the receiver and transmitter optical axes in the object plane in meters, and ψ is the angle between r and the line connecting the transmitter and receiver optical axes in the object plane. The quantities used in the geometrical form factor are illustrated in Figure 3.5. A Gaussian distribution of laser power over the target plane is expected when the laser is in the TEM_{00} mode (Verdeyen 1995). If higher-order transverse modes dominate, then an uniform distribution will suffice.

The geometrical form factor usually leads to a deviation from the R^2 dependence of the basic LADAR/LIDAR equation, especially for short distances in biaxial systems. Riegl and Bernhard investigated this effect for a beam of constant divergence and a uniform distribution for both coaxial and biaxial systems (1974). Earlier the geometrical probability factor was assumed to be unity where the field of view of the receiver optics overlaps the laser beam and zero elsewhere. For a coaxial LADAR/LIDAR system, when the laser beam divergence is less than the acceptance angle of the telescope, the geometrical form factor is unity. For a uniformly illuminated biaxial LADAR/LIDAR without any optical obscurations the geometrical form factor becomes:

$$\xi(R) = \frac{A(r_T(R), W(R))}{\pi W^2(R)}, \tag{3.13}$$

where $A(r_T(R), W(R))$ is the area overlap function, $r_T(R) = r_0 + \phi R$ is the radius of the

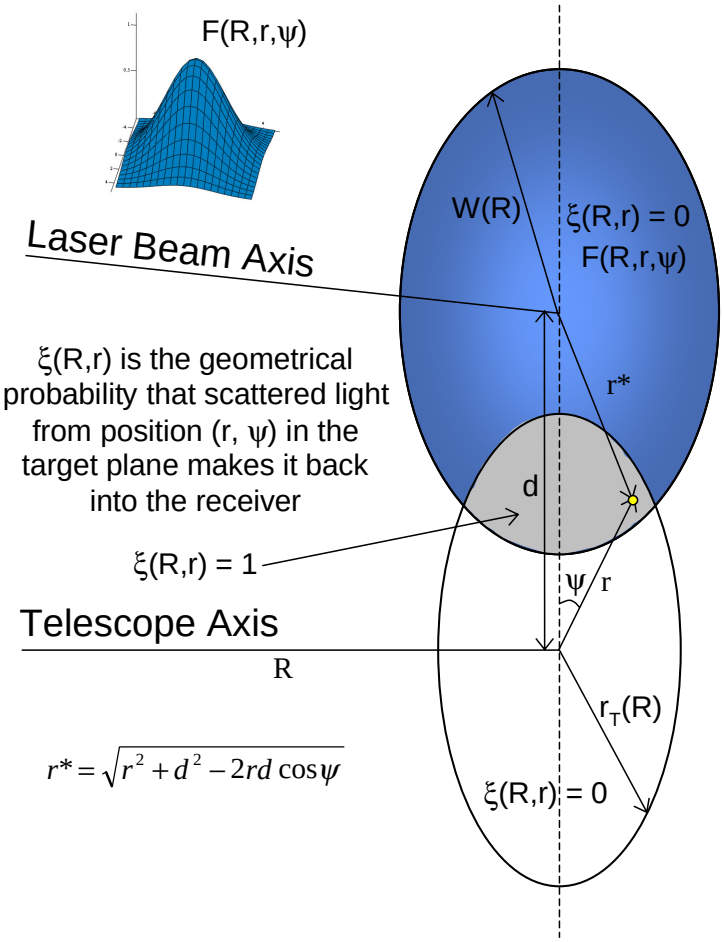

Figure 3.5: The quantities which make up the geometrical form factor include: $F\left(R,r,\psi\right)$ - the distribution of laser power over the target plane, $\xi\left(R,r,\psi\right)$ - the probability that light scattered from position (r,ψ) at range R reaches the detector due to geometry, $W\left(R\right)$ - the radius of the laser pulse in the target plane, R - the range of the scattering volume from the receiver, r_T - the radius of the receiver field of view in the object plane, W_0 - the laser output aperture radius, θ - half of the laser divergence angle, r - the radial distance in the object plane from the receiver optical axis, d - the distance between the receiver and transmitter optical axes in the object plane, and ψ - the angle between r and the line connecting the transmitter and receiver optical axes in the object plane.

receiver field of view in the target plane, r_0 is the effective radius of the telescope lens, and ϕ is the receiver-optics half opening angle. The area overlap function is equal to zero if there is no overlap and unity if the receiver field of view or the area of illumination encloses the other in the target plane. The geometry under consideration is shown in Figure 3.6. When there is partial overlap of the area of illumination and receiver field of view the area overlap function is

$$A\left(r_T, W\left(R\right), d\right) = W^2\left(R\right)\psi_W + r_T^2\psi_r - r_T d\sin\psi_r, \tag{3.14}$$

where

$$\psi_W = \cos^{-1}\left[\frac{d^2 + W^2\left(R\right) - r_T^2}{2W\left(R\right)d}\right], \tag{3.15}$$

$$\psi_r = \cos^{-1}\left[\frac{d^2 + r_T^2 - W^2\left(R\right)}{2r_T d}\right], \tag{3.16}$$

and $d = d_0 - R\delta$ is the separation between the optical axes of the receiver and laser in the target plane, d_0 is the separation between the receiver and laser axes at the LADAR/LIDAR, and δ is the inclination angle between the receiver and laser axes. The geometrical form factor is referred to in the literature as the "overlap factor" if nondimensional parameters are used. The biaxial arrangement is advantageous to eliminate near-field scattering, which might saturate the detector in long-range measurements. The near-field scattering should be eliminated when the separation between the laser and receiver is sufficiently large to cause the overlap factor to remain low for a significant distance. An accurate calculation of the overlap factor is critical in short-range measurements. If the receiver contains a central obscuration or if its objective lens is not the limiting aperture, then the geometrical form factor has a more complicated form, and can be quite complicated for an actual

LADAR/LIDAR system. Halldórsson and Langerholc (1978) investigated a coaxial system with a central obscuration and a Gaussian distribution for a biaxial LADAR/LIDAR.

3.2.2 Geometrical Compression

The basic LADAR/LIDAR equations presented to this point assume that all radiation collected by the receiver is focused onto the detector focal plane. For short-to-intermediate ranges the radiation is actually not focused onto the focal plane. This means that the signal amplitude for an actual system is less than the predicted signal, especially for small detectors. Geometrical compression is more of a concern with atmospheric LIDAR systems that measure the return from shorter distances. The returns from LADAR/LIDAR systems that are focused on the ground should not be affected much.

Harms (1978) calculated the irradiance at the focal plane and the power detected for a coaxial system without a central obscuration for a Gaussian distribution of laser power over the target plane. For a coaxial system without a central obscuration and if the divergence of the laser beam is less than the opening angle of the telescope, the irradiance on the focal plane in watts per meters squared as a function of position is:

$$\begin{aligned} E_f\left(r_f, R\right) &= P_L \frac{c\tau_L}{2} \xi\left(\lambda_L\right) \beta\left(\lambda_L, R\right) \frac{1}{f^2} \exp\left[-2 \int_0^R \kappa(\lambda_L, r) dr\right] \\ &\times \frac{2}{\pi W^2\left(R\right)} \int\limits_{A(r_{op}, r_0)} \exp\left[-2 \frac{r_{op}^{*2}}{W^2\left(R\right)}\right] da, \end{aligned} \tag{3.17}$$

where r_f is position on the focal plane in meters, R is the distance of the scattering volume from the transmitter-receiver in meters, P_L is the average power in the laser pulse in watts, c is the speed of light in meters per second, τ_L is the effective pulse duration in seconds, $\xi\left(\lambda_L\right)$ (unitless) is the receiver's spectral transmission, λ_L is the wavelength of the transmitted

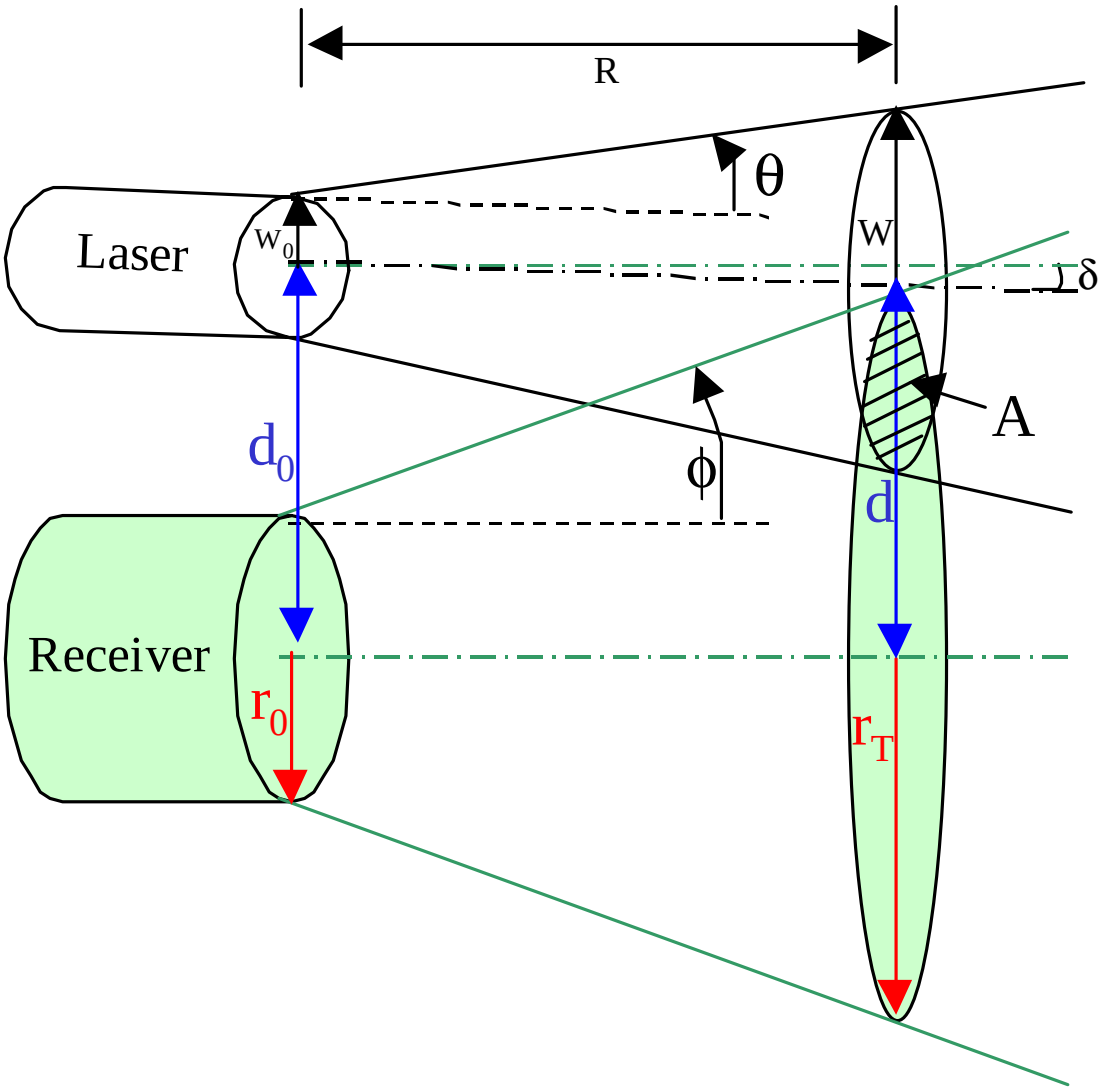

Figure 3.6: The quantities which make up a biaxial LADAR/LIDAR geometry include: W_0 - the laser output aperture radius, d_0 - the separation between the receiver and laser axes at the LADAR/LIDAR, r_0 - the effective radius of the telescope lens, R - the distance of the scattering volume from the transmitter-receiver, θ - the laser's half divergence angle, ϕ - the receiver optics half opening angle, $W(R)$ - the radius of the laser pulse in the target plane, d - the separation between the receiver and laser axes in the target plane, r_T - the radius of the receiver field of view in the target plane, $A(r_T, W(R), d)$ - the area overlap function, and δ - the inclination angle between the receiver and laser axes. (Measures 1984)

light in meters, $\xi(R)$ (unitless) is the geometrical form factor, $\beta(\lambda_L, R)$ is the volume backscatter coefficient in inverse meters inverse steradians, f is the focal length of the system in meters, $\kappa(\lambda_L, R)$ is the total atmospheric extinction in inverse meters including molecular absorption and Mie and Rayleigh scattering, $W(R)$ is the radius of the laser pulse in the target plane in meters, and $r_{op} = \frac{r_f R}{f}$ is the object point in the target plane. The integral is taken over the circular area $A(r_{op}, r_0)$ of radius r_0 centered on r_{op}, where r_0 is the radius of the receiver aperture. The geometry under consideration is shown in Figure 3.7. The irradiance on the focal plane is integrated over the detector area to obtain the total power on the detector. The percentage of detected radiation is larger at large distances than at small distances, and is assumed to be constant for $R \leq 10^3$ meters. At longer distances the power returns to the expected R^{-2} behavior, but with reduced amplitude that depends on the size of the detector.

Harms (1978) extended this work to include biaxial systems with and without central obscurations. The relevant geometry for a biaxial system without a central obscuration is shown in Figure 3.8. The optical axis is along the z axis, the y axis points in the direction of the laser, and the x axis is perpendicular to the other two axes. The irradiance in the object plane is no longer symmetric around the z axis, so that the irradiance pattern is not symmetric in the focal plane. The resulting irradiance on the focal plane as a function of position is

$$\begin{aligned} E_f(x_f, y_f, R) &= P_L \frac{c\tau_L}{2} \xi(\lambda_L)\, \beta(\lambda_L, R)\, \frac{1}{f^2} \exp\left[-2 \int_0^R \kappa(\lambda_L, r) dr\right] \\ &\times \frac{2}{\pi W^2(R)} \int_{A(x_{op}, y_{op}, r_0)} \exp\left[-2 \frac{x_{op}^{*2} + \left[y_{op}^{*2} - a(R)\right]^2}{W^2(R)}\right] da, \end{aligned} \tag{3.18}$$

where (x_f, y_f) is the position on the focal plane, $(x_{op} = \frac{x_f R}{f}, y_{op} = \frac{y_f R}{f})$ is the object point

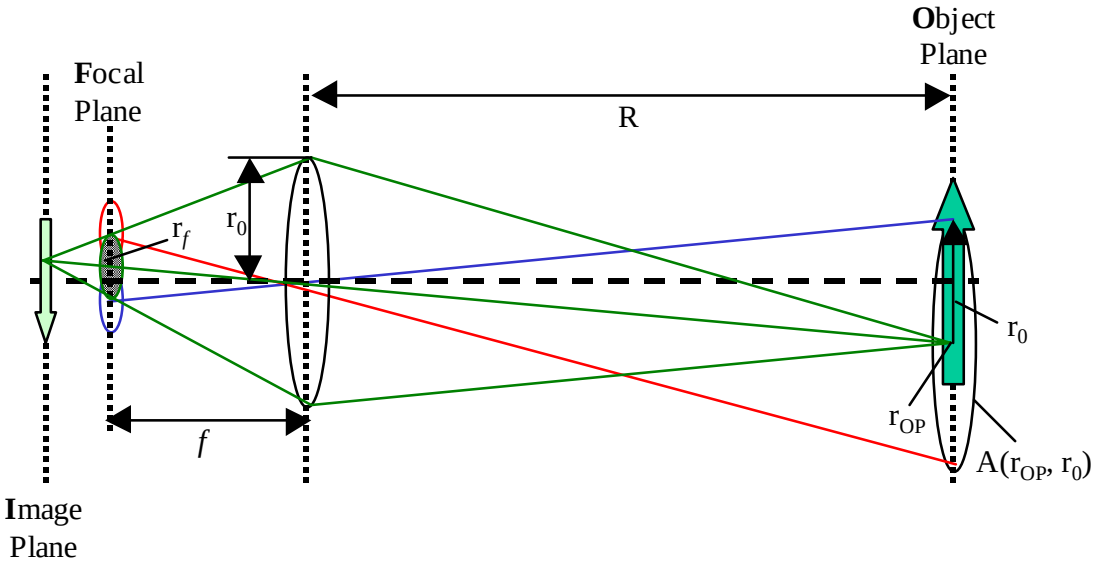

Figure 3.7: The compression effect for a coaxial LADAR/LIDAR geometry. The return from the center of the integration area (green), $A(r_{OP}, r_0)$, focuses in the image plane, which for short distances is behind the focal plane. Therefore the return in the focal plane from the center of the integration area is actually a blur "circle". The returns from the edges (red and blue) of the integration area also form blur circles. These blur circles all overlap at position r_f in the focal plane. To calculate the return at r_f the contribution from every blur circle must be added, which is equivalent to integration over the integration area in the object plane. The additional quantities shown are: f - the focal length of the system, r_0 - the effective radius of the telescope lens, R - the distance of the scattering volume from the transmitter-receiver, and r_{OP} - the object point in the object plane.

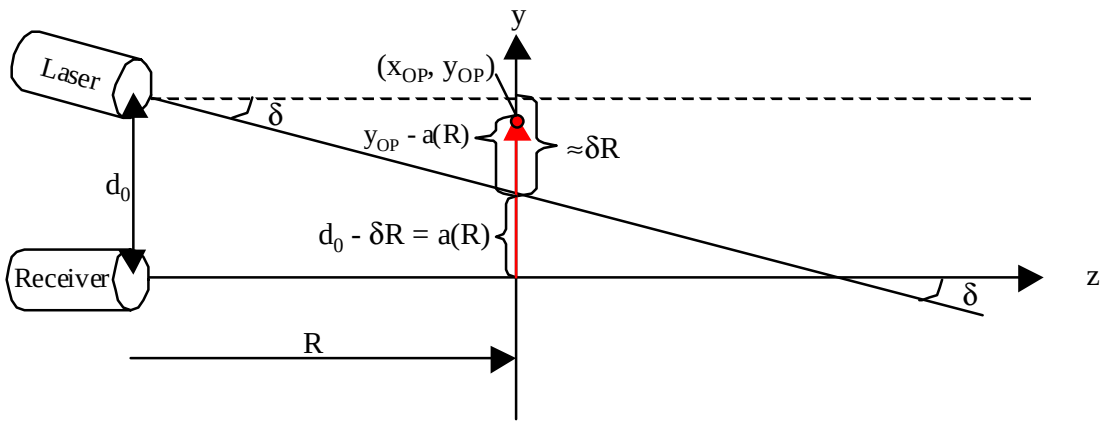

Figure 3.8: The quantities that are relevant for calculating the compression effect for a biaxial LADAR/LIDAR geometry include: d_0 - the separation between the receiver and laser axes at the LADAR/LIDAR, δ - the inclination angle between the receiver and laser axes, R - the distance of the scattering volume from the transmitter-receiver, (x_{op}, y_{op}) - the object point position in the target plane, and $a\,(R)$ - the distance between the receiver and laser axis in the target plane.

in the target plane, and $a\,(R)$ is the distance between the receiver and laser axis in the target plane. The integral is evaluated over the circular area $A\,(x_{op}, y_{op}, r_0)$ of radius r_0 centered on (x_{op}, y_{op}). Consequently, the irradiance in the focal plane is shifted off-axis by $a_f\,(R) = f\left(\frac{d_0}{R} - \delta\right)$ and the total detected power is maximized in the range where the overlap between the receiver and the transmitter is total. This causes an additional deviation from the coaxial case. The total power is very low at short distances, increases to a maximum at some intermediate distance, and then decreases again at long distances. The range where the maximum power occurs and the width of the maximum depends upon d_0 and δ.

The resulting irradiance on the focal plane is similar whether or not a central obscuration is present. However, if a central obscuration is present the integral is evaluated over the

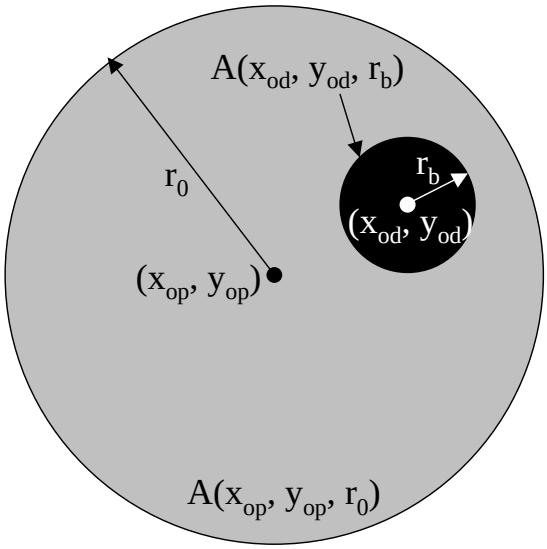

Figure 3.9: To calculate the irradiance on the focal plane when a central obscuration is present, the portion of the return blocked by the central obscuration $A(x_{od}, y_{od}, r_b)$ must be excluded from the contribution area $A(x_{op}, y_{op}, r_0)$.

circular area $A(x_{op}, y_{op}, r_0)$ of radius r_0 centered on (x_{op}, y_{op}) excluding the circular area $A(x_{od}, y_{od}, r_b)$ of radius r_b centered on (x_{od}, y_{od}), where r_b is the radius of the central obscuration, s_b is the distance between the central obscuration and the mirror, $x_{od} = \left[\frac{R-s_b}{R}\right] x_{op}$, and $y_{od} = \left[\frac{R-s_b}{R}\right] y_{op}$. The circular areas are shown in Figure 3.9. The coaxial case is obtained by setting $a(R) = 0$ for all R. A central obscuration in a biaxial system does not significantly affect the total power for small distances and only slightly affects the total power at large distances. Most of this effect is caused by the reduced overlap inherent in a biaxial system. A central obscuration in a coaxial system causes a significant decrease in total power especially for short and medium distances.

DIRSIG calculates the geometrical form factor for both coaxial and biaxial systems with or without a circular central obscuration. DIRSIG also accounts for the compression effect.

How the geometrical form factor is implemented in the model is described in Section 5.5.

3.2.3 Spectral Distribution

The basic LADAR/LIDAR equations introduced in Section 3.2 assume that the laser emission is monochromatic and that it elastically scattered with no change in wavelength. In fact, the output of a general-purpose laser has some spectral distribution $l(\lambda)$. The spectral width of the vibrational-rotational absorption bands in the infrared spectral region are about two orders smaller than ultraviolet electronic transition lines. Therefore, the laser linewidth is often as wide as the absorption feature itself and monochromaticity cannot be assumed. Mégie (1980) addressed this problem by simply multiplying the basic LADAR/LIDAR equation by $l(\lambda)$ and integrating over λ. This approach assumes that the spectral distribution does not change during the scattering process. Bösenberg (1998) derived the following equation, which accounts for changes in the spectral distribution due to inelastic scattering or Doppler broadening:

$$\begin{aligned} P(R) &= P_L \frac{c\tau_L}{2} \frac{A_0}{R^2} \xi(R) \int_{\Delta\lambda} \int_{\Delta\lambda'} l(\lambda)\, \beta(\lambda, R) \exp\left[-\int_0^R \kappa(\lambda, r) dr \right] \cdot \\ & \quad h\left(\lambda - \lambda', R\right) \xi\left(\lambda'\right) \exp\left[-\int_0^R \kappa\left(\lambda', r\right) dr \right] d\lambda' d\lambda, \end{aligned} \tag{3.19}$$

where $h\left(\lambda - \lambda', R\right)$ is the normalized spectral distribution after scattering.

This section has introduced the basic theory necessary to create a simple LADAR/LIDAR model. LADAR/LIDAR equations 3.1 and 3.10, are the fundamental equations to be implemented in the model. The geometrical form factor is a fundamental quantity and will be included in the model for both coaxial and biaxial systems with and without a central

obscuration. How the geometrical form factor is implemented in the model is described in Section 5.5. Finally, the model will calculate the basic equations on a spectral basis based upon a laser spectral distribution of power provided by the user and assuming no change in the laser linewidth during the scattering process. The next section will introduce the concept of atmospheric turbulence and how it affects the return.

3.3 Atmospheric Propagation

The first part of this section will briefly review Maxwell's wave equation, the approximations used to solve it, and the basic wave types. A discussion of the source of atmospheric turbulence and an important measure of its strength, the index-of-refraction structure constant, follows. The effects of atmospheric turbulence on the beam as it propagates will then be addressed. These effects are divided into three categories and include beam effects, image effects, and scintillation.

3.3.1 The Wave Equation

To model the propagation of a laser beam through the atmosphere, one must first solve Maxwell's wave equation. The typical treatments start with Maxwell's equation for the vector amplitude of the electric field, $\overrightarrow{E}(\overrightarrow{R})$, given by

$$\nabla^2\overrightarrow{E}(\overrightarrow{R}) + k^2n^2(\overrightarrow{R})\overrightarrow{E}(\overrightarrow{R}) + 2\nabla\left[\overrightarrow{E}(\overrightarrow{R})\cdot\nabla log\left(n(\overrightarrow{R})\right)\right] = 0, \tag{3.20}$$

where k is the wavenumber of the light and $n(\overrightarrow{R})$ is the index of refraction. This equation can be simplified when the wavelength of interest is much smaller than the smallest scale of turbulence by neglecting the final term, which is related to changes in the polarization of the beam as it propagates. This condition holds throughout the optical and infrared

spectral regions and implies that atmospheric turbulence does not significantly change the polarization of a beam as it propagates through the atmosphere. The resulting equation is then written as three separate equations by breaking the electric field into three scalar components. By letting $U(\overrightarrow{R})$ be one of the scalar components of the plane field transverse to the direction of propagation the problem can be reduced to:

$$\nabla^2 U(\overrightarrow{R}) + k^2 n^2(\overrightarrow{R}) U(\overrightarrow{R}) = 0. \tag{3.21}$$

Even this simplified equation cannot be solved in closed form.

Many different approximations have been used to solve this equation including the method of Green's functions, the geometrical optics approximation, the Born approximation, the Rytov approximation, the extended Huygens-Fresnel principle, and the parabolic equation method. Historically, the first approach used was the method of Green's functions which results in an integral equation. A Green's function, e.g., $G(x; x')$, is the kernel associated with a linear, self-adjoint, invertible differential operator $L(x)$ that satisfies the condition

$$L^{-1} f = \int G(x; x') f(x') \, dx', \tag{3.22}$$

where L^{-1} is the inverse of the differential operator so that $L^{-1}(x) f(x) = u(x)$.

The geometrical optics approximation assumes that light propagates as rays and thus ignores diffraction effects. However, Andrews (1998) notes that since the phase fluctuations in the beam are most responsive to large-scale turbulence fluctuations, the approximation produces phase fluctuations that are similar to those produced by theories that include diffraction effects.

The Born and Rytov approximations are perturbation theories that account for diffrac-

tion effects. The Born approximation uses additive perturbations, the Rytov multiplicative. Both approximations are limited to weak turbulence. Experiment has shown that the Rytov approximation is more accurate than the Born approximation and is therefore the standard used under weak turbulence conditions. The Huygens-Fresnel principle states that each point on a wavefront of light acts as a secondary source of spherical wavefronts and that the wave amplitude at any point beyond the wavefront is a complex superposition of the amplitudes of all wavelets. The advantage of the extended Huygens-Fresnel approximation is that the first- and second-order field moments derived by this technique are valid for all turbulence conditions while the fourth order has only been shown to be valid for weak turbulence.

The parabolic method develops equations for each moment by factoring the operator in an elliptic wave equation, assuming negligible backscatter, and approximating the square root of an operator. The parabolic equations developed for the first and second moments have exact solutions that are valid for all turbulence conditions.

This subsection has introduced the fundamental wave equation and several methods on how to solve it. The turbulence related quantities introduced in subsection 3.3.3 are the scintillation mean, variance, and correlation, the beam spread and wander equations, and the image blur and dancing equations. These equations were derived using the Rytov method. Before introducing these quantities, the next subsection will review the different types of beams.

3.3.2 Beam Types

To solve Maxwell's equation a mathematical form for the wave must be assumed. The two most common types of wave models expressed in the plane of the transmitter are the plane wave

$$U(x, y, 0) = A_0 e^{i\phi_0} \tag{3.23}$$

and the spherical wave

$$U(x, y, 0) = \lim_{R \to 0} \frac{e^{ikR}}{4\pi R}, \tag{3.24}$$

where A_0 is a constant amplitude, ϕ_0 is a constant phase, and $R = \left(x^2 + y^2 + z^2\right)^{\frac{1}{2}}$. Unfortunately these two models do not adequately account for the finite width of a beam and its focusing and divergence characteristics. The Gaussian beam does account for these effects and describes a single transverse (TEM_{00}) electromagnetic wave. The lowest-order Gaussian-beam has the form:

$$U(x, y, 0) = a_0 \exp\left[-\frac{x^2 + y^2}{W_0^2} - \frac{ik}{2F_0}\left(x^2 + y^2\right)\right], \tag{3.25}$$

where a_0 is the on-axis amplitude, W_0 is the beam radius, and F_0 is the radius of curvature of the wavefront. The magnitude of the various beams are shown in Figure 3.10. The LADAR/LIDAR model will use the plane wave and Gaussian wave with the phase-front radius of curvature set to infinity. The spherical wave physically resembles a laser beam only over short distances. Since most LADAR/LIDAR systems propagate over longer distances, the spherical wave will not be included in the LADAR/LIDAR model.

At this point, the governing equation describing the propagation of a wave, a method to solve the equation, and a mathematical description of the types of waves have been reviewed. The next three subsections will introduce the properties of the medium through which the wave is propagating.

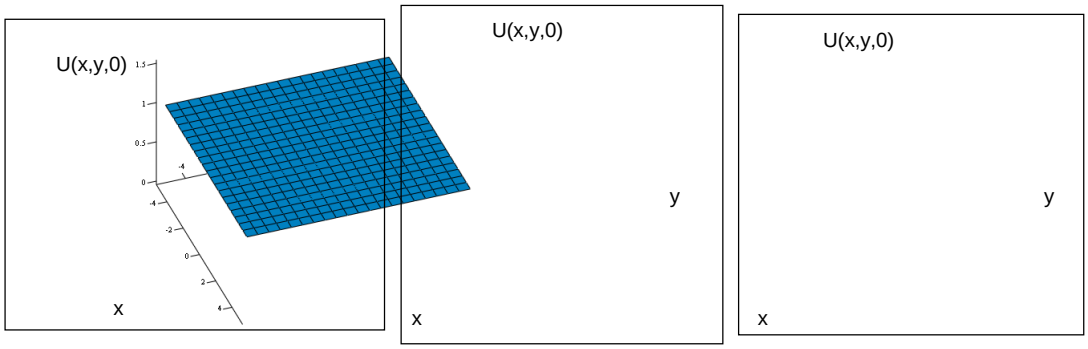

Figure 3.10: The magnitude of a plane, spherical, and Gaussian wave.

3.3.3 Atmospheric Turbulence

This subsection introduces the cause of atmospheric turbulence and the concept of a structure function, which is used extensively in atmospheric optics. The structure function turns out to be a function of the index-of-refraction structure constant which has several models. The Hufnagel-Valley Model best meets the needs of this task and will be included in the LADAR/LIDAR DIRSIG model. The structure function is used in the derivations of the scintillation statistics and of the beam and image effects. To avoid reproducing other work, only the resulting equations are presented. Atmospheric scintillation is included in the LADAR/LIDAR model because it can have a large effect on the return, especially with spaceborne systems. The statistics presented will be used to modify the return as explained in Section 5.7. In a coaxial system, the scintillation statistics must be modified to account for the double passage of the beam through the same effective atmosphere. The resulting equations are complicated and not very illustrative, so they are not reproduced here. This subsection ends with the presentation of the equations governing image blur,

image dancing, beam wander, and beam spread. How these equations are incorporated into DIRSIG is discussed in Section 5.7.

The texts by Andrews (1998) and Thomas (1993) both include comprehensive overviews of atmospheric turbulence and much of the discussion presented here was derived from these sources. Atmospheric turbulence is air motion produced by wind and convection that results in random temperature variations in the atmosphere. These random variations cause small fluctuations in the index of refraction of the air. These fluctuations affect the propagation of a laser beam by modifying the phase and intensity profiles of a transmitted signal. The terms "optical turbulence" and "atmospheric turbulence" tend to be used interchangeably. Atmospheric turbulence limits astronomical seeing, destroys the spatial coherence of light, and causes beam wander, beam broadening, image dancing, image blurring, and fluctuations in the temporal intensity. These effects are generally grouped into three categories: image effects, beam effects, and scintillation. The term "scintillation" includes both spatial and temporal intensity fluctuations. The latter one is responsible for the twinkling of stars.

Atmospheric turbulence is a chaotic nonlinear process that cannot be described theoretically. Turbulence occurs when the velocity of sections of an air flow fluctuate about the mean velocity of the entire flow and possess a continuous power spectrum. In atmospheric turbulence, these chaotic sections mix temperatures, aerosols, and water vapor. The statistical approach of Kolmogorov theory is the most widely accepted.

Kolmogorov theory was first developed by studying velocity fluctuations. The energy transfer process is easily visualized by examining the energy cascade theory presented by Andrews (1998) and shown in Figure 3.11. At large scales, the velocity of the wind increases until it transitions from laminar to turbulent flow. At this point, eddies form that are smaller than the initial flow. The largest eddies define the size L_0 of the outer scale of turbulence. The large eddies may break up into smaller eddies, forming a range of various sizes. This

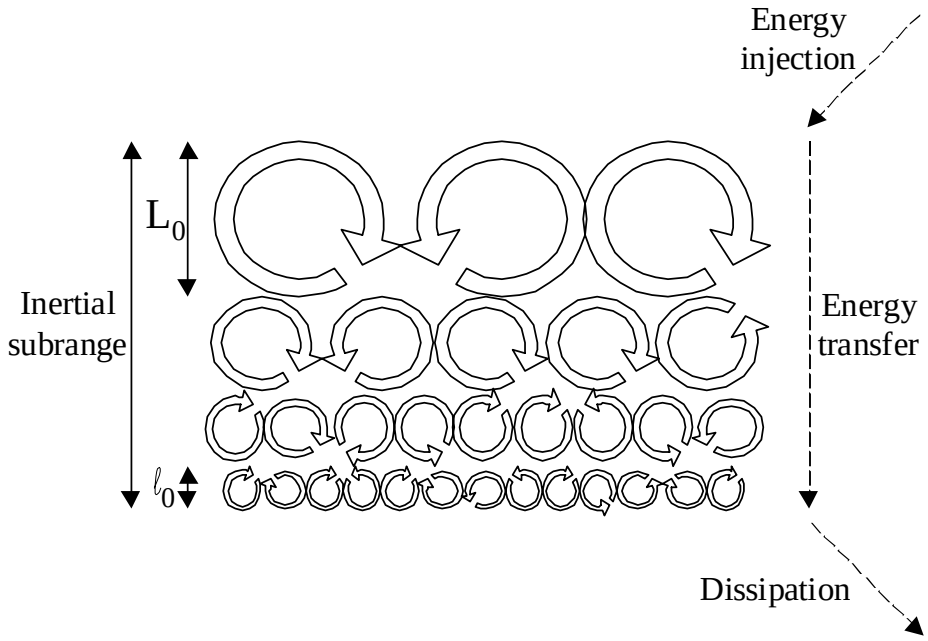

Figure 3.11: The energy cascade theory in which energy is injected at the largest scale defined by the outer scale of turbulence L_0, and dissipated at the smallest scale defined by the inner scale of turbulence l_0. The inertial range is between the outer and inner scale. Within this range, there is a continuous spectrum. (Andrews and Phillips 1998)

process transfers energy from a macroscopic to a microscopic scale. Eventually, the eddies become so small that the remaining energy is dissipated as heat.

The smallest eddies define the size ℓ_0 of the inner scale of turbulence. The inertial subrange is the spatial region where inertial forces dominate and the random fluctuations can be assumed to be spatially homogeneous and isotropic. The upper and lower ends of the inertial range define the outer and inner scale of turbulence, respectively. Similar analysis for fluctuations in temperature and index of refraction result in analogous inner and outer scales.

Index-of-Refraction Structure Constant

An important parameter that quantifies the strength of turbulence is the index-of-refraction structure constant C_n^2, which is derived from the structure function. It is often convenient to assume that a random field is homogeneous, i.e., that the mean, $m = \langle x(\mathbf{R}) \rangle$, is constant and the covariance

$$B_x(\mathbf{R}_1, \mathbf{R}_2) = \int_{-\infty}^{\infty} \int_{-\infty}^{\infty} [x_1(\mathbf{R}_1) - m][x_2(\mathbf{R}_2) - m] p_x(x_1(\mathbf{R}_1), x_2(\mathbf{R}_2); \tau) dx_1 dx_2 \quad (3.26)$$

depends only on $\mathbf{R} = \mathbf{R}_2 - \mathbf{R}_1$. Often even this condition cannot be met because the mean is not constant. However, a solution can be found if the mean varies slowly. First, for mathematical convenience, the random process is divided into an overall mean and a fluctuating part with zero mean

$$x(\mathbf{R}) = m(\mathbf{R}) + x_1(\mathbf{R}). \quad (3.27)$$

The structure function is defined:

$$\begin{aligned} D_x(\mathbf{R}_1, \mathbf{R}_2) &= < [x(\mathbf{R}_1) - x(\mathbf{R}_2)]^2 > \\ &= [m(\mathbf{R}_1) - m(\mathbf{R}_2)]^2 + < [x_1(\mathbf{R}_1) - x_2(\mathbf{R}_2)]^2 > . \end{aligned} \quad (3.28)$$

If the mean varies slowly, then the first term is approximately zero.

For a homogeneous random field, the three-dimensional Wiener-Khintchine theorem yields an expression for the three-dimensional spatial power spectrum

$$\Phi_x(\mathbf{K}) = \left(\frac{1}{2\pi}\right)^3 \int_{-\infty}^{\infty} \int_{-\infty}^{\infty} \int_{-\infty}^{\infty} e^{-i\mathbf{K}\cdot\mathbf{R}} B_x(\mathbf{R}) d\mathbf{R}, \quad (3.29)$$

where $\mathbf{K}$ is the spatial wavenumber, so that $|\mathbf{K}| = \frac{2\pi}{\lambda}$. A field is statistically isotropic if it is invariant under rotation. In other words, the covariance only depends on the scalar distance $R = |\mathbf{R}_2 - \mathbf{R}_1|$. The spatial power spectrum then reduces to

$$\Phi_x(\kappa) = \left(\frac{1}{2\pi^2\kappa}\right) \int_0^\infty B_x(R) \sin(\kappa R) R dR, \tag{3.30}$$

where $\kappa = \frac{2\pi}{\lambda}$ is the scalar spatial wavenumber. The definition of the structure function

$$D_x(R) = 2[B_x(0) - B_x(R)] \tag{3.31}$$

and the inverse Fourier transform of equation 3.30 demonstrate that the spatial power spectral density and the structure function are related by

$$D_x(R) = 8\pi \int_0^\infty \kappa^2 \Phi_x(\kappa) \left(1 - \frac{\sin \kappa R}{\kappa R}\right) d\kappa. \tag{3.32}$$

Kolmogorov used the energy cascade theory discussed previously to show that, in the inertial subrange $\ell_0 \ll R \ll L_0$, the structure function associated with index-of-refraction fluctuations has the form

$$D_n(R) = C_n^R R^{\frac{2}{3}}. \tag{3.33}$$

The spatial power spectral density corresponding to this structure function is the Kolmogorov spectrum and is defined in the inertial subrange, $1/L_0 \ll \kappa \ll 1/\ell_0$, by

$$\Phi_n(\kappa) = 0.033 C_n^2 \kappa^{-11/3}. \tag{3.34}$$

Other forms of the spatial power spectral density exist that more closely fit experimental data. The Tatarskii spectrum is valid for $\kappa \gg 1/L_0$, while the von Kármán and modified

atmospheric spectra are valid for $0 \leq \kappa < \infty$.

The index-of-refraction structure constant is a function of height h above the ground and varies throughout the day with maximum at mid-day. Models for this constant include the Submarine Laser Communication (SLC) Day and Night, the Hufnagel-Valley, the Kunkel-Walters, and the NOAA model. Some models have no parameters and others parametric models can incorporate measured radiosonde data. Beland (1993) compiled a description of these various models, their development, and limitations.

The initial Hufnagel model was developed specifically for altitudes 3 km $< h <$ 24 km at mid-latitudes assuming a "low" tropopause. Stratospheric falloff depends on the tropospheric wind speed, which is not believed to be accurate. Since the model does not include the lower atmosphere, it may be used both day and night.

The Hufnagel-Valley Model extends the Hufnagel Model into the boundary layer. Initially, an exponential term was added, but C_n^2 scales as $h^{-\frac{4}{3}}$ during the daytime and as $h^{-\frac{2}{3}}$ during the night. A variant of the Hufnagel-Valley Model that exhibits an $h^{-\frac{4}{3}}$ dependence and is therefore valid for a mid-latitude location during the day is:

$$C_n^2(h) = 8.2 \times 10^{-26} v^2 h^{10} e^{-h} + 2.7 \times 10^{-16} e^{-\frac{h}{1.5}} + \frac{A}{(1000h)^{\frac{4}{3}}} e^{-10h}, \qquad (3.35)$$

where h is the height above the ground in kilometers, A is the value of C_n^2 for $h = 1m$, and v is the root-mean-square wind speed in meters per second for 5 km $\leq h \leq$ 20 km (Schmitt et al. 1996). Equation 3.35 is graphed in Figure 3.12 for $v = 21m/s$ with $A = 1 \cdot 10^{-14}$ and for $v = 21m/s$ with $A = 1 \cdot 10^{-13}$.

The CLEAR I summer model was developed in New Mexico. The model fits the arithmetic average C_n^2 piecewise. The height used in the model is measured relative mean sea level (MSL) and begins at $h = 1.23$ MSL. The CLEAR I night model is included in Table 3.1.

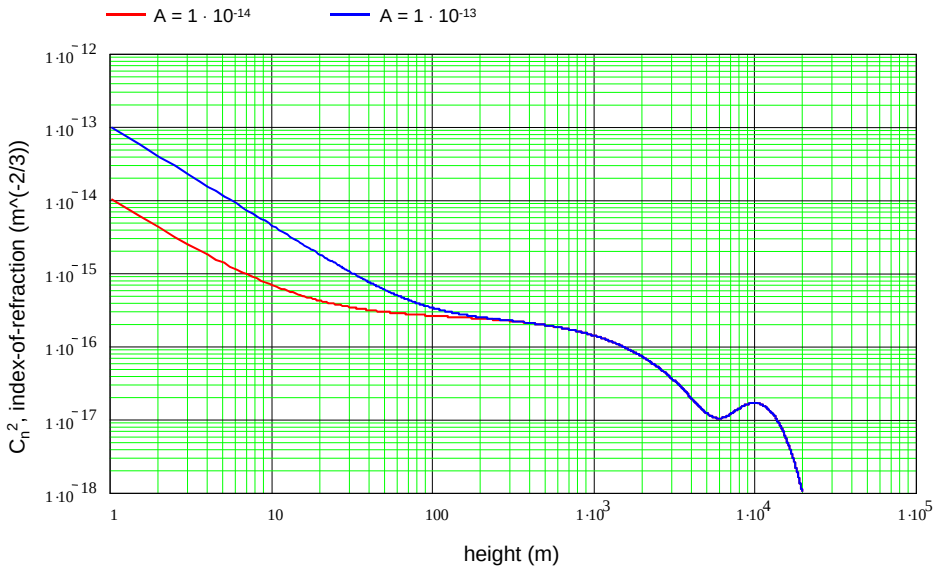

Figure 3.12: The Hufnagel-Valley Model for $v = 21m/s$ with $A = 1 \cdot 10^{-14}$ (in red) and $v = 21m/s$ with $A = 1 \cdot 10^{-13}$ (in blue). The index of refraction can vary over a wide range from weak $1 \cdot 10^{-16}$ to strong $1 \cdot 10^{-12}$

The NOAA model is the most advanced, but also the most difficult to use and does not include the boundary layer. Since a model is needed that extends to the ground and can be easily calculated, the Hufnagel-Valley Model was included in the DIRSIG LADAR/LIDAR model.

Scintillation

Now that a model for the index-of-refraction structure constant has been chosen, it is time to introduce the relevant statistics. The spatial and temporal variation in intensity caused by atmospheric turbulence is called scintillation and resembles a speckle pattern, as

Height Above MSL	**Model**
$1.23 < h \leq 2.13$	$log_{10}\left(C_n^2\right) = A + Bh + Ch^2$ $A = -10.7025$ $B = -4.3507$ $C = 0.8141$
$2.13 < h \leq 10.34$	$log_{10}\left(C_n^2\right) = A + Bh + Ch^2$ $A = -16.2897$ $B = 0.0335$ $C = -0.0134$
$10.34 < h \leq 30$	$log_{10}\left(C_n^2\right) = A + Bh + Ch^2 + D\exp\left\{-0.5\left[\frac{(h-E)}{F}\right]^2\right\}$ $A = -17.0577$ $B = -0.0449$ $C = -0.0005$ $D = 0.6181$ $E = 15.5617$ $F = 3.4666$

Table 3.1: CLEAR I Night Model (h in km MSL) (Thomas et al. 1993)

shown in Figure 3.13. Scintillation is important in any model that will be used to simulate spaceborne systems. Scintillation is due to the effect of turbulence on the logarithm of the amplitude of the wavefront. Experiments have shown that intensity has a log-normal distribution, that is the logarithm of the irradiance has a Gaussian distribution. Following Beland (1993), if χ is a Gaussian-distributed random variable, then

$$\chi = \frac{1}{2} \ln \left(I/A^2 \right), \tag{3.36}$$

where I is irradiance and A is the amplitude of the initial field. The mean irradiance has the form

$$< I >= \exp \left(2 < \chi > +2\sigma_\chi^2 \right) \tag{3.37}$$

and the normalized intensity variance is

$$\sigma_I^2 = \exp \left(4\sigma_\chi^2 \right) - 1 \approx 4\sigma_\chi^2, \tag{3.38}$$

where σ_χ^2 is the log-amplitude variance of χ. The log-amplitude variance is equal to the log-amplitude covariance evaluated at zero, $B_\chi(0)$. For propagation from $R = 0$ to L, the log-amplitude variance in the receiver aperture plane for a plane wave is

$$\sigma_\chi^2 = 0.56 k^{7/6} \left[sec(\varphi) \right]^{11/6} \int_0^L C_n^2(\eta) \left(L - \eta \right)^{5/6} d\eta. \tag{3.39}$$

where φ is the angle from the zenith and k is the wavenumber of light. In general, the log amplitude variance is a function of not only R, but also of the position in the receiver aperture plane. This dependence vanishes only in the special case of a plane or spherical wave. These equations are valid for a point receiver, i.e., where $\ell_0 \ll (\lambda L)^{1/2}$, and for zenith angles less than approximately forty degrees.

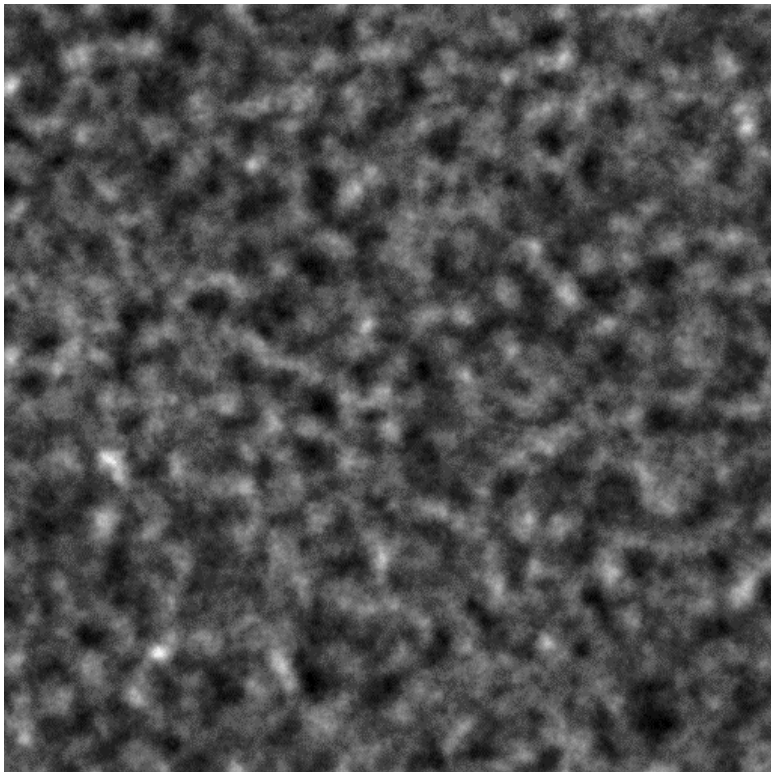

Figure 3.13: A sample scintillation image of a plane wave propagating through two kilometers of atmosphere at a wavelength of eleven microns and a value for C_n^2 of $1 \cdot 10^{-13}$.

To model the effects of scintillation, the spatial size of a "speckle" caused by scintillation as a function of distance must be known. A typical measure that is used is the correlation length, which is the abscissa where the normalized covariance function decreases to $e^{-2} \sim 0.14$ of the maximum. Andrews (1998) plotted the normalized covariance function based on the Kolmogorov spectrum for various beams. The results showed that the correlation length ρ_c is approximately $1.7\,(L/k)^{1/2}$ for a plane wave, where $(L/k)^{1/2}$ is termed the "Fresnel scale".

If the aperture of the receiver is larger than the Fresnel scale, then the log-amplitude variance will decrease due to averaging. Fried (1966) showed that the log-amplitude variance in this case is

$$\sigma_\chi^2\,(L) = 2\pi\left(\pi D^2/4\right)^{-2} \int_0^D \rho B_\chi\,(\rho, L)\,MCF\,(\rho)\,d\rho, \tag{3.40}$$

where D is the aperture diameter, ρ is the position in the receiver aperture plane, and $MCF\,(\rho)$ is the aperture mutual coherence function. The mutual coherence function is generated by the second moment of the aperture.

Unfortunately, the previous discussion on scintillation assumes propagation through a turbulent atmosphere in one direction only. In many LADAR/LIDAR systems the beam propagates through the turbulent atmosphere twice, from the source to the ground and back to the receiver. This double passage causes "enhanced backscatter" effects (EBS). These effects are discussed by Andrews (1998) and increase the mean irradiance via the Backscatter Amplification Effect (BSAE), which is an increase in irradiance fluctuations, and either an increase or decrease in the spatial coherence radius.

In the treatment by Andrews (1998), a reflector is treated either as a point target or as an unbounded target. A target is treated as a point if the radius of the reflector is much

smaller than the Fresnel scale. Andrews defines three types of reflectors: mirror, retroreflector, and Lambertian surface. Finally, he develops equations for the mean irradiance and scintillation index for spherical, Gaussian, and plane waves. Since enhanced backscatter effects were not included in the DIRSIG LADAR/LIDAR model, those results will not be replicated here. Users of the model should be aware of this limitation.

At this point, the equations governing scintillation that will be incorporated into the model, excluding enhanced backscatter, have been reviewed. There are two more categories of effects caused by atmospheric turbulence that will be covered next. As previously discussed, scintillation is due to the effect of turbulence on the log amplitude of the wavefront. In contrast, the beam and image effects of atmospheric turbulence are due to distortions of phase and decrease the amplitude of larger spatial frequencies. As shown in Figure 3.1, beam effects occur as the beam propagates down to the target and image effects occur after reflection as the beam propagates to the detector.

Beam Effects

The two types of beam effects, beam spread and centroid wander are shown in Figure 3.14. Beam spread describes the effect of turbulence on the radius of the laser pulse in the target plane. Large-scale eddies can deflect the beam while small-scale eddies can scatter it. Both long-term and a short-term broadening effects exist. The long-term beam radius ρ_L is related to the short-term beam radius ρ_s and the short-term beam centroid ρ_c:

$$< \rho_L^2 >=< \rho_s^2 > + < \rho_c^2 > . \tag{3.41}$$

The short-term beam radius is the sum of terms due to diffraction, focusing, and turbulence:

$$< \rho_s^2 >= \frac{4L^2}{(kD)^2} + \left(\frac{D}{2}\right)^2 \left(1 - \frac{L}{\gamma}\right)^2 + \frac{4L^2}{(k\rho_{0s})^2} \left[1 - 0.62 \left(\frac{\rho_{0s}}{D}\right)^{1/3}\right]^{6/5}, \tag{3.42}$$

where ρ_{0s} is the short-term transverse coherence length, L is the propagation distance, k is the wavenumber, D is the initial diameter of the beam, and γ is the radius of curvature of the beam. Spatial coherence describes the phase difference between two points on the same wave front of a wave. If the phase difference between these two points remains constant in time, then these two points are coherent. If this is true for any two points, then the wave has perfect spatial coherence. Temporal coherence describes the phase difference of the same point at two different moments in time. If the phase difference is constant over this time interval, then the wave is temporally coherent for that time interval. If this is true for any time interval, then the wave has perfect temporal coherence. According to Schmitt (1996), the short-term transverse coherence length for a Gaussian wave is

$$\rho_{0s,gauss} = \rho_{0s,plane} \left[\frac{\left(1 - \frac{L}{\gamma}\right)^2 + \frac{4L^2}{k^2D^4} \left[1 + \frac{1}{3} \left(\frac{D}{\rho_{0s,plane}}\right)^2\right]}{1 - \frac{13}{3}\left(\frac{L}{\gamma}\right) + \frac{11}{3}\left(\frac{L}{\gamma}\right)^2 + \frac{4L^2}{3k^2D^4} \left[1 + \frac{1}{4} \left(\frac{D}{\rho_{0s,plane}}\right)^2\right]} \right]^{\frac{1}{2}}, \tag{3.43}$$

where the short-term transverse coherence length for a plane wave is

$$\rho_{0s,plane} = \rho_{0,plane} \left[1 + 0.37 \left(\frac{\rho_{0,plane}}{D}\right)\right]^{\frac{1}{3}}. \tag{3.44}$$

The long-term transverse coherence length for a plane wave is

$$\rho_{0,plane} = \left[1.46 \sec(\varphi)\, k^2 \int_0^L C_n^2(z)\, dz\right]^{-\frac{3}{5}}. \tag{3.45}$$

Centroid wander is the motion of the beam centroid from pulse to pulse and is given by the short-term beam centroid:

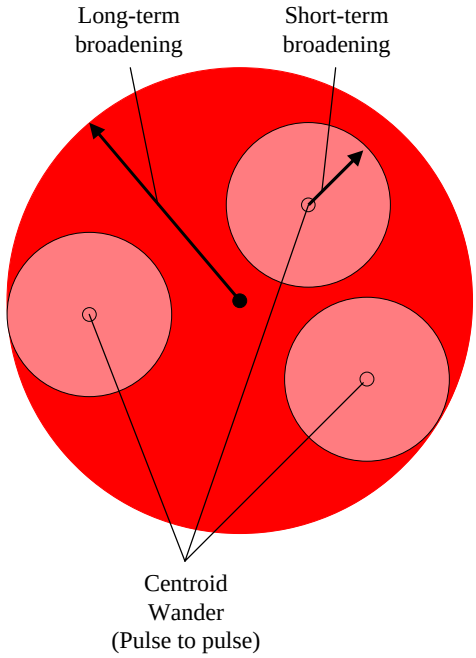

Figure 3.14: The long-term radius of the beam is a combination of two short-term effects: beam spread and centroid wander. Centroid wander is the motion of the beam centroid from pulse to pulse while beam spread is a short-term broadening of the pulse.

$$< \rho_c^2 >= \frac{2.97L^2}{\left(k^2 \rho_{0s}^{5/3} D^{1/3}\right)}. \tag{3.46}$$

Equations 3.42 and 3.46 are valid only for $\rho_{0s} \ll D < L_0$.

The equations presented in this section are used to incorporate the beam effects into the DIRSIG LADAR/LIDAR model as outlined in Section 5.7. Since it is assumed that LADAR/LIDAR systems will have pulse durations less than 0.01 seconds, the short-term equations are incorporated into DIRSIG. Beam wander is incorporated into DIRSIG by varying the centroid of the beam for each pulse.

Image Effects

The two types of image effects, image blurring and image dancing are shown in Figure 3.15. These effects are due to distortion of the phase of the wavefront and decrease the amplitude of large spatial frequencies. Fried (1966) derives the modulation transfer function (MTF) in the focal plane due to image blurring:

$$MTF\left(\nu\right) = \exp\left[-3.44\left(\frac{\lambda f \nu}{r_0}\right)^{5/3}\right], \tag{3.47}$$

where r_0 is Fried's coherence length, f is the focal length, and ν is the spatial frequency (Thomas et al. 1993). Fried's coherence length is related to the long-term transverse coherence length by $r_0 = 2.1\rho_0$. The long-term transverse coherence length is a measure of the spatial coherence of the beam. Propagation through turbulence will reduce the spatial coherence of any beam.

The MTF in equation 3.47 assumes long time averages. Long-term image blurring is caused by small-scale eddies that move or "dance" around the focal plane. This movement is caused by the advection of large eddies that tilt the wavefront. Beland (1993) asserts that

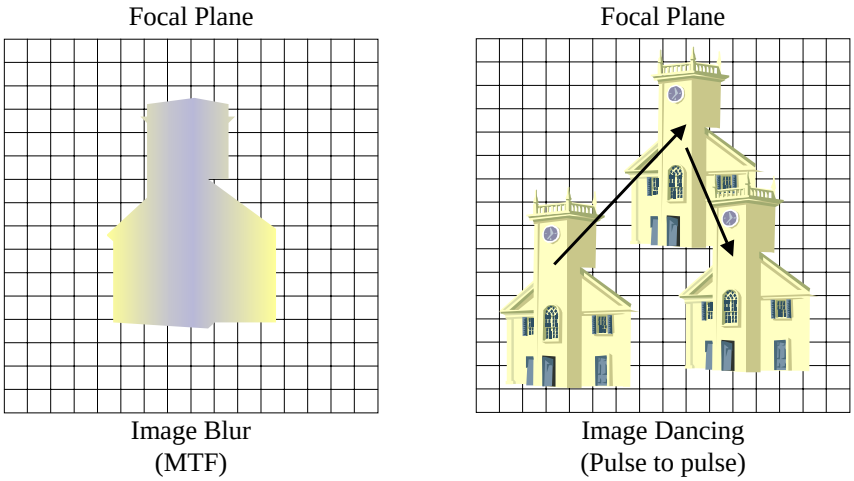

Figure 3.15: The long-term blur in the focal plane is a combination of two short-term effects: image blur and image dancing. Image dancing is caused by the advection of large eddies that tilt the wavefront and cause the short-termed blurred image to move around the focal plane.

time scales less than 0.01 seconds correspond to the short-term case and the corresponding MTF is

$$MTF_s(\nu) = \exp\left\{-3.44\left(\frac{\lambda f \nu}{r_0}\right)^{5/3}\left[1 - b\left(\frac{\lambda f \nu}{D}\right)^{1/3}\right]\right\}, \tag{3.48}$$

where $b = 1$ in the near field and $b = 0.5$ in the far field, D is the diameter of the aperture, and f is the focal length.

The wavefront tilt can be characterized by calculating the mean-square displacement in the focal plane. Beland (1993) gives the expression for the mean-square displacement in the focal plane for a plane wave

$$< \delta^2 >= 2.91 f^2 D^{-1/3} \int_0^L C_n^2(x)\, dx. \tag{3.49}$$

The equations presented in this section are used to incorporate the image effects into the DIRSIG LADAR/LIDAR model as outlined in Section 5.7. As mentioned previously it is the short-term equations that are incorporated into DIRSIG. Image dancing is incorporated in DIRSIG by shifting the location of the focal plane for each pulse. To complete the description of the properties of the medium through which the wave is propagating, atmospheric transmission is reviewed next.

3.3.4 Atmospheric Transmission

Atmospheric attenuation is caused by molecular absorption and scattering. The absorption at a particular wavelength depends upon numerous conditions such as the types of molecules present, their relative strength, temperature, and pressure. The high-resolution transmission molecular absorption database (HITRAN) contains detailed spectral-line parameters. Version 11.0 includes over 1,080,000 spectral lines for 36 different molecules.

The HITRAN database is used by several atmospheric transmission programs currently maintained by the Air Force Research Laboratory Space Vehicles Directorate: Low Resolution Transmittance Code (LOWTRAN), Moderate Resolution Transmittance Code (MODTRAN), and Fast Atmospheric Signature Code (FASCODE). Currently, DIRSIG uses either MODTRAN or FASCODE, depending on the resolution needed, to calculate atmospheric transmission and upwelled and downwelled radiance (Schott et al. 1999). MODTRAN calculates atmospheric transmittance and radiance for wave numbers from 0 to 50,000 cm^{-1} at up to 2 cm^{-1} spectral resolution. FASCODE is similar to MODTRAN except FASCODE has higher spectral resolution and does not calculate scattering coefficients. Documentation of MODTRAN and FASCODE can be found at http://www-vsbm.plh.af.mil/.

3.3.5 Thermal Blooming

The final atmospheric effect considered is thermal blooming, which is a nonlinear effect. Thermal blooming is caused by absorption of energy from the laser beam by molecules and particles in the path (Thomas et al. 1993). The absorbed energy causes the atmosphere to heat up and expand. This expansion creates a distributed nonlinear thermal lens which usually defocuses and spreads the beam. The effects of thermal blooming are mentioned for completeness, but they will not be included in DIRSIG.

At this point the governing equation describing the propagation of a wave, a method to solve the equation, a mathematical description of the types of waves, and the properties of the medium through which the wave is propagating have been reviewed. How the properties of the reflecting surface affect the return LADAR signal will be explored next.

3.4 Speckle

The following discussion draws heavily from the statistical properties of speckle developed by J.W. Goodman (1984). A speckle pattern is produced when coherent light scatters from a surface whose roughness is of the order of a wavelength of light. As shown in Figure 3.16, images that exhibit speckle effects have a grainy appearance due to the different distances travelled by the wavelets that make up the wavefront. The coherent, but now dephased, wavelets interfere to produce the speckle pattern. Figure 3.17 shows how speckle patterns are produced from free-space propagation and in imaging systems. For a speckle pattern to show up in an image, the diffraction-limited amplitude point spread function (PSF) of the system must be broad compared to the variations in the surface. A broad PSF guarantees that many dephased wavelets add at each image point.

Speckle theory is closely related to coherence theory. Speckle theory develops the statistical properties of a field due to a collection of scatterers, whereas coherence theory develops the statistical properties of a field that is emitted from various sources. Since the measured quantity is the intensity of the scattered light, the statistical properties of intensity are relevant. Several assumption are made to develop the statistics. In the ideal case, the surface is modeled as a collection of unrelated scattering regions. The amplitude and phase of a scattered component are assumed to be statistically independent. The surface produces phase variations much larger than 2π radians, which results in an uniform distribution in phase over the interval from -π to π. The resulting probability density function has the form:

$$p_{I,\theta}\left(I,\theta\right) = p_I\left(I\right) p_\theta\left(\theta\right), \tag{3.50}$$

where the probability density function for the intensity is

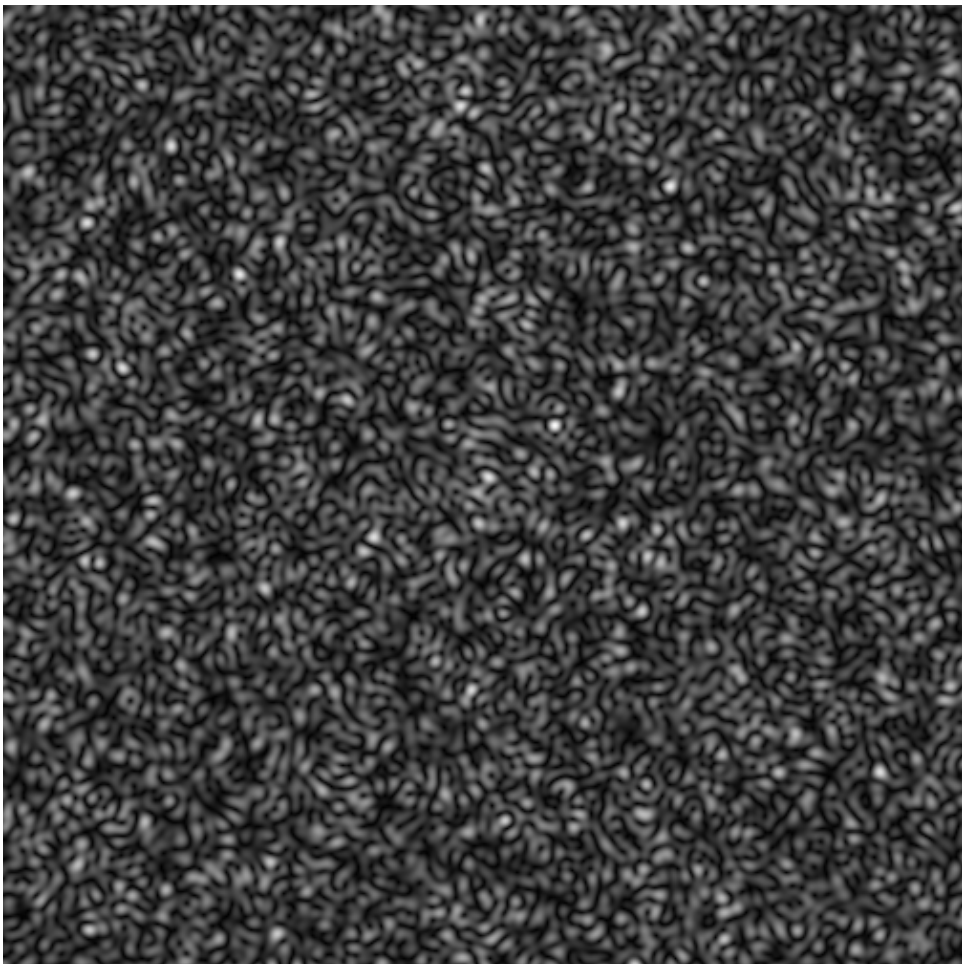

Figure 3.16: A sample speckle pattern produced by propagating light in a pupil with a random phase to the Fresnel diffraction region.

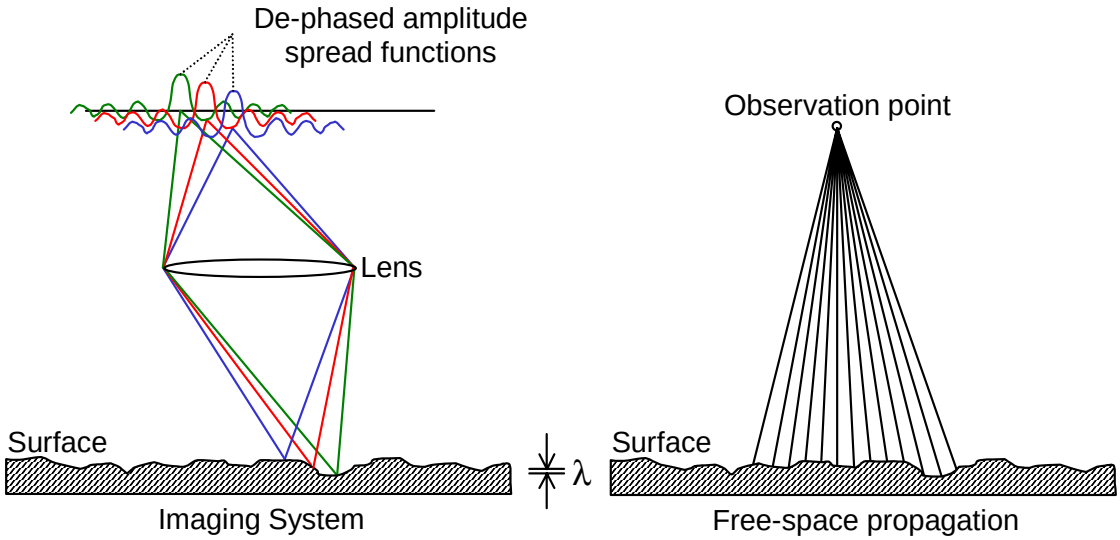

Figure 3.17: Speckle occurs when wavelets that make up the wavefront travel different distances and interfere. This interference can occur in an imaging system and also in free-space propagation (Dainty 1984).

$$p_I(I) = \int_{-\pi}^{\pi} p_{I,\theta}(I,\theta)\, d\theta = \begin{cases} \frac{1}{2\sigma^2}\exp\left(-\frac{I}{2\sigma^2}\right) & I \geq 0 \\ 0 & otherwise \end{cases} \tag{3.51}$$

and for the phase is

$$p_\theta(\theta) = \int_{-\pi}^{\pi} p_{I,\theta}(I,\theta)\, dI = \begin{cases} \frac{1}{2\pi} & -\pi \leq \theta < \pi \\ 0 & otherwise. \end{cases} \tag{3.52}$$

One can easily show that the mean value of the intensity $< I >$ is equal to $2\sigma^2$ and that the n$^{\text{th}}$ moment $< I^n >= n! < I >^n$. The resulting variance σ_I^2 is $< I >^2$. The contrast C is usually defined

$$C = \frac{\sigma_I}{< I >} \tag{3.53}$$

and is always equal to one.

In a real LADAR system the finite size of the detector smooths the ideal point intensity. Goodman (1984) shows that the resulting signal-to-noise ratio is no longer unity, but has the following form

$$SNR_{spec} = \left[\frac{1}{S^2}\int_{-\infty}^{\infty}\int_{-\infty}^{\infty} R_S(\Delta x, \Delta y)\left|\mu_A(\Delta x, \Delta y)\right|^2 d\Delta x d\Delta y\right]^{-\frac{1}{2}}, \tag{3.54}$$

where S is the area of the aperture

$$S = \int_{-\infty}^{\infty}\int_{-\infty}^{\infty} \zeta(x,y)\, dxdy, \tag{3.55}$$

$\zeta(x,y)$ is the receiver aperture function, $R_S(\Delta x, \Delta y)$ is the aperture autocorrelation function

$$R_S(\Delta x, \Delta y) = \int_{-\infty}^{\infty}\int_{-\infty}^{\infty} \zeta(x_1, y_1)\,\zeta(x_1 - \Delta x, y_1 - \Delta y)\,dx_1 dy_1, \tag{3.56}$$

$\mu_A(\Delta x, \Delta y)$ is the complex coherence factor

$$\mu_A(\Delta x, \Delta y) = \frac{\int_{-\infty}^{\infty}\int_{-\infty}^{\infty} I(\xi,\eta)\, e^{i\frac{2\pi}{\lambda R}(\xi\Delta x + \eta\Delta y)} d\xi d\eta}{\int_{-\infty}^{\infty}\int_{-\infty}^{\infty} I(\xi,\eta)\, d\xi d\eta}, \tag{3.57}$$

and $I(\xi, \eta)$ is the spatial intensity profile across the target. According to Schmitt (1996), the speckle signal-to-noise ratio (SNR) for an ensemble of independent speckle patterns, a circular aperture without a central obscuration, and a Gaussian beam is

$$SNR_{spec} = 1 + \frac{\pi D_{tar} D_{rec}}{4\lambda R} = 1 + \frac{D_{rec}}{D_{corr}}, \tag{3.58}$$

where

$$D_{corr} = \frac{4\lambda R}{\pi D_{tar}}, \tag{3.59}$$

D_{rec} is the diameter of the telescope aperture, D_{tar} is the diameter of the beam in the target plane at range R, D_{corr} is the speckle correlation diameter in the receiver plane, and λ is the wavelength of the laser. In static geometries where both the receiver and transmitter are fixed, the speckle patterns cannot be assumed independent and Schmitt (1996) introduces a correction factor to the speckle-induced intensity standard deviation. The signal-to-noise ratio for speckle in static geometries can be improved if many shots are averaged.

In addition to the first-order statistics that describe speckle measured at a single point, second-order statistics are also needed to describe the spatial structure of the speckle pattern. The width of the autocorrelation function gives a reasonable estimate of the average

width of a speckle. Goodman (1984) derives the following expression for the autocorrelation of the speckle intensity:

$$R_I(\Delta x, \Delta y) = \langle I \rangle^2 \left[1 + |\mu_A(\Delta x, \Delta y)|^2 \right]. \tag{3.60}$$

The power spectral density is the Fourier transform of the autocorrelation according to the Wiener-Khintchine theorem:

$$\varphi(\nu_X, \nu_Y) = \langle I \rangle^2 \left\{ \delta(\nu_X, \nu_Y) + \frac{\int_{-\infty}^{\infty} \int_{-\infty}^{\infty} |I(\xi, \eta)|^2 |I(\xi - \lambda R \nu_X, \eta - \lambda R \nu_Y)|^2 \, d\xi d\eta}{\left[\int_{-\infty}^{\infty} \int_{-\infty}^{\infty} |I(\xi, \eta)|^2 \, d\xi d\eta \right]^2} \right\}. \tag{3.61}$$

These equations for the autocorrelation and power spectral density need to be modified when used for an imaging system. When the size of the speckle is small compared to the receiver aperture, the spatial intensity profile across the target can be replaced with the receiver aperture function. Goodman (1984) calculates for a circular receiver aperture of diameter D the autocorrelation

$$R_I(r) = \langle I \rangle^2 \left[1 + \left| 2 \frac{J_1\left(\frac{\pi D r}{\lambda f}\right)}{\frac{\pi D r}{\lambda f}} \right|^2 \right] \tag{3.62}$$

and power spectral density

$$\varphi(\rho) = \langle I \rangle^2 \left\{ \delta(\nu_X, \nu_Y) + \left(\frac{\lambda f}{D} \right)^2 \cdot \frac{4}{\pi} \left[\cos^{-1}\left(\frac{\lambda f}{D} \rho \right) - \frac{\lambda f}{D} \rho \sqrt{1 - \left(\frac{\lambda f}{D} \rho \right)^2} \right] \right\}, \tag{3.63}$$

where $< I >$ is the mean intensity, J_1 is a first order Bessel function of the first kind, $r = \left[(\Delta x)^2 + (\Delta y)^2 \right]^{\frac{1}{2}}$ is the position on the focal plane, f is the focal length, $\rho = \left(\nu_X^2 + \nu_Y^2 \right)^{\frac{1}{2}}$

is the spatial frequency, and $\delta(\nu_X, \nu_Y)$ is a Dirac delta function. The power spectral density is valid for $\rho \leq \frac{D}{\lambda f}$ and is 0 otherwise.

The speckle return is incorporated into the model as outlined in Section 5.6. The DIRSIG LADAR model is valid even in the long-wave infrared spectral region because most surfaces are still rough on the order of a wavelength. Therefore, fully developed speckle, i.e., an uniform distribution in phase over the interval from -π to π, will be assumed.

3.5 Detection Methods

Most LADAR/LIDAR systems either use direct or heterodyne detection. The DIRSIG LADAR/LIDAR model incorporates only direct detection. The theory of heterodyne detection will also be reviewed with an eye toward incorporating it into the model at a future date.

3.5.1 Pulsed Direct Detection

The two types of detectors used at infrared wavelengths include photodetectors (photovoltaic and photoconductive) and thermal detectors. Photovoltaic detectors are used most often because of their large quantum efficiency at longer wavelengths. Their main limitation is thermal noise. The liquid-nitrogen-cooled InSb photodiode, which is sensitive from 1 μm to 5.5 μm, is widely used.

According to Yariv (1991), the signal current for a photoconductive detector is

$$I = \frac{P_L e \eta}{h \nu_L} \left(\frac{\tau_0}{\tau_d} \right), \tag{3.64}$$

where P_L is the average laser power, η is the quantum efficiency, ν_L is the frequency of the laser, τ_0 is the average lifetime of an excited carrier, and τ_d is the drift time for a carrier

across the length of the semiconductor crystal. Silicon cannot be used for $\lambda > 1.1\ \mu m$, other detectors such as InAs, InSb, and HgCdTe must be used. Because of the lower scattering cross section at infrared wavelengths, the increased noise of infrared detectors, and the steep dependence of the SNR with range, direct detection aerosol range-resolved measurements can only be acquired for short distances. Because of this limitation, topographic DIAL is used instead to obtain integrated path concentration measurements. Direct detection systems experience detection linearity problems and need dynamic compression because the LADAR/LIDAR signal has a wide dynamic range. Finally, the SNR for direct infrared detection is directly proportional to the energy of the emitted pulse. Therefore, in direct detection systems it is better to concentrate the average laser power into a few shots rather than spreading it over many shots. In heterodyne, ultraviolet (UV), and visible direct detection systems, the SNR depends on not only the energy of the emitted pulse, but also on the number of pulses.

3.5.2 Coherent or Heterodyne Detection

Heterodyne detection increases the signal-to-noise ratio of weak signals, especially in the $5 - 12\ \mu m$ region. Currently, heterodyne detection is usually used only in systems where the phase of the return is exploited, such as Doppler LIDAR, vibrometry, and synthetic aperture radar. In heterodyne detection, the return signal is mixed with a local oscillator at the detector, as shown in Figure 3.18. Heterodyne detection mixes two signals with the same phase and polarization. Most background light is not in phase with the transmitted signal and is rejected. The local oscillator can either have the same or a different frequency than the return signal. If the same frequency, it is termed a homodyne detector. Homodyne detectors have noise that is inversely proportional to frequency. Generally, a frequency is employed that is shifted by a few megahertz from the return signal. The electric fields of the

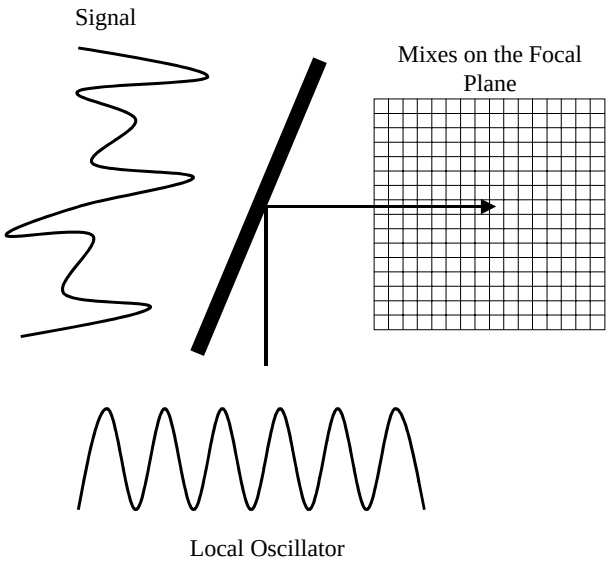

Figure 3.18: In heterodyne detection, the return signal is mixed with a signal with the same phase and polarization, but a slightly different freqency. The resulting intensity is proportional to the product of the intensities of the two signals, and its beat frequency is proportional to the frequency difference between the two signals.

returned signal and the local oscillator are mixed on the focal plane. If $E(t)$ varies slowly compared to ω_0, then the rate at which carriers are produced is proportional to the squared magnitude $V(t)V^*(t)$ of the analytic signal $V(t) = E(t)\exp(i\omega_0 t)$. The combined field an the focal plane is

$$e(t) = E_{LO}\cos(\omega_{LO}t + \phi_{LO}) + E_s\cos(\omega_s t + \phi_s) \quad (3.65)$$

$$= Re\left[\left(E_s e^{i\phi_s} + E_{LO}e^{i(\omega t+\phi_{LO})}\right)e^{i\omega_s t}\right], \quad (3.66)$$

where the subscript s refers to the returned signal, the subscript LO to the local oscillator, ω is the angular frequency, ϕ is the phase, $\omega = \omega_{LO} - \omega_s$, and $\phi = \phi_{LO} - \phi_s$. If $\omega \ll \omega_s$ then $V(t) = \left(E_s e^{i\phi_s} + E_{LO} e^{i(\omega t + \phi_{LO})}\right) e^{i\omega_s t}$ and the resulting intensity is

$$V(t)\, V^*(t) = E_s^2 + E_{LO}^2 + 2E_s E_{LO} \cos(\omega t + \phi). \tag{3.67}$$

The resulting intensity is proportional to the product of the intensities of the two signals and its beat frequency is proportional to the frequency difference between the two signals. The zero-frequency terms are filtered out by the electronics and the beat frequency is measured.

The current is found by starting with the differential equation describing N_c the number of excited carriers

$$\frac{dN_c}{dt} = aVV^* - \frac{N_c}{\tau_0}, \tag{3.68}$$

where τ_0 is the average carrier lifetime and a is a proportionality constant. Yariv (1991) substituted a trial solution of the form $N_c(t) = N_0 + N_1 e^{i(\omega t + \phi)} + N_1^* e^{-i(\omega t + \phi)}$ and obtained values for N_0 and N_1 by equating like terms. The current through the sample is

$$i(t) = \frac{N_c(t)\, e\overline{\nu}}{d}, \tag{3.69}$$

where $\overline{\nu}$ is the drift velocity and d is the length of the semiconductor crystal. Yariv (1991) determined the proportionality constant a by equating the currents through the sample with $E_s = 0$ and through a photoconductive detector when exposed to a constant flux. The resulting equation for the current through the sample is:

$$i(t) = \frac{e\eta}{h\nu_{LO}} \left(\frac{\tau_0}{\tau_d}\right) \left[P_s + P_{LO} + 2\sqrt{\frac{P_s P_{LO}}{1 + \omega^2 \tau_0^2}} \cos\left(\omega t + \phi - \tan^{-1}(\omega\tau_0)\right)\right], \tag{3.70}$$

where P is the power, η is the quantum efficiency, ν_{LO} is the frequency of the local oscillator, τ_0 is the average carrier lifetime, and τ_d is the drift time for a carrier across d. A drawback to this technique is that atmospheric turbulence, non-uniform aerosol distributions, and the texture of a topographical target all distort the phase front of the return signal. Therefore, the wavefront of the returning signal cannot be entirely in phase with the local oscillator wavefront, resulting in large random fluctuations in the signal intensity due to speckle.

As mentioned previously, the DIRSIG LADAR/LIDAR model incorporates direct detection, so the mixing of the return signal with a local oscillator will not be modeled. At this point the governing equation describing propagation of a wave, a method to solve the equation, a mathematical description of the types of waves, the properties of the medium through which the wave is propagating, the properties of the reflecting surface, and various detectors have been reviewed. As shown in Figure 3.1, there are only two effects left to discuss, the passive return and multiple bounce. The passive return is not a part of the LADAR/LIDAR model but, rather, is a source of noise.

3.6 Passive Return

Types of noise in a LADAR/LIDAR system not yet discussed include detector noise, amplifier/digitization noise, albedo inhomogeneities, and composition fluctuations in the atmosphere. The DIRSIG sensor model can account for some of these additional sources of noise, such as detector and amplifier/digitization noise. The major remaining source of noise incorporated in the model is background-radiation noise, which is the irradiance received by the sensor due to all passive sources

$$Q_b^N(\lambda) = \frac{A_0}{f^2} \int_{\Delta\lambda_0} L\left(l, \theta_0, \phi_0, \lambda'\right) \xi\left(\lambda'\right) d\lambda', \tag{3.71}$$

where A_0 is the area of the objective lens or mirror, f is the focal length of the system, $L(l, \theta_0, \phi_0, \lambda)$ is the spectral radiance reaching the sensor, l is the slant range from the target, θ_0 is the view angle, ϕ_0 is the azimuthal angle, and $\xi\left(\lambda^{'}\right)$ is the receiver's spectral transmission. The background-radiation noise is particularly significant in the daytime and must be accounted for in the model. The passive sources that DIRSIG models are shown in Figure 3.19 and Figure 3.20 and include direct solar illumination, solar illumination reflected from the moon, starlight, self emission, and incoherent lighting.

The final effect to be discussed occurs when parts of the laser beam reflect from more than one surface before making it back to the detector. The overall contribution of this multiple bounce to the return is usually not very large, but can be a significant source of noise in a multilayered scene, such as, a tank hidden under camouflage or trees where the light may bounce around many times before returning to the sensor.

3.7 Multiple Bounce

Multiple scattering occurs in the aerosol return while multiple bounce occurs in the topographic return. Most literature focuses on multiple scattering within clouds, fog, and water, which is beyond the scope of this work. Multiple bounce from topographical targets is already accounted for in the passive return calculated by DIRSIG. The passive return is treated as constant, so it is not calculated as a function of time. The LADAR return is a function of time and multiply bounced photons encounter a time delay in reaching the target plane. To extend this capability to the LADAR return, the multipath time $\tau = t - \frac{z}{c}$ must be considered so that the scattered return is added into the overall return at the correct time. This is illustrated in Figure 3.21. First, each pixel on the focal plane is subsampled. A ray is cast into the scene from each of these subsamples to find what

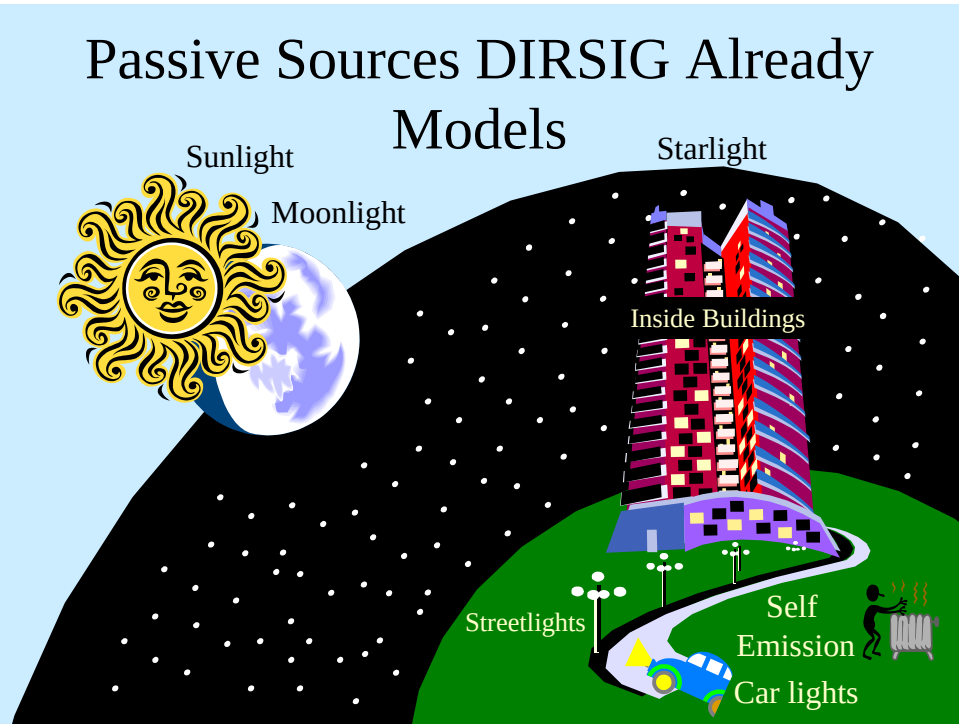

Figure 3.19: The passive sources already included in DIRSIG are solar illumination, solar illumination reflected from the moon, starlight, and incoherent lighting. Sources of incoherent lighting include headlights, streetlights, and light from inside buildings.

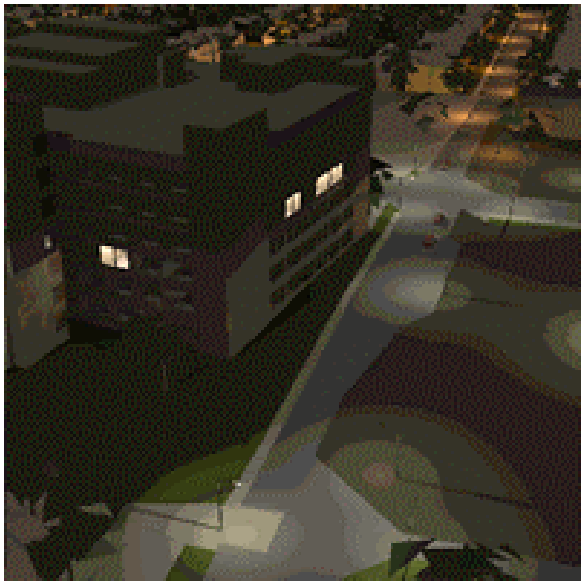

Figure 3.20: A low-light DIRSIG image, showing sources of incoherent lighting, including streetlights and light from inside buildings.

it illuminates. When a ray encounters a opaque object, several additional rays are sent out from this object to determine the radiation load onto the surface and the ray is then reflected back to the sensor. The distance from the laser to this first surface is R_{S1} and the reflected return from that surface is I_{S1}. For each surface, one ray is sent into the specular direction and to either the solar or lunar position. Additional rays are sent out to sample the skydome. Any ray that encounters an object requires that the radiation load on that surface be calculated in a similar manner and the ray is then reflected back to the sensor. The distance from the first reflecting surface to the second reflecting surface is $R_{S1:S2}$, from the second to the third is $R_{S2:S3}$, etc. The reflected return I_{S2} from this second surface depends how much radiation was reflected onto the second surface from the first reflection. This additional path difference will be calculated, so that the additional return can be added into the overall return at the correct time, as shown in the graph of I versus R or t

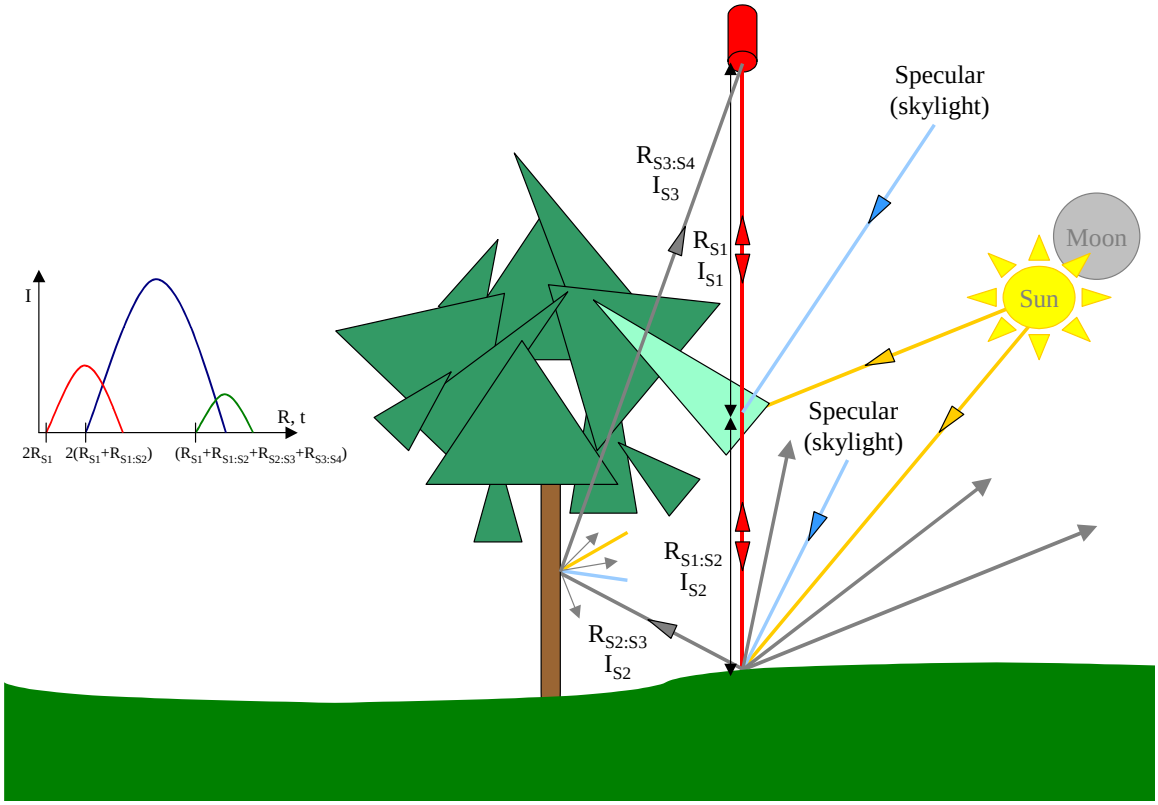

Figure 3.21: In a three-dimensional scene photons, can bounce multiple times. For example, the beam might first hit a leaf where part of the beam is reflected back to the sensor while the rest is transmitted and continues on to the ground. At the ground, part of the beam is again reflected back to the sensor while part of the beam is scattered and hits a tree before heading back to the sensor. The travel time must be accounted for to add the return from each surface into the overall return at the correct time.

in Figure 3.21.

Finally the model is complete and includes all the effects shown in Figure 3.1. Section 3.2 introduced the basic aerosol and topographical LADAR/LIDAR equations, which are the fundamental equations implemented in the model. Subsections 3.2.1 and 3.2.2 covered the geometrical form factor and compression effect, which gives the power versus range curve its overall shape. DIRSIG is inherently a spectral model and the new LADAR/LIDAR model is not any different as explained in Subsection 3.2.3. Section 3.3 described how the atmosphere affects the wave as it propagates. The first subsection of this section gave the equations governing the propagation of a wave and the method used to solve it, the Rytov approximation. Subsection 3.3.2 gave the mathematical description of the types of waves modeled. Subsection 3.3.3 reviewed atmospheric turbulence including scintillation, image effects, and beam effects. The enhanced backscatter effect introduced in this subsection is not included in the model. Section 3.4 introduced the concept of speckle, which is produced by the reflection of the beam, and is included in the model. Section 3.5 reviewed the two different detection methods, direct and heterodyne. Both types of detection are used in actual LADAR/LIDAR systems, but only direct detection is included in the model. Section 3.6 reviewed a dominant source of noise, the passive return. Finally, Section 3.7 reviewed the concept of multiple bounce, which is included in the model to allow the detection of hidden objects. The resulting model built from this theory includes capabilities that current LADAR/LIDAR models do not. The next chapter summarizes some of the current LADAR/LIDAR models and contrasts their capabilities with the capabilities of the DIRSIG LADAR/LIDAR model.

Chapter 4

Current Models

This chapter summarizes current LADAR/LIDAR models. These models come in two types, those that calculate the return or signal-to-noise ratio for a particular system without attempting to model the return from an actual scene and those that produce a synthetic image. Many different models simulate systems without producing synthetic images, though only some are summarized. This is not meant to be an exhaustive list. The only known current model that produces an actual synthetic image is the Infrared Modeling and Analysis (IRMA) code. Its capabilities and limitations are reviewed.

4.1 BACKSCAT Lidar Backscatter Simulation

BACKSCAT is a US Air Force Research Lab program included in LOWTRAN that models the aerosol and topographic return at a single wavelength from a monostatic LIDAR as a function of altitude, viewing angle, and atmospheric conditions. It calculates both the molecular and aerosol backscatter and attenuation coefficients for various atmospheres. BACKSCAT has the capability to evaluate both elastic and Raman scattering. This work

deals exclusively with elastic scattering, but can easily be extended to include Raman scattering based upon AFRL's work. BACKSCAT also has the capability to model cirrus and water clouds. Furthermore, it corrects the LIDAR viewing angle to account for the curvature of the earth. Finally, it calculates the signal-to-noise ratio for numerous detectors including both direct and coherent detection. Because BACKSCAT is based upon LOWTRAN, it is not capable of modeling problems that require good spectral fidelity. AFRL issued a series manuals describing the capabilities of the model (N.R. Guivens et al. 1988) (Hummel et al. 1991) (Hummel et al. 1992) (Longtin et al. 1994). BACKSCAT was considered as a way to calculate the backscatter coefficient. Unfortunately, because BACKSCAT revisions have not kept up with MODTRAN releases it could not be incorporated into our model that uses the current release of MODTRAN.

4.2 System Optimization Numerics for DIAL

The System Optimization Numerics for DIAL (SONDIAL) model developed by Los Alamos is a comprehensive numerical model of CO_2 DIAL (Schmitt et al. 1996). The model links various individual models together that calculate the LIDAR signal-to-noise ratio. The individual models are divided into two categories: LIDAR hardware models and natural environment models. The latter use FASCODE and BACKSCAT to calculate the return signal. The other natural environment models calculate the signal-to-noise ratio due to external noise effects, such as beam effects due to atmospheric turbulence, speckle, target albedo variations, and plume absorption. These signal-to-noise calculations are combined into an overall system signal-to-noise ratio. This model could not be used to create a synthetic image. Because BACKSCAT does not work with the current release of MODTRAN, the part of the model that calculates the return signal could not be incorporated

into DIRSIG.

4.3 Lidar-PC

Lidar-PC is a topographical and aerosol LIDAR model for both direct detection and DIAL systems (W. E. Wilcox 1995). The model is not designed to produce synthetic imagery, but instead calculates the signal-to-noise ratio as a function of altitude, range, and wavelength for a particular LIDAR system and a particular atmosphere. The model is capable of simulating both monostatic and bistatic systems by calculating the overlap factor. This model uses the HITRAN database for molecular absorption and the LOWTRAN7/BACKSCAT program for aerosol and cloud backscatter and attenuation coefficients. By using the HITRAN database, Lidar-PC overcomes the limitation of BACKSCAT and is capable of modeling problems that require high spectral fidelity. The program itself is free, but requires the use of the University of South Florida (USF) HITRAN-PC software which can be purchased from Ontar Corporation. This model was interesting because it implements most of the geometrical form factors. Like the SONDIAL model, this model could not be used directly because the overall return is needed, not the signal-to-noise ratio and because BACKSCAT does not work with the current release of MODTRAN.

4.4 Atmospheric Lidar End-to-end Simulator

Atmospheric Lidar End-to-end Simulator (ALIENS) is a Doppler LIDAR model developed by the German Aerospace Center (Streicher et al. 1998). ALIENS differs from other models in that it produces a stochastic rather than a deterministic return. For identical inputs ALIENS will produce a different output each time it is run. The program includes a complex heterodyne detection model that includes the effect of atmospheric turbulence

in the low signal-to-noise regime. The model is valid for even a few photons per detection interval. The model also includes the effects of signal digitization and frequency estimation. The program requires the use of LabVIEW, which is available from National Instruments. This model was useful because of its ability to model heterodyne detection. ALIENS uses beam propagation instead of ray tracing to model heterodyne detection. The advantages and disadvantages of the two methods and the decision to retain the ray-tracing method is presented in Section 5.4.

4.5 Infrared Modeling and Analysis (IRMA)

The IRMA model was developed for the Air Force Research Laboratory Munitions Directorate by CSC/Nichols (Vechinski et al. 2000). IRMA is a fully developed synthetic-image generation model that can model detailed sensor effects. IRMA contains a passive channel that runs from the visible through the millimeter spectral range, an active millimeter channel, and a LADAR channel. Some advantages of IRMA are that the passive channel considers polarization and the thermal model is well validated. It has both direct and coherent detector models. IRMA tracks relative not absolute phase. It models the speckle return from surfaces. IRMA currently has several limitations that restrict its use. It can model a spectral system, but each wavelength must be processed separately unlike DIRSIG which is inherently a spectral model. Additionally, the LADAR channel only models time-of-flight pulsed laser rangefinders. It can not model the aerosol return. It does not include atmospheric turbulence effects. Furthermore, it cannot model bistatic systems, i.e., the source and the receiver must be in the same position. The LADAR channel does not add the passive return in the spectral range of the detector. Finally, it does not account for multiple bounces.

In summary, BACKSCAT could not be used because it does not work with the current release of MODTRAN, nor are there any plans to make it compatible. Since SONDIAL and Lidar-PC rely on BACKSCAT, these models could not be used. ALIENS could not be used because it is inherently a beam-propagation model. Finally, IRMA could not be used because there were too many effects to be included into DIRSIG that IRMA was unable to model. Since nothing significant could be borrowed from these previously developed models, an new approach was developed, which is outlined in the next chapter.

Chapter 5

Approach

This chapter begins with a description of how the basic aerosol and topographic equations are implemented in the DIRSIG model. First, the convolved topographic equation is introduced. A description of how the aerosol and topographic returns are merged in the model follows. How the return is calculated on a spectral basis and what quantities vary as a function of wavelength are explained in Section 5.2. Section 5.3 describes how the atmospheric parameters in the basic equations are obtained. The reasons behind the decision to use a ray-tracing approach versus a beam-propagation approach are discussed in Section 5.4. Section 5.5 reviews the initial implementation scheme for the geometrical form factor calculation and the initial accounting scheme for multiple bounce photons. Problems encountered with these initial implementation schemes are then discussed, leading to the introduction of the photon map. The section concludes with a description of how photon maps are created in the DIRSIG model, how they are queried to duplicate the geometrical form factor calculation, and how the photon map implementation helps solve the problems encountered in the initial implementation. Section 5.6 introduces the speckle simulation

used to derive the speckle implementation approach. The mathematical approximation upon which the resulting texture map method is based is reviewed along with a description of how it is implemented in the DIRSIG model. Section 5.7 describes the strategy for implementing the beam and image atmospheric turbulence effects into the model. The scintillation simulation used to derive the scintillation implementation approach is described in Section 5.8. Finally, the chapter ends with Section 5.9, which lists all primary and secondary variables and describes how the model obtains them.

5.1 Basic Equation Implementation

The basic aerosol LIDAR equation (eq. 3.1) accounts for the temporal width of the laser pulse while the topographical equation (eq. 3.10) does not. Figure 5.1 illustrates how the aerosol LIDAR equation already accounts for the temporal shape of the pulse. The returns from each range (shown on the left) are summed to give the overall return (on the right). Mathematically, the return from each range is the convolution of a Dirac delta function with the temporal shape of the pulse and the overall aerosol return is the sum of all the convolved Dirac deltas. Each term produces a Gaussian curve whose center is shifted by $\frac{c\tau_L}{2}$. Since the topographic equation has not been convolved with the temporal shape of the pulse, the convolution must be performed before adding it to the modeled aerosol return. This process is illustrated in Figure 5.2. The Dirac delta function is the return calculated from the topographical LADAR equation (eq. 3.10). By convolving the Dirac delta function with a Gaussian temporal pulse shape and evaluating the geometrical form factor, the resulting equation for the topographical irradiance is

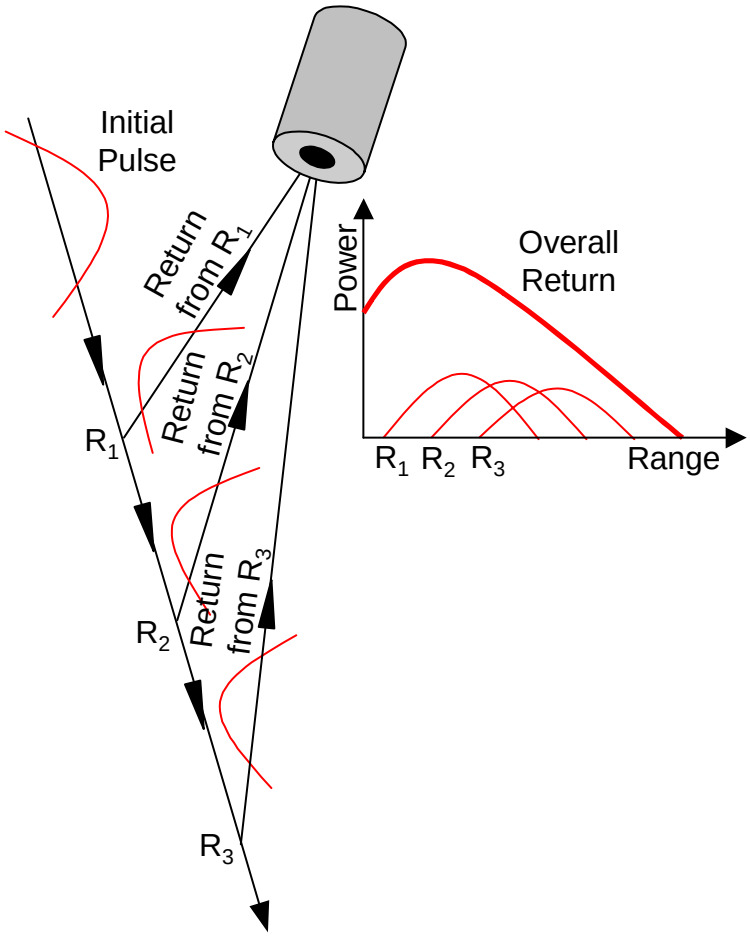

Figure 5.1: The aerosol LIDAR equation already accounts for the temporal shape of the pulse. The returns from each range, shown on the left, are summed together to give the overall return, as shown in the graph on the right. Mathematically, the return from each range is the convolution of a Dirac delta function with the temporal shape of the pulse.

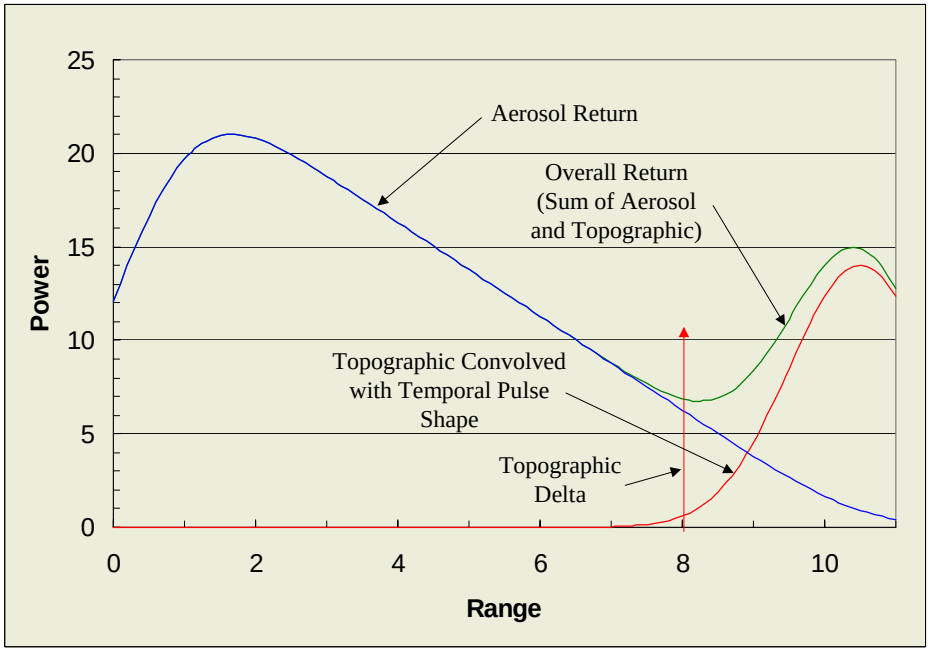

Figure 5.2: The aerosol and topographic returns must be merged together. The aerosol return is the overall blue curve. The return calculated from the topographical LADAR equation is the red delta function. The topographical curve (in red) is the convolution of this Dirac delta function with a Gaussian temporal pulse shape. The total return (in green) is the sum of the aerosol curve and the convolved topographic curve.

$$
\begin{aligned}
E_f\left(x_f, y_f, R\right) &= 2P_L\xi\left(\lambda_L\right)\frac{\rho^s}{\pi}\frac{1}{f^2}\exp\left[-2\int_0^{R_T}\kappa(\lambda_L, r)dr\right]\frac{2}{\pi W^2\left(R_T\right)} \\
&\times \int_{A(x_{op},y_{op},r_0)-A(x_{od},y_{od},r_b)} \exp\left[-2\frac{x_{op}^{*2}+\left[y_{op}^{*2}-a\left(R_T\right)\right]^2}{W^2\left(R_T\right)}\right]da \\
&\times \exp\left[-\pi\frac{\left(R-R_T-\frac{c\tau_L}{2}\right)^2}{\left(\frac{c\tau_L}{2}\right)^2}\right], \qquad (5.1)
\end{aligned}
$$

where x_f, y_f is the position on the focal plane in meters, R is the distance of the scattering

volume from the transmitter-receiver in meters, P_L is the average power in the laser pulse in watts, ρ^s is the topographical target's scattering efficiency, c is the speed of light in meters per second, τ_L is the effective pulse duration in seconds, $\xi(\lambda_L)$ (unitless) is the receiver's spectral transmission, λ_L is the wavelength of the transmitted light in meters, f is the focal length of the system in meters, $\kappa(\lambda_L, r)$ is the total atmospheric extinction in inverse meters including molecular absorption and Mie and Rayleigh scattering, $W(R_T)$ is the radius of the laser pulse at the range of the topographical target R_T in meters, and $(x_{op} = \frac{x_f R_T}{f}, y_{op} = \frac{y_f R_T}{f})$ is the object point in the target plane. The integral is evaluated over the circular area $A(x_{op}, y_{op}, r_0)$ of radius r_0 centered on (x_{op}, y_{op}) excluding the circular area $A(x_{od}, y_{od}, r_b)$ of radius r_b centered on (x_{od}, y_{od}), where r_0 is the radius of the objective lens or mirror, r_b is the radius of the central obscuration, s_b is the distance between the central obscuration and the mirror, $x_{od} = \left[\frac{R_T - s_b}{R_T}\right] x_{op}$, and $y_{od} = \left[\frac{R_T - s_b}{R_T}\right] y_{op}$. Physically, the topographic return cannot begin until the pulse reaches the topographic range; therefore the topographic return is not Gaussian, but actually begins abruptly at the topographic range. The topographic and aerosol return are merged by summing as a function of time or range. Additionally, as the pulse reflects from a topographical surface, part generates a topographical return while the portion of the pulse still in the air is generating an aerosol return. Care must be taken in the model to decrease the contribution from the aerosol return as the topographic return is added in because the basic aerosol LIDAR equation (eq. 3.1) assumes that the entire pulse contributes to the aerosol return. Given that the aerosol return cannot physically exist after the entire pulse reflects from the topographic range, the aerosol return is calculated for each range step after the topographic range by

$$E_f(x_f, y_f, R) = E_f(x_f, y_f, R_T)\left[1 - \left(\frac{n \cdot dR}{c\tau_L}\right)\right], \tag{5.2}$$

where dR is the size of a range step and n is the number of range steps after the topographic

range. This partial aerosol return is added into the overall return until the quantity becomes negative. This decrease of the aerosol return as the topographical return is added in is not currently implemented in the DIRSIG LADAR model, but will be soon.

5.2 Spectral Approach

The spectral DIRSIG LADAR/LIDAR return is calculated as outlined in Section 3.2.3 with the assumption that the spectral distribution does not change after scattering. The factors that depend upon wavelength include the backscatter coefficient, the focal length, the atmospheric transmission, the laser power, the passive return, the speckle texture pattern, the atmospheric turbulence effects, and the detector sensitivity. The return is calculated as a function of wavelength across the detector sensitivity at intervals determined by the user.

5.3 Atmospheric Parameters

The atmospheric propagation models, FASCODE and MODTRAN, used to calculate the atmospheric parameters were reviewed in Section 3.3.4. Due to the required resolution, FASCODE is used in the normal fashion to calculate the atmospheric absorptance. Since spectral resolution is not an issue with scattering, because the scattering functions are assumed to be spectrally uniform across the narrow spectral range of interest for a laser beam, a modified version of MODTRAN is used to calculate the transmission loss due to scattering, reflectance, and the scattering phase functions. Since the DIRSIG LADAR/LIDAR model includes bistatic systems, the volume backscattering coefficient (i.e., angular scattering coefficient) is used. Some models use the volume backscattering coefficient integrated over the hemisphere perpendicular and opposite to the direction of propagation. The DIRSIG LADAR/LIDAR model preserves the angular dependence of the volume backscattering co-

efficient. Scattering phase functions $p(\theta)$ are used to calculate the volume backscatter coefficient in inverse meters inverse steradians

$$\beta(\lambda_L, R, \theta) = p(\theta)\frac{\beta}{4\pi}, \tag{5.3}$$

where β is the angular scattering coefficient

$$\beta = \int \beta(\lambda_L, R)\, d\Omega. \tag{5.4}$$

The scattering phase functions for each layer in MODTRAN are in the subroutine "ssrad" which calculates the single scattered radiance for a layer. The single scattered radiance is shown in Figure 5.3 and is given by

$$L(\lambda, R, \overrightarrow{r}, \theta, \phi) = p(\lambda, R, \overrightarrow{r}, \theta, \phi)\, E(R, \overrightarrow{r}), \tag{5.5}$$

where $E(R, \overrightarrow{r})$ is the transmitted solar irradiance, R is the range to the layer, $\overrightarrow{r}$ is the position within the layer, λ is the wavelength, θ is the incoming angle, and ϕ is the outgoing angle. The transmitted solar irradiance is equal to the product of the exo-atmospheric solar irradiance and the transmittance to the layer. DIRSIG uses a modified version of MODTRAN to calculate a range of incoming and outgoing angles and the resulting scattering phase functions in inverse steradians at each layer. The angular scattering coefficient over all possible solid angles is obtained by evaluating a vertical path in MODTRAN and obtaining the transmittance loss due to scattering τ_{layer} for each layer. The angular scattering coefficient in inverse meters over all possible solid angles for a layer for a slant path is then given by

$$\beta_{layer} = \frac{\ln(\tau_{layer})}{\cos(\theta)\,\Delta z}, \tag{5.6}$$

$$L\left(\lambda, R, \vec{r}, \theta, \phi\right) = p\left(\lambda, R, \vec{r}, \theta, \phi\right) E\left(R, \vec{r}\right)$$

$$L\left[\frac{W}{m^2 sr}\right] = p\left[\frac{1}{sr}\right] E\left[\frac{W}{m^2}\right]$$

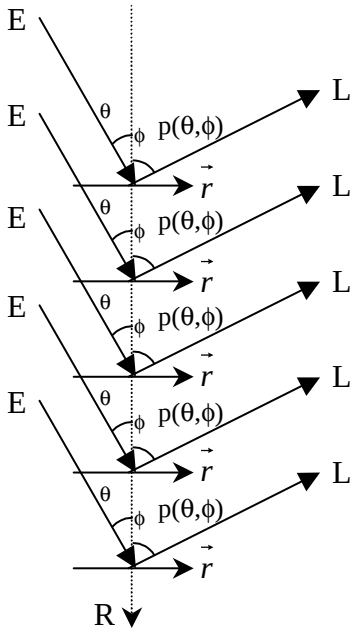

Figure 5.3: The quantities used by MODTRAN to calculate the single scattered radiance for each layer. The single scattered radiance, $L\left(\lambda, R, \overrightarrow{r}, \theta, \phi\right)$, is equal to the transmitted solar irradiance, $E\left(R, \overrightarrow{r}\right)$, times the scattering phase function, $p\left(\lambda, R, \overrightarrow{r}, \theta, \phi\right)$. These quantities are a function of the range to the layer, R, the position within the layer, $\overrightarrow{r}$, the wavelength, λ, the incoming angle θ, and the outgoing angle, ϕ. The transmitted solar irradiance is equal to the exoatmospheric solar irradiance times the transmittance to the layer.

where Δz is the thickness of the layer and θ is the incoming angle relative to the layer surface normal, as shown in Figure 5.3. Once the scattering phase functions and the angular scattering coefficients over all possible solid angles are obtained for a layer, the volume backscatter coefficient for that layer can be calculated using equation 5.3.

Conservation of energy requires that the coefficients of absorption, transmittance, and reflection sum to unity:

$$\alpha + \tau + \rho = 1, \tag{5.7}$$

where α is the absorptance, τ is the transmission, and ρ is the reflectance. Since both FASCODE and MODTRAN are used, it is possible to violate this relationship if working at an absorption line. When that occurs, the atmospheric absorptance from FASCODE is the trusted quantity and the transmission is adjusted to

$$\tau = 1 - \alpha - \rho, \tag{5.8}$$

so that energy conservation is not violated.

Finally, the user should be aware that the accuracy of any particular simulation depends upon the accuracy of spectral parameters from the HITRAN database. It is recommended that the user verify the parameters in the HITRAN database before using the results of a simulation to make decisions.

5.4 Beam Versus Ray Propagation

The first choice to be made in developing the DIRSIG LADAR/LIDAR model was whether to use a beam or a ray-tracing approach. DIRSIG is inherently a ray-tracing model. As such, effects of atmosphere turbulence, such as scintillation, image effects, beam effects,

and speckle, can be modeled effectively through the use of statistical parameters. Beam propagation approaches use the properties of the Fourier transform to propagate a beam. Since IRMA models neither atmospheric turbulence effects nor the aerosol return, it is able to define a transfer function that allows it to calculate the image plane distribution using a complex convolution of the impulse response and a two-dimensional object field sample. Since the effects of atmospheric turbulence are included in the model, some thought was given to implementing a beam-propagation approach as formulated by Nelson (2000) and described in further detail in Section 5.8.

The work by Nelson (2000) demonstrated the modeling of beam propagation through atmospheric turbulence and reflection from a rough surface, but it did not consider bistatic systems and it did not reflect the beam off of non-uniform surfaces. To model a bistatic system, the overlap between the beam and the receiver field of view must be considered. Therefore, to calculate the aerosol return in a beam model each pulse must be propagated from the transmitter to each reflection distance, multiplied by the backscatter coefficients, projected into the plane perpendicular to the receiver optical axis, and then propagated back to the sensor. The process becomes more difficult when reflecting the beam off of non-uniform surfaces. A method would have to be developed that accounts for the fact that only a portion of the beam hits a topographical target at each distance. Additionally, the beam-propagation method cannot account for multiply bounced photons. Finally, the return from a three-dimensional scene is being modelled, and care must be taken in the bistatic case so that the beam is not propagated back through portions of a solid object.

Therefore, it was decided to use the ray-tracing approach for several reasons. There were concerns with computation time, as will be discussed in Section 5.5. The beam-propagation approach requires fast Fourier transforms be evaluated for each pulse and for every distance. Additionally, aliasing artifacts of the discrete Fourier transform must be

avoided. Also, it was unclear whether this approach would produce the correct answer in the bistatic case and did not account for multiply bounced photons.

5.5 Implementation Issues

The ray-tracing approach had its own implementation issues. First, the initial geometrical form factor calculation was slow and had artifacts due to uniform sampling, as will be discussed in Section 5.5.1. It was unclear how to account for multiply bounced photons and objects in the beam path in a computationally efficient manner. These issues lead to the adoption of the photon map approach as outlined in Section 5.5.3.

5.5.1 Geometrical Form Factor Initial Approach

From the beginning, the plan was to model both monostatic and bistatic LADAR/LIDAR systems with and without central obscurations and several types of beams. The initial choices were Gaussian, spherical, and a plane wave apodized by the aperture (also called a "top hat"). The spherical beam was dropped because it can be approximated by a plane wave for any significant propagation distance. This resulted in twelve possible scenarios summarized in Table 5.1.

How the geometrical form factor calculation was performed initially is shown in Figure 5.4. For each point (x_f, y_f) in the focal plane there is a contribution area in the target plane. The integration is performed by drawing a box around this circular region and then sampling the area in the box. Each sample point is tested to see if it is within the contribution area, the beam field of view, the receiver field of view, and to see if it is outside the obscuration shadow. If all these conditions are true, then the contribution from that point is added. The value that is added is based upon whether a Gaussian or a "top hat"

Case	Coaxial or Biaxial	Central Obscuration	Top Hat or Gaussian
1	Coaxial	Yes	Top Hat
2	Coaxial	Yes	Gaussian
3	Coaxial	No	Top Hat
4	Coaxial	No	Gaussian
5	Biaxial	Yes	Top Hat
6	Biaxial	Yes	Gaussian
7	Biaxial	No	Top Hat
8	Biaxial	No	Gaussian

Table 5.1: The beam and receiver configurations included in the model.

weighting function is being used to describe the beam, as shown in Figure 5.5.

Numerical Integration

The initial numerical integration used to calculate the geometrical form factor was not adequate. As can be seen in Figure 5.6, discontinuities resulted if the object plane was not sampled sufficiently. Unfortunately, increasing the the number of samples led to unacceptable computation times. A simple test was performed in which the power as a function of distance was calculated for a single scenario. The only variable that was changed was the number of samples in the object plane. These curves were integrated to evaluate the total power. As sampling increases, the total power should approach a limiting value as shown in Figure 5.7. The time required to run the model was recorded in Figure 5.8. Figure 5.7, shows that the curve approaches the asymptotic value at about 100, which corresponds to a run time of 281 seconds in Figure 5.8. This is the run time to calculate the return from a single subsampled pixel, which is unacceptable.

Monte Carlo integration was tried. The Monte Carlo technique produced no systematic discontinuities, but it still required fine sampling to get a smooth curve, as shown in

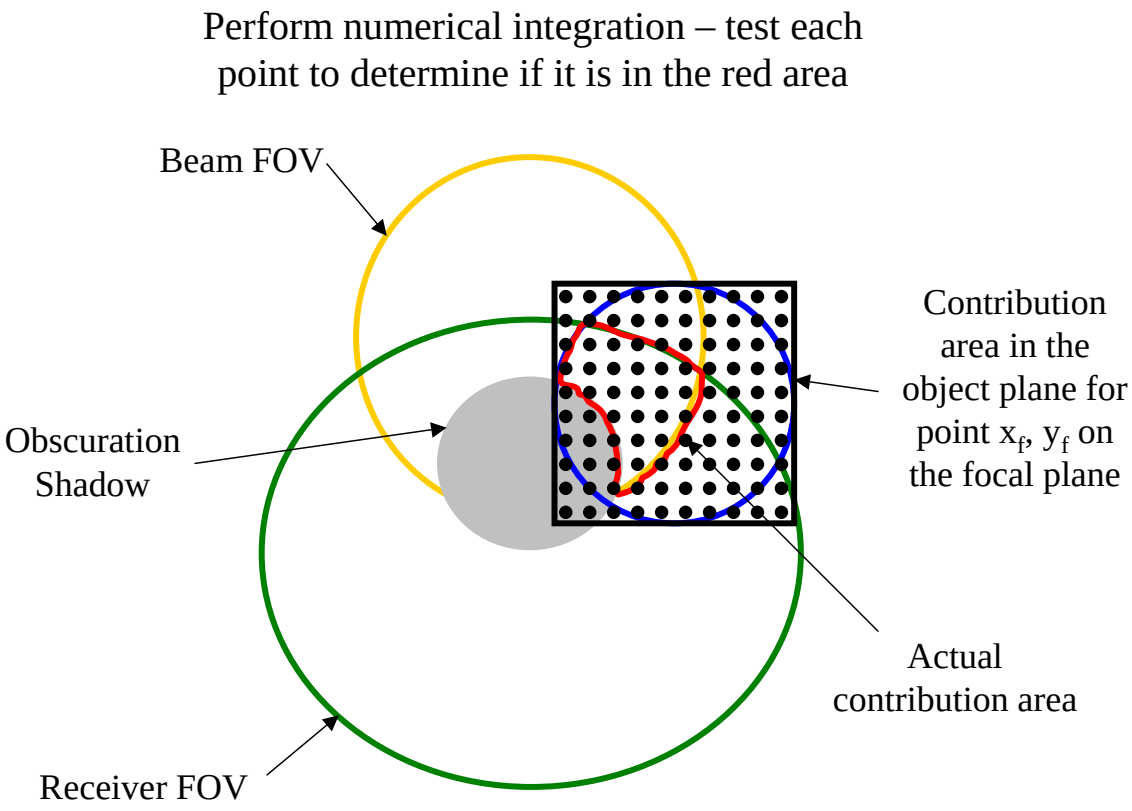

Figure 5.4: The geometrical form factor was initially calculated by uniformly sampling within a box formed around the possible contribution area in the object plane. Each point was tested to ensure that it was within the contribution area, within the beam field of view, within the receiver field of view, and outside the obscuration shadow. If all these conditions were true then that point was multiplied by the weighting function and then added to the numerical integration.

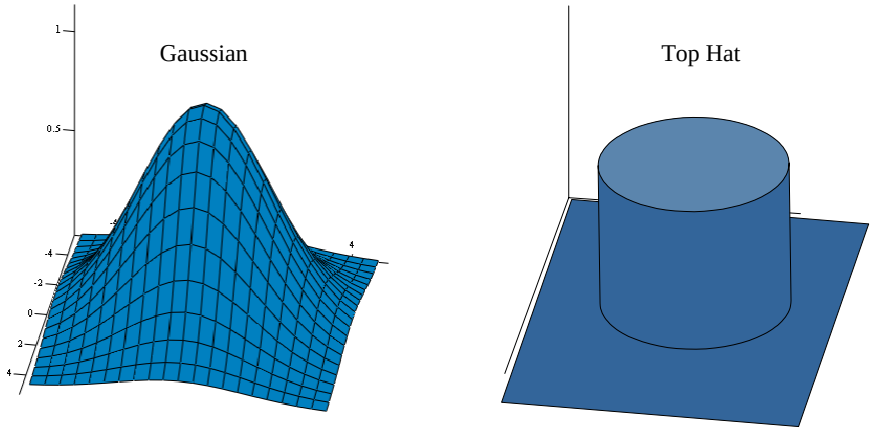

Figure 5.5: Beams included in the model: the Gaussian beam and the "top hat". The beam profile acts as a weighting function in the geometrical form factor calculation.

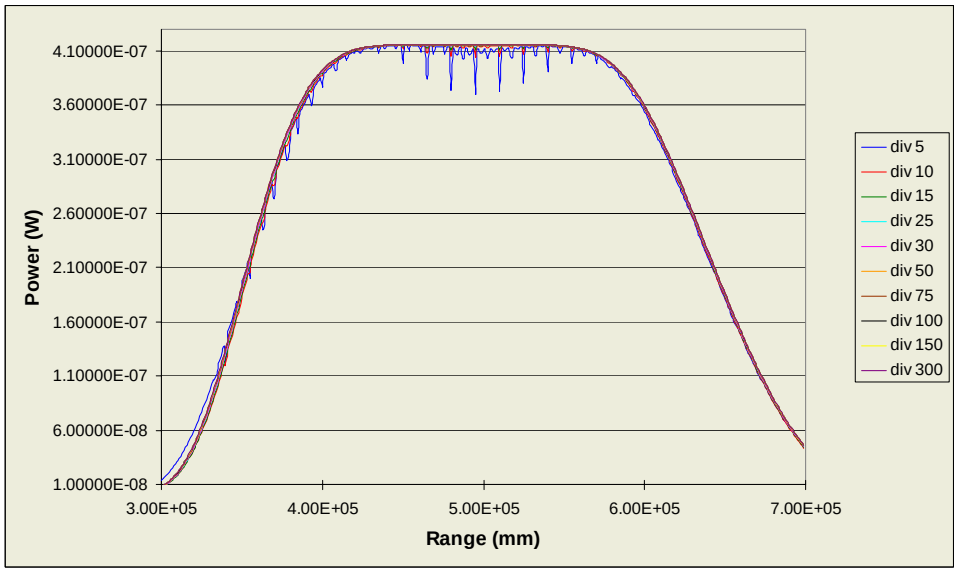

Figure 5.6: The return as a function of range for a bistatic system. As the object plane is sampled more and more finely (divided into more cells), the curve approaches a consistent shape. If the sampling is not fine enough, artifacts can result, as shown by the blue curve.

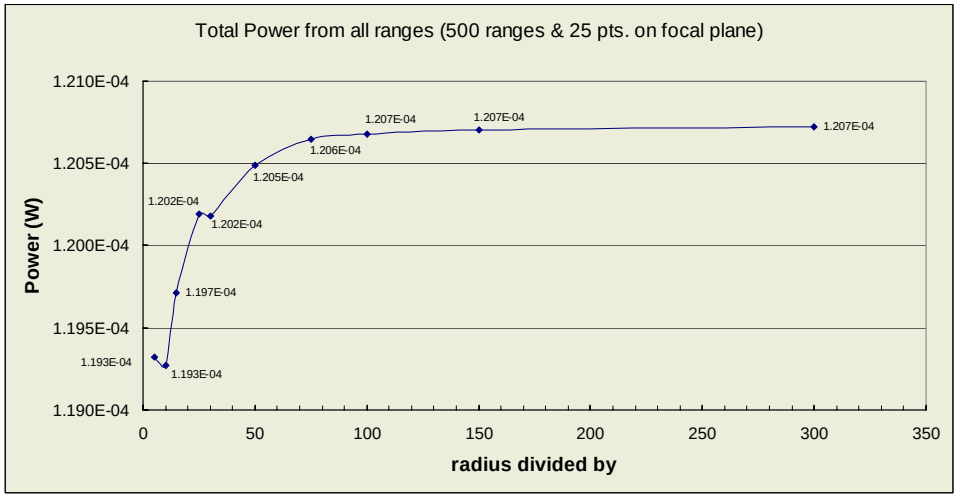

Figure 5.7: As the sampling increases, the area under the power versus range curve approaches a limiting value. This test was conducted to determine the number of samples needed.

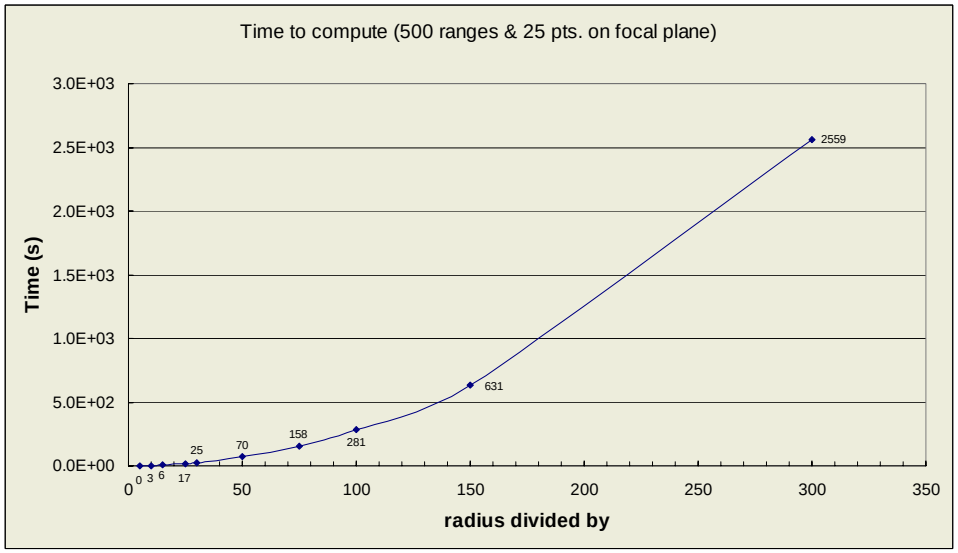

Figure 5.8: The computation time for a single subsampled pixel as the object plane sampling increases. The curve in Figure 5.7 begins to approach its asymptotic value at about 100, which corresponds to a run time of 281 seconds.

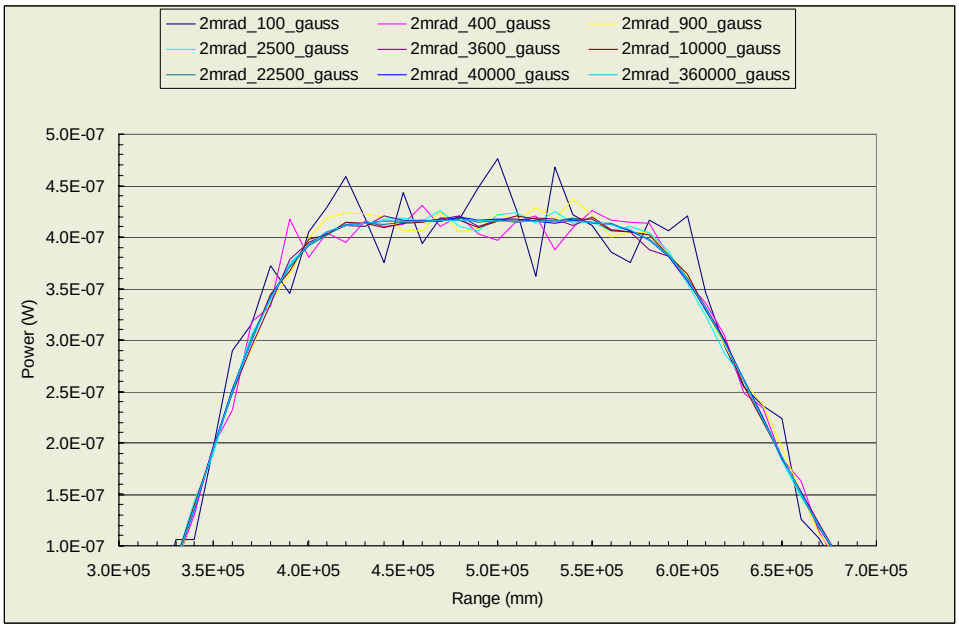

Figure 5.9: The return as a function of range for a bistatic system with Monte Carlo sampling. Again, as the object plane is sampled more and more finely (divided into more cells), the curve approaches a consistent shape. The monte carlo sampling got rid of the systematic artifacts, but still requires fine sampling to get a smooth curve.

Figure 5.9. Again, a test was performed in which the power as a function of distance was calculated for a single scenario. The only variable that was changed was the sampling in the object plane. These curves were integrated to yield the total power. This time, as the sampling increases the total power should be random about a limiting value, as shown in Figure 5.10. Again, the time it took for the model to run was also recorded in Figure 5.11. It can be seen that the curve approaches the asymptotic value at about $100,000$ points, which corresponds to a run time of $3,650$ seconds in Figure 5.11. Again, this is an unacceptable time for a single subsampled pixel.

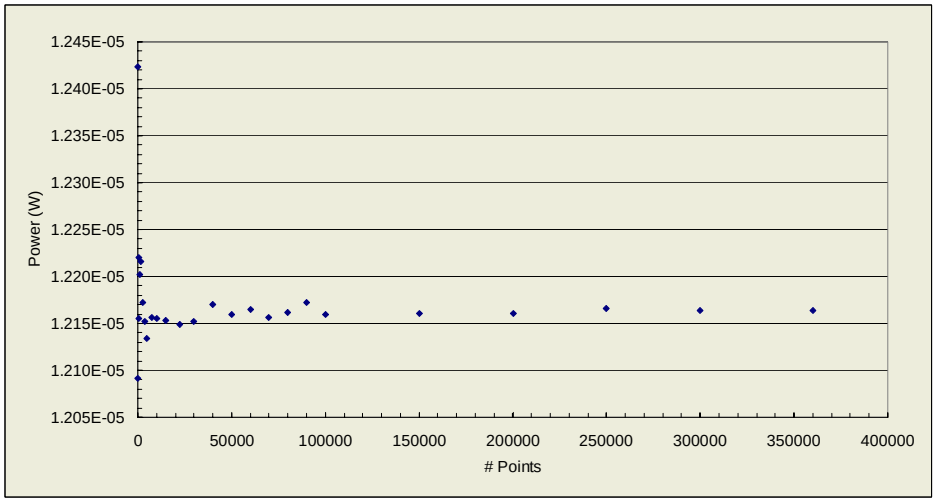

Figure 5.10: As the Monte Carlo sampling increases, the area under the power versus range curve bounced around a limiting value. This test was conducted to determine the number of samples needed.

5.5.2 Multiple Bounce Approach

The next question was how to calculate the geometrical form factor for multiply bounced photons, which can hit several targets and the return from each target must be added into the overall return at the correct time, as was shown in Figure 3.21. The defocused point on the focal plane may actually be the contribution from multiple objects at different distances. This difficulty caused us to first begin thinking about using a photon map approach, which is described in the next section.

5.5.3 Photon Mapping

The biggest problem in the initial approach was numerical integration of the overlap region in the GFF calculation. The numerical integration was slow and is a source of

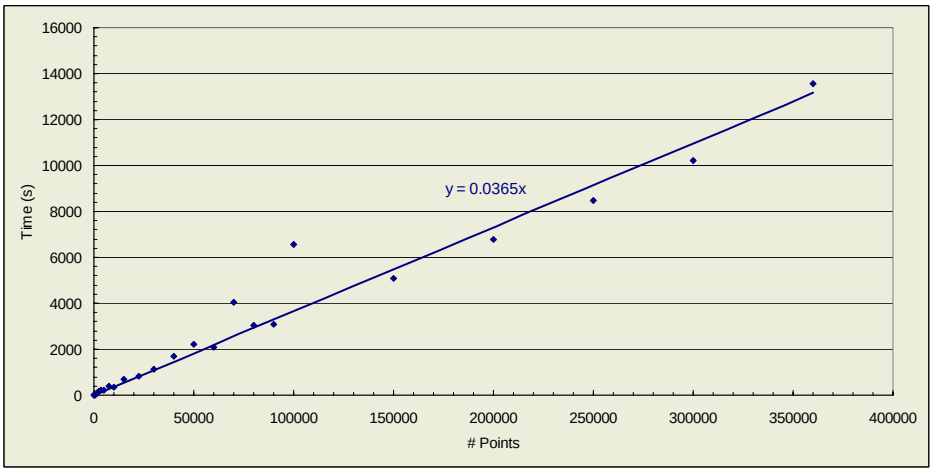

Figure 5.11: The computation time for a single subsampled pixel as the object plane Monte Carlo sampling increases. By comparing this Figure to Figure 5.10, it can be seen that the curve in Figure 5.10 begins to approach its asymptotic value at about $100,000$ points, which corresponds to a run time of $3,650$ seconds.

error. A possible solution was to precompute a large database and use interpolation, but additional ray tracing would then be needed to compute any shadowing and/or absorption of the beam, as shown in Figure 5.12. Additionally, the initial GFF technique assumed that the object plane within the overlap region was uniform. When a ray hit object A. This might not occur, as shown in Figure 5.13. The entire overlap region cannot be sampled with the raytracer, since this calculation is performed at each range and for each sub-pixel sample. Again, these problems with the GFF calculation and the failure to account for multiply bounced photons motivated the search for another method and led to replacing the traditional raytracer with photon mapping, where the photon map search radius is analogous to the extended area due to defocusing.

Photon mapping has been shown to be an efficient replacement for combination radiosity/raytracing methods that are computationally intense and use memory inefficiently. The results generated from the photon mapping technique are comparable, and may even surpass those of the radiosity/raytracing method. Additionally, photon mapping can be implemented into traditional raytracers simply by adding an additional module to the existing program because photon maps are formed with intersection tests already used by the raytracer.

A photon map is a three-dimensional data structure that stores photons that have been forward propagated from sources in the scene. Photons start at the sources and are bounced around the scene, as shown in Figure 5.14. The angular distribution of the photons from the source is determined from the divergence angle of the transmitter and the energy distribution of the source as shown in Figure 5.15. First a random x and y position is generated within a square of unit radius. The distance of this position from the center of the circle is calculated. The distance *dist* is tested to determine that it lies within a circle of unit radius. If this test is passed, the value of the spatial energy distribution at this

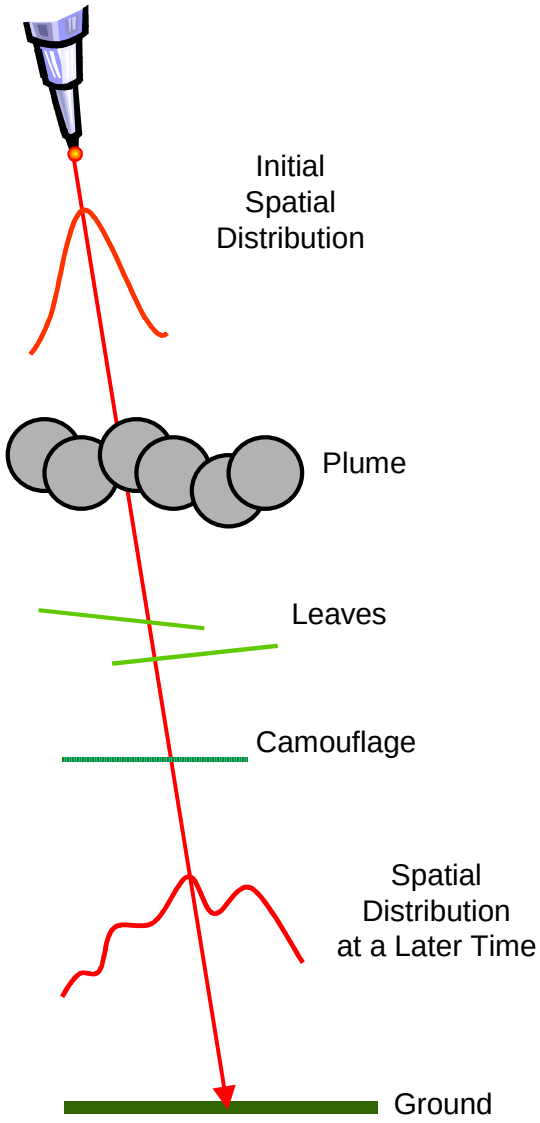

Figure 5.12: The spatial distribution of the beam changes over time due to propagation through objects, such as plumes, leaves, and camouflage. A precomputed GFF would assume that the beam distribution was still Gaussian, when in fact it was not. Additional retracing would be needed to compute the additional absorption and shadowing of the beam.

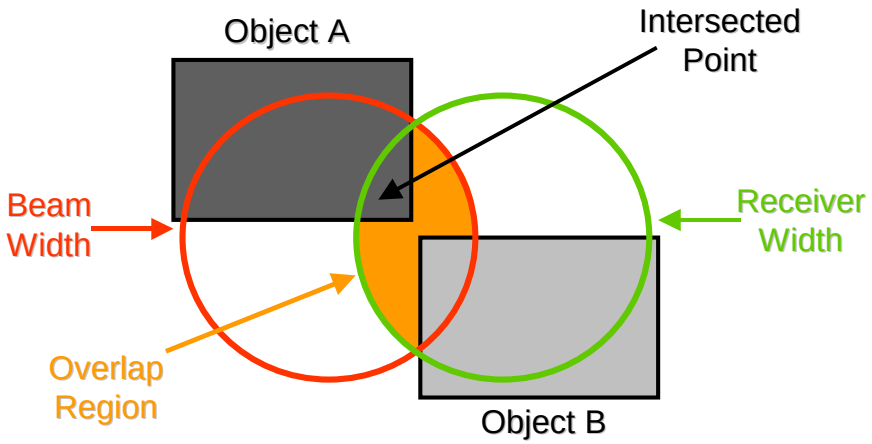

Figure 5.13: The overlap region may be filled with more than one material. There is no way to know how many materials are in the overlap region or where they are located without sending out additional rays.

position is generated and compared to a random number. The photon is kept only if the distribution value is above this random number. Since more photons are rejected in the tails of the distribution, this process ensures that the spatial energy distribution of the source is met. DIRSIG uses the distribution

$$distribution = \exp\left[-2 * \left(\frac{dist}{\frac{1}{3}}\right)^2\right]. \tag{5.9}$$

This distribution ensures that the Gaussian beam is sampled out into the tails of the distribution. This process is repeated until obtaining the desired number of photons. These photons are then assigned an angle based upon their position, with those in the middle having no deflection and those at the edge having the greatest. The deflection for a Gaussian beam is

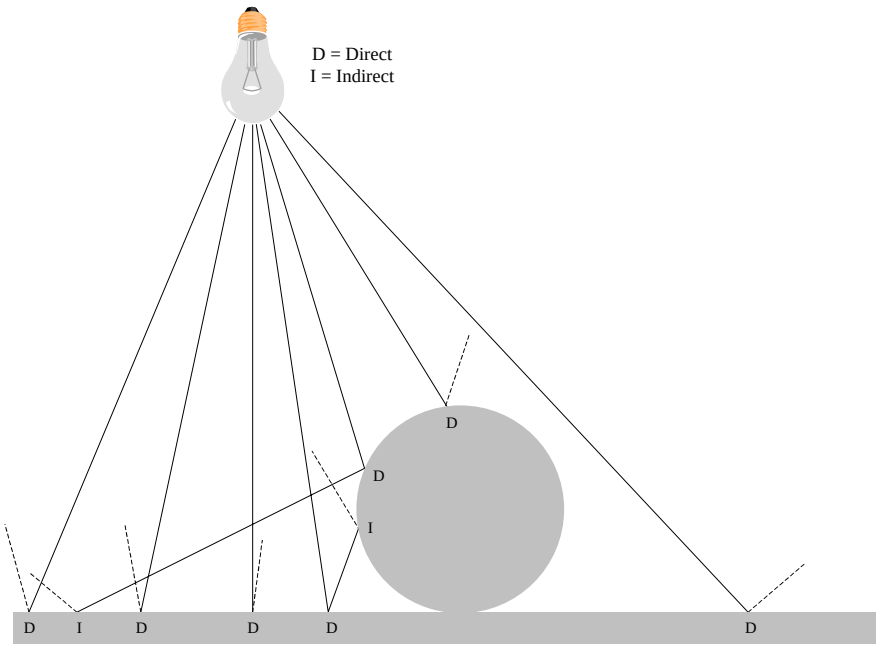

Figure 5.14: The propagation of photons from a single source in the creation of a photon map. Photons are shot out from the source until they encounter an object, at which time their location, energy, direction, and time of incidence is stored in the map. The first hit of a photon is direct illumination, while subsequent hits are indirect illumination.

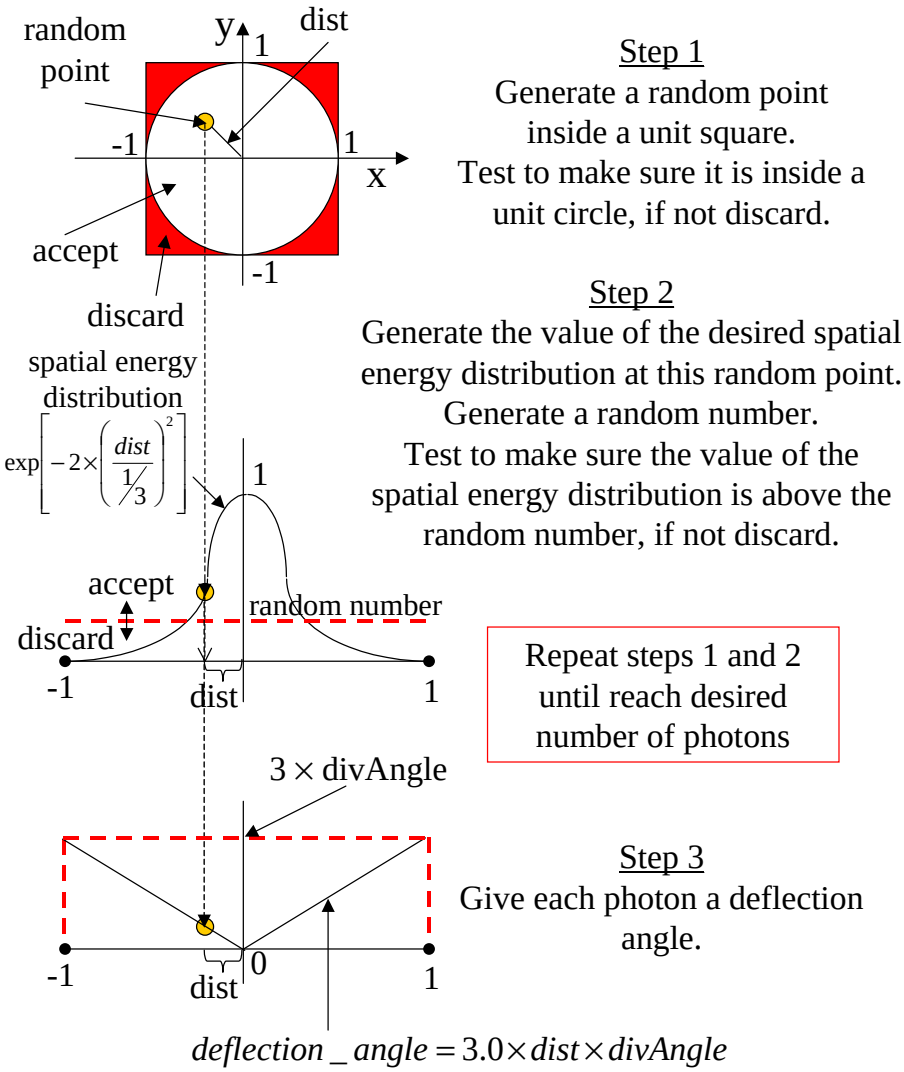

Figure 5.15: DIRSIG determines the position and angular deflection of the photons from a source by first generating a random (x, y) position such that $x^2 + y^2 \leq 1$. The value of the desired spatial energy distribution at this (x, y) position is compared to a random number. Only if the distribution value is above this random number is the photon kept. This process is repeated until the desired number of photons is reached and ensures that the source mimics the desired spatial energy distribution. These photons are then assigned an deflection angle based upon their position, with those in the middle having no deflection and those at the edge having the greatest deflection.

$$deflection = 3.0 \times dist \times \phi, \tag{5.10}$$

where ϕ is the divergence angle. This definition and that of the spatial distribution, puts the radius of the beam at 2σ, where σ is the standard deviation of the spatial energy distribution.

At each bounce, the location, energy, direction, and time of incidence of the photon is stored in the map. This allows multiply bounced photons to be tracked with their total travel time. The direct and indirect loads at a location are computed by querying the map for photons that are nearby in space and time. Photon map works by using the density of photons with the same energy to estimate the power/irradiance at a location. There are various ways to query the map, as shown in Figure 5.16. One method is to find the N nearest photons. The resulting search radius is then inversely proportional to the intensity of the light. Another method is to use a set search radius and the resulting intensity is proportional to the number of photons contained in the search radius.

The photon map approach implemented into DIRSIG uses a set search radius that is equal to the radius of the receiver because this search radius is analogous to the extended area due to defocusing as outlined in Section 3.2.2. Once the photon map is generated, rays are sent out into the scene from the focal plane. When a ray encounters an object, the photon map is queried both spatially and temporally. The spatial query is similar to the initial geometrical form factor calculation shown in Figure 5.4, except instead of using systematic or Monte Carlo integration, simple intersection tests are used, saving computational time at the expense of memory. As in the initial approach, each photon within the search radius is tested to make sure it lies within the receiver field of view and outside the obstruction shadow, as shown in Figure 5.17. Unlike the initial approach, the energy stored in the photon map accounts for any obstruction of the beam by plumes, leaves, or camouflage.

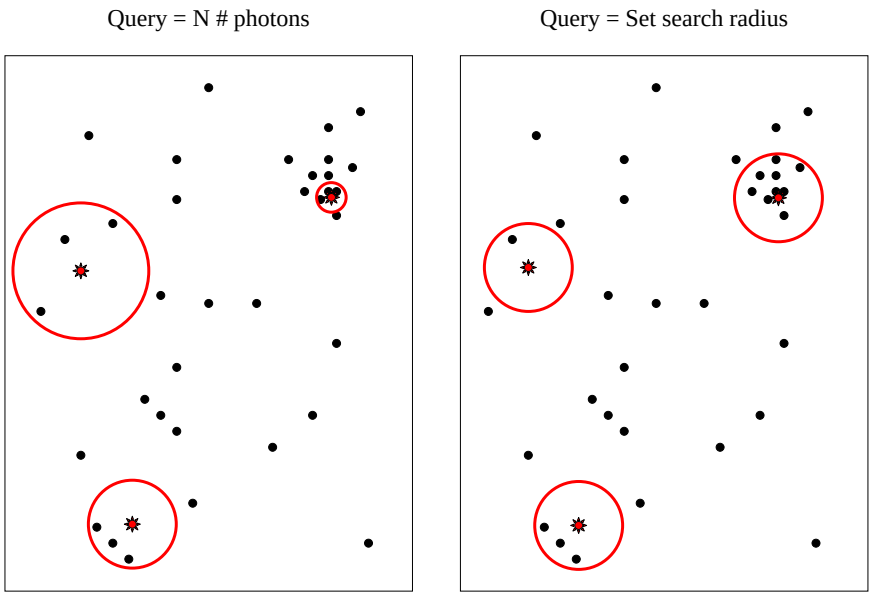

Figure 5.16: There are two methods of querying a photon map. The photon map can be queried for the N closest photons, as shown on the left. The resulting search radius is inversely proportional to the intensity of the light at that position. On the right, the photon map can be given a set search radius. The intensity is then proportional to the number of photons contained within the search radius.

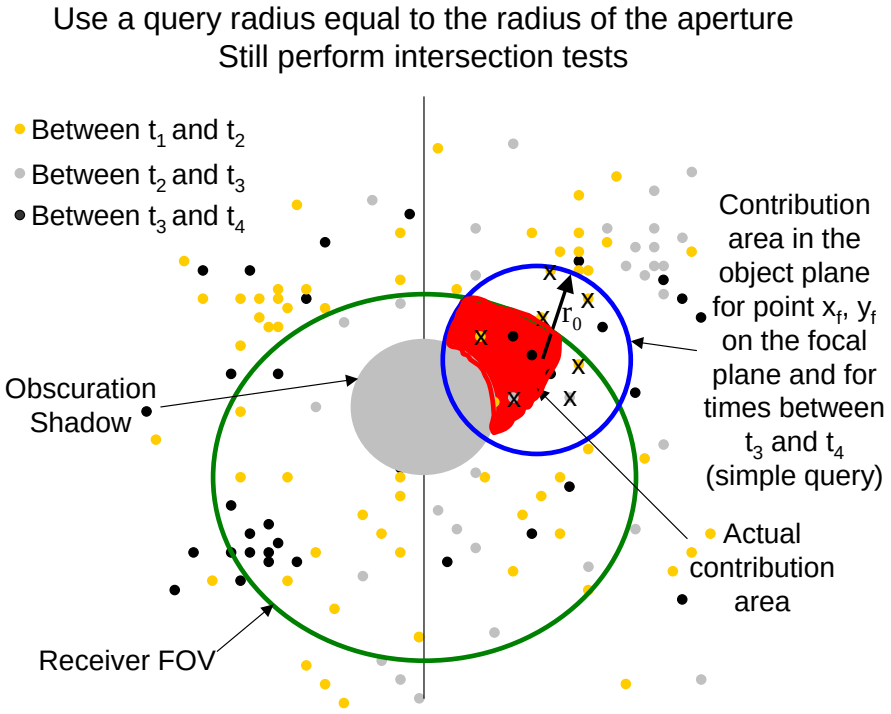

Figure 5.17: How the GFF calculation is performed in the photon map implementation. A simple intersection test is used to collect all the photons within the spatial search radius. These photons are then tested to ensure that they are inside the receiver field of view, outside the obscuration shadow, and within the temporal time gate.

The temporal search distance is the integration time of the detector. This allows multiply bounced photons to be added into the return at the correct time with the correct geometrical form factor.

5.6 Speckle Approach

Several methods are used to model speckle. IRMA uses Fourier optics, the Fresnel diffraction equation, and the lens law to evaluate an impulse response. It then numeri-

cally integrates the convolution of this impulse response with the two-dimensional object field samples to calculate a return on the focal plane. Since the object field samples are complex and incorporate a random phase, the resulting image is speckled. An impulse response cannot be defined because the effects of atmospheric turbulence, multiple bounces, and the aerosol return are included in the model. As mentioned previously, another approach is to do a full beam propagation that accounts for both turbulence and speckle in a monostatic system with a two-dimensional scene (Nelson et al. 2000). To create a model that accounts for turbulence effects, speckle, and complex three-dimensional scenes, a full beam-propagation model is not practical nor is its implementation path clear, as discussed in Section 5.4. Additionally, beam-propagation programs experience difficulties with the discrete nature of the Fourier transform. Therefore, it is desirable to create a texture pattern that can be applied to the geometrical optic solution and produce an image with the correct statistics. To explore this approach, a speckle simulation study was completed.

5.6.1 Speckle Simulation

A speckle simulation was produced based upon Fresnel propagation. The simulation was used to determine the statistics for the texture pattern. According to Goodman (1996), the propagation of a beam between planes is given by

$$g(x,y) = b(x,y) * h(x,y) = \int_{-\infty}^{\infty}\int_{-\infty}^{\infty} b(\xi,\eta)\, h(x-\xi, y-\eta)\, d\xi d\eta, \tag{5.11}$$

where $b(x,y)$ is the beam in the initial plane, $g(x,y)$ is the beam in the final plane, and $h(x,y)$ is the Fresnel impulse response given by

$$h(x,y) = \frac{e^{ikz}}{i\lambda z} e^{\frac{ik}{2z}\left(x^2+y^2\right)}, \tag{5.12}$$

where z is the propagation distance along the optical axis, $k = \frac{2\pi}{\lambda}$ is the wavenumber of the light, and λ is the wavelength of the light.

The speckle simulation began at ground level. First a random phase was given to the initial beam, either a Gaussian or "top hat". The phase ranged from zero to 2π and had a uniform distribution. The now complex beam was then propagated to an aperture using equation 5.11. The resulting beam was multiplied by the aperture function

$$L(x,y) = e^{-i\frac{k}{2f}\left(x^2+y^2\right)} p(x,y), \tag{5.13}$$

where f is the focal length of the lens and $p(x,y)$ describes the shape of the aperture. The resulting beam was propagated to the focal plane using equation 5.11.

The graphical user interface (GUI) in Figure 5.18 was used to propagate the beam with and without the random phase. The ratio of these arrays gave the desired texture map. Texture maps were produced for various types of beams, apertures, wavelengths, initial beam diameters, propagation distances, focal lengths, and lens diameters. Figure 5.19 includes some sample images showing the variation in speckle size with beam diameter for the beam before the aperture, with aperture size for the image at the focal plane, and again with aperture size for the resulting texture pattern. The statistics of the texture maps were calculated using the statistical GUI shown in Figure 5.20. Regions of interest (ROIs) can be defined in the statistical GUI. Since the beam did not fill the entire array, statistics had to be calculated based on a subset of the array. Additionally, the edges of the texture map arrays often exhibited large spikes due to the discrete nature of the model that resulted in small numbers being divided by small numbers. All GUIs created for this work had the ability to model square arrays of any size. To strike a balance between run-time and the number of pixels available to calculate statistics, a 512 by 512 array was typically used with the initial beam diameter set to 15 percent of the array size. The final statistics, unless

otherwise noted, were calculated using the 64 by 64 pixels in the center of the array.

The speckle GUI provided us with a way to measure the statistics of the resulting texture map, but a method for predicting the statistics without running the Fresnel propagation model was needed. By revisiting the mathematics, a method was found to approximate the statistics modeled by the speckle model. This method is covered in the next section.

5.6.2 Speckle Approximation

The system consists of a beam reflecting from a rough surface, propagation to the aperture/lens, and then propagation to the focal plane, as shown in Figure 5.21. Using the Fraunhofer approximation, the propagation step from one plane to the next is

$$g(x,y) = \frac{e^{ikz}}{i\lambda z} e^{\frac{ik}{2z}\left(\left(\frac{x}{\lambda z}\right)^2+\left(\frac{y}{\lambda z}\right)^2\right)} B\left(\frac{x}{\lambda z}, \frac{y}{\lambda z}\right), \tag{5.14}$$

where x and y are the coordinates in the plane, $B\left(\frac{x}{\lambda z}, \frac{y}{\lambda z}\right)$ is the Fourier transform of the beam at the starting plane evaluated at $\left(\xi \rightarrow \frac{x}{\lambda z}, \eta \rightarrow \frac{y}{\lambda z}\right)$, k is the wavenumber of the light, λ is the wavelength of the light, and z is the distance between the planes (Goodman 1996). The irradiance is of interest, which is the squared magnitude of equation 5.14 such that

$$|g(x,y)|^2 = \frac{1}{(\lambda z)^2}\left|B\left(\frac{x}{\lambda z}, \frac{y}{\lambda z}\right)\right|^2 = \frac{1}{(\lambda z)^2}\varepsilon(x,y), \tag{5.15}$$

where $\varepsilon(x,y)$ is the total energy contained in the beam at the starting plane. Again, the desired discrete texture map can be generated by propagating a beam without a random phase (NR) through the system to the focal plane, propagating the beam with a random phase (R) through the system, and then evaluating the ratio.

The mean of the texture map can be approximated by evaluating the ratio of the total intensity of the random and nonrandom beam after propagation through the aperture. To

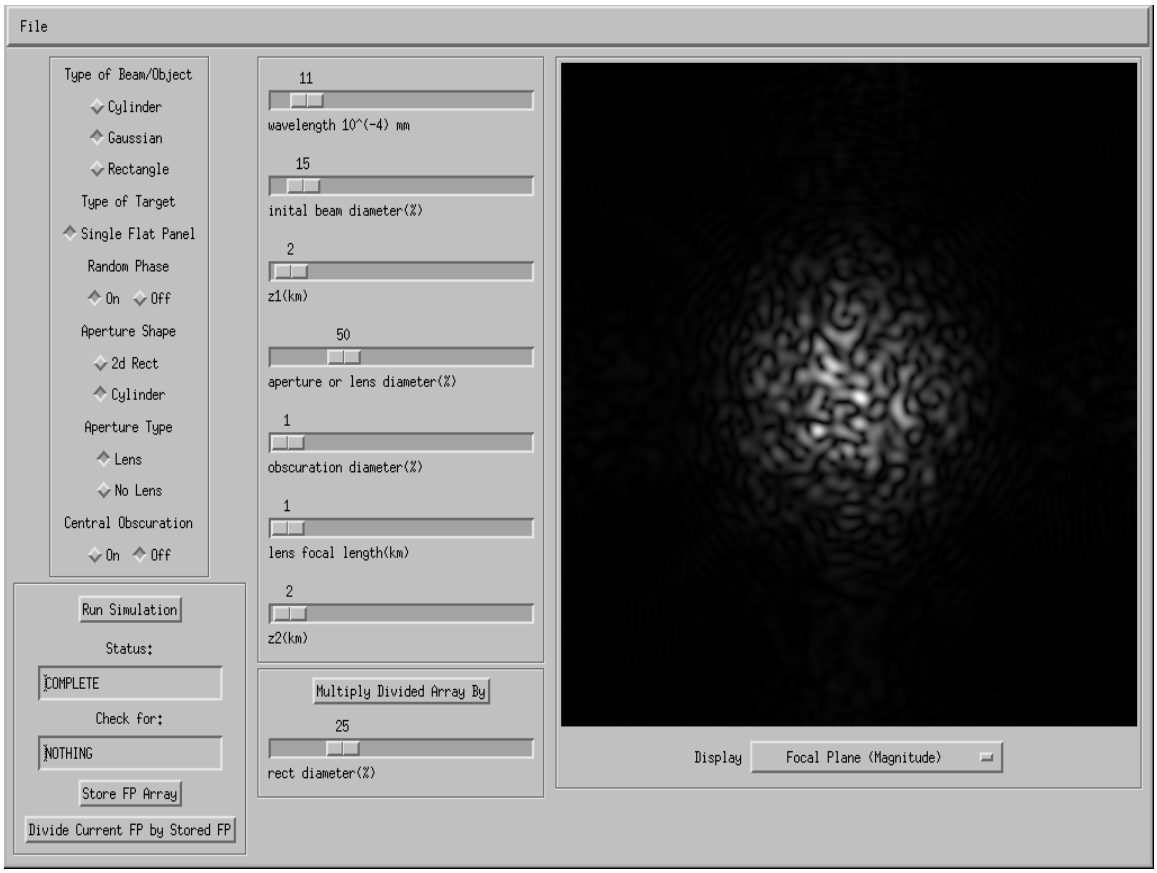

Figure 5.18: The speckle GUI uses Fresnel propagation to calculate the speckle texture map statistics. The user chooses the type of beam, the aperture shape, the presence of a central obscuration, the wavelength, the initial beam diameter, the distance from the ground to the aperture, the aperture and obscuration diameters as a percentage of the array size, the focal length of the lens, and the distance from the lens to the focal plane. The GUI has a status window. It checks for aliasing and displays a message when the conditions for aliasing have been exceeded. The GUI was used to propagate the beam to the focal plane with the random phase turned off and then with the random phase turned on. The ratio of the on and off arrays, calculated using the buttons in the lower left, gave the desired texture map. The resulting and intermediate arrays could then been viewed in the display window or saved for later analysis or viewing using the file menu.

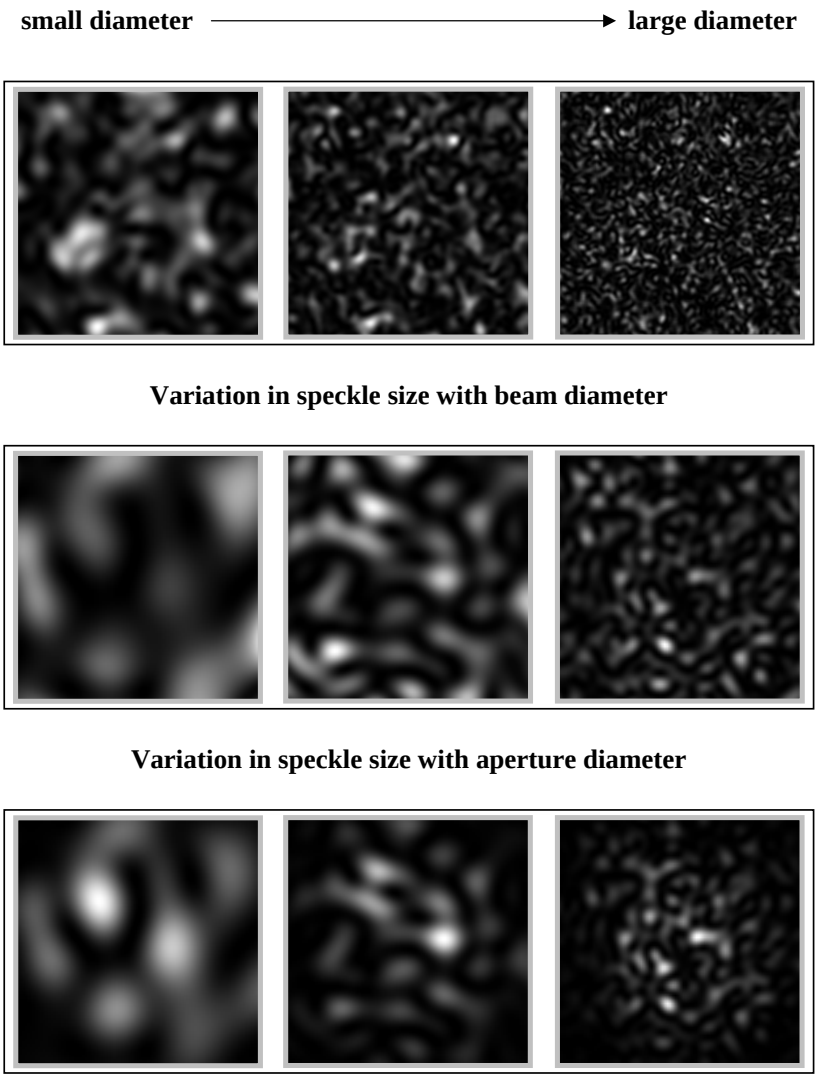

Figure 5.19: Sample speckle patterns generated with the speckle GUI. The top row shows speckle patterns at the aperture and the variation in speckle size with the size of the beam. The middle row shows speckle patterns on the focal plane and the variation in speckle size with the size of the aperture. The bottom row shows the ratio of the arrays with and without random phase and the variation in speckle size with the size of the aperture.

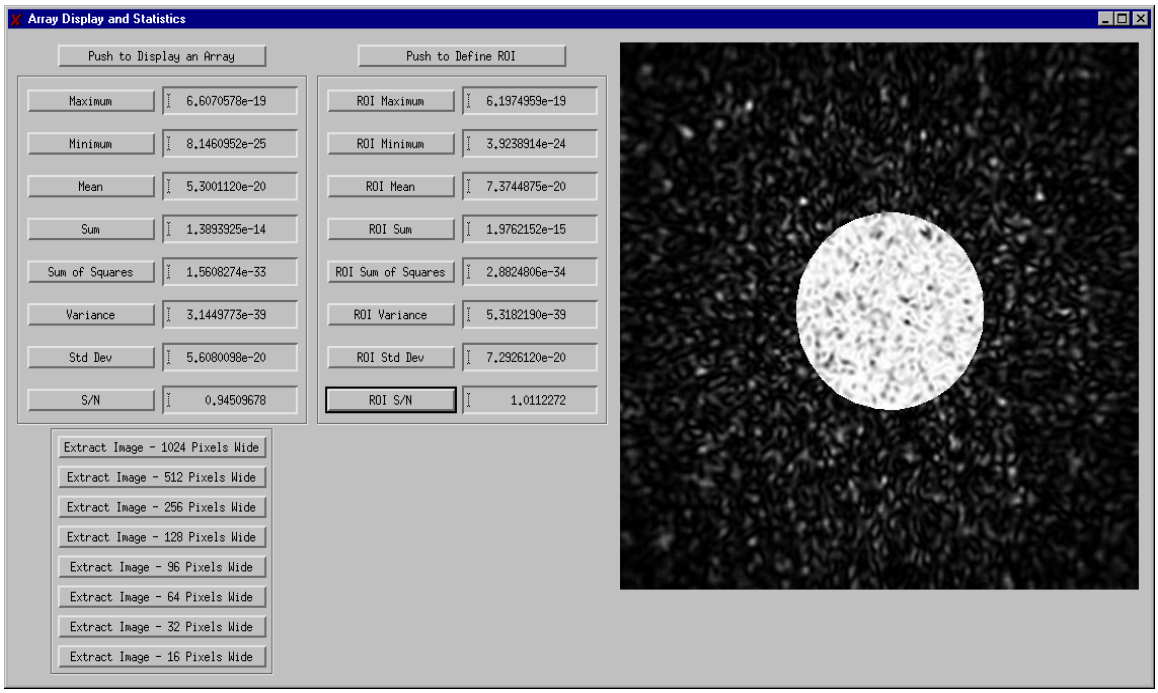

Figure 5.20: The statistics GUI used to display an array, define a region of interest (ROI), and calculate the desired statistics for either the entire array or just the ROI. ROIs could be defined with an arbitrary shape using the define ROI button or an N by N square subset of the center of the array could be extracted using the buttons on the lower left. The extract buttons have the added feature of bringing up additional windows showing the autocorrelation of the ROI.

prove this result, the mean t of the texture map must first be defined

$$\overline{t} = \frac{1}{N} \sum_i \sum_j \frac{|b_{f,R}\left(x'_i, y'_j\right)|^2}{|b_{f,NR}\left(x'_i, y'_j\right)|^2}. \tag{5.16}$$

Since propagation in the Fraunhofer region is proportional to the Fourier transform (FT), the total energy contained in the beam at the focal plane is equal to the product of the total energy contained in the initial beam and the aperture. By backpropagating the beam, one can show that the ratio of the total energy in the random and non-random beams at the focal plane (f) is given by

$$\begin{aligned} \frac{\sum_i \sum_j \varepsilon_{f,R}\left(x'_i, y'_j\right)}{\sum_i \sum_j \varepsilon_{f,NR}\left(x'_i, y'_j\right)} &= \frac{\sum_i \sum_j |FT\left\{b_{f,R}\left(x'_i, y'_j\right)\right\}|^2}{\sum_i \sum_j |FT\left\{b_{f,NR}\left(x'_i, y'_j\right)\right\}|^2} \\ = \frac{\sum_i \sum_j |b_{AA,R}\left(x'_i, y'_j\right)|^2}{\sum_i \sum_j |b_{AA,NR}\left(x'_i, y'_j\right)|^2} &= \frac{\sum_i \sum_j |A\left(x'_i, y'_j\right) b_{BA,R}\left(x'_i, y'_j\right)|^2}{\sum_i \sum_j |A\left(x'_i, y'_j\right) b_{BA,NR}\left(x'_i, y'_j\right)|^2}, \end{aligned} \tag{5.17}$$

where $A\left(x'_i, y'_j\right)$ is the aperture, $b_{BA}\left(x'_i, y'_j\right)$ is the beam at the input side of the aperture, and $b_{AA}\left(x'_i, y'_j\right)$ is the beam at the output side of the aperture. Parseval's theorem states that

$$\int_{-\infty}^{\infty} \int_{-\infty}^{\infty} |f(x,y)|^2 dxdy = \int_{-\infty}^{\infty} \int_{-\infty}^{\infty} |FT\{f(x,y)\}|^2 d\xi d\eta. \tag{5.18}$$

The ratio becomes

$$\frac{\sum_i \sum_j |A\left(x'_i, y'_j\right) b_{BA,R}\left(x'_i, y'_j\right)|^2}{\sum_i \sum_j |A\left(x'_i, y'_j\right) b_{BA,NR}\left(x'_i, y'_j\right)|^2} = \frac{\sum_i \sum_j |b_{f,R}\left(x'_i, y'_j\right)|^2}{\sum_i \sum_j |b_{f,NR}\left(x'_i, y'_j\right)|^2}. \tag{5.19}$$

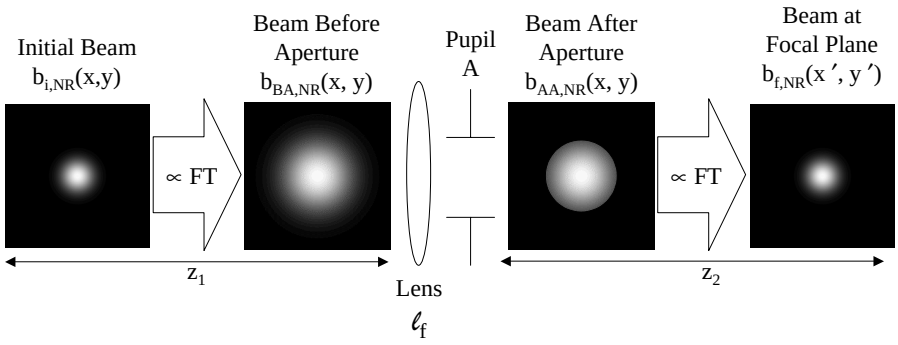

Figure 5.21: After reflection from a rough surface, the beam is propagated twice. The first propagation distance from the point of reflection to the aperture/lens system is z_1. The second distance z_2 is from the aperture/lens system to the focal plane. The act of propagation in the Fraunhofer region is proportional to the Fourier transform.

If the non-speckled irradiance is approximately constant over the aperture, $|b_{f,NR}(x'_k, y'_l)|^2$ can be replaced with a constant, C, which results in

$$\frac{\sum_i \sum_j |b_{f,R}\left(x'_i, y'_j\right)|^2}{\sum_i \sum_j |b_{f,NR}\left(x'_i, y'_j\right)|^2} \approx \frac{1}{N} \sum_i \sum_j \frac{|b_{f,R}\left(x'_i, y'_j\right)|^2}{C} = \overline{t}, \tag{5.20}$$

where N is the total number of points in the array. Figure 5.22 shows the mean calculated by using the Fresnel propagation model versus the mean calculated by using the approximation technique. The means are essentially identical though the beam varied over the aperture. Therefore, the condition of the beam being approximately constant over the aperture is not hard to achieve.

5.6.3 Speckle Texture Map Generation

To generate a texture map with the correct statistics, the signal-to-noise ratio is also needed

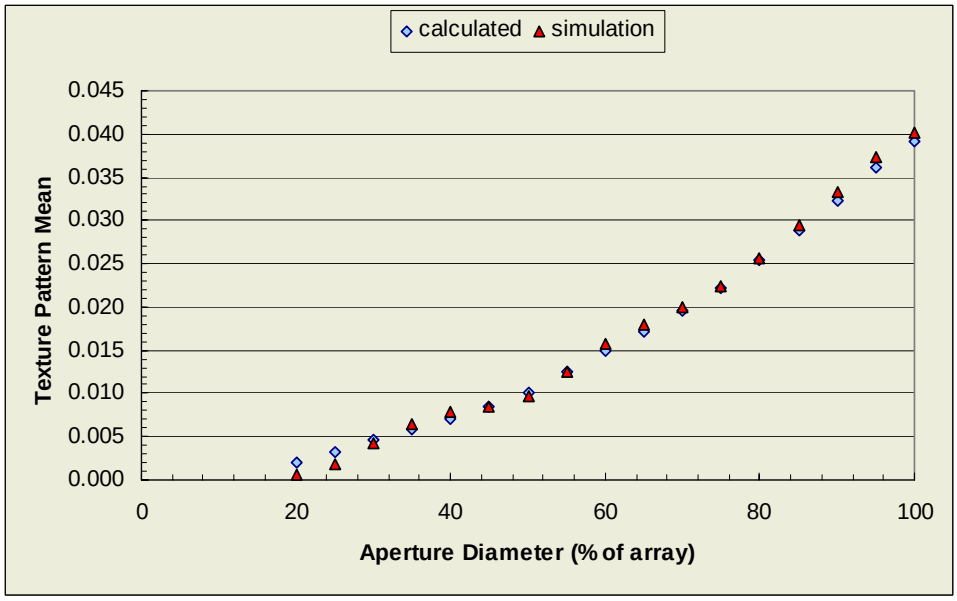

Figure 5.22: The mean as a function of aperture size using the approximation technique (diamonds) versus actually generating the texture map image using beam propagation and calculating the mean of the texture map image (triangles).

$$t_{\left(\frac{S}{N}\right)_{tex}} = \frac{\overline{t_{tex}}}{\sigma_{tex}} = \frac{\frac{\sum_i \sum_j |b_{f,R}(x'_i,y'_j)|^2}{\sum_i \sum_j |b_{f,NR}(x'_i,y'_j)|^2}}{\sqrt{\frac{1}{N}\sum_i \sum_j \left(\frac{|b_{f,R}(x'_i,y'_j)|^2}{|b_{f,NR}(x'_i,y'_j)|^2} - \frac{\sum_i \sum_j |b_{f,R}(x'_i,y'_j)|^2}{\sum_i \sum_j |b_{f,NR}(x'_i,y'_j)|^2}\right)^2}} \tag{5.21}$$

where $\overline{t_{tex}}$ is the mean of the texture map and σ_{tex} is the standard deviation of the texture map. If the beam is approximately constant over the aperture, $|b_{f,NR}(x'_k, y'_l)|^2$ can again be replaced with the constant C:

$$t_{\left(\frac{S}{N}\right)_{tex}} = \frac{\overline{t_{tex}}}{\sigma_{tex}} = \frac{\frac{1}{C}\frac{\sum_i \sum_j |b_{f,R}(x'_i,y'_j)|^2}{N}}{\sqrt{\frac{1}{N}\sum_i \sum_j \left(\frac{1}{C}|b_{f,R}\left(x'_i, y'_j\right)|^2 - \frac{1}{C}\frac{\sum_i \sum_j |b_{f,R}(x'_i,y'_j)|^2}{N}\right)^2}}, \tag{5.22}$$

which is equal to

$$t_{\left(\frac{S}{N}\right)_{tex}} = \frac{\overline{t_{tex}}}{\sigma_{tex}} = \frac{\frac{1}{C}\overline{t_R}}{\frac{1}{C}\sqrt{\frac{1}{N}\sum_i \sum_j \left(|b_{f,R}\left(x'_i, y'_j\right)|^2 - \overline{t_R}\right)^2}} = \frac{\overline{t_R}}{\sigma_R} = t_{\left(\frac{S}{N}\right)_R} = 1, \tag{5.23}$$

where $\overline{t_R}$ is the mean of the random beam at the focal plane and σ_R is the standard deviation of the random beam at the focal plane.

The procedure for generating a new random texture map is shown in Figure 5.23. First, the size of the speckle incident on the aperture is derived from equation 3.60. For a Gaussian beam, this equation reduces to

$$R_I(\Delta x, \Delta y) = \langle I \rangle^2 \left[1 + |Gaus\left(\frac{dx}{\lambda z}, \frac{dy}{\lambda z}\right)|^2\right], \tag{5.24}$$

where the Gaussian beam is defined by

$$Gaus\left(\frac{x}{d}\right) = exp\left[-\pi\left(\frac{x}{d}\right)^2\right], \tag{5.25}$$

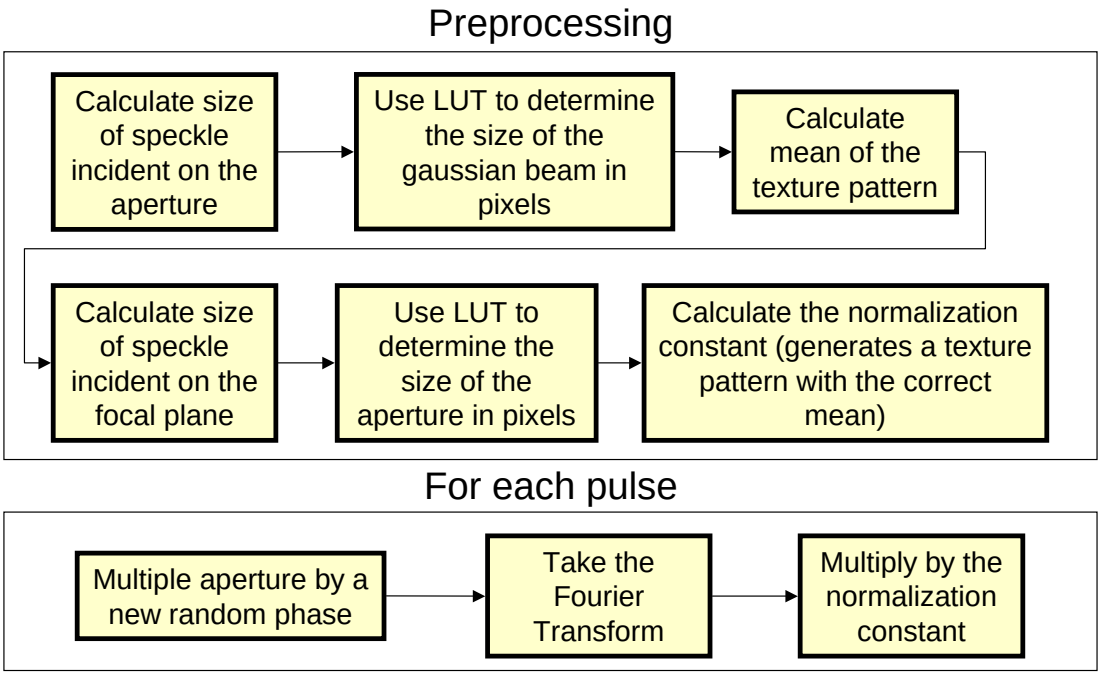

Figure 5.23: The speckle texture map creation process is divided into two sections: preprocessing and the processing required for each pulse. The preprocessing is done only once. It includes calculating the size of the speckle according to theory and the normalization constant required to produce a texture pattern with the correct mean. The processing for each pulse uses the results of the calculations performed in the preprocessing step.

where z is the propagation distance from the hard target to the aperture and d is the radius of the Gaussian beam. The effective radius of the autocorrelation is taken to be at the point where $\frac{dx}{\lambda z} = \frac{\sqrt{2}}{2}$ and $\frac{dy}{\lambda z} = \frac{\sqrt{2}}{2}$, which results in a speckle radius of

$$\rho_{speckle} = \frac{\lambda z}{d}. \tag{5.26}$$

The next step in the process is the choise of a value N such that the generated texture pattern has sufficient sub-samples based on the size of the detector array. The aperture

width is defined to be half of this size, i.e., $\frac{N}{2}$. Therefore the radius of the speckle at the aperture in pixels is

$$\rho_{speckle} = \frac{\lambda z}{d} \frac{N}{2D_A}, \tag{5.27}$$

where D_A is the diameter of the aperture. The size of the Gaussian beam needed to generate speckles of this size is determined using a look-up table (LUT). The LUT relates the diameter of the speckle in pixels to the radius of the Gaussian beam in pixels. The mean of the texture pattern is calculated using the method derived in Section 5.6.2. Two arrays are generated with a Gaussian beam of the size determined by the LUT; one with a random phase and one without. The Fourier Transform of each array is evaluated. Then each array is multiplied by the aperture, followed by taking the magnitude squared, and finally summed. The summation of the random array divided by the summation of the nonrandom array then gives the mean of the texture pattern.

After determining the mean of the texture pattern, the size of the speckle incident on the focal plane is derived from equation 3.60. For a circular aperture, this equation reduces to:

$$R_I(\Delta x, \Delta y) = \langle I \rangle^2 \left[1 + somb^2 \left(\frac{dr}{\lambda z} \right) \right], \tag{5.28}$$

where z is the propagation distance from the aperture to the focal plane, d is the diameter of the aperture, and the sombrero function is defined by

$$somb\left(\frac{r}{d}\right) = 2\frac{J_1\left(\frac{\pi r}{d}\right)}{\frac{\pi r}{d}}, \tag{5.29}$$

where J_1 is a first-order Bessel function of the first kind. The radius of the sombero is taken to be at the point where $\frac{\pi dr}{\lambda z} = 1.22$, which results in a speckle radius of

$$\rho_{speckle} = \frac{1.22\lambda z}{\pi d}. \tag{5.30}$$

Another LUT is then used that relates the diameter of the speckle on the focal plane in pixels to the aperture diameter in pixels. The LUTs were generated for various $N \times N$ arrays by varying the size of the Gaussian beam or the aperture. Each case was run 10 to 1000 times, depending on the size of N, to generate an average value. The Gaussian LUTS are shown in Figure 5.24 on a log scale. The steps are due to the discrete nature of the data. The aperture LUTs are similar. To implement the LUTs in DIRSIG, trendlines were fitted to the data and are summarized in Table 5.2.

The normalization constant for each range is calculated by taking the sum of the magnitude squared of the Fourier Transform of the aperture and dividing by the total number of pixels; resulting in the mean of the non-normalized texture pattern, $\overline{t_{non}}$. The normalization constant is then given by

$$C_{tex}(z) = \frac{\overline{t_{tex}}}{\overline{t_{non}}}. \tag{5.31}$$

The generation of a new texture pattern reduces to applying a new random phase to the aperture determined by the second LUT, taking the Fourier Transform, and then multiplying by C_{tex}. The resulting signal-to-noise ratio of the texture map will be unity and the autocorrelation will depend on the aperture size as described by equation 3.60. A sample texture map was shown in Figure 3.16.

The speckle texture map is generated using the method described in this section. Since the equations describing the compression effect assume a circular aperture, only a circular aperture will be modeled. Fully developed speckle will also be assumed since most surfaces are "rough" on the order of a wavelength at the wavelengths of interest. The final assumption is that the source has a narrow spectral width. Therefore, this research will

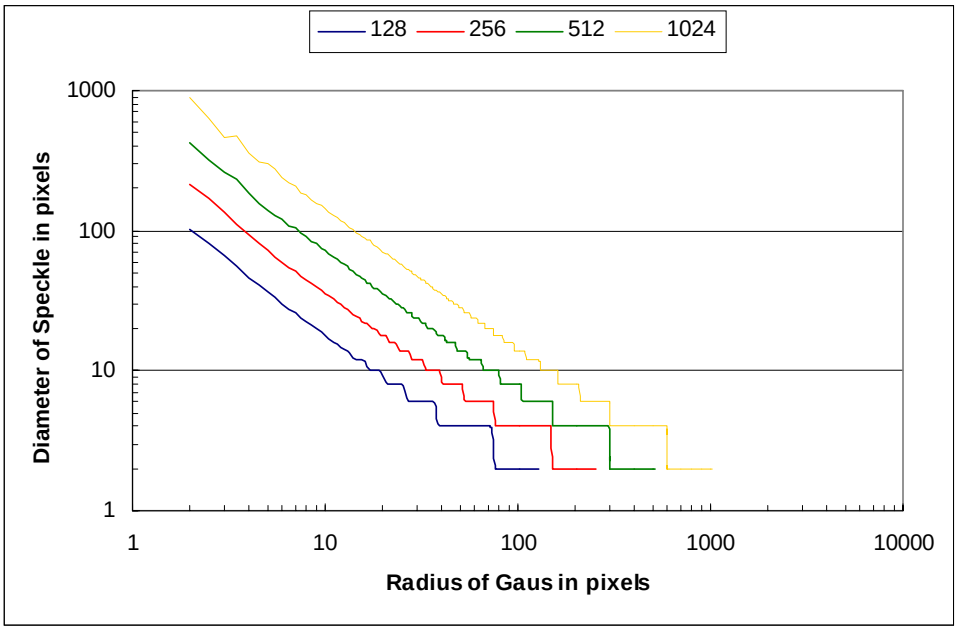

Figure 5.24: The Gaussian LUTs relating the radius of the Gaussian beam in pixels to the diameter of the resulting speckle in pixels for various sized $N \times N$ arrays. The LUTs are displayed on a log scale. The steps are due to the inability to calculate the width of the speckle in anything other than integer values.

not attempt to model the correlation between the speckle pattern as a function of wavelength. The model will apply the same speckle pattern at each wavelength when a spectral line shape is given to the beam. As long as systems are modeled that have a narrow line shape, this assumption should not introduce much error. Even in a DIAL system when two lasers are used (one tuned to a peak of an absorption feature and one tuned to the tail) the error should be minimal due to the narrow width of most absorption features of interest. DIRSIG only uses the same speckle pattern for both wavelengths when the atmospheric time constant is greater than the pulse separation and the transmitter/receiver platform does not move between pulses.

Beam or Aperture	N	Trendline
Beam	128	$\rho_{speckle} = \frac{153.67}{(d-0.459)^{0.9301}}$
Beam	256	$\rho_{speckle} = \frac{294.49}{(d-0.597)^{0.9317}}$
Beam	512	$\rho_{speckle} = \frac{561.65}{(d-0.680)^{0.9317}}$
Beam	1024	$\rho_{speckle} = \frac{1110.1}{(d-0.745)^{0.9398}}$
Aperture	128	$\rho_{speckle} = \frac{216.50}{(d-0.144)^{0.9908}}$
Aperture	256	$\rho_{speckle} = \frac{424.34}{(d-0.305)^{0.9884}}$
Aperture	512	$\rho_{speckle} = \frac{824.46}{(d-0.419)^{0.9849}}$
Aperture	1024	$\rho_{speckle} = \frac{1620.3}{(d-0.647)^{0.9839}}$

Table 5.2: This table lists the trendlines for the LUTs relating the radius of the Gaussian beam in pixels to the diameter of the speckle at the aperture in pixels and the size of the aperture diameter in pixels to the diameter of the speckle at the focal plane in pixels.

5.7 Atmospheric Turbulence Approach

The atmospheric turbulence effects implemented into DIRSIG include beam spread, beam wander, image blurring, and image displacement. Based upon the equations presented in Section 3.3.3, beam spread is taken into account by using equation 3.42 to calculate the radius of the beam in the target plane ρ_c and the corresponding divergence angle

$$\phi = \tan^{-1}\left(\frac{\rho_c - \frac{D}{2}}{R}\right), \tag{5.32}$$

where D is the diameter of the beam at the aperture and R is the range to the target. If the user decides not to account for turbulence, the divergence angle of the transmitter is used in the photon map creation process, as outlined in Section 5.5.3.

Beam wander is accounted for by generating a random angular deflection of the beam centroid in the photon map creation process. This deflection is a total deflection of the entire path, versus a step-wise random walk. The random centroid is generated in the

farthest object plane using a Gaussian distribution and a variance of

$$\sigma^2 = \frac{\left\langle \rho_c^2 \right\rangle}{2}, \tag{5.33}$$

where $\left\langle \rho_c^2 \right\rangle$ is defined by equation 3.46. The angular deflection of the center of the beam is calculated using

$$\delta = \tan^{-1}\left(\frac{r_d}{R}\right), \tag{5.34}$$

where r_d is the distance from the randomly generated beam centroid to the initial centroid position and R is the maximum range.

Image blurring is taken into account by applying the total short-term MTF to the image, based upon the equations presented in Section 3.3.3. The total short-term MTF is the multiplication of the short-term MTF (eq. 3.48) and the diffraction limited MTF

$$MTF_d = \left(\frac{2}{\pi}\right)\left[\cos^{-1}\left(\frac{\lambda f \nu}{D}\right) - \left(\frac{\lambda f \nu}{D}\right)\left[1 - \left(\frac{\lambda f \nu}{D}\right)^2\right]^{\frac{1}{2}}\right], \tag{5.35}$$

where λ is the wavelength of the light, f is the focal length of the receiver, D is the diameter of the receiver, and ν is the spatial frequency.

Image dancing is accounted for by shifting the position of the focal place from pulse to pulse based upon the mean square displacement, as shown in Figure 5.25. A Gaussian distributed random offset in x and y is generated for each pulse based on the variance given in equation 3.49. The corresponding shift of the focal plane in x and y is

$$D_x = \frac{R\sqrt{\langle \delta_x^2 \rangle}}{f} \tag{5.36}$$

and

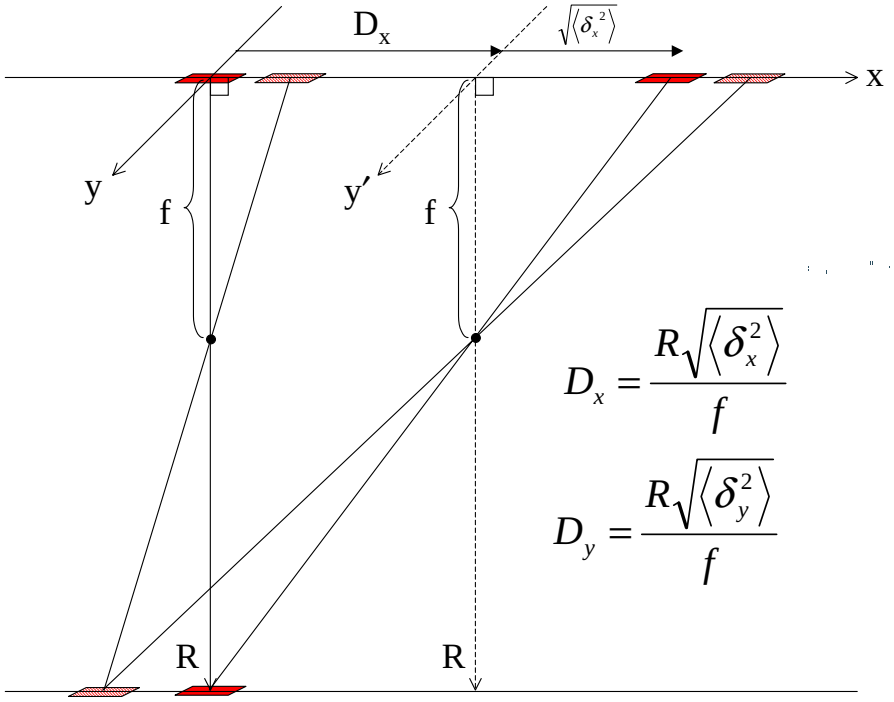

Figure 5.25: DIRSIG accounts for image wander by shifting the location of focal plane for each pulse. The desired offsets $\langle\delta_x^2\rangle$ and $\langle\delta_x^2\rangle$ of the image are obtained by shifting the optical axis of the focal plane the amount D_x and D_y.

$$D_y = \frac{R\sqrt{\langle\delta_y^2\rangle}}{f}, \tag{5.37}$$

where R is the range to the target, f is the focal length of the receiver, and $\sqrt{\langle\delta_x^2\rangle}$ and $\sqrt{\langle\delta_y^2\rangle}$ are the random offsets in x and y. The return in the focal plane is not shifted within a pulse period because the pulse period is shorter than the atmospheric time constant.

5.8 Scintillation Approach

An approach similar to the speckle solution was investigated for scintillation. A texture pattern was needed that when applied to the geometrical optics result would produce an image with the correct statistics. To explore this approach, a scintillation simulation study was completed. The scintillation study implemented the full beam propagation model by Nelson (2000). In this approach, atmospheric turbulence is simulated using a series of equally spaced phase screens. The initial $N \times N$ complex array contains the transmitted beam. The electric field after a propagation step is given by

$$E\left(\hat{\rho}, \Delta z\right) = IFT\left(\exp\left(-i\pi\lambda\Delta z|\hat{f}|^2\right) FT\left\{E\left(\hat{\rho}, 0\right)\exp\left[i\theta\left(\hat{\rho}\right)\right]\right\}\right), \tag{5.38}$$

where $E\left(\hat{\rho}, 0\right)$ is the electric field at the beginning of a propagation step, the Fresnel propagator is $\exp\left(-i\pi\lambda\Delta z|\hat{f}|^2\right)$, FT stands for Fourier transform, IFT stands for inverse Fourier transform, and the phase screen is given by

$$\begin{aligned} \Theta\left(\hat{\rho}\right) &= 0.0984k_0\sqrt{C_n^2\left(z\right)\Delta z}\left(N\delta x\right)^{5/6} \\ &\times FT\left[\left(\sqrt{n_x^2+n_y^2}\right)^{-11/6}\Theta_0\left(n_x, n_y\right)\right], \end{aligned} \tag{5.39}$$

where Δz is the step size, $\delta x = \sqrt{\frac{\lambda L}{N}}$ is the ideal pixel size for a target distance L, n_x and n_y are array indices, and $\Theta_0\left(n_x, n_y\right)$ is an array of complex unit-variance Gaussian random numbers. Since they are independent, either the real or imaginary portion of the generated phase screen may be used in equation 5.38. Equation 5.39 is derived in articles by Knepp (1983), Martin (1988), Welch (1990), Davis (1994), and Frehlich (2000). Occasionally, in either the real or imaginary part of the phase screen, a spike is produced in the center of the array. Therefore, the phase screen must be tested for the presence of this

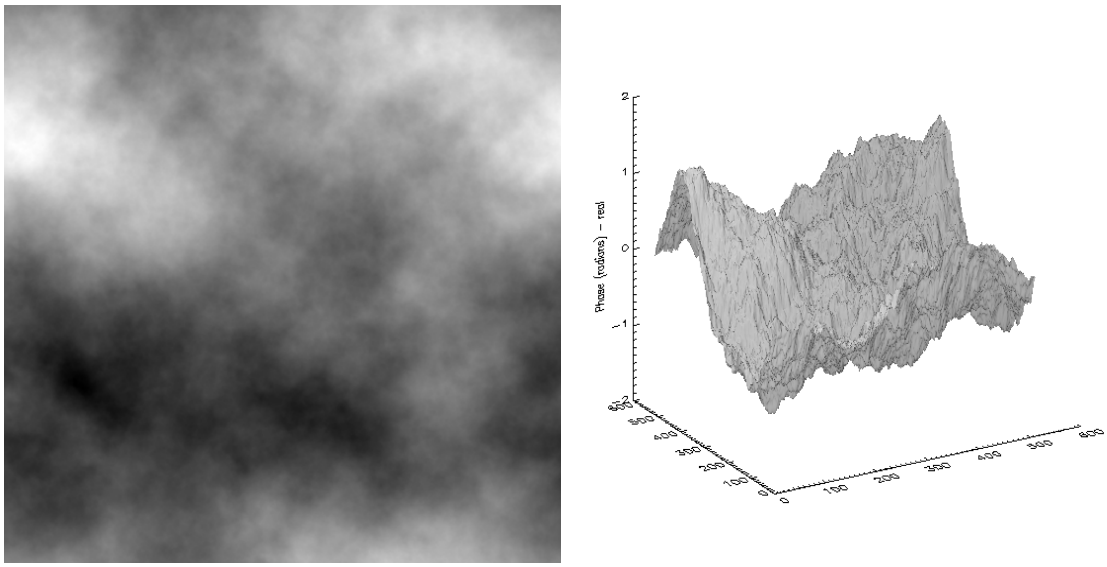

Figure 5.26: A sample random phase screen produced by the scintillation simulation. The phase screen follows a Kolmogorov spectrum.

spike and discarded if it occurs. The size of the propagation steps must meet certain criteria as outlined by Nelson (2000). Once the beam reaches the hard target, fully developed speckle is assumed and the reflected electric field is of the form

$$E\left(n_x, n_y\right)_{reflected} = E\left(n_x, n_y\right)_{target} \times \exp\left[i2\pi random\left(n_x, n_y\right)\right], \tag{5.40}$$

where $random\left(n_x, n_y\right)$ is an array of uniformly distributed random numbers between zero and one. For a monostatic system the same phase screens are used for propagation back to the sensor. This procedure is graphically depicted in Figure 5.27.

The speckle GUI was modified to include the effects of turbulence, as shown in Figure 5.28. The simulated beam was propagated from the transmitter through the random phase screens to the ground, reflected from the ground (either with or without a random

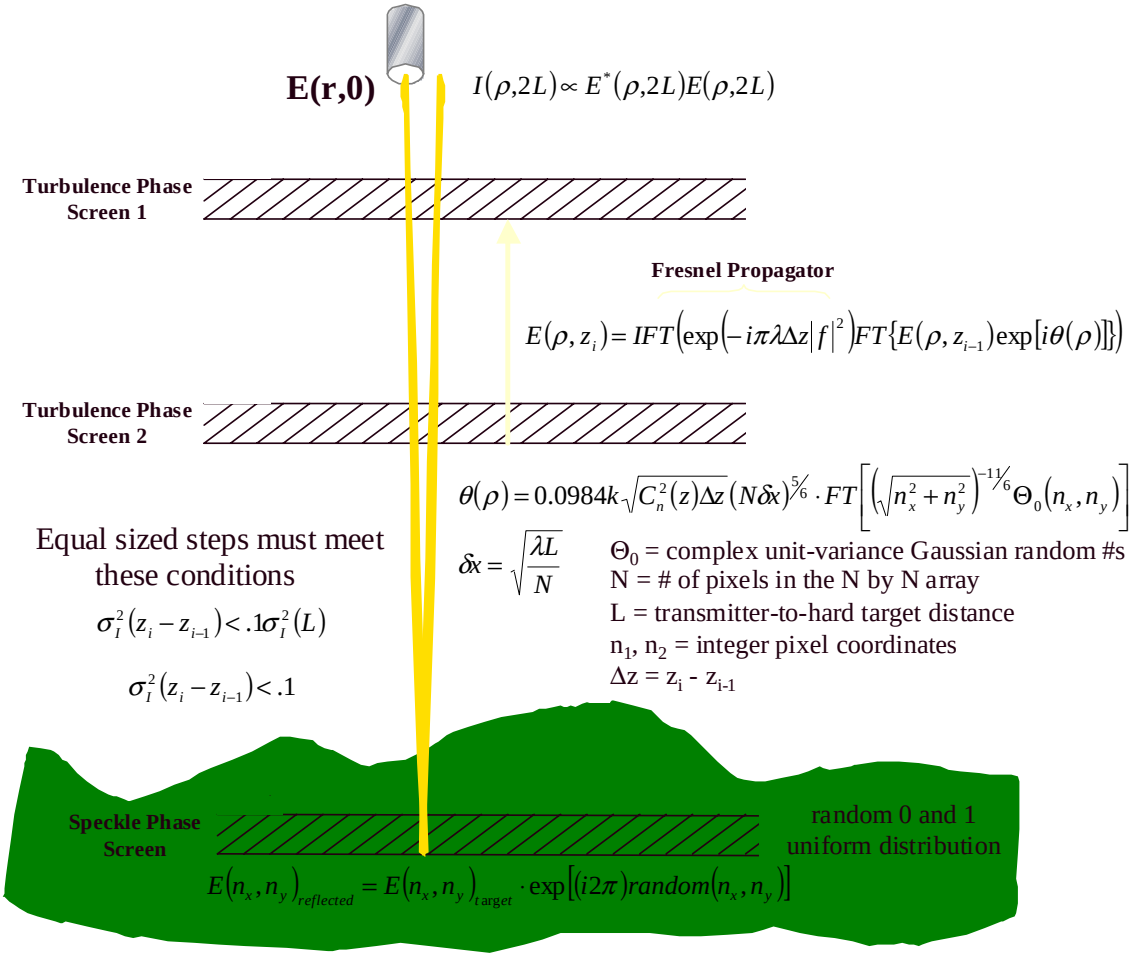

Figure 5.27: The scintillation simulation divides the propagation path into equal sized steps where the normalized irradiance variance for each step must meet the criteria shown on the lower left. Random phase screens $\theta(\rho)$ are generated for each propagation step from the equation in the middle right. Once the phase screens are generated, the beam is propagated from one phase screen to the next using the Fresnel propagator. The initial beam $E(r, 0)$ is propagated using the Fresnel propagator to the ground. Once at the ground, it is multiplied by a random phase to simulate speckle. After reflection, the beam is propagated back to the sensor. The return is multiplied by the aperture function and propagated to the focal plane using the Fresnel propagator. The intensity at the focal plane is proportional to the squared magnitude of the electric field.

phase to simulate speckle), propagated through the random phase screen to the aperture, multiplied by the aperture function, and finally propagated to the focal plane. One can show that the propagation method used by Nelson (2000) is equivalent to the Fresnel approximation without the constant phase factor $\exp(ikz)$. Since the speckle simulation used the Fresnel approximation, this constant phase factor was eliminated in the scintillation simulation. The beam was propagated to the focal plane with turbulence, without turbulence, with turbulence and speckle, and without turbulence and speckle. Texture maps were generated by taking the ratio of the arrays. The statistics GUI was again used to calculate the array statistics.

Depending on what files the GUI was compiled with, the index-of-refraction structure constant was either kept constant along the path (simulating horizontal propagation) or varied according to the Hufnagel-Valley model (simulating vertical propagation). The number of phase screens was determined using the conditions

$$\sigma_I^2(\Delta z) < 0.1\sigma_I^2(L) \tag{5.41}$$

and

$$\sigma_I^2(\Delta z) < 0.1, \tag{5.42}$$

where σ_I^2 is the normalized irradiance variance (Nelson et al. 2000). The GUI initially divides the propagation path into ten steps. The normalized irradiance variance of the step with the highest index-of-refraction structure constant was checked to make sure it was less than 0.1 and less than a tenth of the normalized intensity variance of the entire path. If not, the propagation path is divided into more sections and the conditions are checked again. This process continues until the conditions are met. The normalized irradiance standard

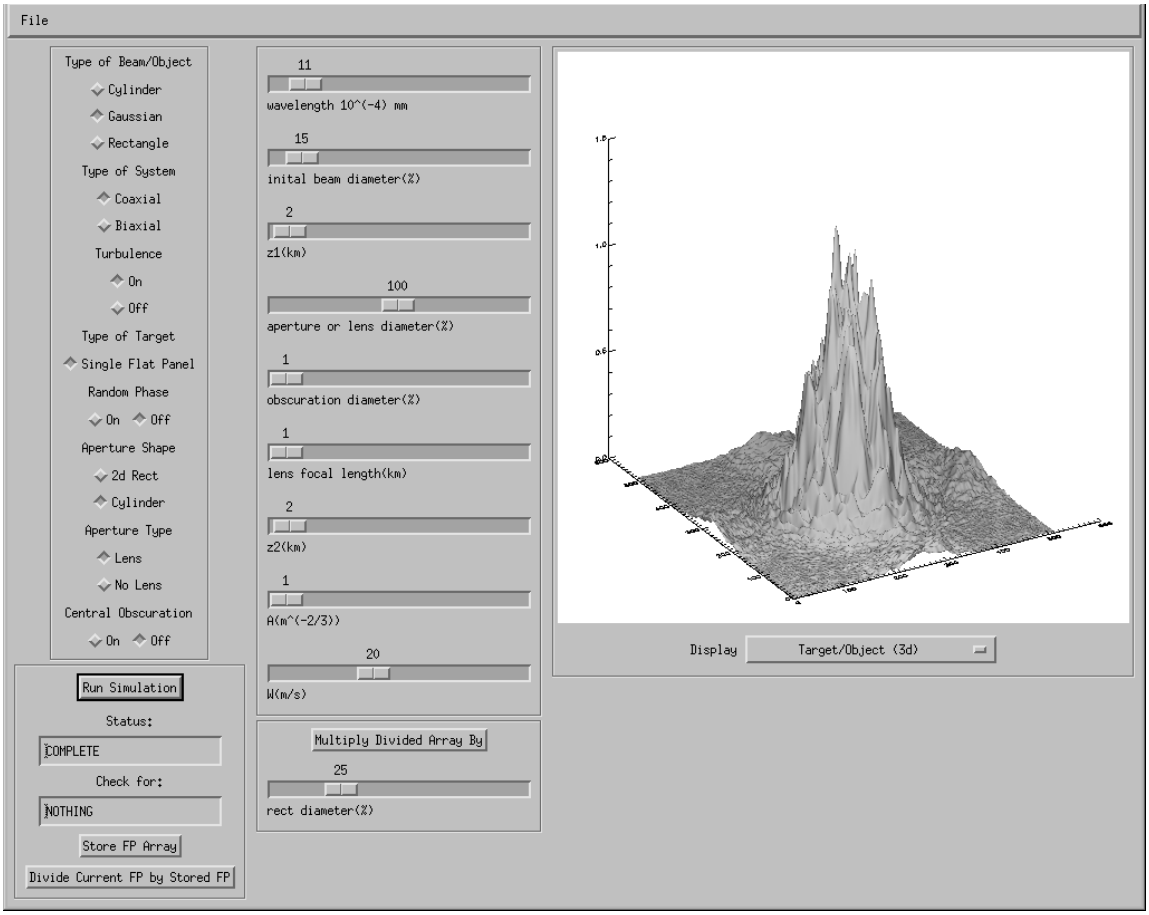

Figure 5.28: The scintillation GUI added sliders for the value of the index-of-refraction structure constant one meter above the ground A and the root-mean-square wind speed W between five and twenty kilometers. If compiled for a horizontal path, the value of W was ignored and the index-of-refraction structure constant was given the constant value A. If compiled for a vertical path, the Hufnagel-Valley model was used with the parameters A and W.

deviation for a spherical wave is given by

$$\sigma_{\overline{I}} = \left(e^{4\sigma_{\chi}^2} - 1\right)^{\frac{1}{2}}, \tag{5.43}$$

where σ_{χ}^2 is the spherical wave log-amplitude variance for a point detector

$$\sigma_{\chi}^2(\Delta z) = 0.56k^{7/6} \int_{z_i}^{z_f} C_n^2(\eta) \left(\frac{\eta}{\Delta z}\right)^{\frac{5}{6}} (\Delta z - \eta)^{\frac{5}{6}} \, d\eta, \tag{5.44}$$

where k is the wavenumber of the light, z_i is position along the optical axis at the beginning of the propagation step, z_f is the position along the optical axis at the end of the propagation step, and $\Delta z = |z_f - z_i|$.

The main result of the scintillation study was that scintillation can be ignored in the presence of speckle for the fidelity modeled in DIRSIG. A scintillation texture map with accurate statistics could not be produced. Therefore, DIRSIG allows the user to input a scintillation texture map generated off-line, but DIRSIG itself does not generate them. The results of the scintillation study are covered in more detail in Section 6.7.

5.9 Variable List

This section summarizes how DIRSIG either receives from the user or calculates each variable in the basic aerosol and topographic equations. The variables and where they are obtained is summarized in Table 5.3.

A	Value of C_n^2 one meter above the ground	User input
A_0	Area of the objective lens or mirror	Calculated using user inputted receiver radius
C_n^2	Index of refraction structure constant	Hufnagel-Valley model
f	Focal length of the receiver	User input
P_L	Average power in the laser pulse	User input
R_T	Range to the ground	Calculated using the position of the transmitter and the scene geometry
v	Root-mean-square wind speed between 5 and 20 kilometers	User input
$W(R)$	Radius of the laser pulse in the target plane	Calculated using either the beam divergence angle or from the beam spread due to turbulence
W_0	Laser output aperture radius	User input
$\beta(\lambda_L, R)$	Volume backscatter coefficient	Calculated using a modified version of MODTRAN
$\kappa(\lambda_L, r)$	Total atmospheric extinction	Scattering calculated using MODTRAN and absorption calculated using FASCODE
ρ^s	Topographical target's scattering efficiency	User inputted as part of the scene description
τ_d	Integration time of the detector	User input
τ_L	Effective pulse duration	User input
θ	Transmitter's half divergence angle	User input
$\xi(\lambda_L)$	Receiver's spectral transmission factor	User input
$\xi(R)$	Geometrical form factor	Calculated using the separation between the transmitter and receiver, the inclination angle between the transmitter and receiver, and by querying the photon map for each position on the focal plane
δ	Inclination angle between the receiver and laser axes	User input

Table 5.3: Basic equation quantities and how DIRSIG either acquires or calculates them.

Chapter 6

Results

This chapter contains the results of this work. The first section includes results that demonstrate the spectral nature of the DIRSIG LADAR/LIDAR model. Geometrical form factor and compression effect results are included in Section 6.2. The next section contains results that demonstrate multiple bounce photons. Section 6.4 contains beam spreading, centroid wander, modulation transfer function, and image dancing results. The next section contains the initial test images including terrain maps and intensity images. Section 6.6 contains images that exhibit speckle. In conclusion, Section 6.7 presents the results of the scintillation study and shows that the effects of scintillation can be ignored in the presence of speckle in the low turbulence regime.

6.1 Spectral Results

The parameters in the DIRSIG LADAR/LIDAR model that are wavelength dependent include the laser lineshape, atmospheric absorption, transmission, and scattering, the receiver's spectral transmission factor, and the turbulence equations. One way to verify

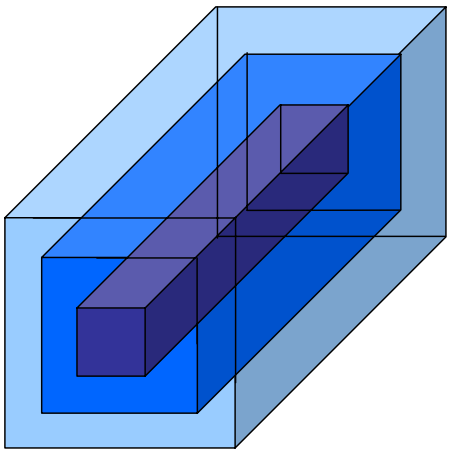

Figure 6.1: The DIRSIG scene used in the SF6 DIAL demonstration contains nested rectangular boxes of SF6 with varying concentrations.

that the atmospheric parameters are varying as a function of wavelength is to do a DIAL demonstration. A DIRSIG scene was created that contained nested rectangular boxes of SF6 with varying concentrations as shown in Figure 6.1. The scene was interrogated with two different single-frequency pulses, one tuned to the peak of an absorption feature at 811.16 cm^{-1} and one to the tail of the same absorption feature at 810.67 cm^{-1} as shown in Figure 6.2. The total column integration of the return from each pulse along with the ratio of the two returns are shown in Figure 6.3. The results of the simulation were excellent. The return from the tail did not show any absorption while the return from the peak is clearly attenuated. The ratio of the two returns maps out not only the position of the cloud, but its intensity is proportional to the concentration of the gas.

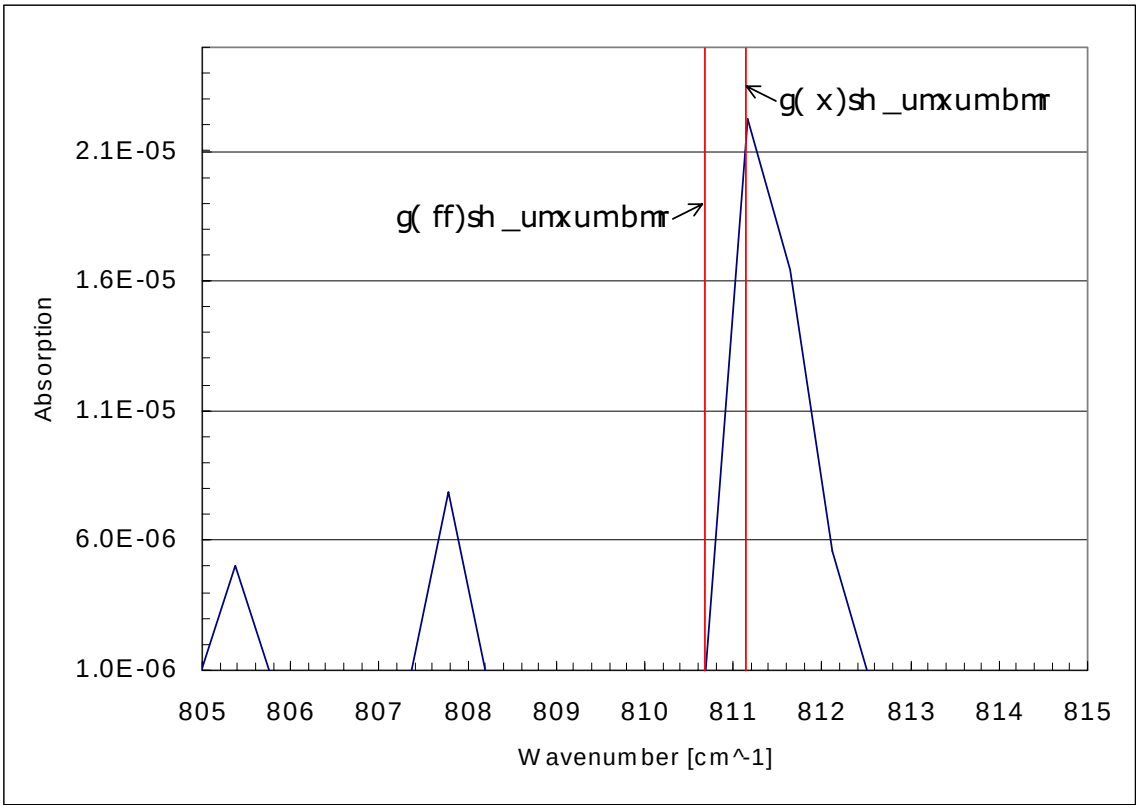

Figure 6.2: The SF6 DIAL demonstration had the "on" wavenumber tuned to the peak of the absorption feature at 811.16 cm^{-1} and the "off" wavenumber tuned to the tail of the same absorption feature at 810.67 cm^{-1}.

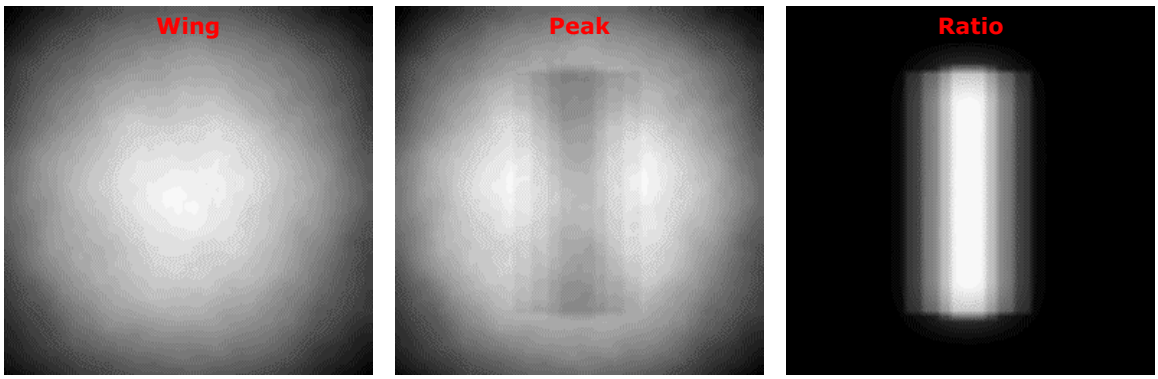

Figure 6.3: A simulated DIAL system is shown above. The image on the left is the total column integration of the return from the pulse centered at the tail of the absorption feature. The image in the middle is the total column integration of the return from the pulse centered at the peak of the absorption feature. Finally, the image on the right is the ratio of the tail to the peak and maps out the position of the gas cloud. Its intensity is proportional to the concentration of the gas.

6.2 GFF and Compression Results

To verify that the coded geometrical form factors were giving valid results, the results presented by Harms (1978) were reproduced. The system specifications and atmospheric constants used by Harms are summarized in Table 6.1. Excellent agreement was achieved between Harms' results and those calculated using DIRSIG. Figure 6.4 shows how increasing propagation distance attenuates the return in a bistatic system. It also shows that in a bistatic system the position of the return on the focal plane varies as a function of propagation distance. Figure 6.5 shows how a central obscuration affects the return on the focal plane in a bistatic system as a function of propagation distance. The affect of varying the diameter of the central obscuration in a monostatic system is shown in Figures 6.6 through 6.8. The propagation distance in Figure 6.6 is 100 m, in Figure 6.7 1000 m, and in Figure 6.8 10000 m. Finally, Figure 6.9 shows the power as a function of range for a coaxial system and for a bistatic system with varying inclination angles. By varying the inclination angle, a bistatic system can be tuned to a specific distance. As Figure 6.10 shows, the ability to tune a bistatic system allows targets at specific ranges to be interrogated, such as a plume coming out of a factory smoke stack. It may be possible to tune a system finely enough that electronic range gating is not needed.

Average pulse power (single line)	50 kW
Pulse duration	500 nsec
Expanded beam diameter	150 mm
Expanded beam divergence (full angle, 50% of energy)	0.25 mrad
Diameter of receiving mirror	600 mm
Focal length	3 m
Radius of detector	0.4 mm
Extinction coefficient	0.05 km^{-1}
Backscattering coefficient	0.001 $km^{-1}sr^{-1}$

Table 6.1: System Parameters and Atmospheric Constants used by Harms (1979)

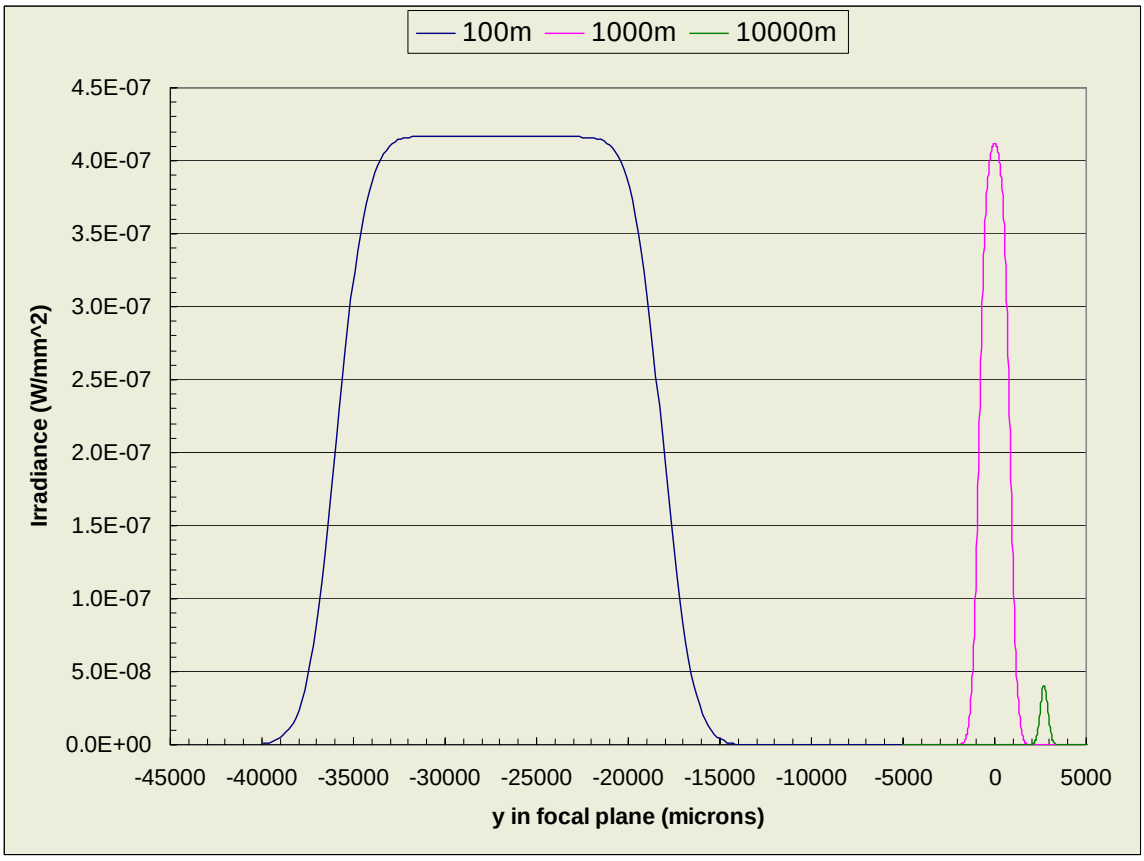

Figure 6.4: Irradiance in the focal plane of a noncoaxial LADAR/LIDAR system; separation of transmitter and receiver is 1m, inclination angle is 1 mrad, distance (100 m, 1 km, 10 km), and other parameters are as listed in Table 6.1

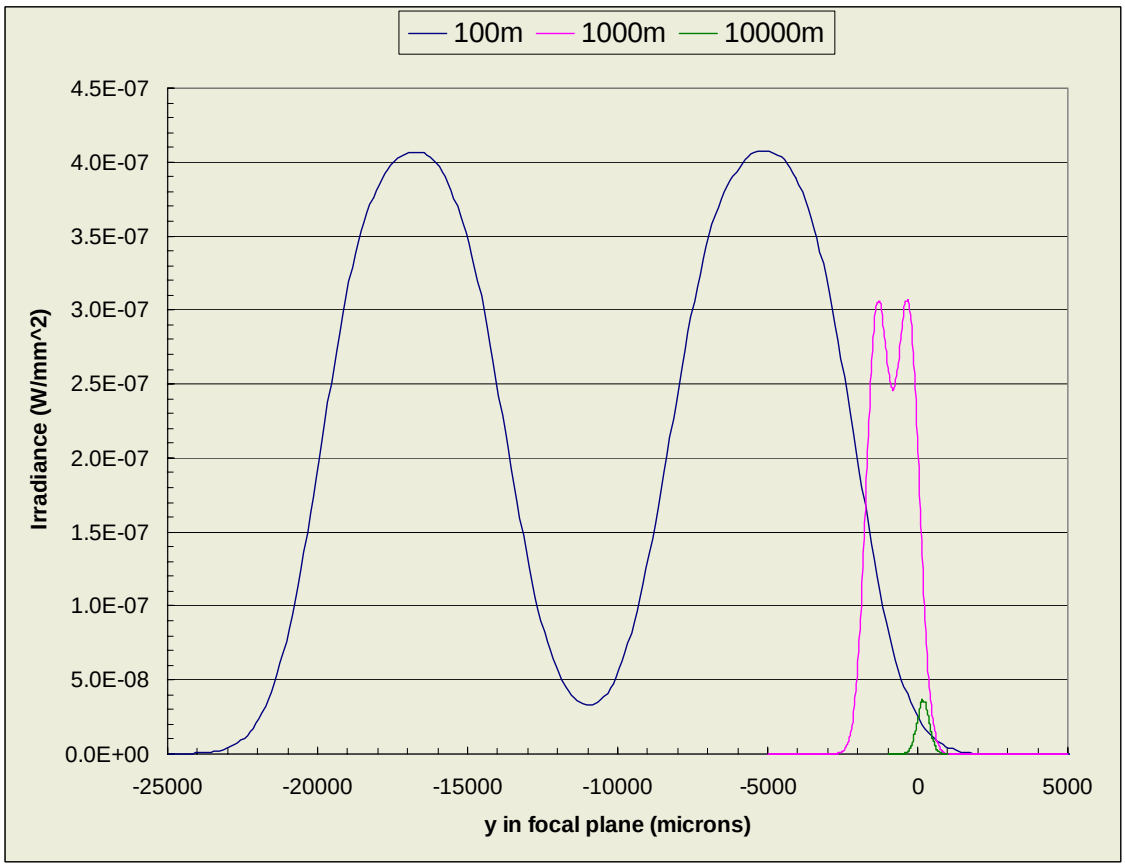

Figure 6.5: Irradiance in the focal plane of a noncoaxial LADAR/LIDAR system with central obscuration; obscuration radius is 100 mm, separation of transmitter and receiver is 375 mm, inclination angle is 0.1 mrad, distance (100 m, 1 km, 10 km), and other parameters are as listed in Table 6.1

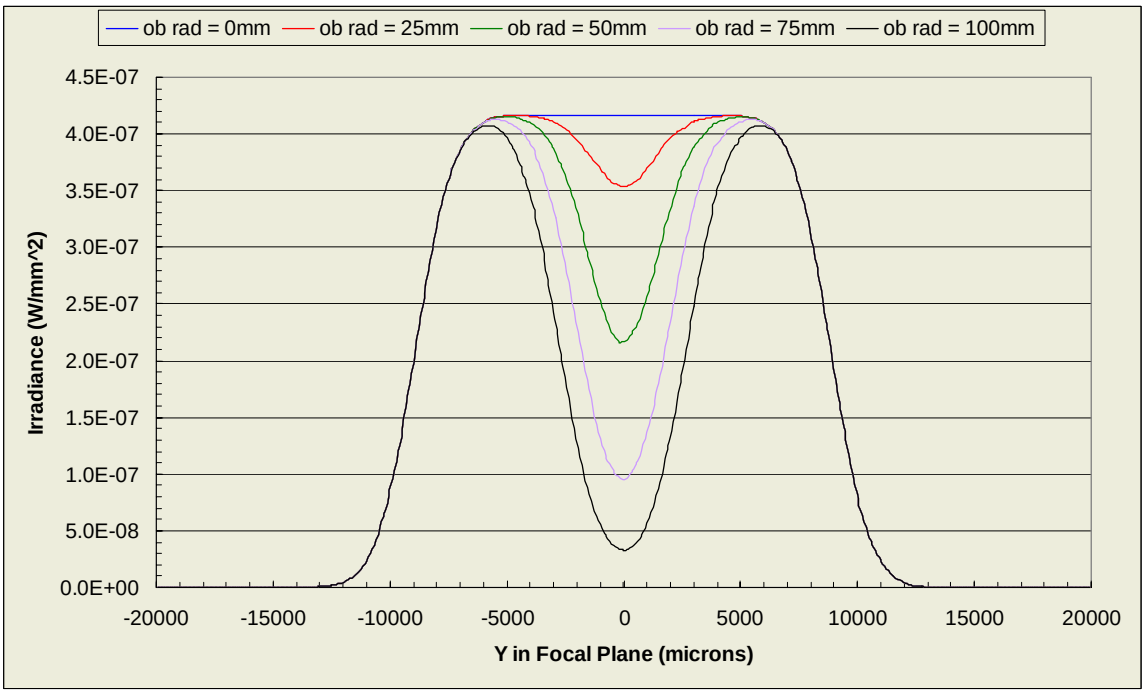

Figure 6.6: Irradiance in the focal plane of a coaxial LADAR/LIDAR system with central obstruction; obstruction radii are 0, 25, 50, 75, and 100 mm, distance is 100 m, and other parameters are as listed in Table 6.1

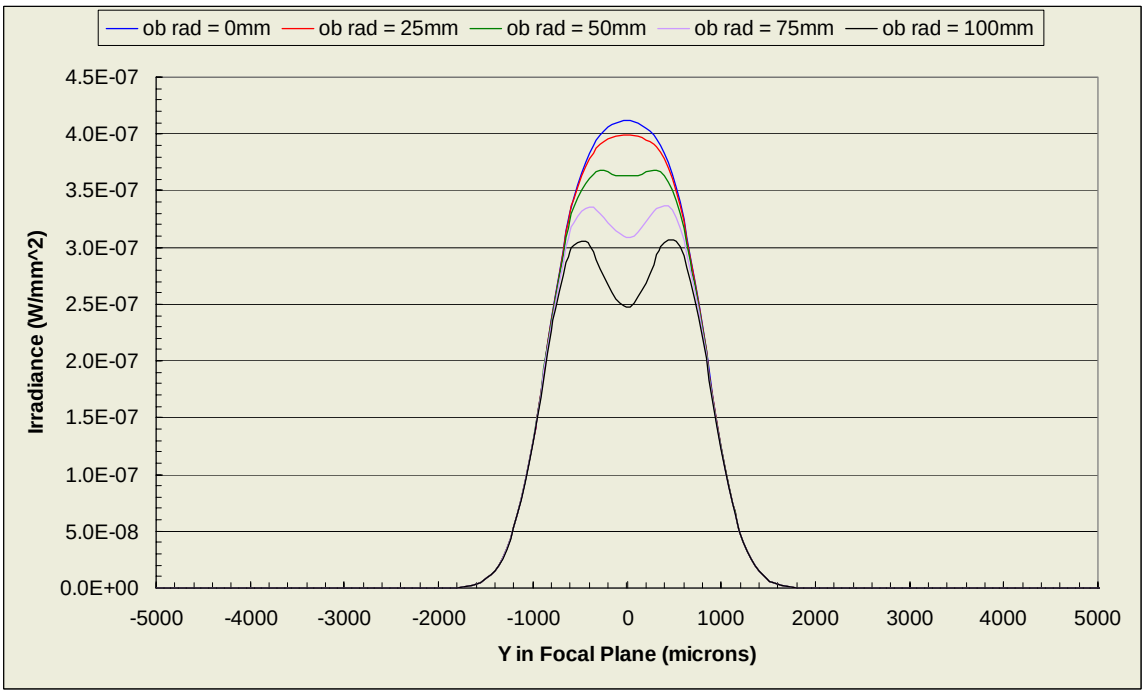

Figure 6.7: Irradiance in the focal plane of a coaxial LADAR/LIDAR system with central obstruction; obstruction radii are 0, 25, 50, 75, and 100 mm, distance is 1000 m, and other parameters are as listed in Table 6.1

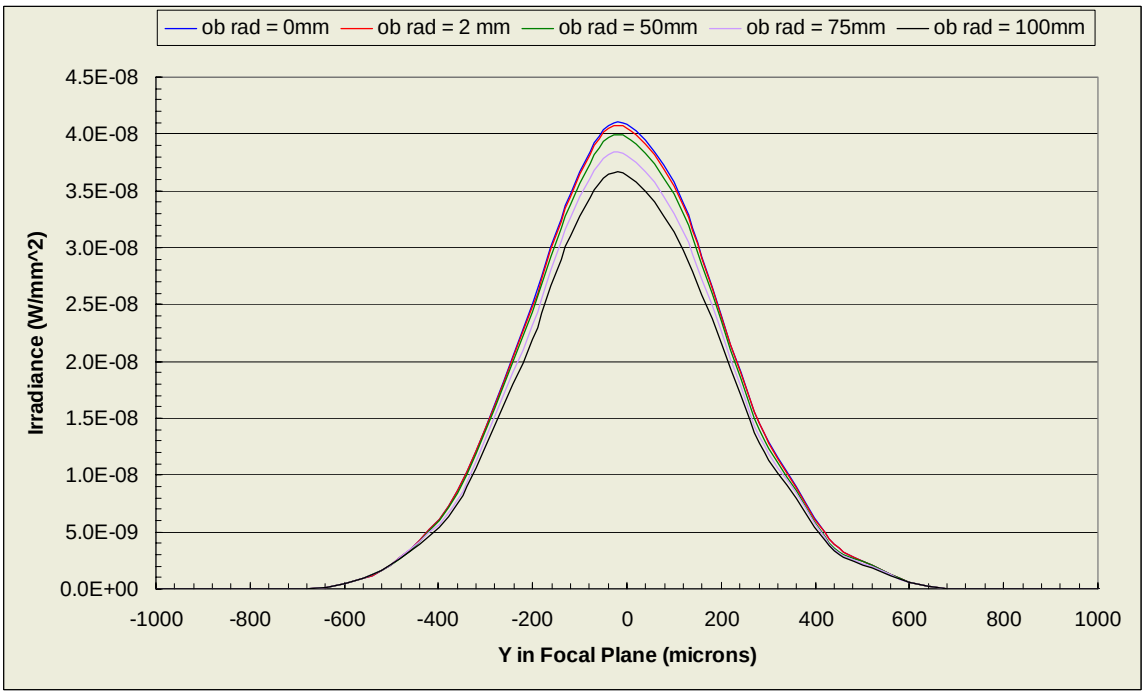

Figure 6.8: Irradiance in the focal plane of a coaxial LADAR/LIDAR system with central obstruction; obstruction radii are 0, 25, 50, 75, and 100 mm, distance is 10000 m, and other parameters are as listed in Table 6.1

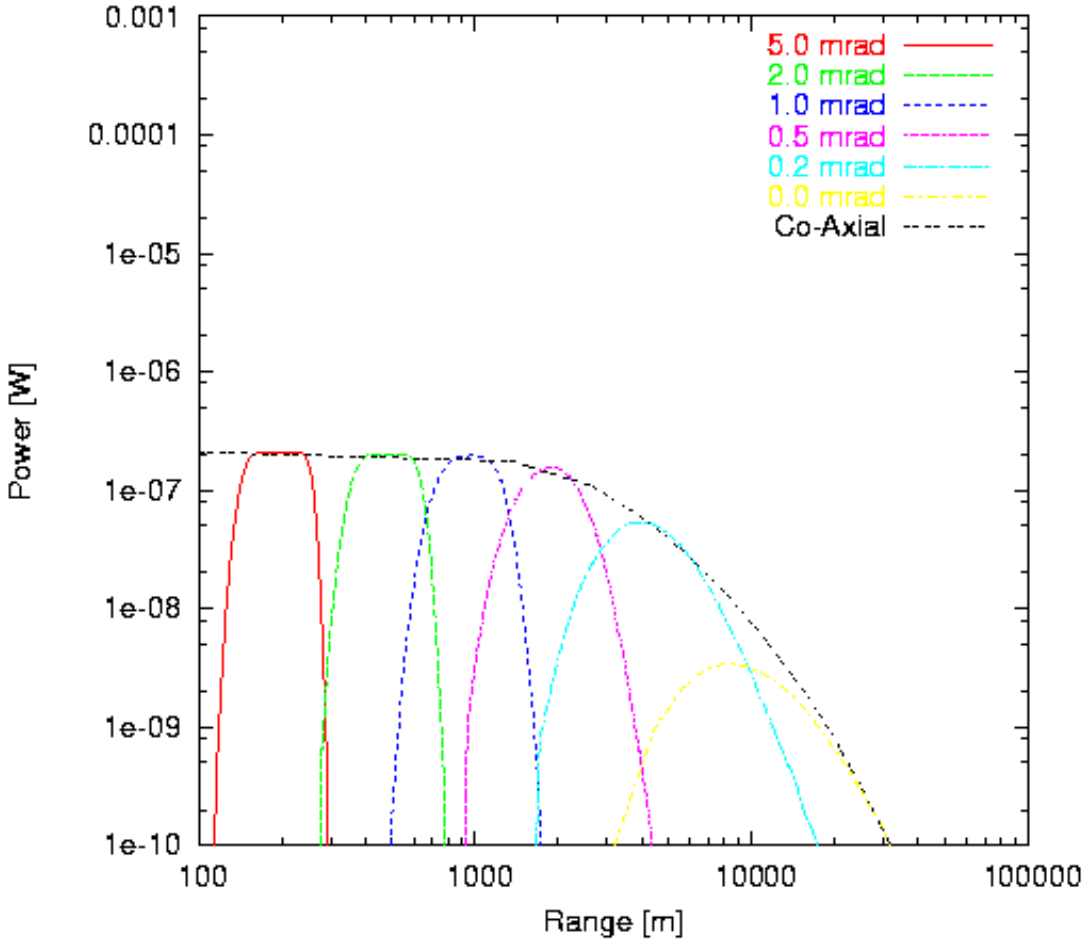

Figure 6.9: Power as a function of range for a coaxial LADAR/LIDAR system and for a biaxial LADAR/LIDAR system with varying inclination angles; inclination angles are 0.2, 0.5, 1.0, 2.0, and 5.0 mrad, system separation of 1 m, and other parameters are as listed in Table 6.1

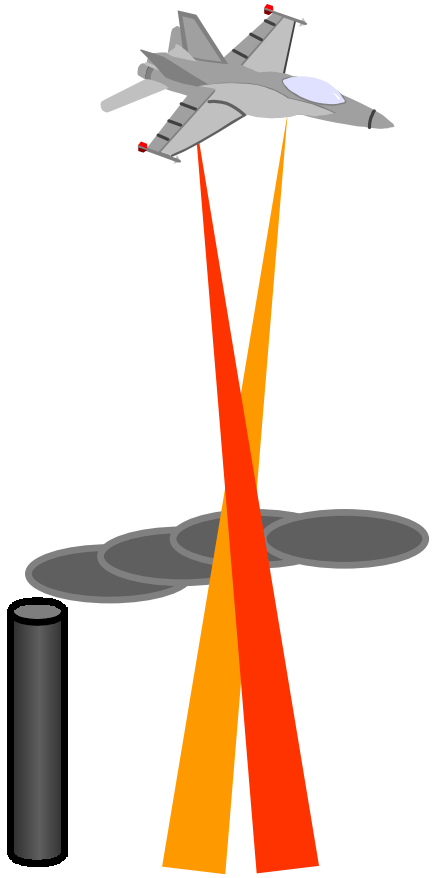

Figure 6.10: By varying the inclination angle in a bistatic system, targets at specific ranges can be interrogated, such as a plume coming out of a factory smoke stack.

6.3 Multiple Bounce Results

A DIRSIG scene was constructed to demonstrate the existence of multiple bounce photons. As shown in Figure 6.11, the scene consisted of four "chunky" bars on a flat plate. A "chunky" bar is essentially a pyramid with its top cut off. Figures 6.12 and 6.13 contains temporal slices of the return. The first slices show just the return from the top of the "chunky" bars because a narrow temporal pulsewidth was modeled. As the returns from the top of the "chunky" bars begin to fade, the edges become bright and then finally the flat plate. As the edges begin to fade, returns between the "chunky" bars begin to brighten. Finally, as the returns between the "chunky" bars begin to fade, returns on the edges of the "chunky" bars begin to brighten. The returns between the "chunky" bars and on the edges are caused by multiple bounce photons. The position of these multiple bounce photons is dependent on the scene geometry and the spreading of the beam. Each photon in the photon map creation process is given a deflection angle to simulate beam spread. Therefore, photons at the center of the scene travel almost straight down while photons at the edges of the scene do not. These edge photons skim off the sides of the "chunky" bars and onto the ground before reflecting back to the sensor.

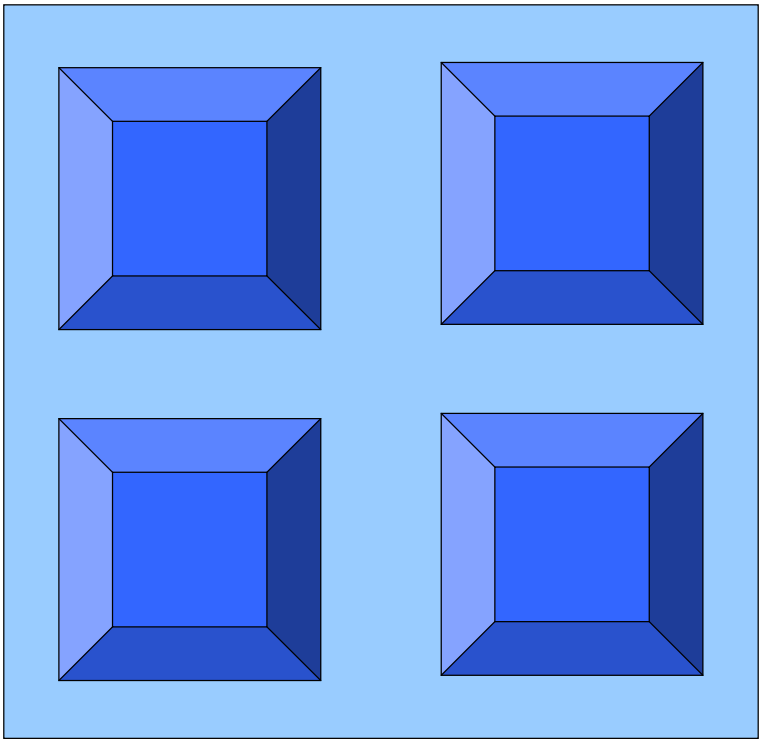

Figure 6.11: The DIRSIG scene used to demonstrate the existence of multiple bounce photons. The scene consists of four "chunky" bars on a flat plate. A "chunky" bar is essentially a pyramid with its top cut off.

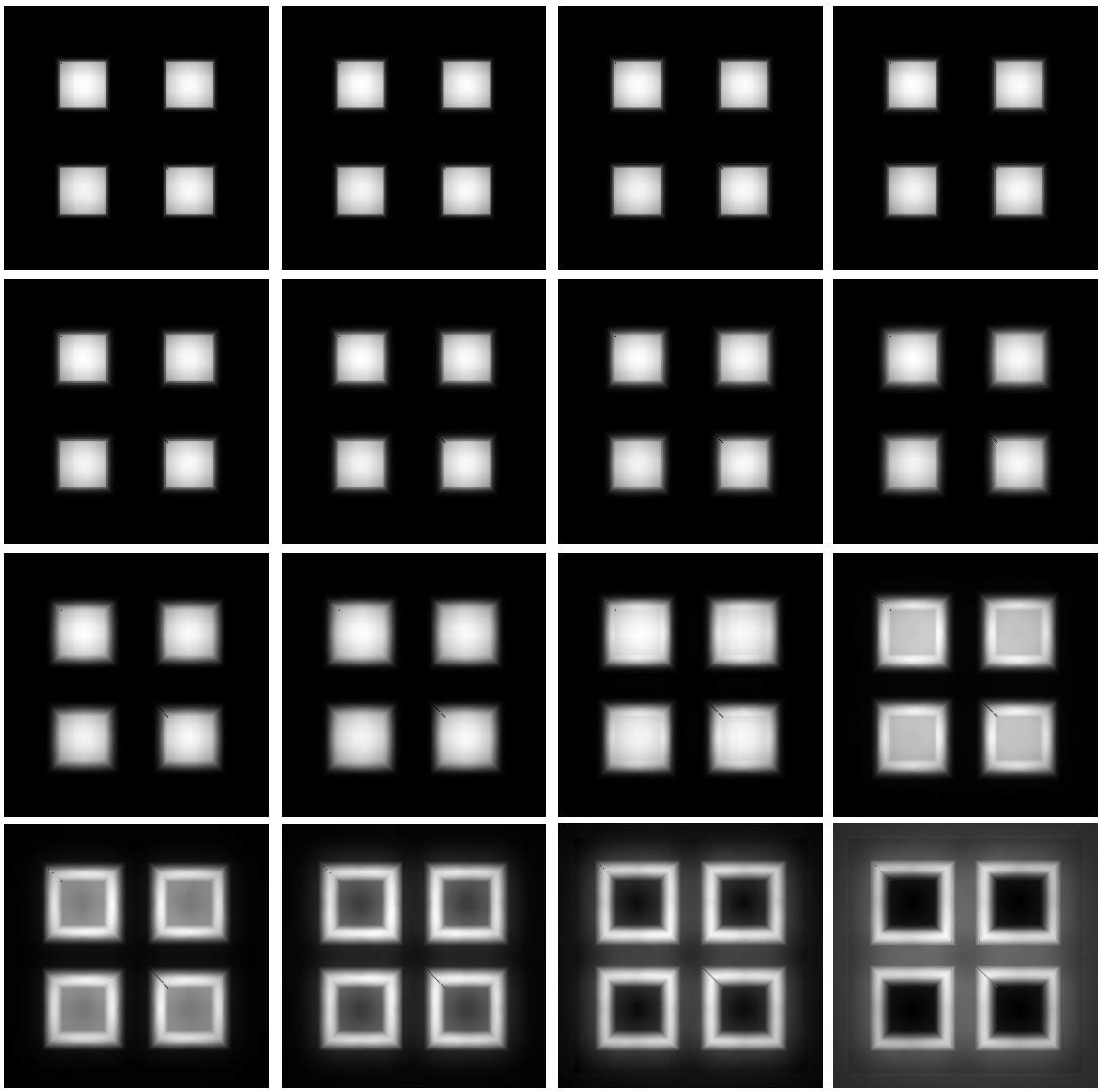

Figure 6.12: Temporal slices from the multiple bounce example. The beginning slices show just the return from the top of the "chunky" bars because a narrow temporal pulsewidth was modeled. As the returns from the top of the "chunky" bars begin to fade, the edges become bright

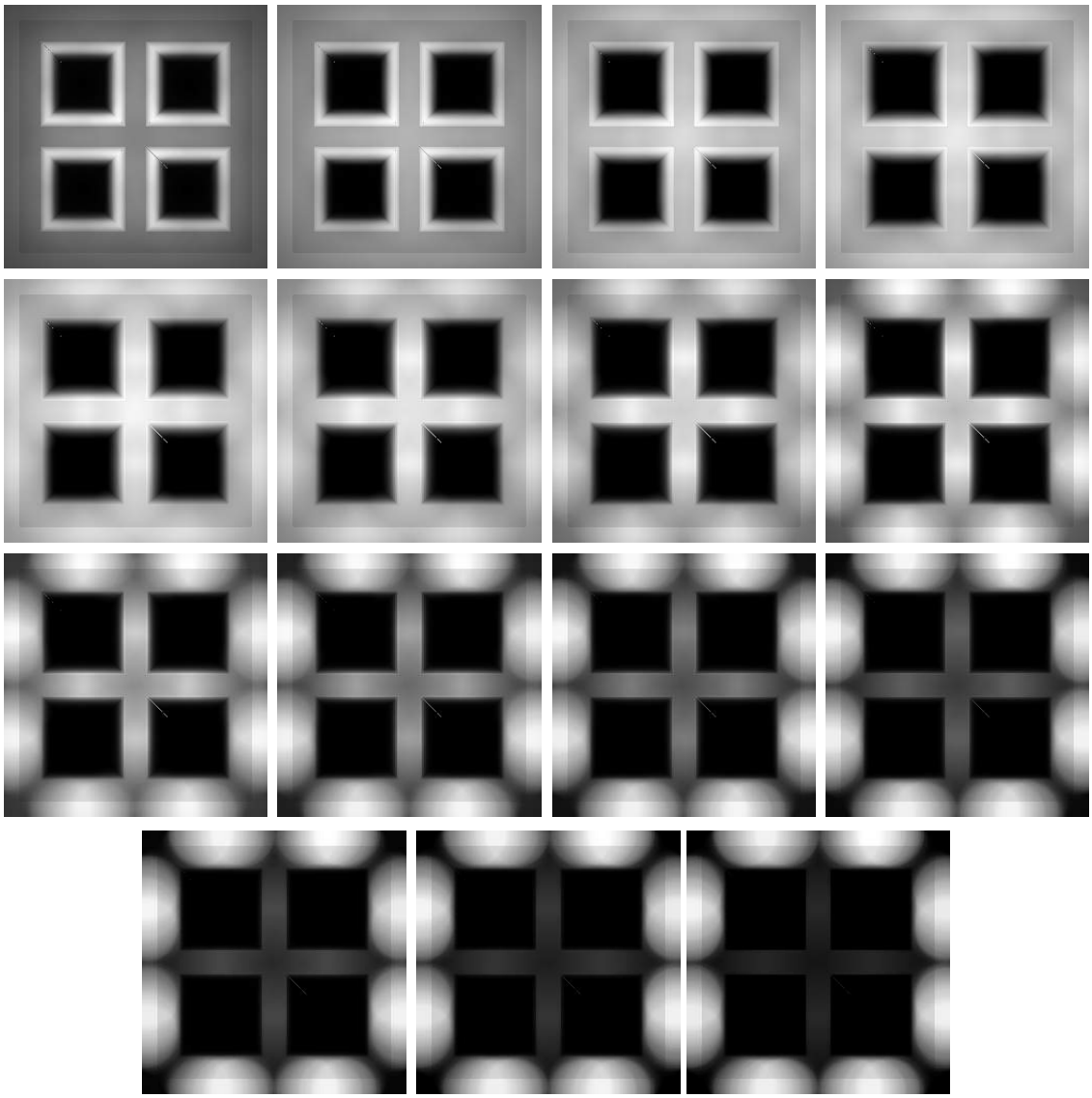

Figure 6.13: The remaining temporal slices from the multiple bounce example. The edges of the "chunky" bars begin to fade and the flat plate becomes bright. As the flat plate begins to fade, returns between the "chunky" bars begin to brighten. As the returns between the "chunky" bars begin to fade, returns on the edges of the "chunky" bars begin to brighten. The returns between the "chunky" bars and on the edges are caused by multiple bounce photons.

6.4 Results for Beam and Image Effects

6.4.1 Results for Beam Spread

DIRSIG calculates the radius of the beam in the object plane using either the half divergence angle of the transmitter or the turbulence equations. The initial radius of the beam is supplied by the user. DIRSIG defined the radius of the beam used in the photon map creation process to be at 2σ. An initial Gaussian beam with a radius of 0.075 meters is shown in the upper left corner of Figure 6.14. The points represent "photons" shot from the source. The density of the shot "photons" is Gaussian. Figure 6.14 also shows the beam propagated a distance of 100, 1000, and 10000 meters using a half divergence angle of 0.000125. Table 6.2 shows the radius of the beam calculated from the half divergence angle and the resulting radius at 2σ for the beam propagated a distance of 100, 1000, and 10000 meters. Figure 6.15 shows a beam propagated 10000 meters using the turbulence equations. The Hufnagel-Valley model was used with C_n^2 set to $1 \cdot 10^{-13}$ at the ground and the rms wind speed to 21 meters per second.

Range (m)	Calculated Beam Radius (m)	DIRSIG Beam Radius x axis - 2σ (m)	DIRSIG Beam Radius y axis - 2σ (m)
0	0.075	0.0757	0.0749
100	0.088	0.0883	0.0874
1000	0.200	0.2019	0.1997
10000	1.325	1.3374	1.3230

Table 6.2: The radius calculated at various distances using a half divergence angle of 0.000125 radians and an initial radius of 0.075 meters. The resulting beam radius at 2σ calculated using DIRSIG is also shown in both the x and y directions.

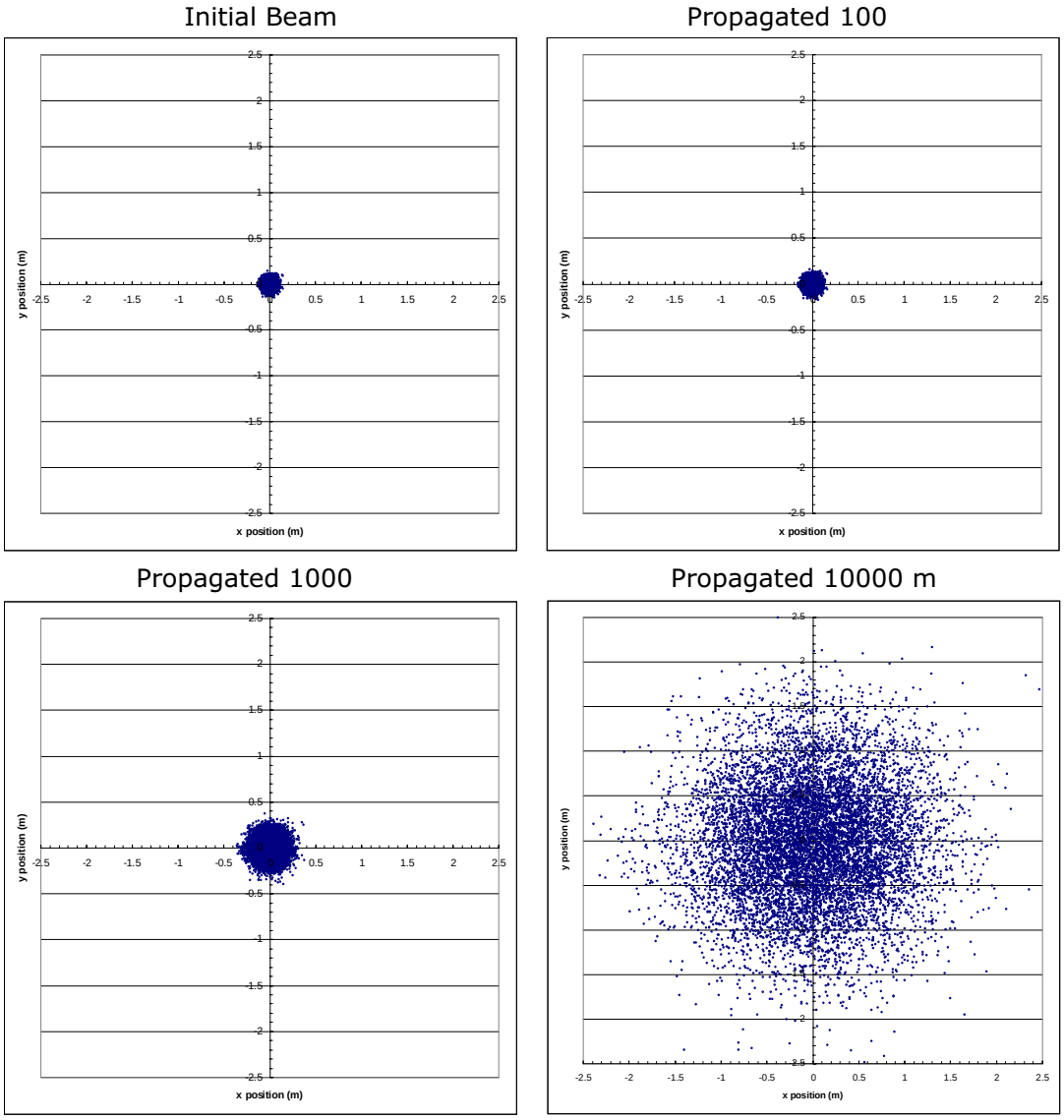

Figure 6.14: A beam with an initial radius of 0.075 meters and a half divergence angle of 0.000125 radians propagated 100, 1000, and 10000 meters in the absence of turbulence. The radius is defined to be 2σ.

initial		
xpos (2sigma)	ypos (2sigma)	given
0.0757	0.0749	0.0750
at 10 km		
xpos (2sigma)	ypos (2sigma)	calcaulted
0.0788	0.0780	0.0781

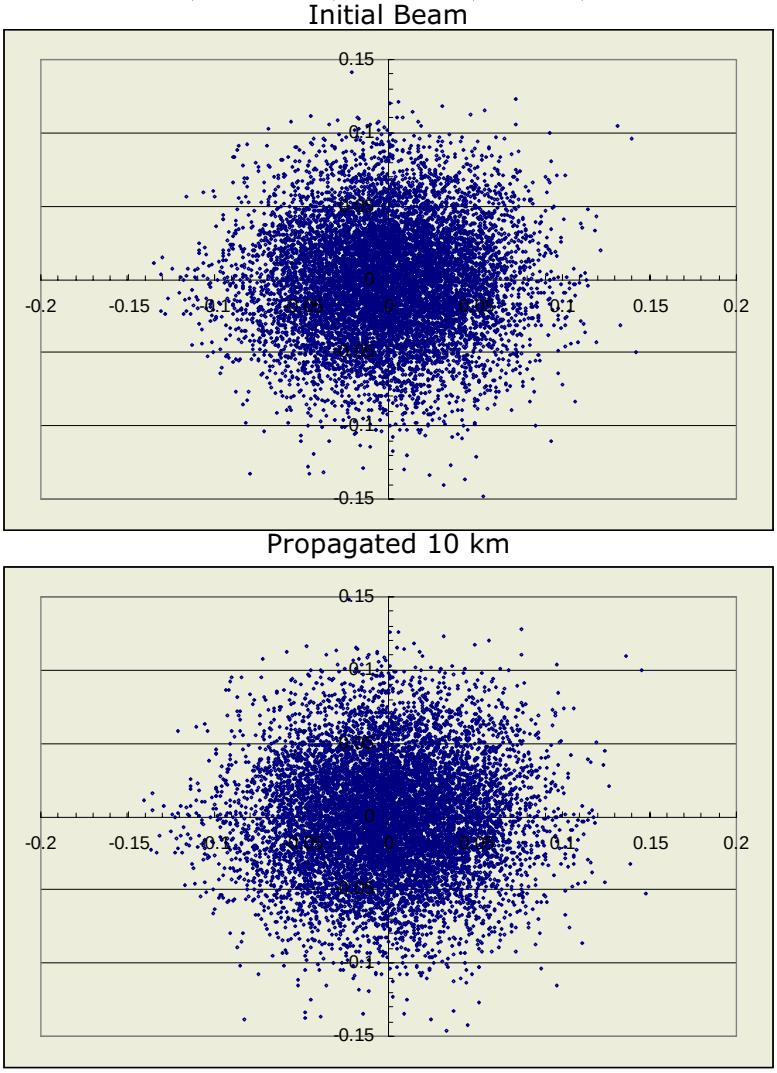

Figure 6.15: A beam propagated 10000 meters through turbulence with an initial radius of 0.075 meters. The Hufnagel-Valley model was used with C_n^2 set to $1 \cdot 10^{-13}$ at the ground and the rms wind speed to 21 meters per second. The table at the top shows the calculated radius of the beam in both the x and y directions for the initial beam and for the propagated beam. The initial beam is the graph in the middle and the propagated beam is the graph at the bottom.

6.4.2 Results for Beam Wander

When turbulence is taken into account, a new beam centroid is computed for each pulse. The position of the beam centroid is Gaussian distributed with a variance given by

$$\sigma^2 = \frac{\langle \rho_c^2 \rangle}{2}, \tag{6.1}$$

where $\langle \rho_c^2 \rangle$ is given by equation 3.46. For a plane wave with an initial diameter of 0.15 meters at a wavelength of 0.7 microns, propagating a distance of 2 kilometers straight down the short-term beam centroid is equal to $1.2 \cdot 10^{-5}$ meters. Therefore, the Gaussian plane wave variance is $6.0 \cdot 10^{-6}$ meters squared. Ten thousand beam centroid positions were randomly generated based on a variance of $6.0 \cdot 10^{-6}$ meters squared. Figure 6.16 is a histogram of the x positions and Figure 6.17 is a histogram of the y positions. The calculated variance in the x positions, $5.82 \cdot 10^{-6}$, and in the y positions, $6.01 \cdot 10^{-6}$, are close to the expected value of $6.0 \cdot 10^{-6}$. Figure 6.18 is a scatter plot of the ten thousand points showing that the points are distributed evenly in the x, y plane.

Mean	-3.67375E-05
Standard Error	2.41274E-05
Median	-3.00467E-06
Mode	-0.00111582
Standard Deviation	0.002412736
Sample Variance	5.82129E-06
Kurtosis	0.017735617
Skewness	-0.038043049
Range	0.01877895
Minimum	-0.00920009
Maximum	0.00957886
Sum	-0.367374846
Count	10000
Confidence Level(95.0%)	4.72945E-05

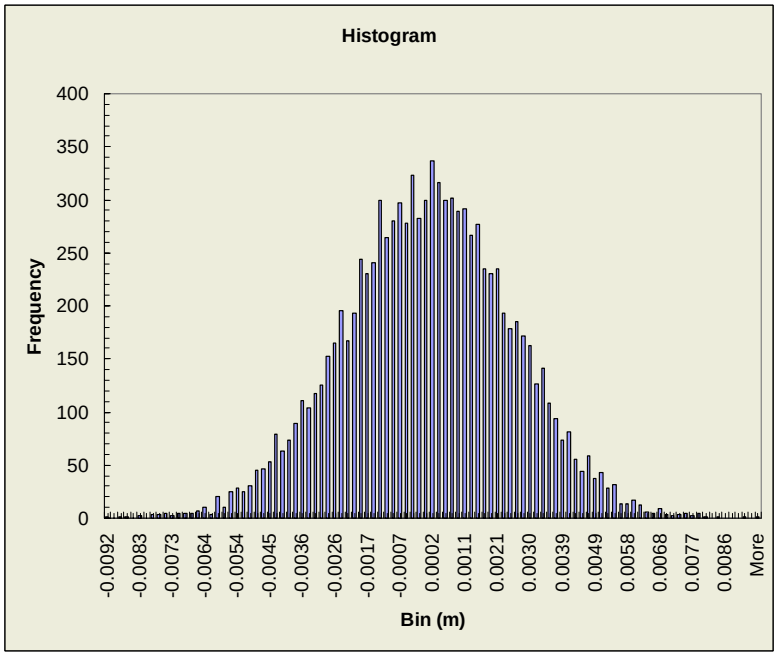

Figure 6.16: The histogram of the x positions of ten thousand randomly generated beam centroid positions based on a variance of $6.0 \cdot 10^{-6}$. The histogram is Gaussian and has a variance of $5.82 \cdot 10^{-6}$.

Mean	2.80354E-05
Standard Error	2.45182E-05
Median	3.41285E-05
Mode	-0.00153906
Standard Deviation	0.00245182
Sample Variance	6.01142E-06
Kurtosis	0.045816892
Skewness	0.033708901
Range	0.0188667
Minimum	-0.00923638
Maximum	0.00963032
Sum	0.280354043
Count	10000
Confidence Level(95.0%)	4.80606E-05

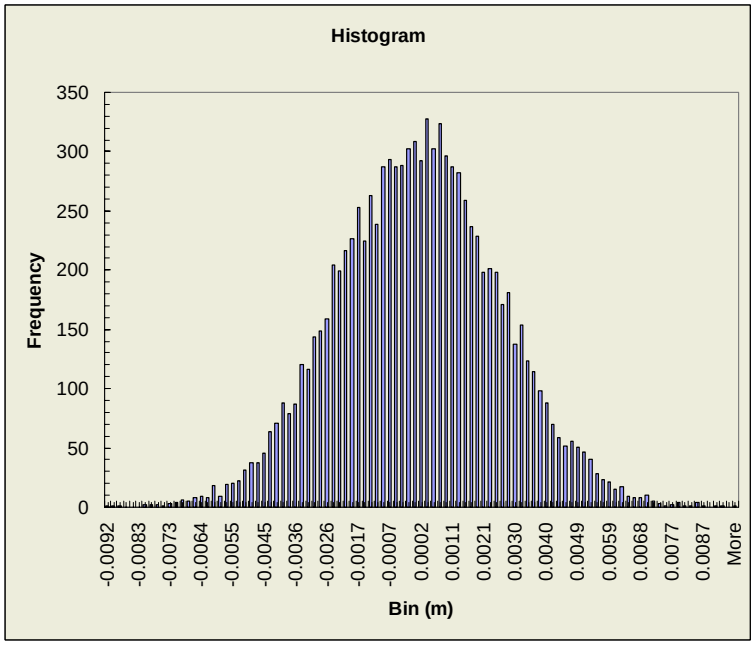

Figure 6.17: The histogram of the y positions of ten thousand randomly generated beam centroid positions based on a variance of $6.0 \cdot 10^{-6}$. The histogram is Gaussian and has a variance of $6.01 \cdot 10^{-6}$.

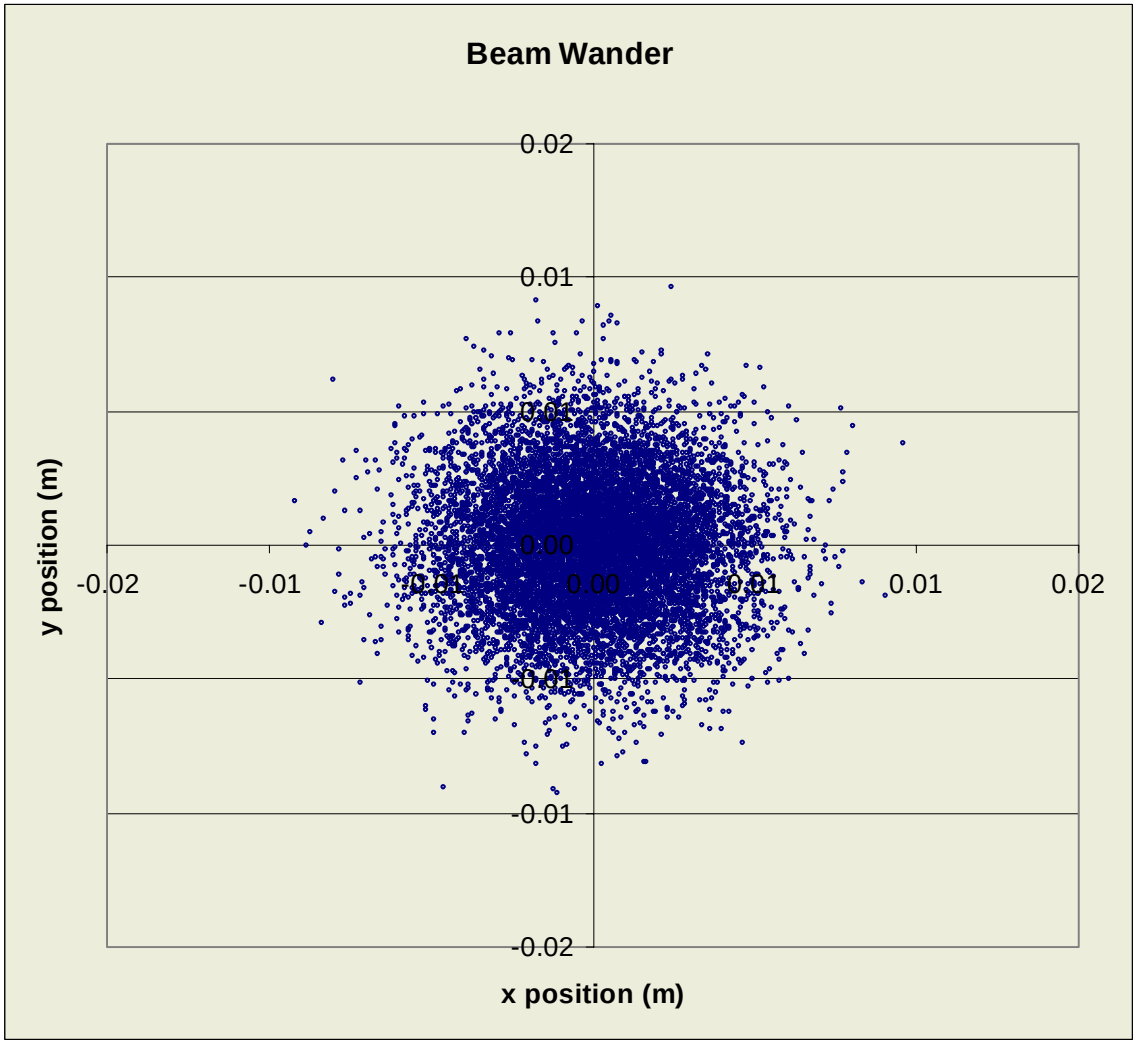

Figure 6.18: A scatterplot of ten thousand randomly generated beam centroid positions based on a variance of $6.0 \cdot 10^{-6}$. The generated positions are randomly distributed in the x, y plane.

6.4.3 Results for Image Dancing

The random shift of the return in the focal plane, image dancing, is calculated using equation 3.49. Ten thousand shifts were randomly generated based on a variance of $2.51 \cdot 10^{-11}$ meters squared. Figure 6.19 is a scatterplot of the random shifts. The calculated variance in the x positions, $2.55 \cdot 10^{-11}$,and in the y positions, $2.55 \cdot 10^{-11}$, are close to the expected value of $2.51 \cdot 10^{-11}$.

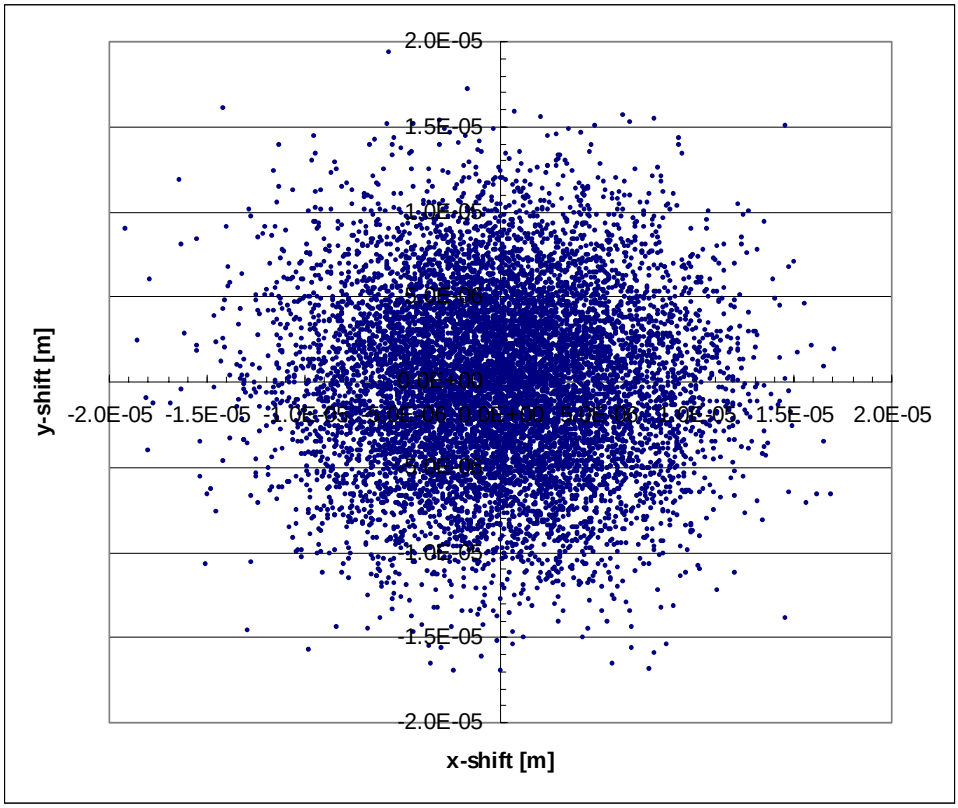

Calculated variance [m^2]
2.51405E-11

x_stats	
Mean	-1.64777E-08
Standard Error	5.05197E-08
Median	5.94688E-09
Mode	0.000010221
Standard Deviation	5.05197E-06
Sample Variance	2.55224E-11
Kurtosis	-0.023025927
Skewne	-0.013904998
Range	3.62757E-05
Minimum	-0.000019178
Maximum	1.70977E-05
Sum	-0.000164777
Count	10000

y_stats	
Mean	2.45522E-08
Standard Error	5.0492E-08
Median	6.78195E-08
Mode	2.74724E-06
Standard Deviation	5.0492E-06
Sample Variance	2.54944E-11
Kurtosis	-0.03389924
Skewne	-0.016152776
Range	3.96647E-05
Minimum	-2.02555E-05
Maximum	1.94092E-05
Sum	0.000245522
Count	10000

Figure 6.19: A scatterplot of ten thousand randomly generated shifts in the focal plane based on a variance of $2.51 \cdot 10^{-11}$. The generated positions are randomly distributed in the x, y plane.

6.4.4 Results for Image Blur

The blurring of the image in the focal plane for multiple pulses is defined by the long-term modulation transfer function (MTF) given in equation 3.47. This equation accounts for both image blurring and image dancing. Since DIRSIG calculates the return on a pulse-to-pulse basis, the long-term MTF is not appropriate and the short-term MTF as defined by equation 3.48 is used instead. As Figure 6.20 shows, the short-term MTF does not go to zero at high frequencies because it does not account for the effects of diffraction. Therefore, the short-term MTF is multiplied by the MTF due to diffraction, resulting in the total short-term MTF. The total short-term MTF is shown also in Figure 6.20. The total short-term MTF is the MTF DIRSIG applies to the image.

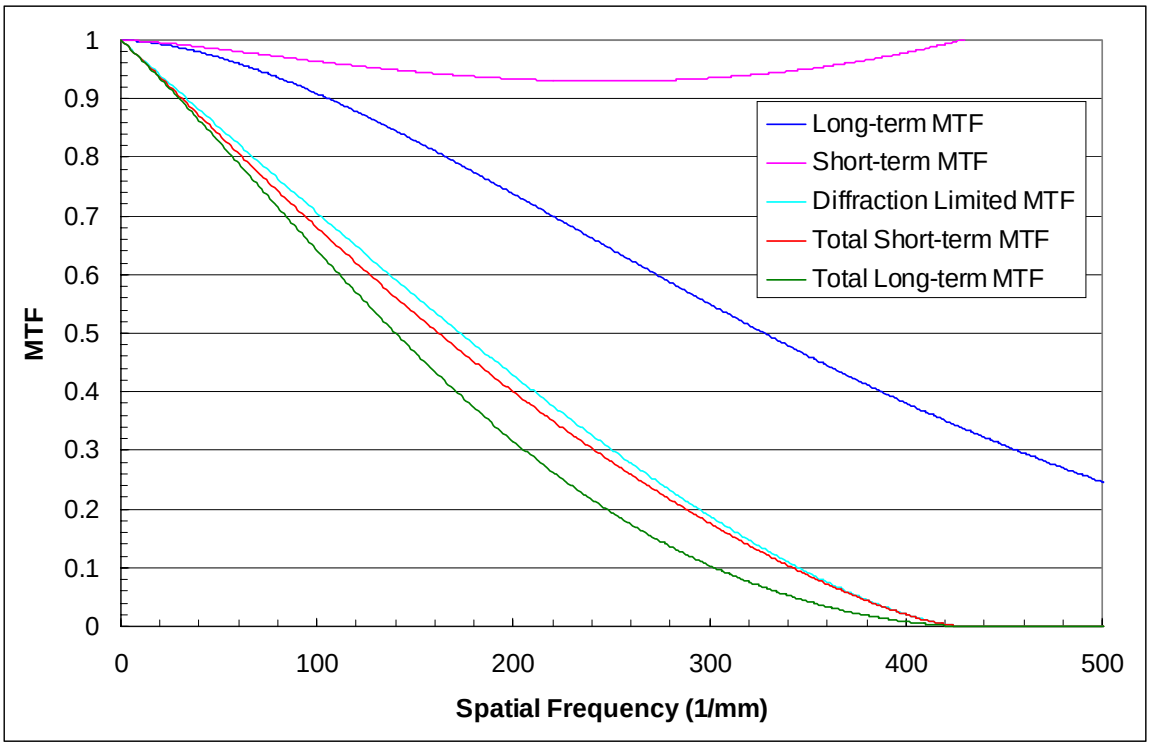

Figure 6.20: Sample long-term, short-term, diffraction-limited, total long-term, and total short-term MTF calculations. The long-term MTF is appropriate for many pulses averaged together and takes into account both image blurring and image dancing. The short-term MTF is appropriate for a single pulse and does not take into account image dancing. The short-term MTF does not go to zero at high frequencies because it does not account for diffraction. The total short-term MTF that is applied to the image is the multiplication of the short-term MTF and the MTF due to diffraction.

6.5 Initial Images

To demonstrate that the code was working, to identify any problems, and to give some examples of how the code can be used, several test images were generated. Section 6.1 already showed an example DIRSIG image generated by simulating a DIAL system and Section 6.3 showed an example DIRSIG intensity image that contained multiple bounced photons. The first test image was a simple rectangular box. This test image was used to determine if DIRSIG could generate a datacube with the aerosol layers turned on. Figure 6.21 shows a terrain map generated from this test scene. The terrain map was produced by assigning a range value to each pixel. The leading edge of the topographic return begins at the topographic range. Therefore, the range assigned to each pixel was calculated by determining the minimum of each curve before the topographic maximum, as shown in Figure 6.22. Figures 6.23 and 6.24 show intensity slices of the same datacube. The early slices show the profile of the beam. Once the pulse hits the top of the box, the rest of the return dims in comparison. After the return from the top of the box fades away the rest of the return is again visible. Notice the image all the way on the right in the fourth row from the top. There is a dark line around the box. The dark line is a shadow due to the light source being directly above the center of the box.

The next test scenes were of a tank resting on a flat plate and a tank under a camouflage net resting on a flat plate. Figures 6.25 through 6.28 show intensity slices of these two simulations. The range gating was working as expected, but the resulting leading edge images were noisy because the temporal width of the pulse was too broad, as shown in Figure 6.29. The tank-under-camouflage scene was generated again, this time with a temporal pulse width of approximately one-third of a meter. The resulting intensity slices are shown in Figures 6.30 through 6.32. Because the temporal width of the pulse was now shorter

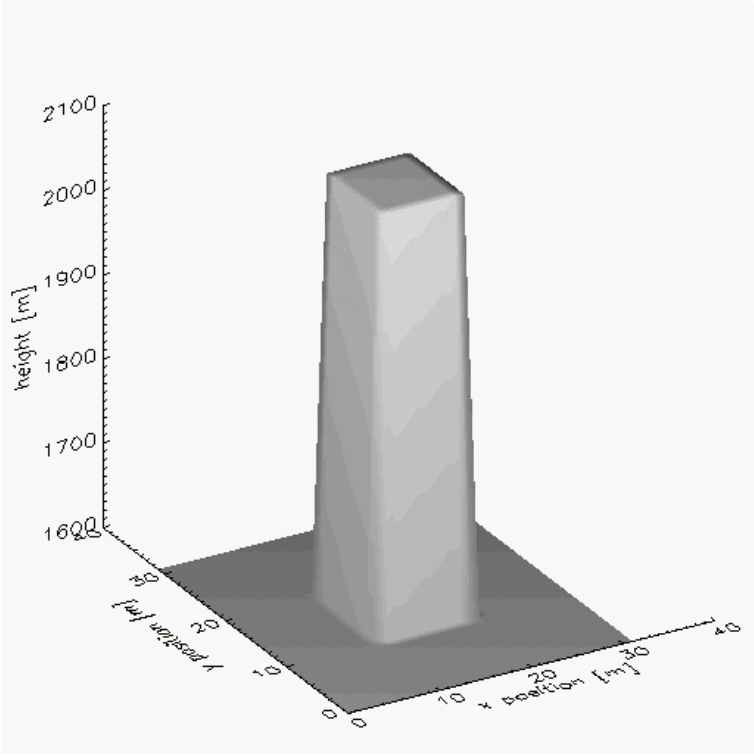

Figure 6.21: An example terrain map generated from DIRSIG data. The scene was a simple rectangular box. This test image was used to determine if DIRSIG could generate a datacube with the aerosol layers turned on.

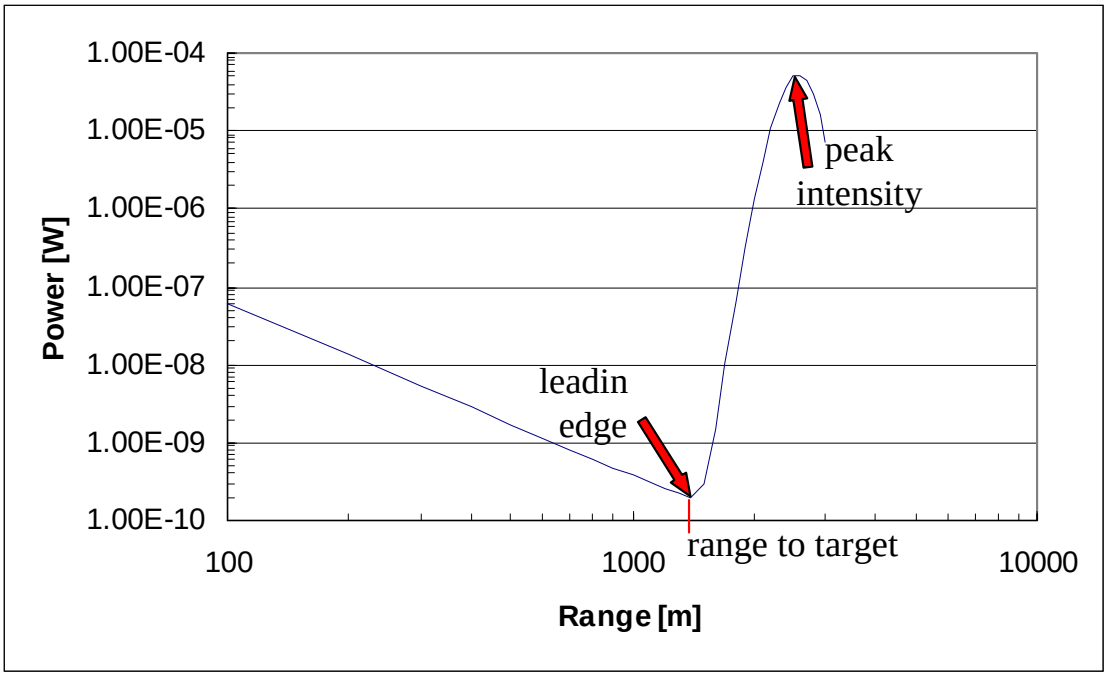

Figure 6.22: The leading edge of the topographic return begins at the topographic range. The range assigned to each pixel in the sample terrain maps is calculated by determining the range at which the leading edge occurs.

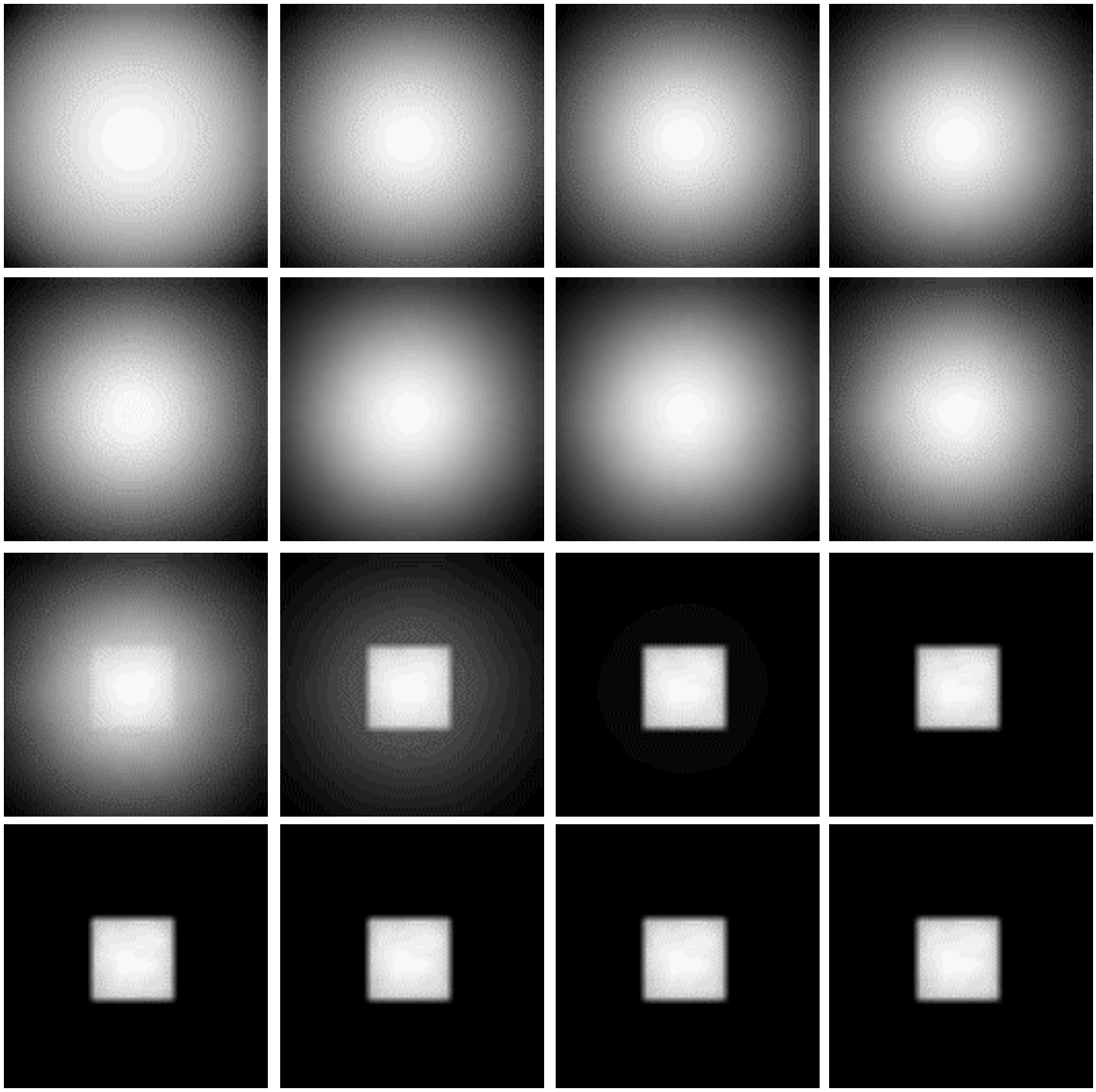

Figure 6.23: The initial intensity slices of the simple rectangular box datacube. As expected, the early slices show the profile of the beam. Once the pulse hits the top of the box, the rest of the return dims in comparison.

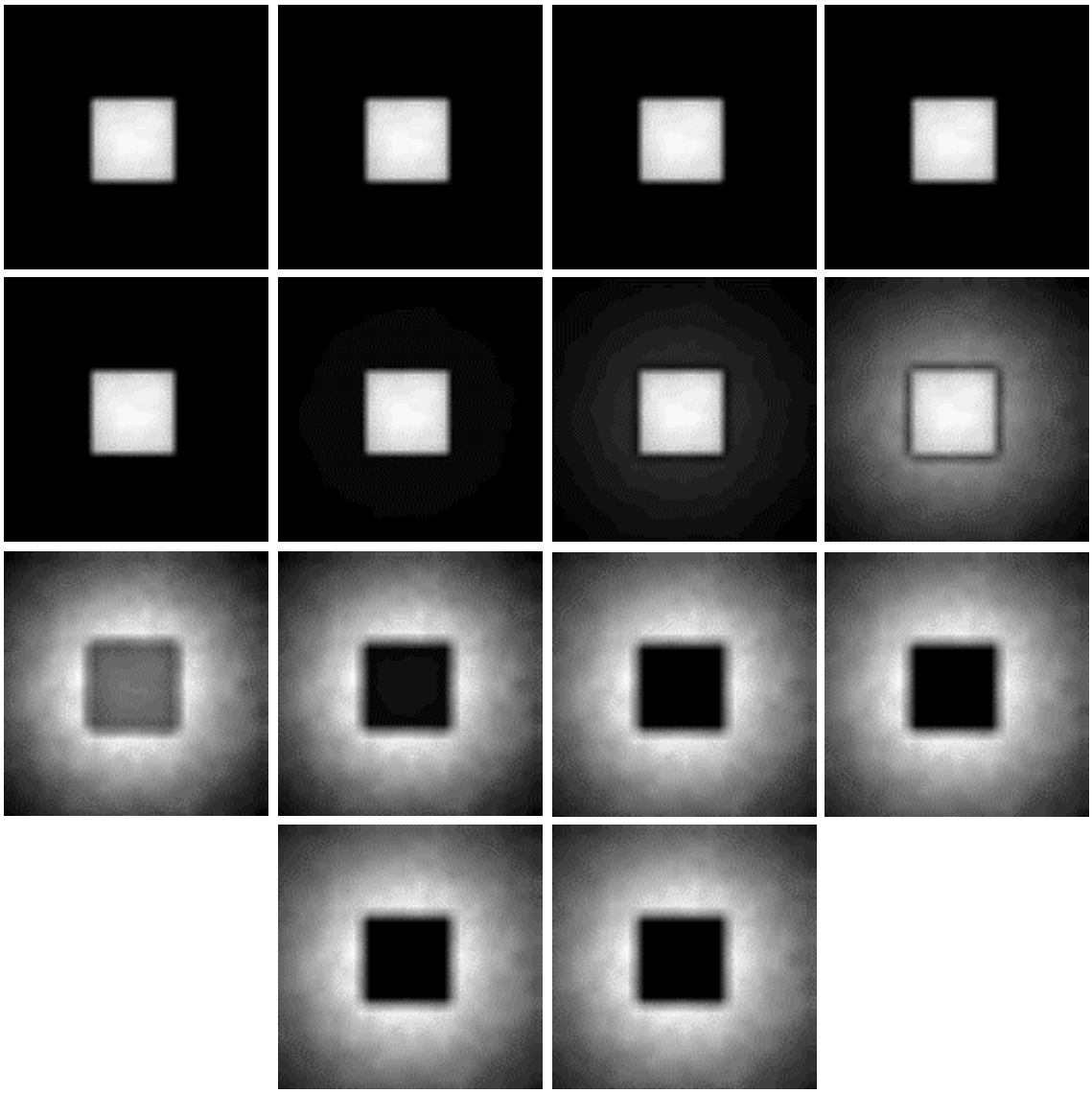

Figure 6.24: The remaining intensity slices of the simple rectangular box datacube. After the return from the top of the box fades away, the rest of the return is again visible.

than the separation between the tank and the camouflage, the return from the camouflage could be distinguished from the return from the tank, as shown in Figure 6.33. The datacube processing was modified for the tank-under-camouflage scene to account for multiple peaks in the return. To process the datacube, the position of the highest peak was found first. Next, the data was checked to see if the signal kept decreasing after the first peak or if a second peak existed. If a second peak existed, the position of the first peak was discarded and the position of the second peak was retained. The resulting image is shown in Figure 6.34 along with the intensity image generated from the first peak alone.

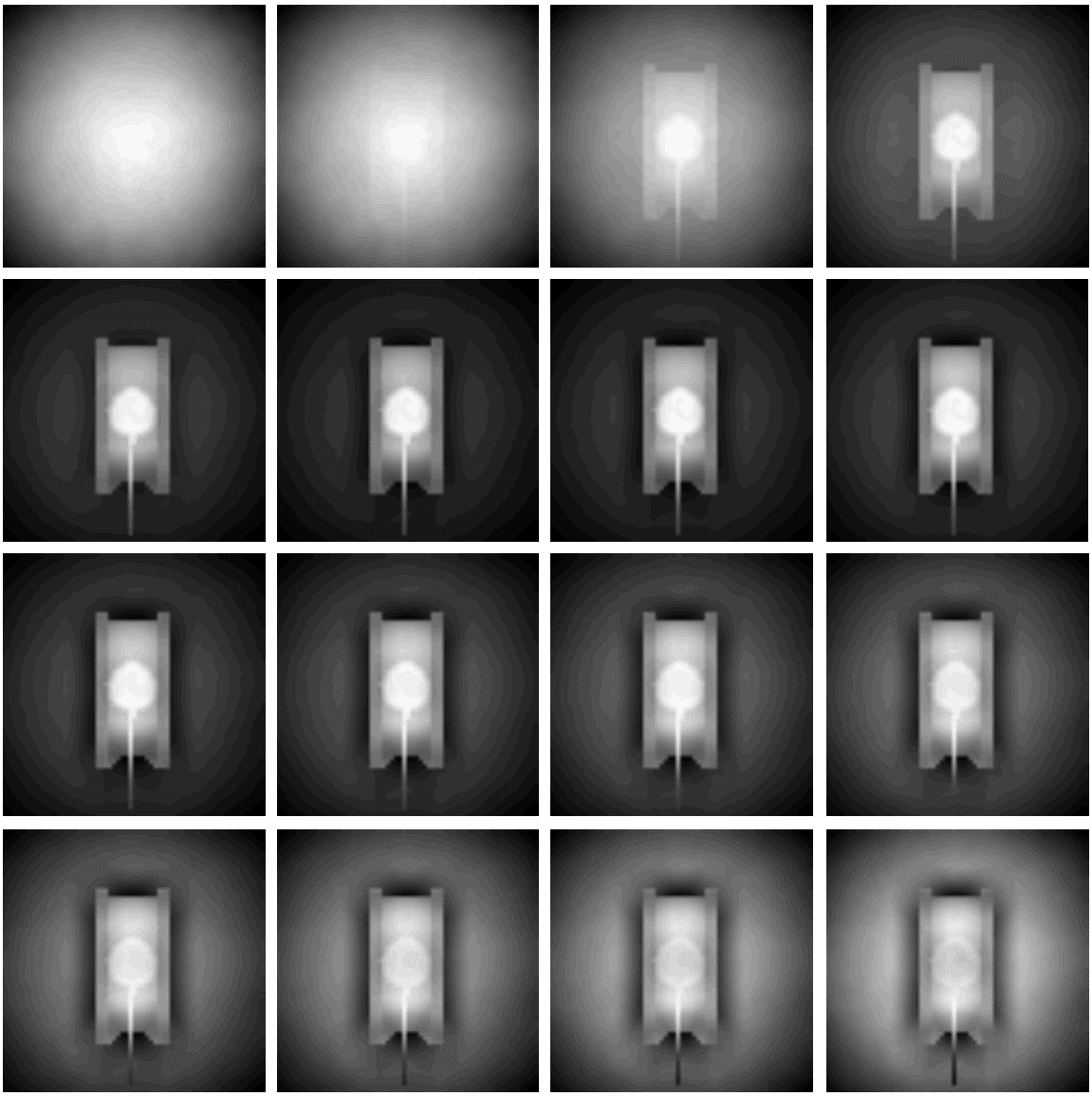

Figure 6.25: The initial intensity slices of a tank resting on a flat plate. As expected, the early slices show the profile of the beam. Once the top of the tank is hit, the rest of the return dims in comparison. As the return from the tank begins to fade, the rest of the return is again visible.

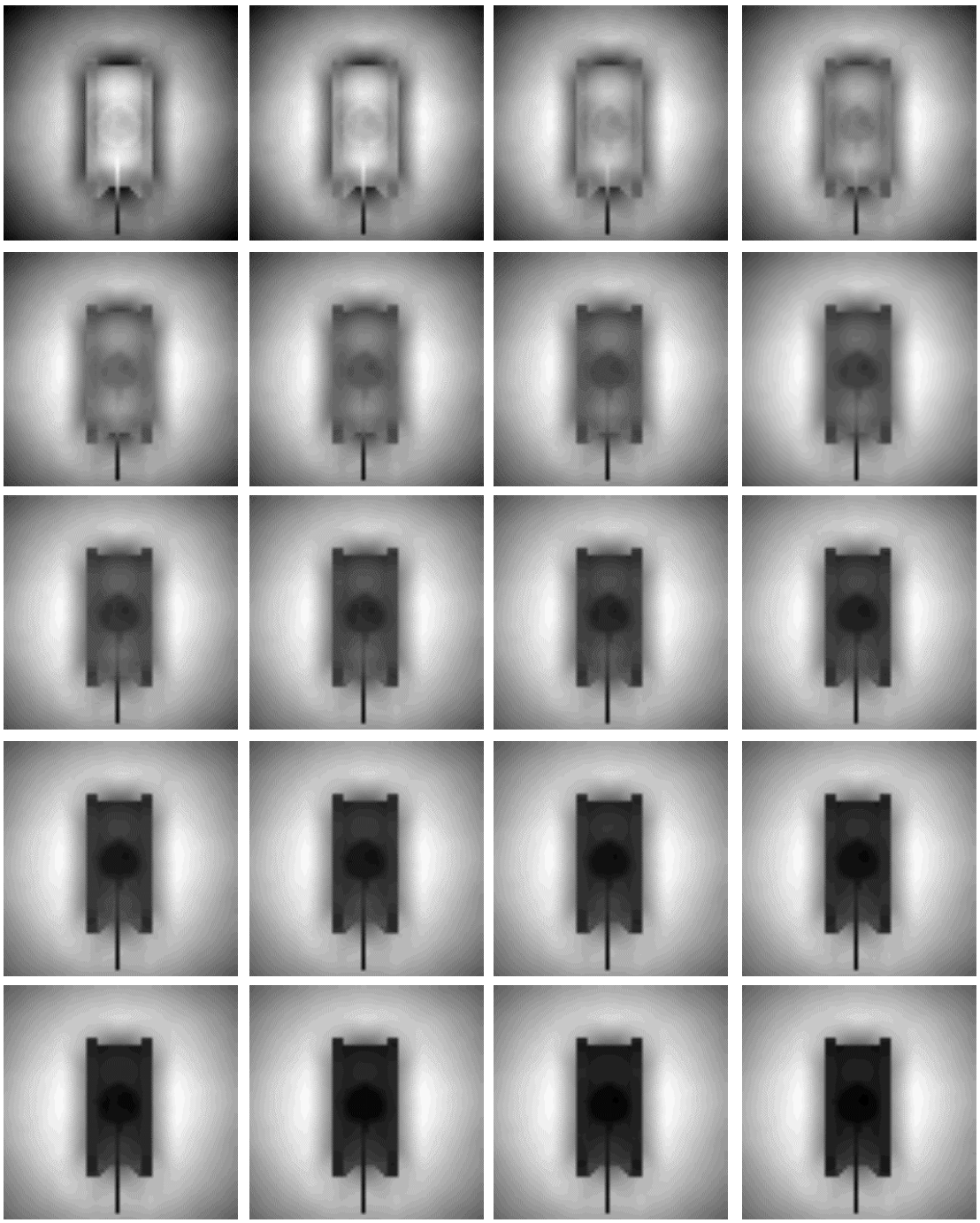

Figure 6.26: The remaining intensity slices of a tank resting on a flat plate. The return from the tank continues to fade.

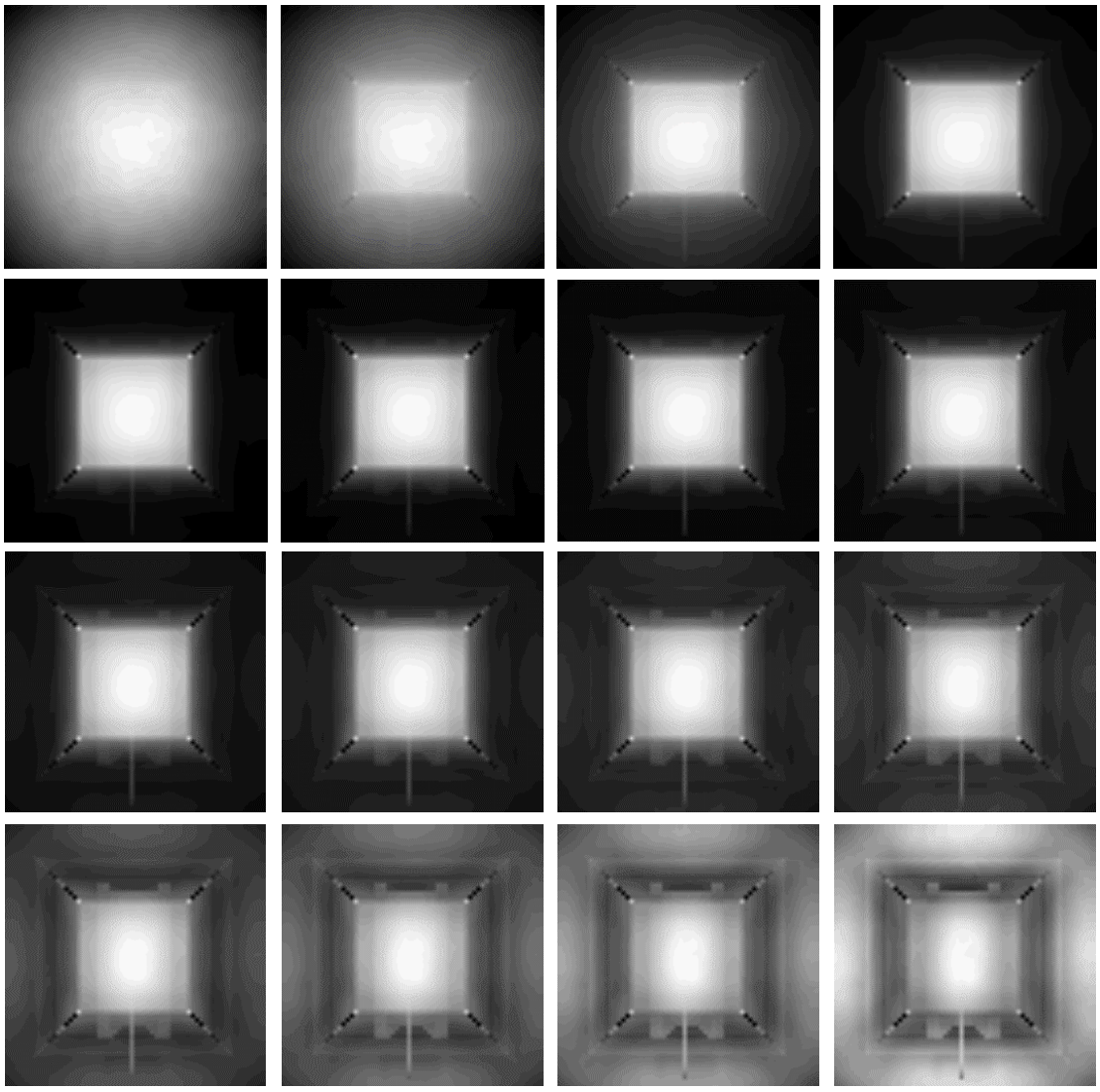

Figure 6.27: The initial intensity slices of a tank under camouflage resting on a flat plate. As expected, the early slices show the profile of the beam. Once the top of the camouflage is hit, the rest of the return dims in comparison. The portions of the tank which are not under the camouflage are easily visible. The general outline of the tank is visible, but no details are discernable. As the return from the camouflage begins to fade, the rest of the return is again visible.

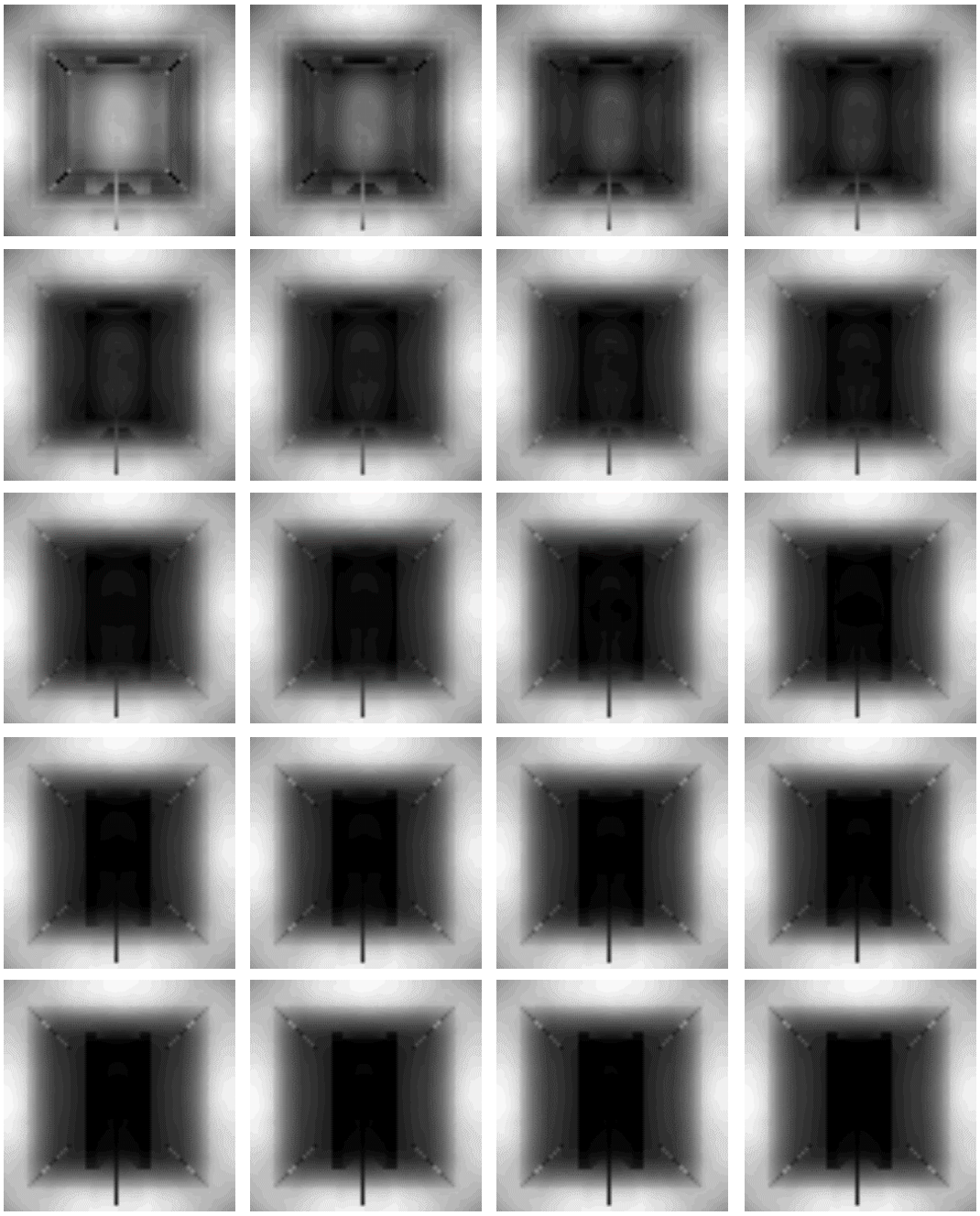

Figure 6.28: The remaining intensity slices of a tank under camouflage resting on a flat plate. The return from the camouflage continues to fade.

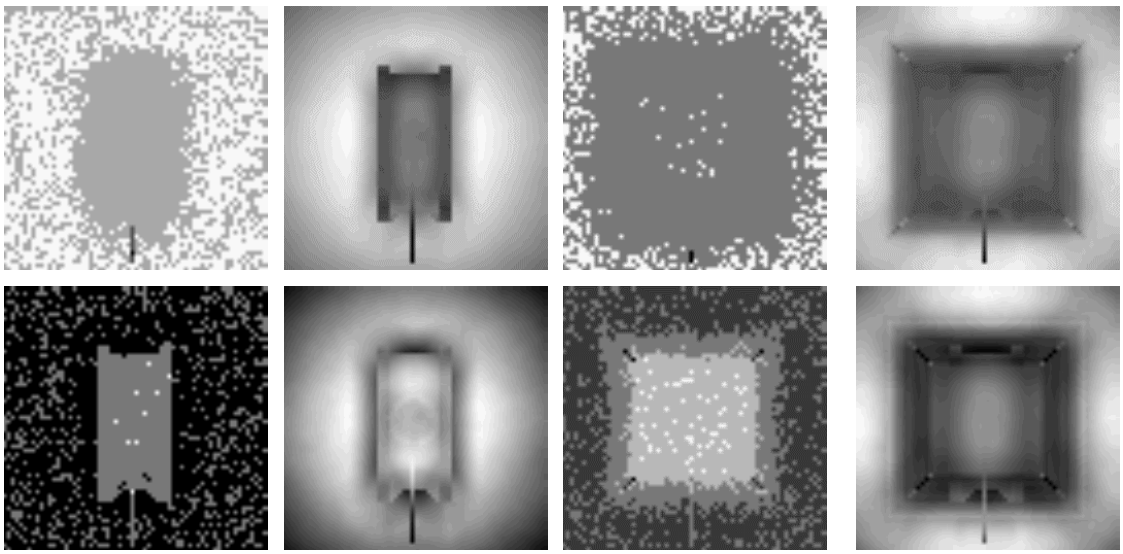

Figure 6.29: The temporal width of the pulse can affect the ability to recover an object. Two different scenes were imaged: a tank on a flat plate and a tank under camouflage on a flat plate. The first row of images were produced with a broad temporal pulse. The second and last columns are intensity images produced by detecting the leading edge of the pulse. The first and third columns are range images produced by detecting the leading edge of the pulse. The range images in the first row are very noisy because the width of the pulse is broader than the distance between the top of the tank and the ground. The images in the second row were produced with a temporal pulse that was less broad and the resulting range images are less noisy and show more gray values. The pulse width was still too broad to distinguish between the return from the camouflage and the return from the tank.

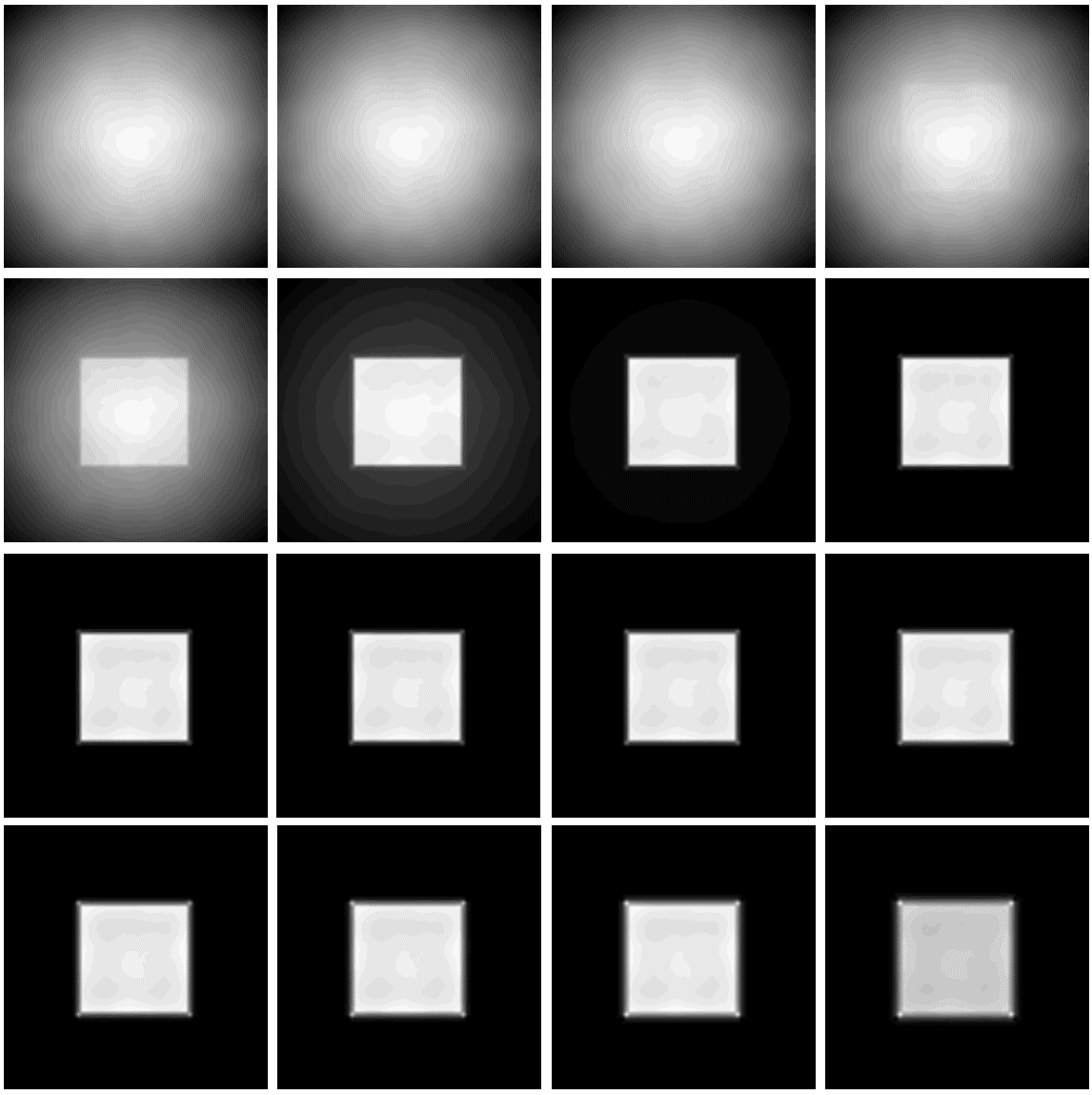

Figure 6.30: The initial intensity slices of a tank under camouflage resting on a flat plate produced with a narrower pulse. As expected, the early slices show the profile of the beam. Once the top of the camouflage is hit, the rest of the return dims in comparison.

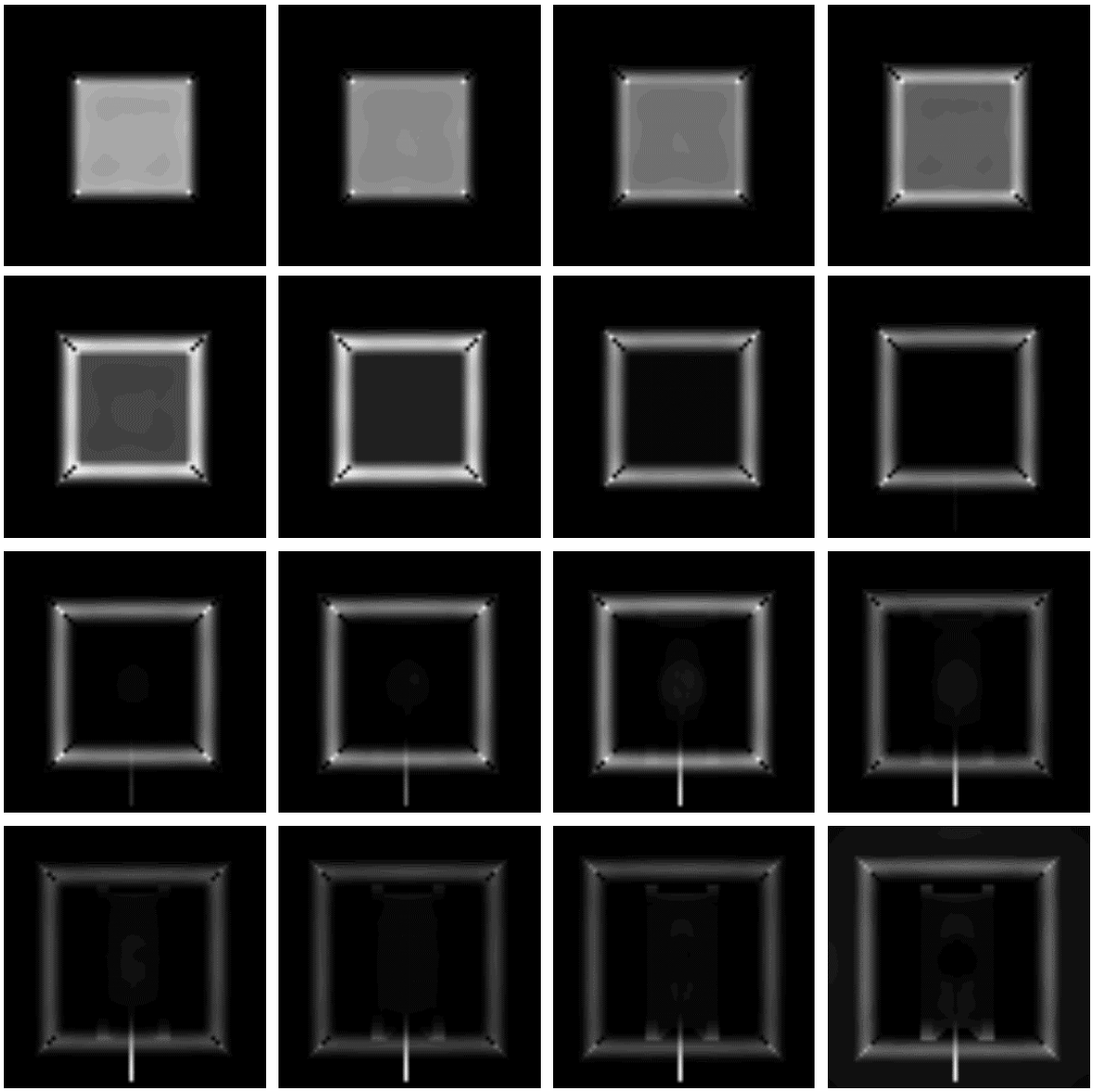

Figure 6.31: The subsequent intensity slices of a tank under camouflage resting on a flat plate produced with a narrower pulse. Once the bright return from the top of the camouflage begins to dim the sides of the camouflage begin to brighten. The bright return expands outward as it "walks" down the side of the camouflage. The portions of the tank that are not under the camouflage are easily visible.

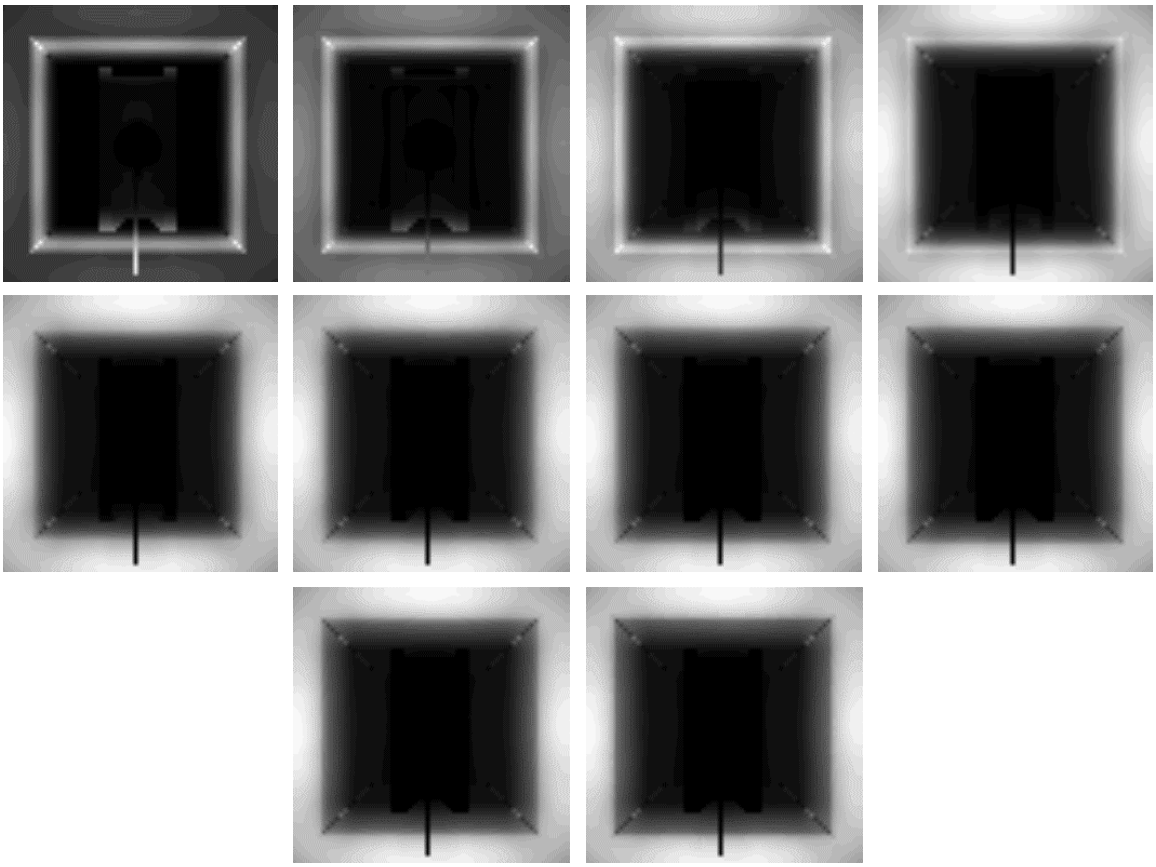

Figure 6.32: The remaining intensity slices of a tank under camouflage resting on a flat plate produced with a narrower pulse. The general outline of the tank is visible, but no details are discernable. As the return reaches the bottom of the camouflage, the return from the ground begins to brighten.

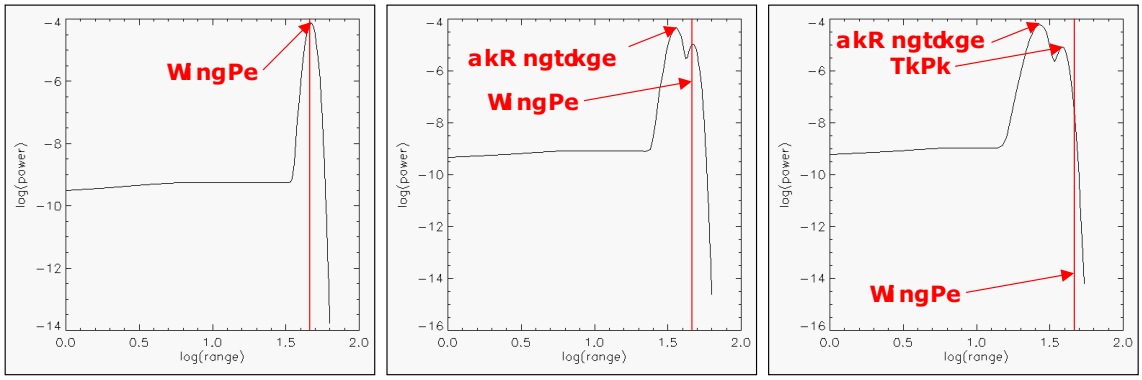

Figure 6.33: The power as a function of range for various pixels. The first graph shows the return from a pixel that only contained the ground, the second graph shows the return from a pixel containing both camouflage and the ground, and the final graph shows the return from a pixel containing both camouflage and the tank. Because the temporal pulse width is narrow, the returns containing more than one object show two peaks.

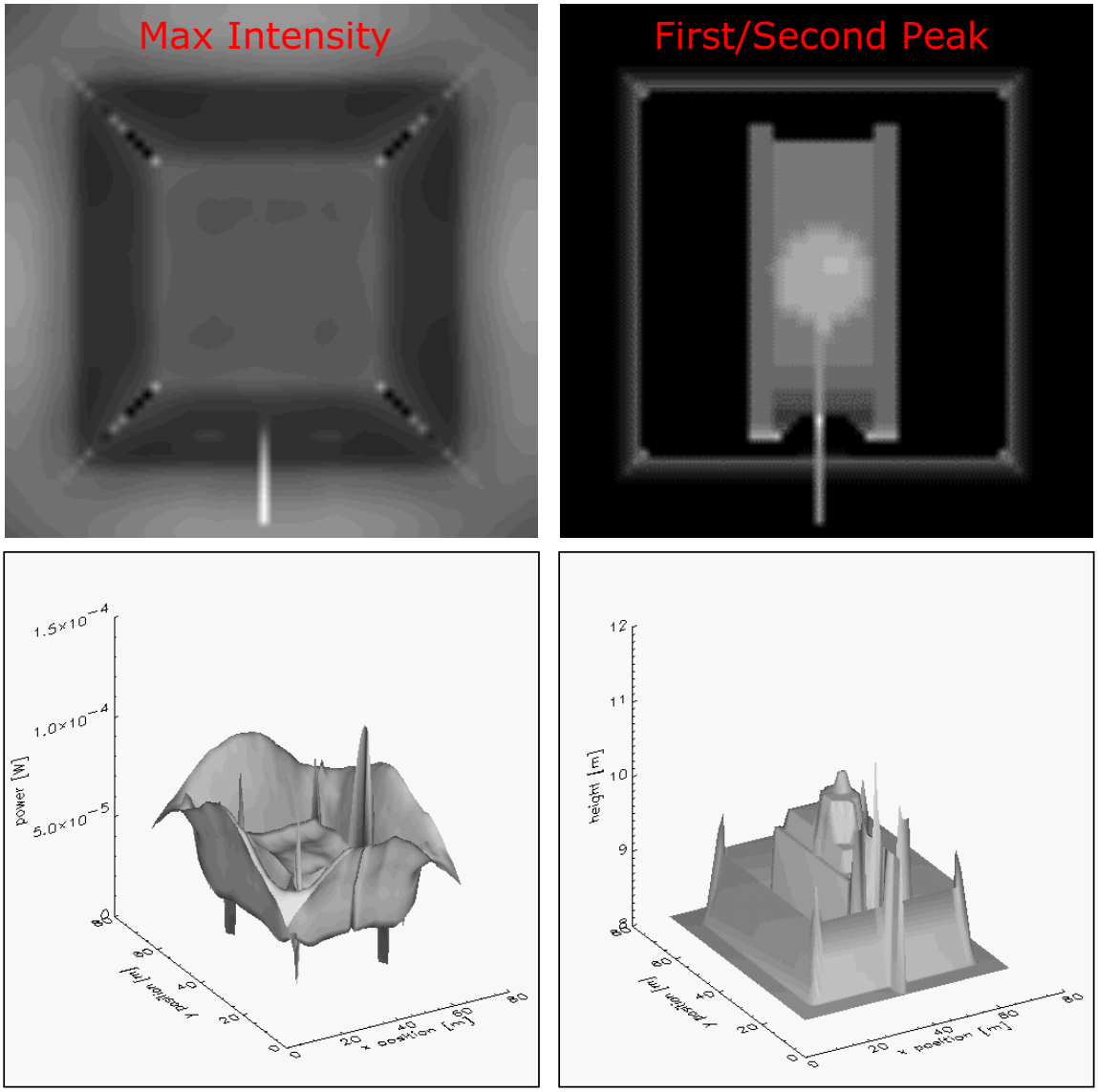

Figure 6.34: Objects hidden under camouflage or other obscurants can be imaged given a sufficiently narrow pulse width. The intensity image on the left was generated from the first peak alone. The only parts of the tank that are visible are the portions of the tank that extend beyond the camouflage. The image on the right was generated by throwing away the first peak if a second peak existed. The position of the peak was then translated into a range that was then converted into a height above the last range.

6.6 Speckle Results

DIRSIG generates a speckled image any time the beam is reflected from a topographical target and the speckle option is turned on. Figure 6.35 contains some example speckle texture patterns generated with various sized "apertures". The size of the "aperture" used by DIRSIG to generate the speckle texture pattern is determined by the technique outlined in Section 5.6. The speckle texture pattern is applied during the creation of the photon map. When each ray hits its last topographical target the texture map is queried. The texture map is produced at the focal plane, so to query the texture pattern at the object plane, the focal plane texture pattern is projected into the object plane. The intensity of the ray is then multiplied by the texture map value at that position. A sample DIRSIG intensity image exhibiting speckle with an autocorrelation several pixels wide is shown in Figure 6.36. For this example the detector integration started when the pulse left the transmitter and ended after the reflected pulse from the ground reached the detector. Therefore, the image is a measure of the total column content and is not a temporal slice.

If the size of the speckle autocorrelation is less than one pixel and each pixel is subsampled the variation in intensity due to speckle is smoothed. Figure 6.37 shows the effects of speckle averaging. All six images are of the same tank, taken with the same optical configuration. The only parameter that varies from image to image is the pixel size on the focal plane and how much subsampling occurs. The top left image is 512 pixels wide and 512 pixels high with no subsampling. For each pixel the speckle texture pattern is queried only once. The next image is 256 pixels wide and 256 pixels high with 4 subsamples per pixel. For each subsample the speckle texture pattern is queried. The resulting pixel value is the summation of the subsamples. This results in an image where the variation in intensity due to speckle is reduced because of speckle averaging. In subsequent images the number

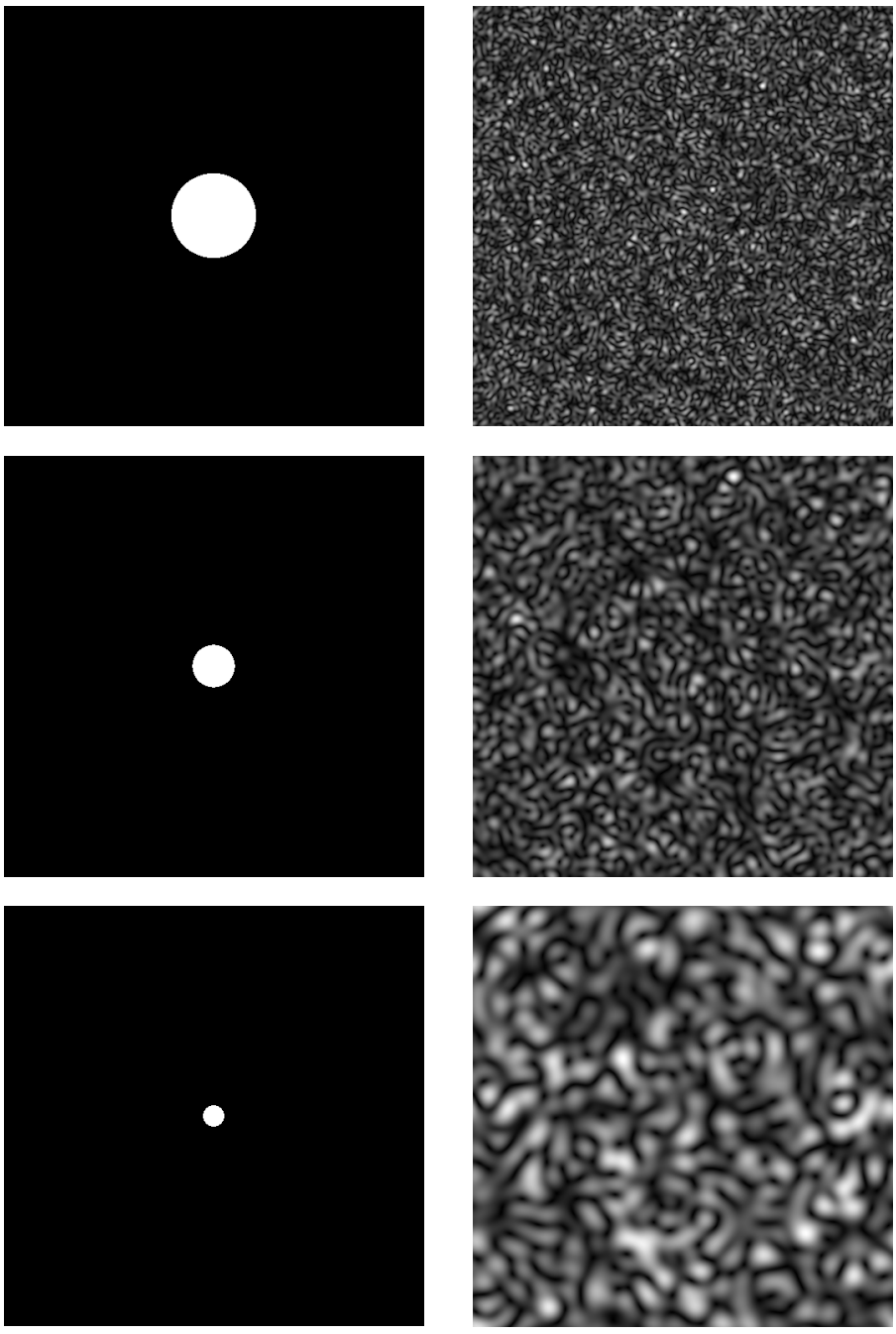

Figure 6.35: Example speckle texture patterns generated by the “apertures” on the left. on the left.

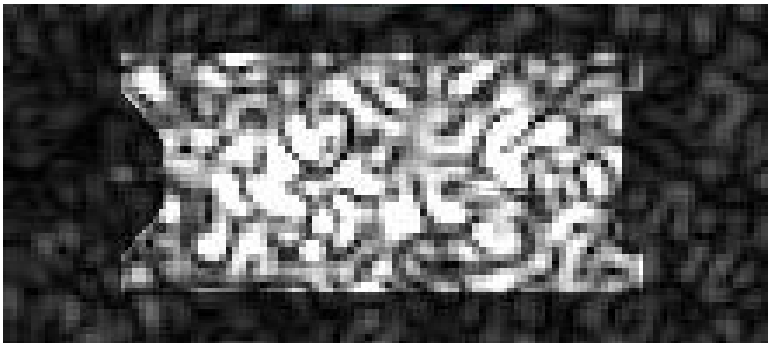

Figure 6.36: An example DIRSIG total column content intensity image that exhibits speckle with an autocorrelation several pixels wide.

of pixels is further reduced while the number of subsamples increases correspondingly. As the pixel size is increased the speckle is averaged together and the variation in intensity is reduced.

To demonstrate a speckled range-gated datacube, the tank on a flat plate and the tank under a camouflage net on a flat plate test scenes were rerun with speckle turned on. Figures 6.38 and 6.39 contain temporal slices of the tank on a flat plate speckled datacube. As Figure 6.40 shows, even with a highly speckled return an image of the tank can be recovered. Figure 6.41 through 6.43 contain temporal slices of the tank under a camouflage net on a flat plate speckled datacube. Again the tank is recoverable, but the resulting three dimensional model contains quite a bit of noise, as shown in Figure 6.44.

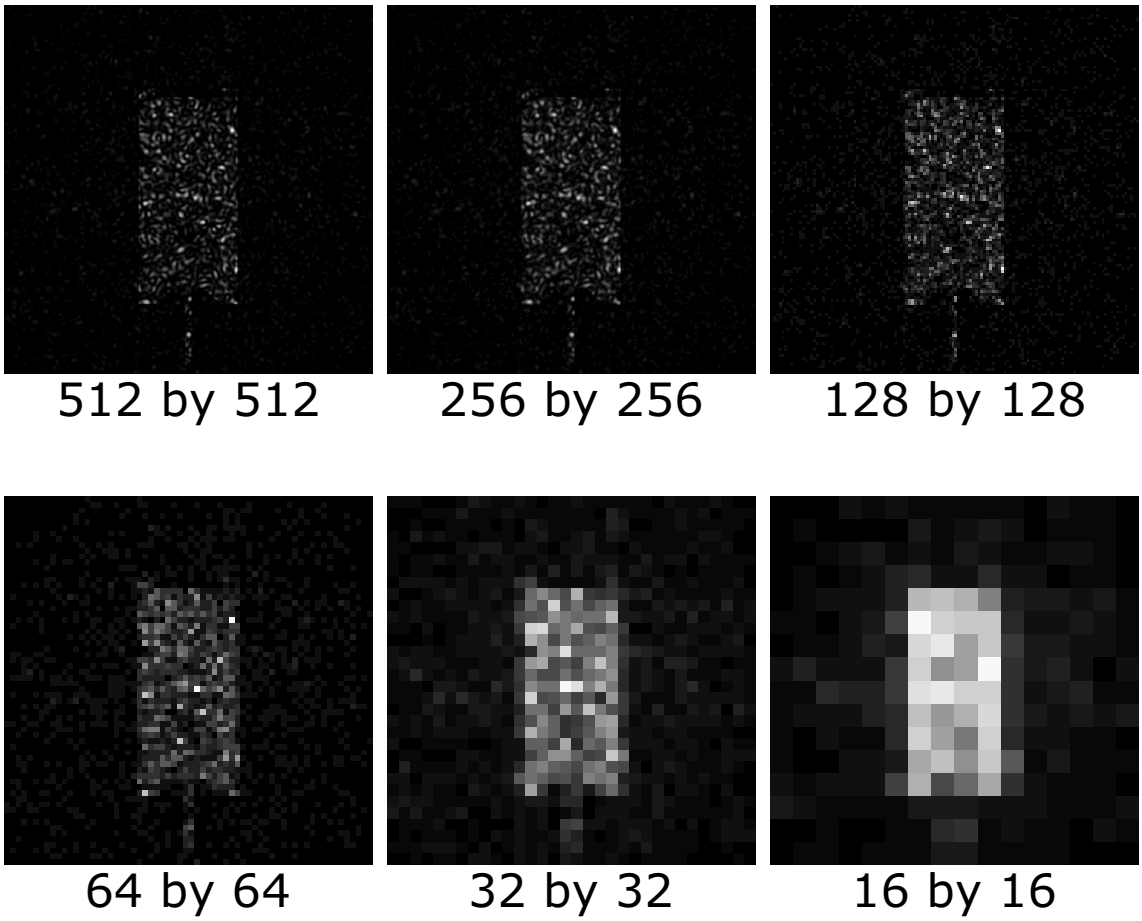

Figure 6.37: The effects of speckle averaging. In the top left image there are 512×512 pixels. The autocorrelation of the speckle is larger than the pixel size in this image. In each subsequent image the number of pixels is reduced while the overall size of the detector is kept constant. The bigger pixels are then subsampled to created the resulting image. When the pixel size becomes larger than the autocorrelation of the speckle, the speckles are averaged together and the variation in intensity is reduced.

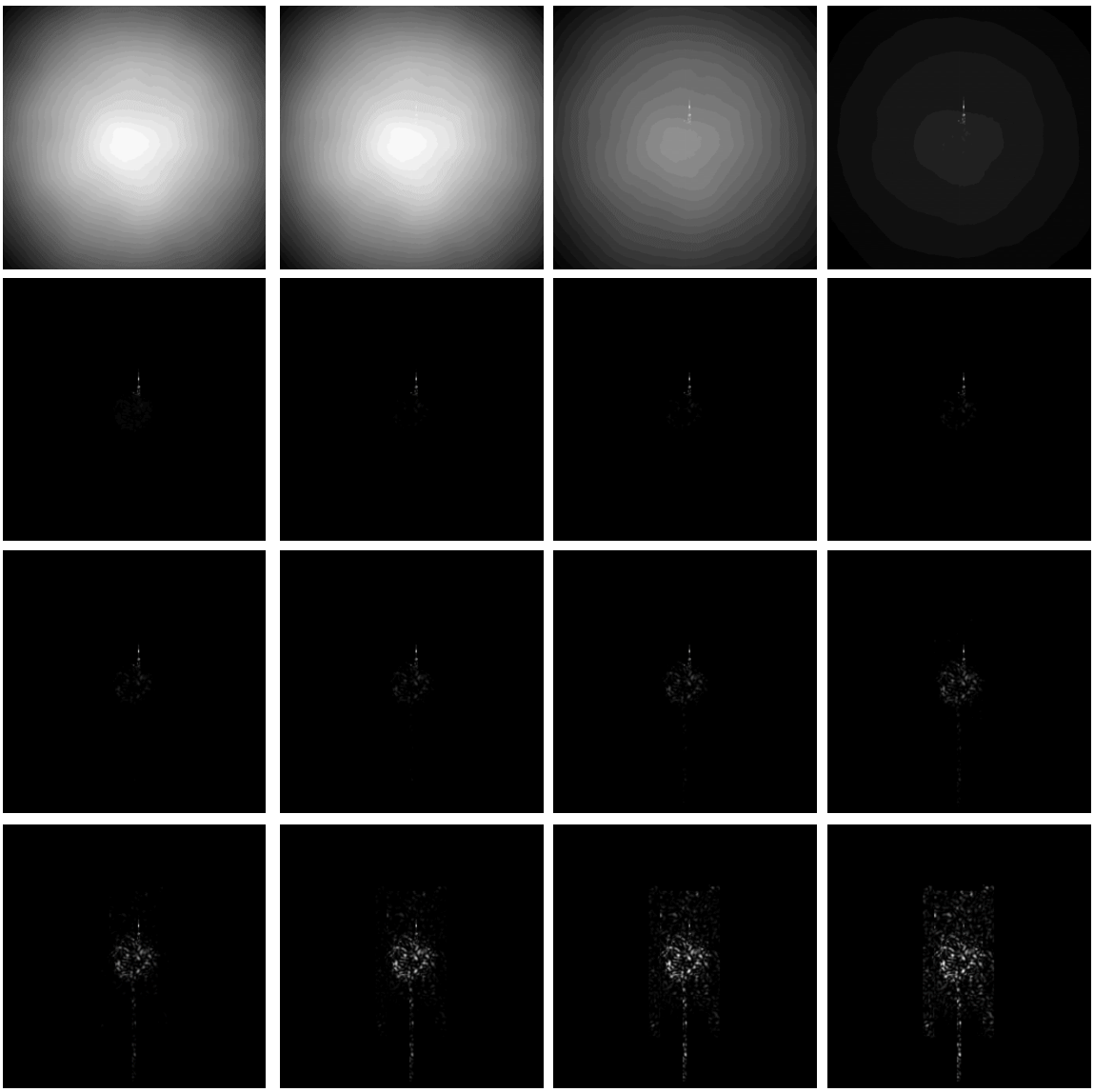

Figure 6.38: The initial speckled intensity slices of a tank under camouflage resting on a flat plate. As expected, the early slices show the profile of the beam. These early return do not contain speckle because the pulse has yet to reflect off of a hard target. Once the top of the tank is hit, the rest of the return dims in comparison and only the speckled tank is observed.

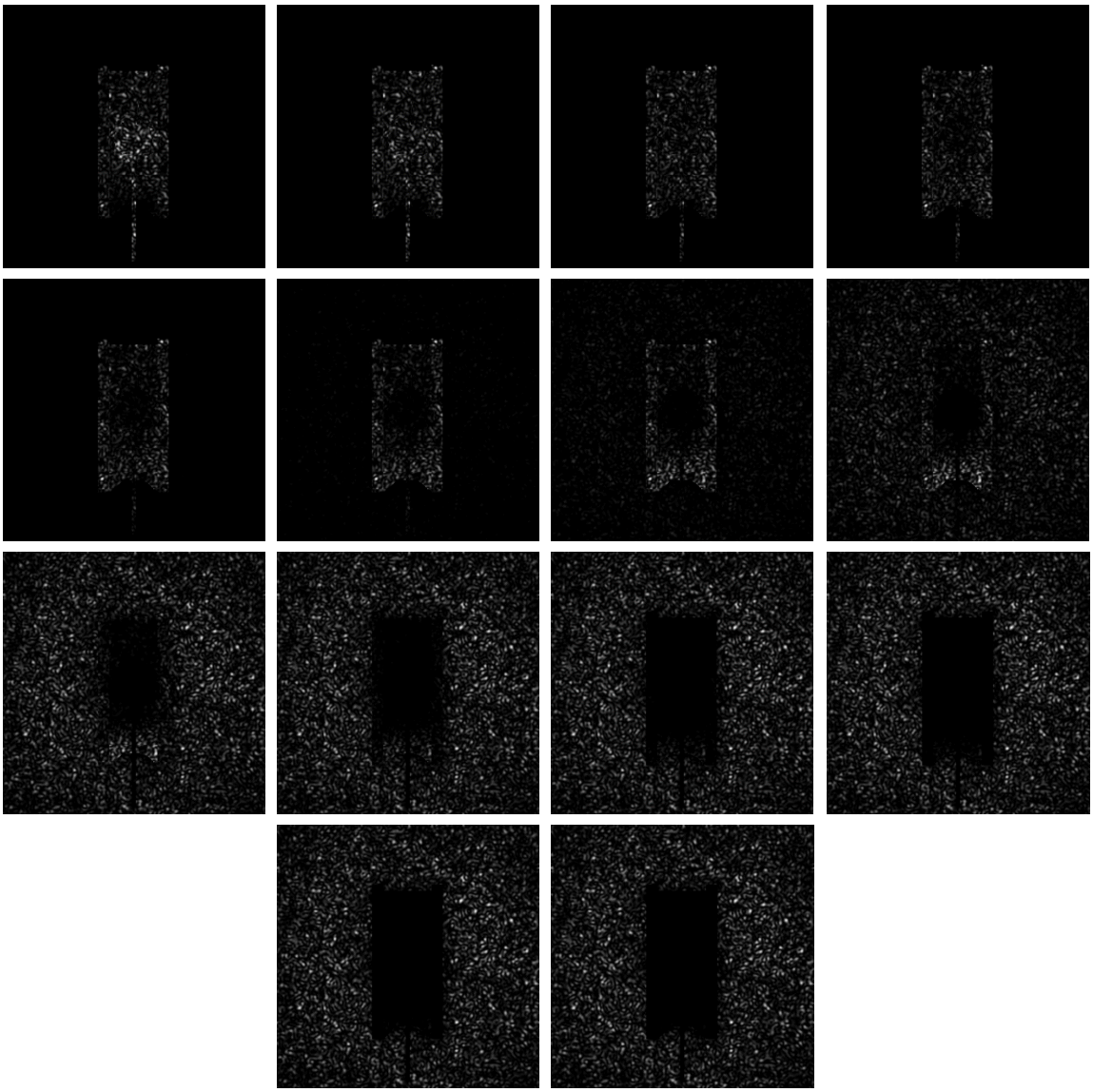

Figure 6.39: The remaining speckled intensity slices of a tank under camouflage resting on a flat plate. As the return from the tank begins to fade, the rest of the return is again visible, but now speckled due to reflection from the flat plate.

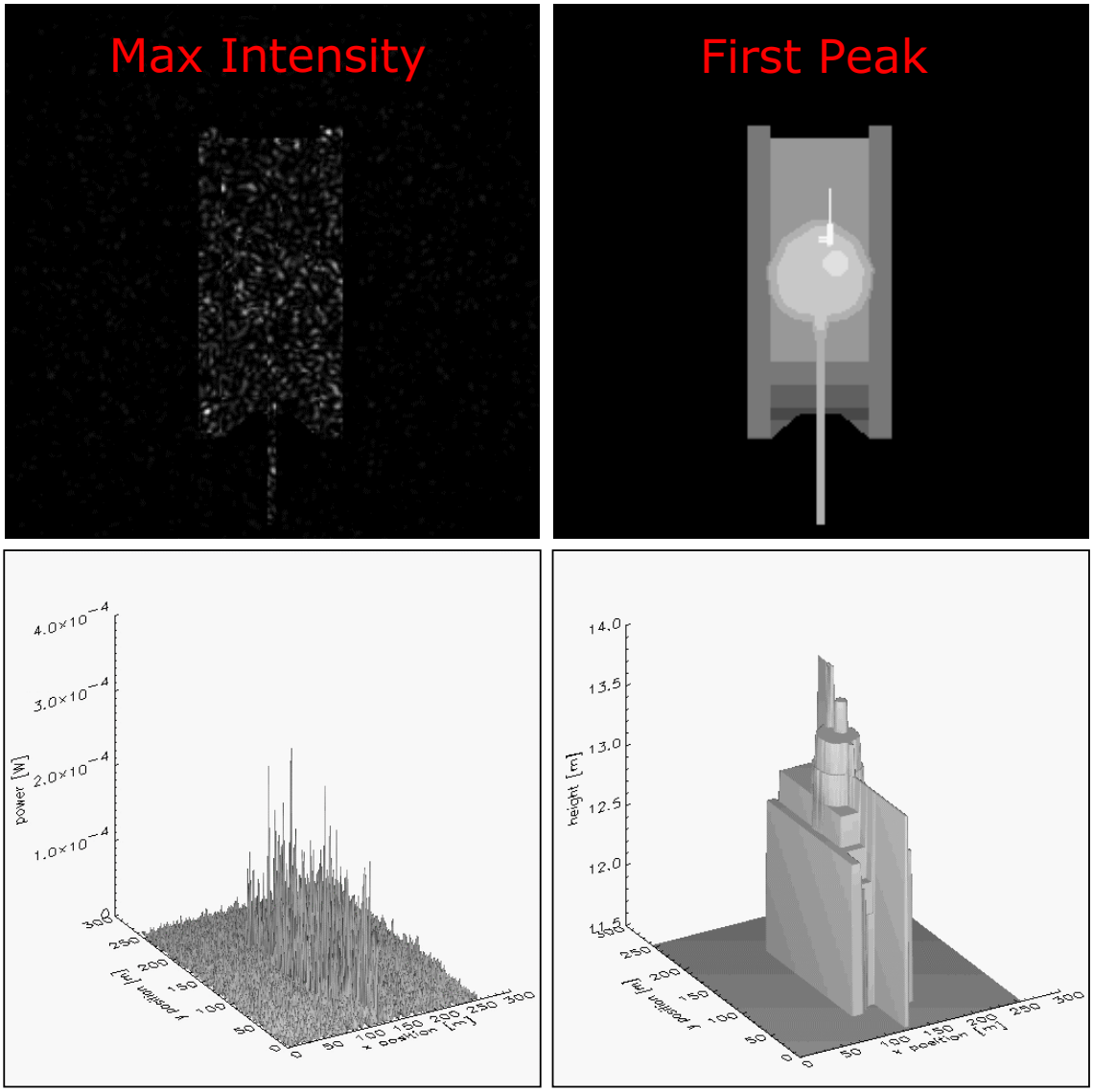

Figure 6.40: The images on the left were produced by finding and assigning to each pixel the maximum intensity of the intensity versus range curve for each position on the focal plane. The resulting maximum intensity images are very noisy and no details of the tank are discernable besides the general outline. The images on the right were produced by determining and assigning the range at which the maximum intensity occurred to each pixel. These images contain little noise and details of the tank design are apparent.

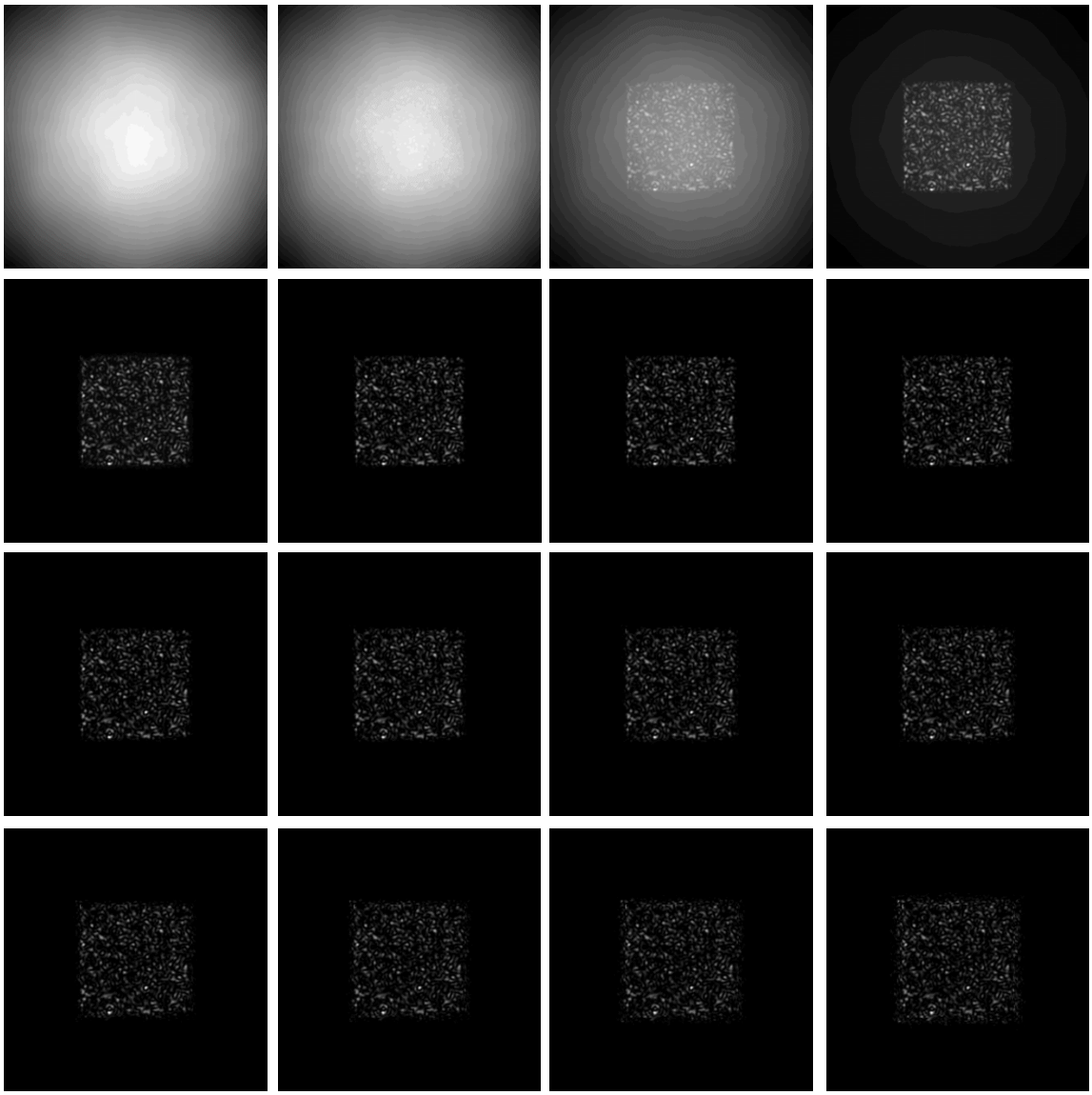

Figure 6.41: The initial speckled intensity slices of a tank under camouflage resting on a flat plate. As expected, the early slices show the profile of the beam. These early return do not contain speckle because the pulse has yet to reflect off of a hard target. Once the top of the camouflage is hit, the rest of the return dims in comparison and only the speckled tank is observed.

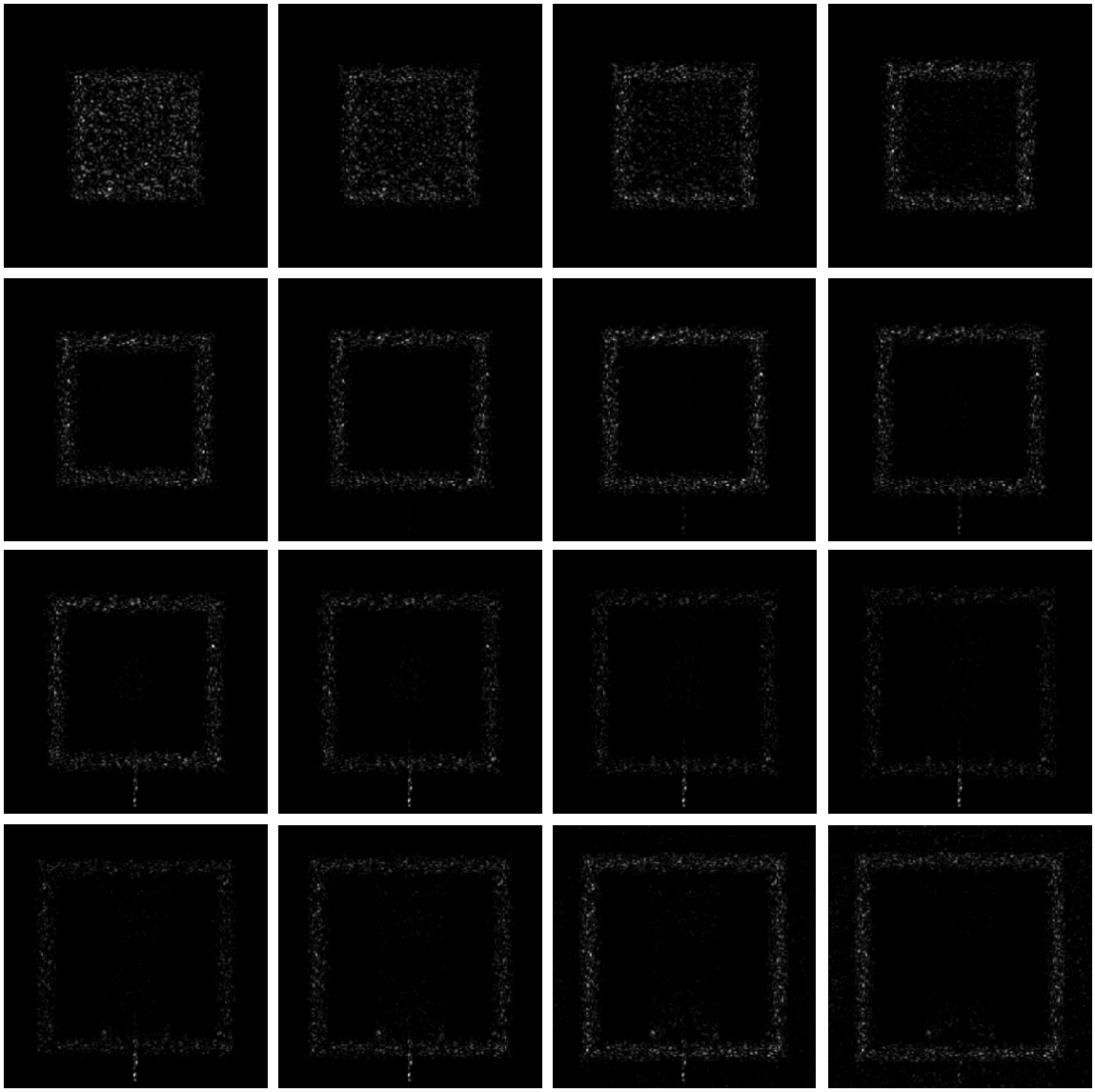

Figure 6.42: The subsequent speckled intensity slices of a tank under camouflage resting on a flat plate. Once the bright return from the top of the camouflage begins to dim the sides of the camouflage begin to brighten. The bright speckled return expands outward as it "walks" down the side of the camouflage. The portions of the tank that are not under the camouflage are visible.

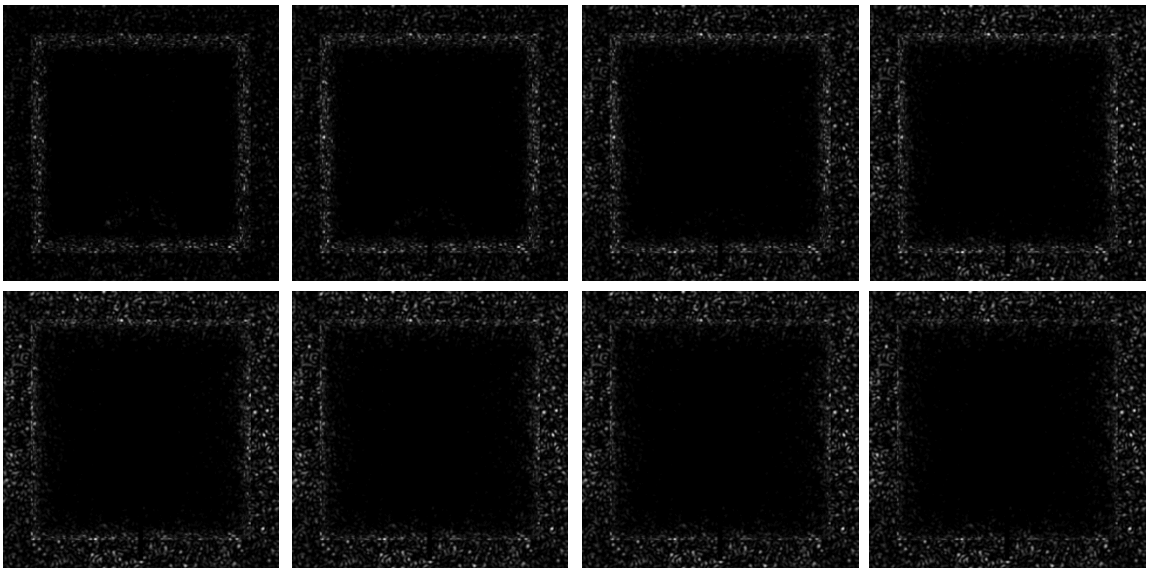

Figure 6.43: The remaining speckled intensity slices of a tank under camouflage resting on a flat plate. As the return reaches the bottom of the camouflage, the return from the ground begins to brighten, but now speckled due to reflection from the flat plate. The outline of the tank is not visible.

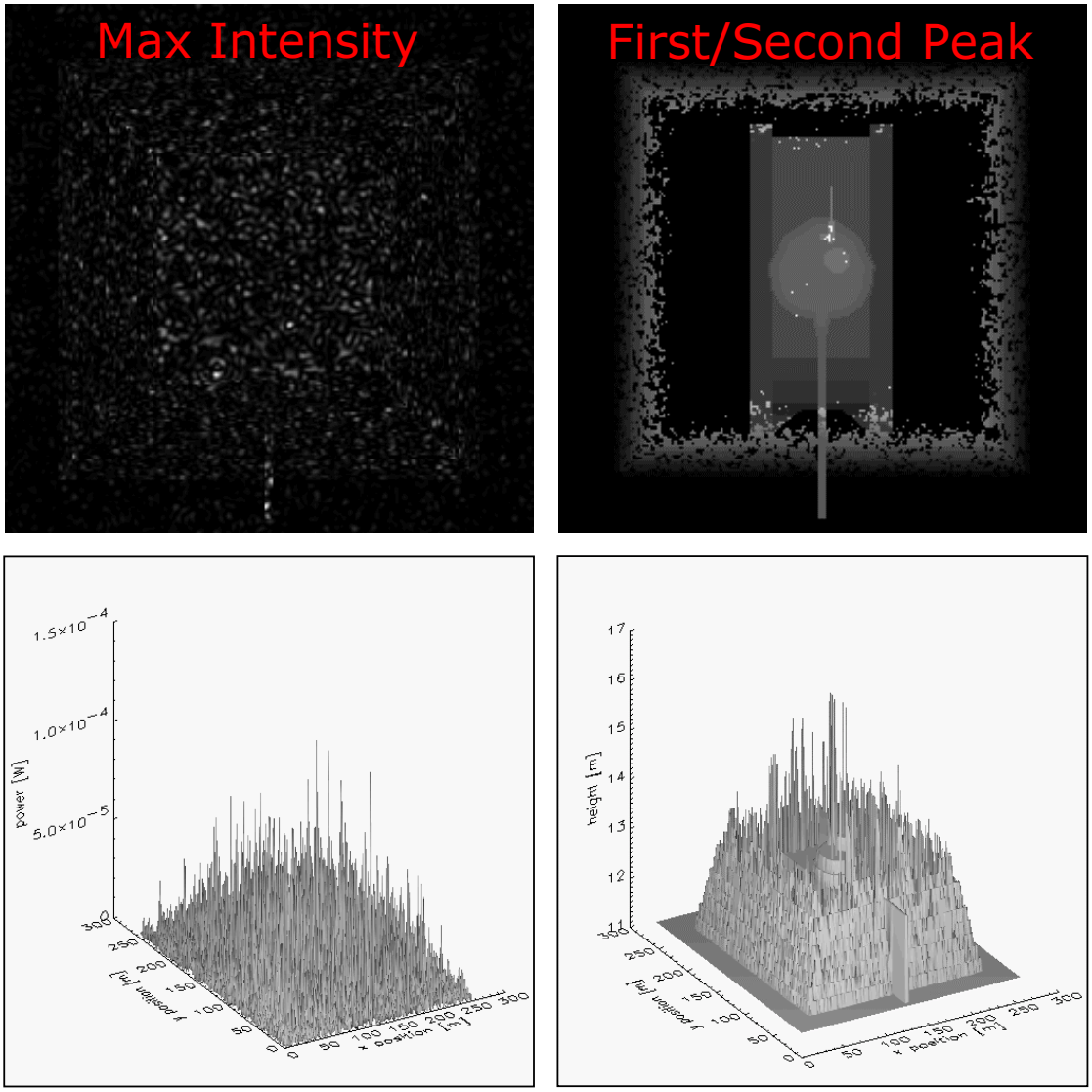

Figure 6.44: The resulting maximum intensity images for the tank under camouflage resting on a flat plate are very noisy. Only the general outline of the camouflage is present and no details of the tank are discernable. The images on the right were produced by determining and assigning the range at which the maximum of the second peak occurred to each pixel. If only one peak was present, the maximum intensity of that peak was assigned. These images are also noisy, but the presence of the tank under the camouflage and some details of the tank design are apparent.

6.7 Scintillation Results

The results of the scintillation simulation showed that for the fidelity modeled in DIRSIG turbulence can be ignored in the presence of speckle. This can be seen in Figures 6.45 through 6.46 that show that the mean, variance, and signal-to-noise ratio in the presence of both turbulence and speckle is the same as the mean, variance, and signal-to-noise ratio in just the presence of speckle for various values of the index-of-refraction structure constant. According to Nelson (2000), the rms noise increases above the amount excepted for speckle alone only for larger values of C_n^2. Additionally, Figure 6.47 shows that the signal-to-noise ratio for turbulence alone approaches one as the index-of-refraction structure constant increases. Figure 6.48 shows that the autocorrelation of the return at the focal plane in the presence of both turbulence and speckle is the same as the autocorrelation in just the presence of speckle. Visually, the patterns do seem to differ slightly as shown in Figure 6.49. The same parameters were used for the simulation in each case, the only thing that changed from run to run was the random values. The speckle images on the left are more consistent from run to run and seem to resemble a Gaussian spatial distribution. For large values of C_n^2, the speckle and turbulence images are more variable and no longer follow a Gaussian spatial distribution.

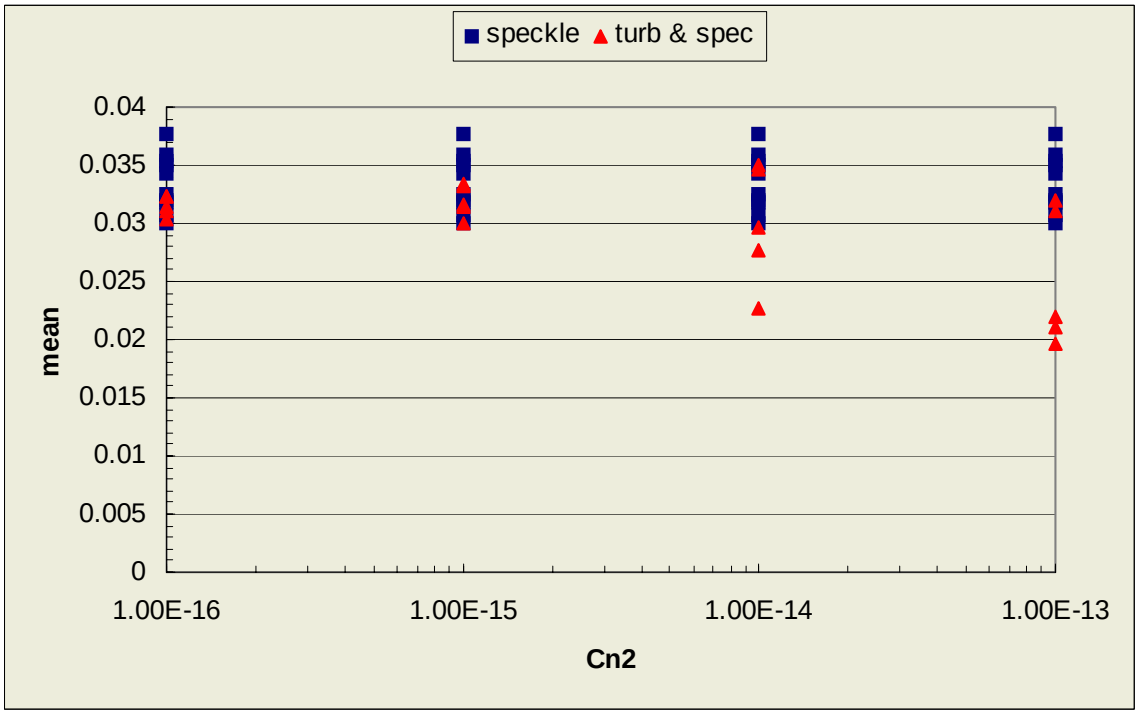

Figure 6.45: The mean of the center 64 by 64 pixels of a 512 by 512 simulation at the focal plane. The simulation was run for various values of the index-of-refraction structure constant with just the speckle turned on, and with both the speckle and turbulence turned on.

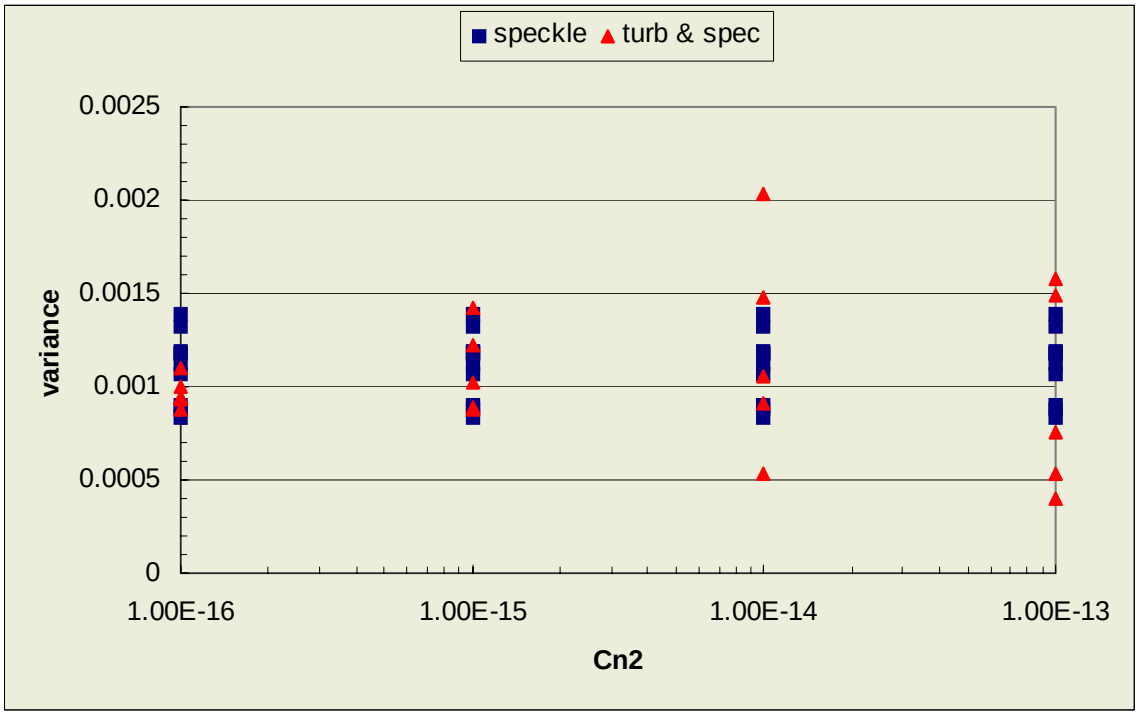

Figure 6.46: The variance of the center 64 by 64 pixels of a 512 by 512 simulation at the focal plane. The simulation was run for various values of the index-of-refraction structure constant with just the speckle turned on, and with both the speckle and turbulence turned on.

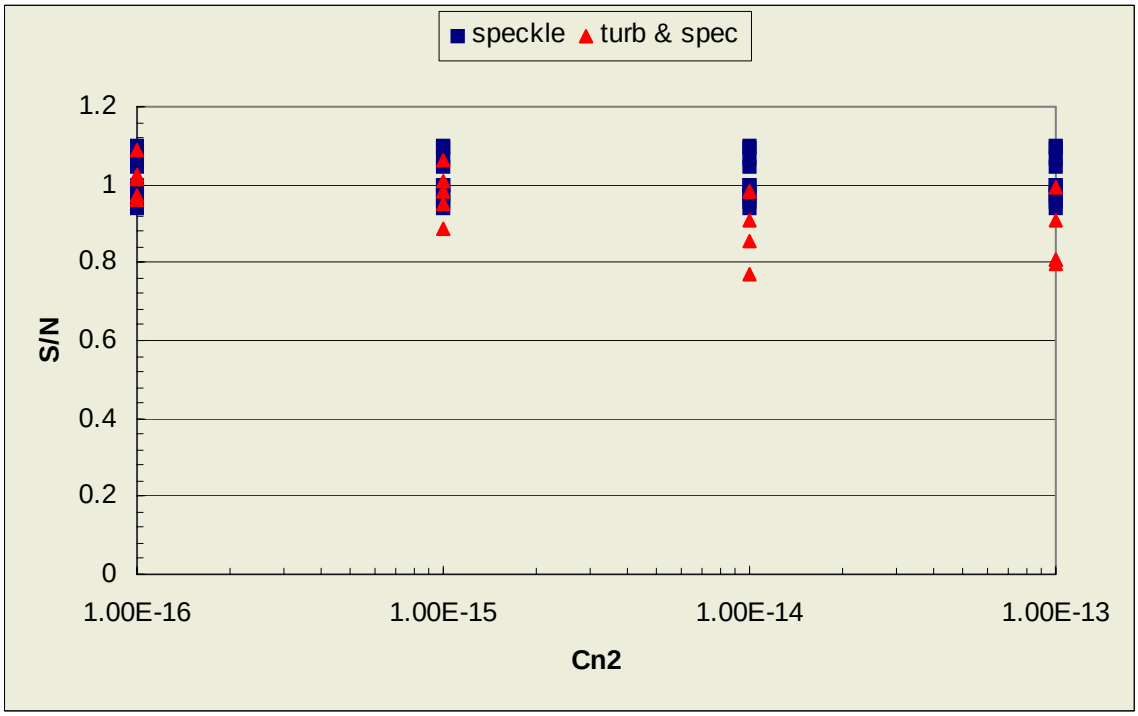

Figure 6.47: The signal-to-noise of the center 64 by 64 pixels of a 512 by 512 simulation at the focal plane. The simulation was run for various values of the index-of-refraction structure constant with just the speckle turned on, and with both the speckle and turbulence turned on.

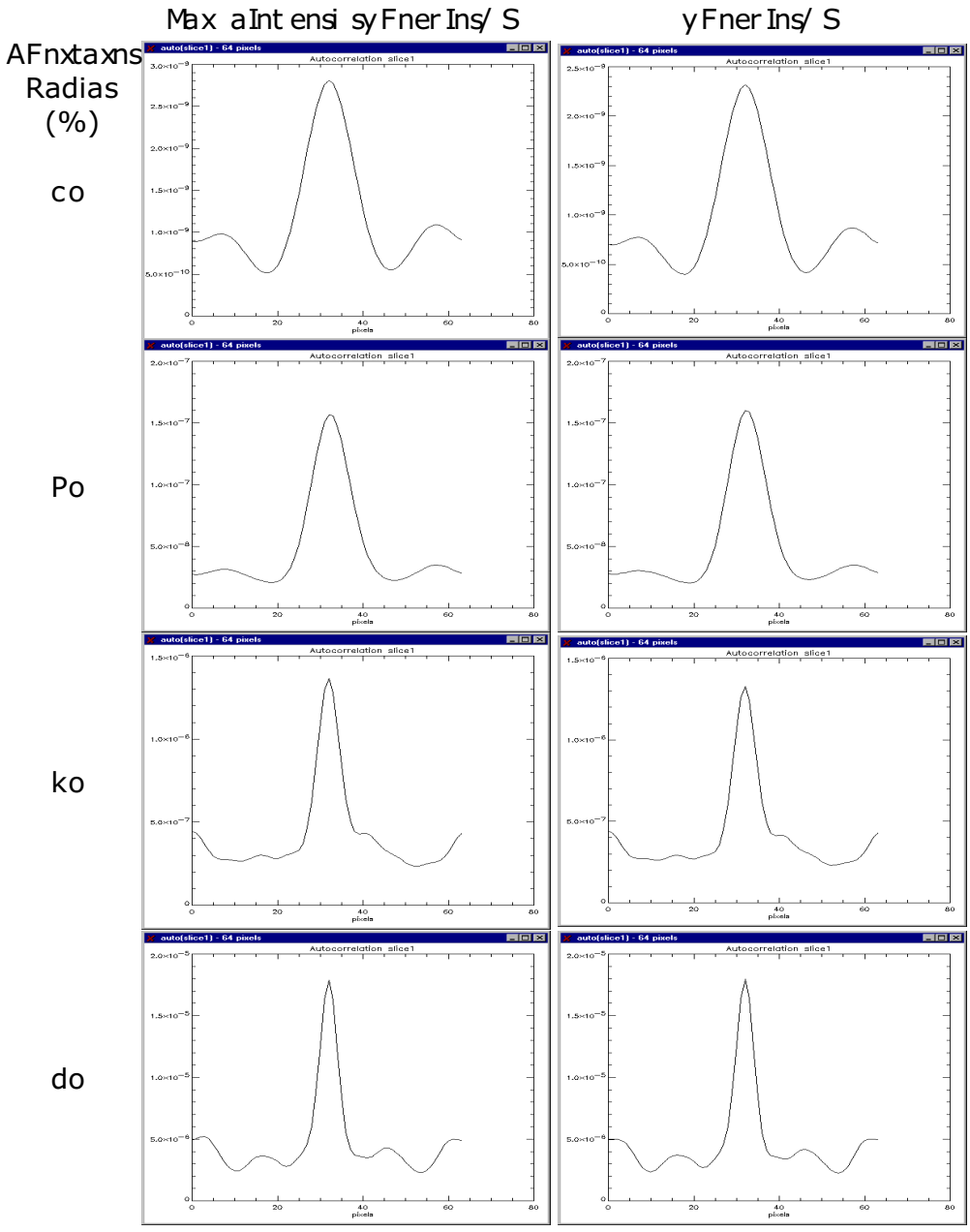

Figure 6.48: The autocorrelation of the center 64 by 64 pixels of a 512 by 512 simulation at the focal plane. The simulation was run for various aperture sizes with just the speckle turned on and with both the speckle and turbulence turned on.

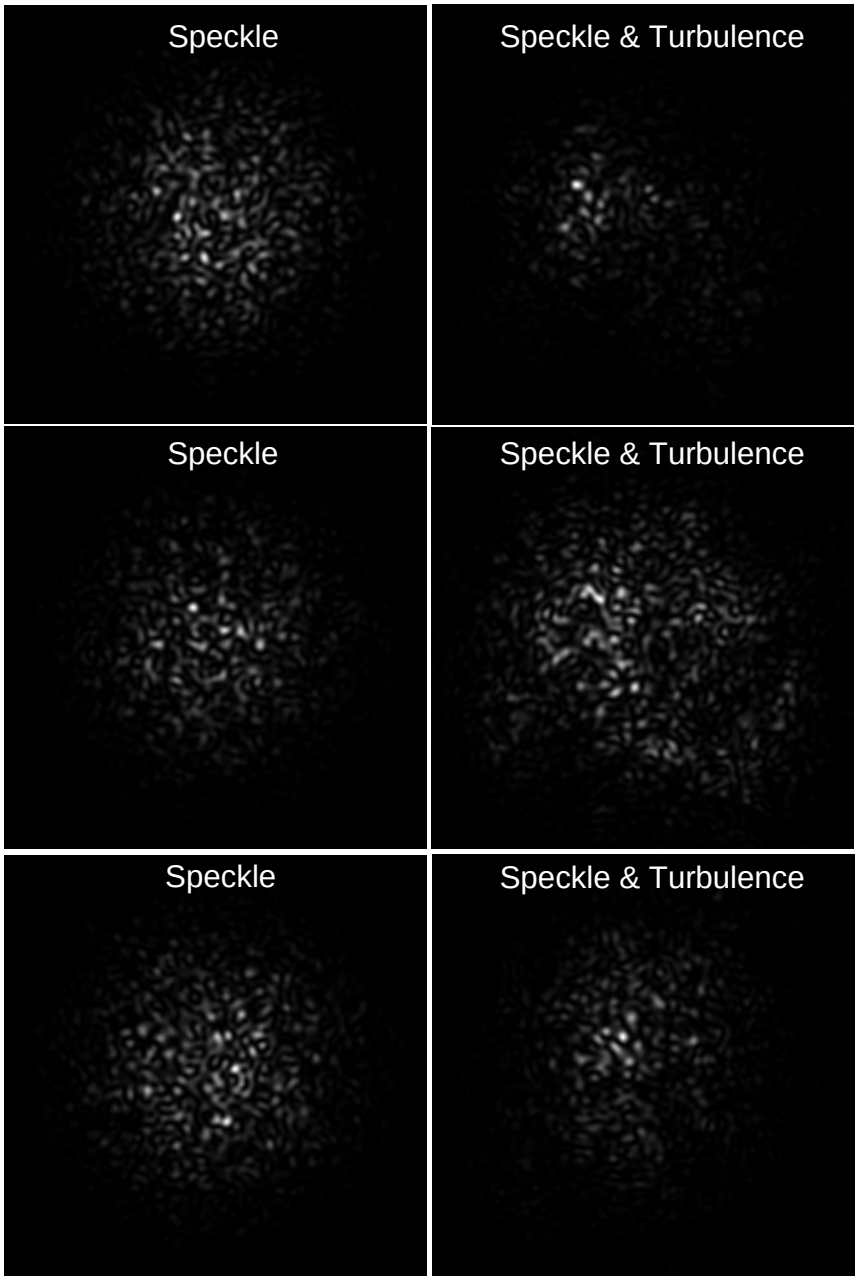

Figure 6.49: The return on the focal plane for speckle alone and for both speckle and turbulence. The speckle images on the left are more consistent from run to run and seem to resemble a Gaussian spatial distribution. The speckle and turbulence images are more variable and no longer follow a Gaussian distribution.

For the aerosol return, scintillation cannot be ignored. Figure 6.50 shows the mean, variance, and signal-to-noise ratio of a Gaussian beam propagated various distances and at the focal plane. The mean stays approximately constant, but has increased variability. The shift in the mean for larger propagation paths is probably an artifact of the statistics being taken from the center 64 by 64 pixels of the array. Beam wander is more pronounced for longer propagation paths and only a portion of the return was contained in the center 64 by 64 section. The variance increased and the variability of the variance increased with C_n^2. Finally, the signal-to-noise ratio tended to one, but values less than one are allowed by theory. To generate a texture map, an array of all ones was also propagated various distances. The resulting statistics are shown in Figure 6.51. The means for 3 km and 6 km propagation paths are lower for lower values of C_n^2. The trends in the variance and signal-to-noise ratio are the same as in the Gaussian case. Figure 6.52 compares the statistics of two texture patterns. One was produced by propagating a Gaussian beam and the other was produced by propagating an array of all ones, that is, a plane wave. The mean of the plane wave texture pattern remains constant while the mean of the Gaussian beam texture pattern increases as a function of C_n^2. The variances are similar, but the variability of the variance seems to be less for the plane wave texture pattern. Finally, the signal-to-noise ratios exhibit the same trend, but the plane wave texture pattern has lower values for identical values of C_n^2. Figure 6.53 shows scintillation patterns generated by propagating a plane wave for various values of C_n^2 and for various path lengths. For increasing values of C_n^2, the bright regions become tighter, that is, show more variability, and stay approximately the same distance apart. For increasing propagation distances, the bright regions seem to increase in size. Figure 6.54 shows texture maps generated using the simulation for various values of C_n^2 and for a path length of 4 kilometers. Notice the variety in the patterns for the same simulation parameters. Additionally, on the far right of Figure 6.54 is a corresponding

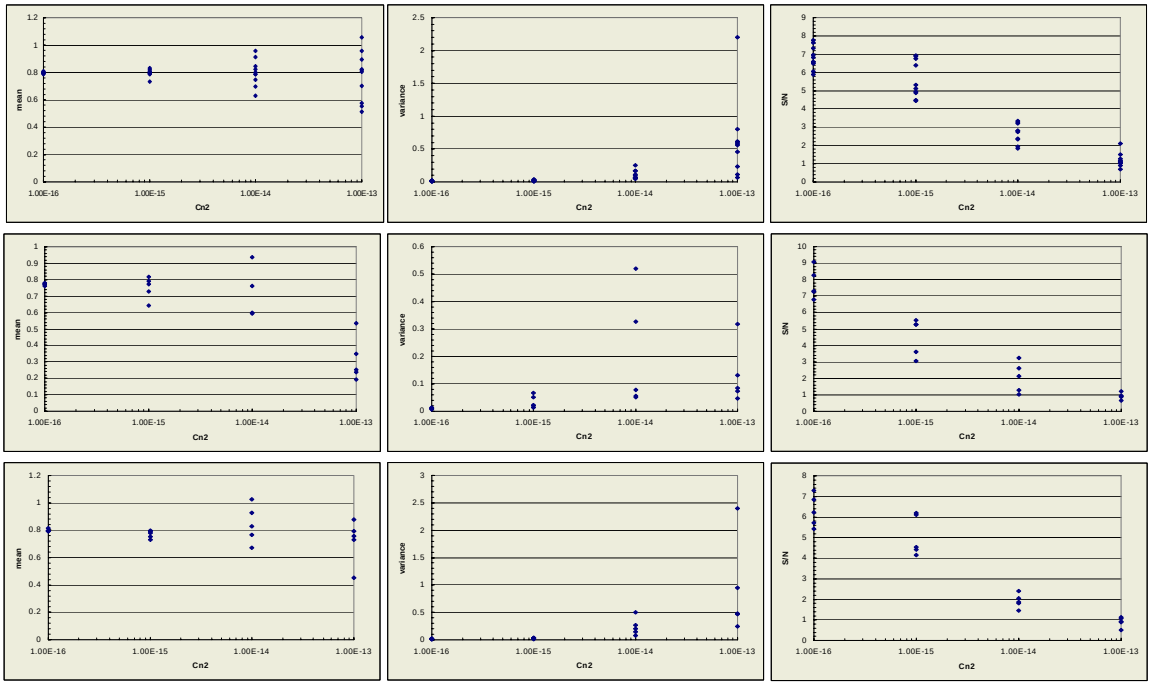

Figure 6.50: The mean, variance, and signal-to-noise ratio for various values of C_n^2 as a result of propagating a Gaussian beam. The top row shows the statistics at 2 km, the middle row the statistics at 4 km, and the bottom row the statistics at the focal plane.

scintillation pattern generated by propagating a plane wave for the corresponding value of C_n^2 and for a path length of 4 kilometers. Visually, the texture patterns and the scintillation patterns right before the aperture are similar, but the scintillation pattern seems to have less pronounced peaks. The trend between the scintillation pattern before the aperture and the texture pattern as C_n^2 increases is the same, the bright regions become more distinct. Texture maps could not be generated using the simulation for $C_n^2 = 1 \cdot 10^{-13}$ because the values between the speckles became small enough that the process of dividing the no turbulence return by the turbulence return resulted in spikes in the center of the array.

Figure 6.55 compares the rms noise, the inverse of the signal-to-noise ratio, generated

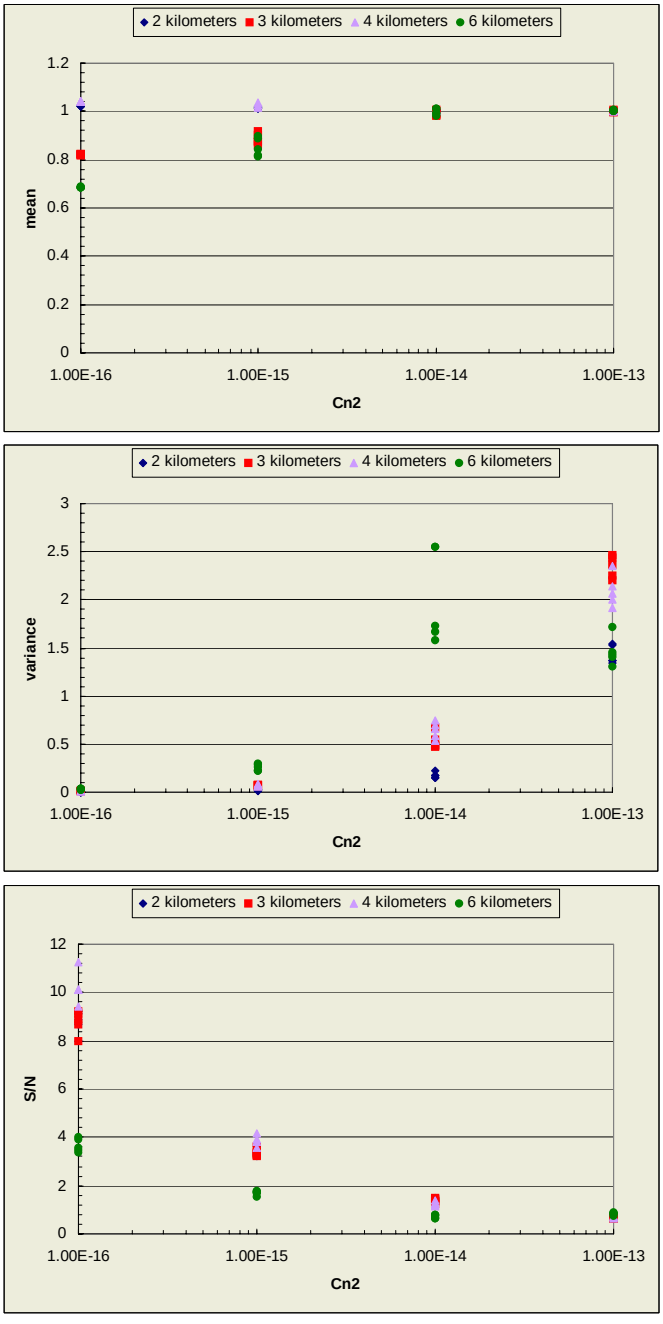

Figure 6.51: The mean, variance, and signal-to-noise ratio for various values of C_n^2 as a result of propagating a plane wave for various distances.

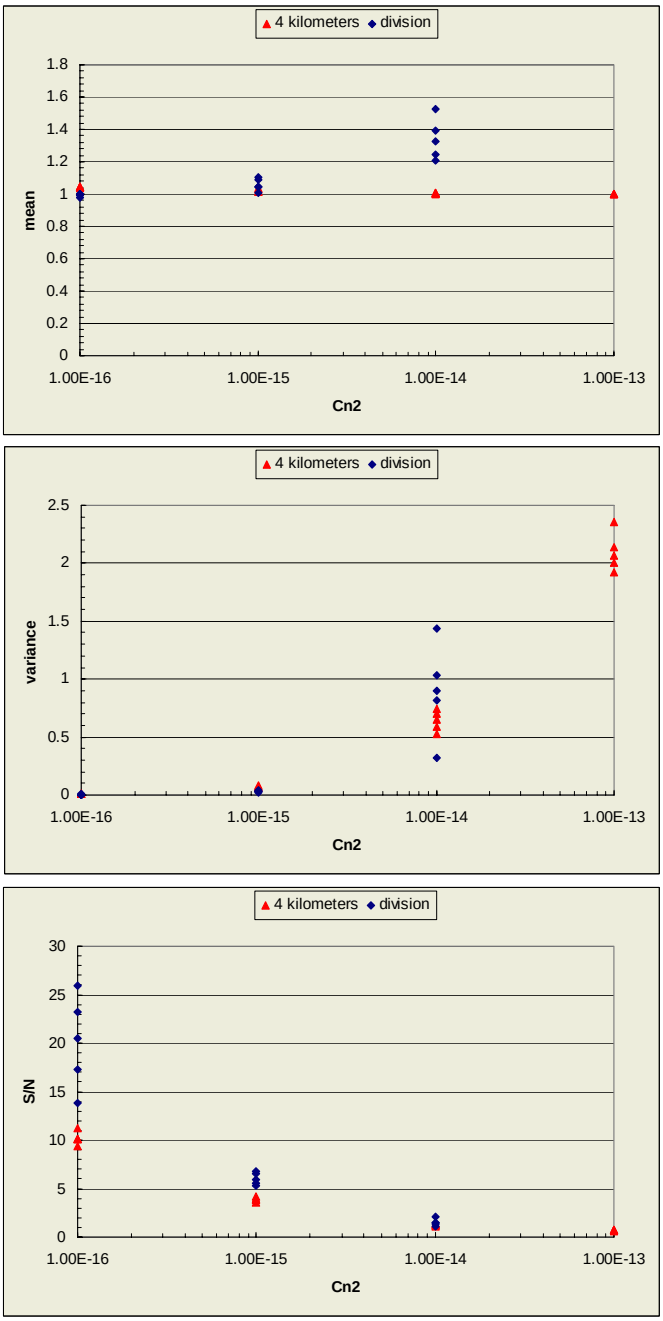

Figure 6.52: The mean, variance, and signal-to-noise ratio for various values of C_n^2 as a result of propagating a plane wave a distance of 4 km and as a result of computing a focal plane texture pattern for a Gaussian beam propagated a distance of 4 km.

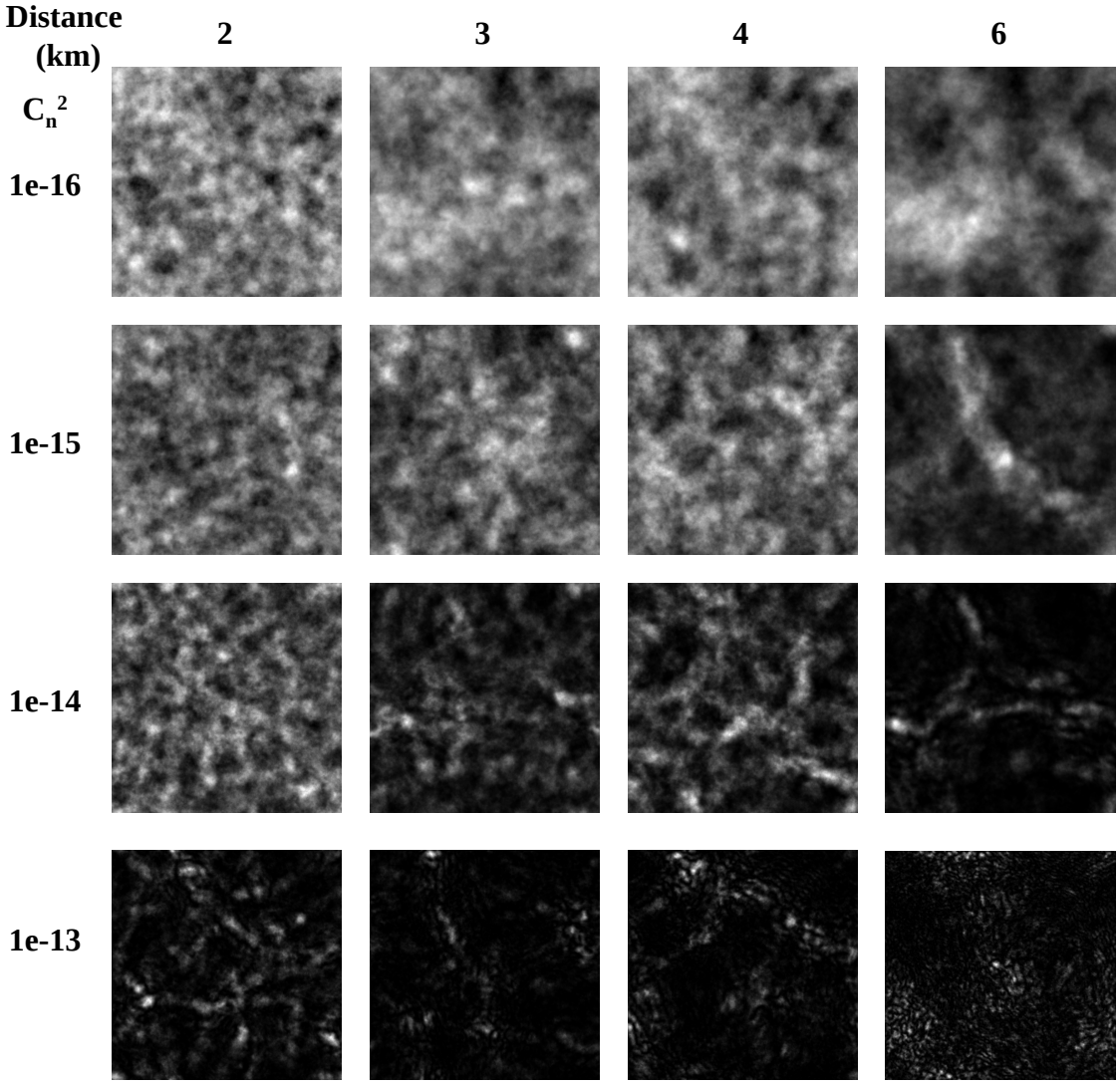

Figure 6.53: Scintillation patterns generated by propagating a plane wave using the scintillation simulation for various values of C_n^2 and for various path lengths. The bright regions become tighter for increasing C_n^2 and seem to increase in size for increasing propagation distances.

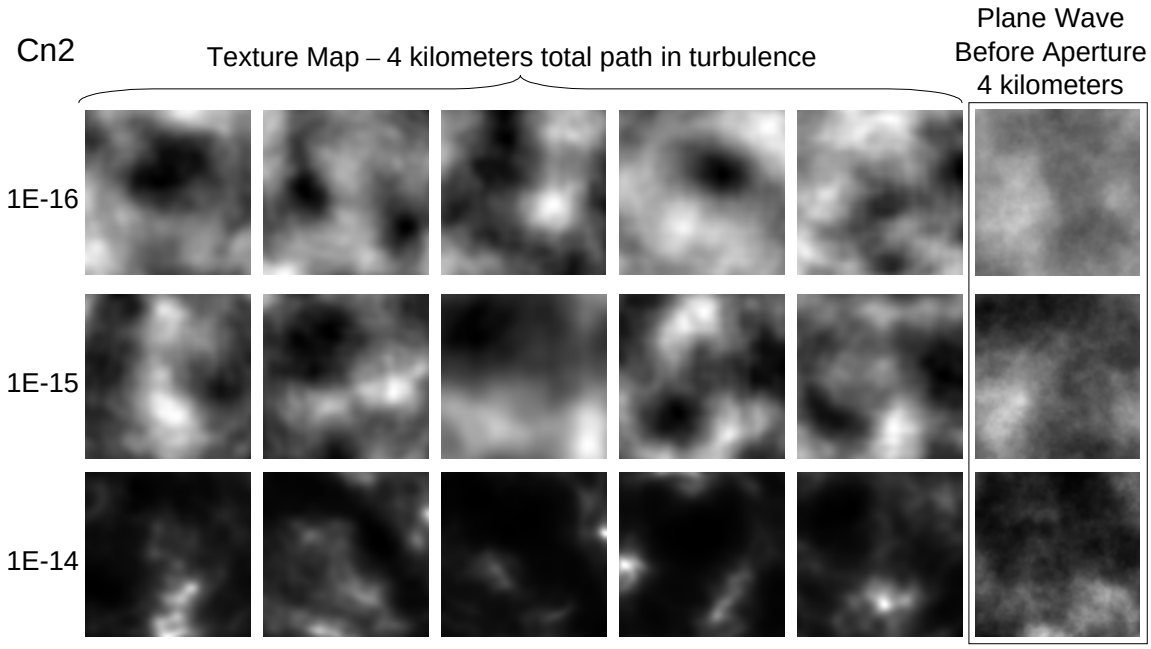

Figure 6.54: Texture maps generated using the scintillation simulation for various values of C_n^2 and for a path length of 4 kilometers to show the variety in the patterns generated. On the far right are scintillation patterns generated by propagating a plane wave 4 kilometers for the corresponding value of C_n^2 for comparison. As C_n^2 increases the bright regions become more distinct.

from the simulation and the rms according to theory. The plane wave case shows good agreement with the shape of the plane wave theoretical curve, but is off by a multiplicative constant. Theoretically, for a Gaussian beam the rms curve should have the same shape as the plane wave theoretical rms curve, but be multiplied by a constant which depends upon numerous factors. The rms noise for the Gaussian beam simulation did increase with increasing values of C_n^2, but it does not have quite the same shape as predicted by theory.

Because of these differences, DIRSIG does not automatically calculate and apply a scintillation texture map. DIRSIG can accept a precomputed scintillation texture map and apply it. The capability to insert a precomputed scintillation texture map was included because for the aerosol return, scintillation is the only source of noise. A proof of concept texture map was produced offline and is shown in Figure 6.56. The process for producing a scintillation texture pattern is similar to the process for producing a speckle texture pattern. The mean and normalization constant of the texture pattern are calculated the same way, except the beam is now propagated through phase screens from the transmitter to the receiver. A random scintillation texture pattern is then produced by propagating a plane wave through phase screens from the transmitter to the receiver and applying the normalization constant. Because of aliasing issues, not all systems can be modelled in this manner. For example, the wavelength times the propagation distance must be greater than N. By expressing the the wavelength and propagation distance in the correct units, this condition can be met, but it might lead to an unrealistic focal length. Scintillation texture patterns produced in this manner will not have accurate statistics, but will exhibit the correct trends. For some applications this may be good enough, since the exact value of C_n^2 is never known precisely.

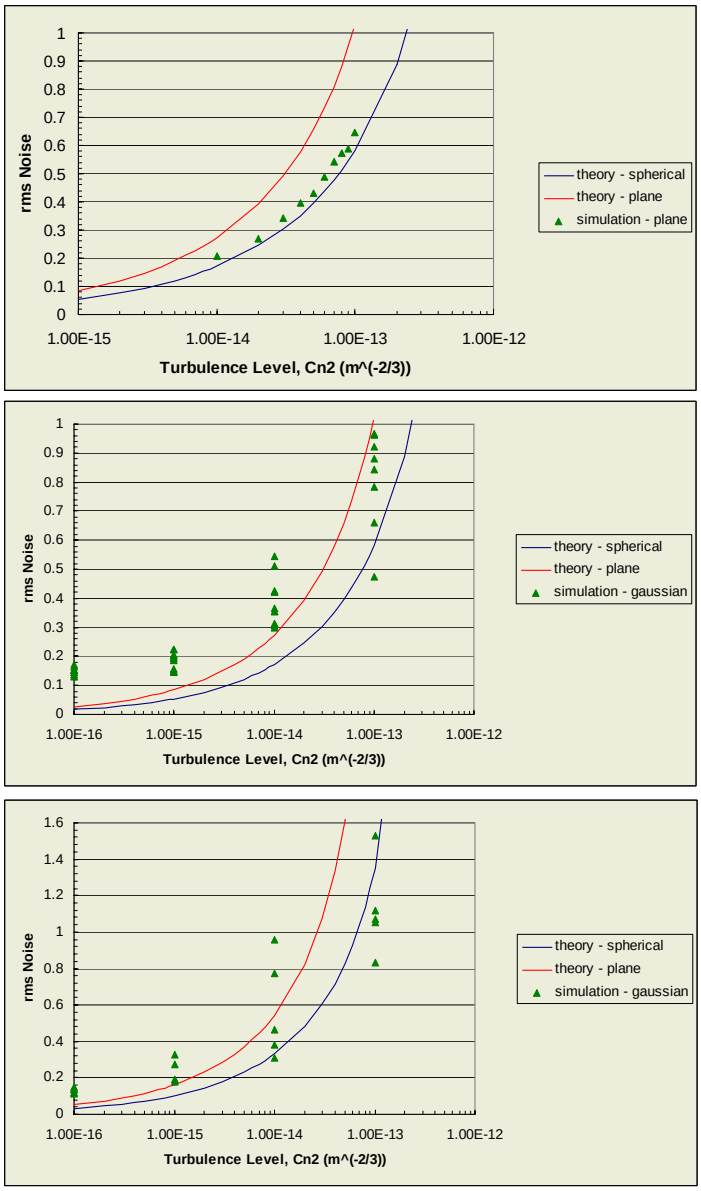

Figure 6.55: The rms as a function of C_n^2. The red line in each graph is the theoretical value for a plane wave while the blue line is the theoretical value for a spherical wave. For a Gaussian wave the theoretical value is a constant times the theoretical plane wave curve. The top graph is the rms for an initial array of all 1s propagated a distance of 2 km. The middle graph is the rms for a Gaussian beam propagated a distance of 2 km. The lower graph is the rms for a Gaussian beam propagated a distance of 4 km.

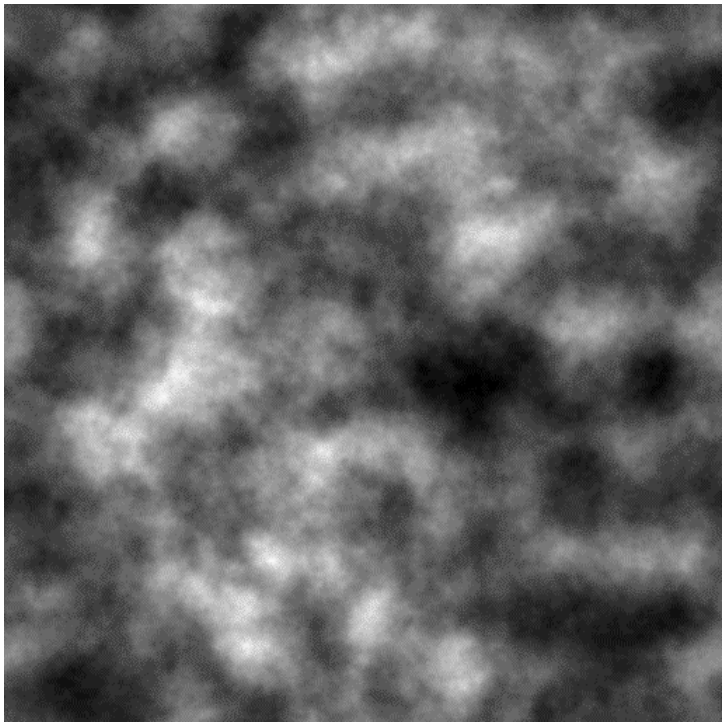

Figure 6.56: To show that a texture map could be generated offline and then passed to DIRSIG, a proof of concept texture map was generated for a specific scenario. The scenario included a 0.01 m detector array diameter, a 2 km range to the scattering layer, a 4 m focal length, a 1 m receiver radius, a 2 m beam diameter, no divergence angle, a 1.1 μm wavelength, and a constant $1 \cdot 10^{-16}$ $m^{-\frac{2}{3}}$ index-of-refraction structure constant along the path. To determine what the statistics of the texture map should be, the scintillation GUI was used to simulate both a scintillated and an unscintillated beam at the receiver. The mean, standard deviation, and signal-to-noise ratio of the ratio of the modulated beam to the unmodulated beam was obtained. The texture map generated for DIRSIG had to match these statistics. The texture map was generated by propagating a plane wave from the transmitter to the receiver through a series of phase screens of a certain strength. The strength of the phase screens was varied until the closest match was obtain between the statistics of the texture map and the desired statistics. The desired statistics had a mean of 0.995, a standard deviation of 0.251 and a signal to noise ratio of 3.960. The texture map had a mean of 1.020, a standard deviation of 0.275, and a signal to noise ratio of 3.705.

Chapter 7

Summary

The model as outlined in this dissertation provides the user community with a needed modeling capability not currently available. Besides IRMA, this work is the only simulation code capable of producing synthetic imagery. The DIRSIG LADAR/LIDAR model simulates both the topographical and the aerosol return. This allows DIRSIG to model not only time-of-fight pulsed laser rangefinders, but also LIDAR systems that detect, track, and quantify gases in the atmosphere. Additionally, it can model bistatic systems, that is the source and the receiver do not need to be co-located. Figure 2.1 summarized the various types of LADAR/LIDAR systems. DIRSIG models Elastic Scattering, DIAL, Topographic Backscatter DIAL, Broadband, Bathymetry, and LADAR. DIRSIG is inherently a spectral model, so no additional runs are needed to model a DIAL system. DIRSIG includes several sources of noise, such as the speckle return off of surfaces and atmospheric turbulence effects. Furthermore, DIRSIG includes the passive return in the spectral range of the detector and accounts for multiple bounce.

Chapter 8

Considerations for Future Work

This work is the first step in the development of a comprehensive LADAR/LIDAR model. The next step should be an extensive validation effort, including the comparison of the model results to the results from an actual system. Ideally, a commercial LADAR system would collect data over the same area covered by Mega-Scene, a synthetic scene that covers over 2.5 square miles on the northeast side of Rochester, NY that includes urban residential, urban commercial, rural and coastal regions. Flying Mega-Scene would not only provide a significant amount of comparison data for a DIRSIG LADAR validation, but also would provide extensive ground truth for the Mega-Scene effort itself.

After the model validation is complete, several improvements should be made to the model to make it more robust before additional phenomenology is added. Currently, the computational time it takes to produce a datacube from a single pulse is more than twenty-four hours. This time needs to be drastically reduced before the DIRSIG LADAR/LIDAR model can be routinely used. To add more flexibility to the model, an initial phase front radius of curvature can be given to the beam. The phase front radius of curvature affects

how the beam spreads and more accurately models real LADAR/LIDAR systems. The DIRSIG LADAR model has not yet been tested to ensure that it can correctly model a horizontal path. In particular, the routines that integrate C_n^2 over a path length must be assessed. The final improvement is to modify the way speckle is simulated by giving each photon a relative phase in the photon map creation process. In this manner, a speckled return can be generated by simply querying the photon map. According to theory the size of the speckle should be a function of the size of the aperture, the focal length, and the wavelength of the light. Since the size of the query area is related to the size of the aperture and the position of the query area is related to the focal length, this method should produce speckle whose size depends on these two parameters. If a surface roughness that depends on wavelength was added to the model to determine the relative phase added to each photon at the rough surface then the speckle size should also depend on the wavelength of the light. Preliminary tests generated modulated images, but the modulation more closely resembled a scintillation pattern than a speckle pattern. If viable, this method would allow various aperture shapes to be modeled, would eliminate the need for look-up tables, and enable the development of a coherent detection model. Currently, the DIRSIG LADAR model creates an independent speckle pattern for each pulse. If the LADAR system does not move position by approximately the radius of the aperture between one pulse and the next, the speckle patterns may be correlated. Whether they are correlated depends upon how much the turbulent eddies in the atmosphere have changed. These changes are usually slow compared to the time it takes for the wind to blow the turbulent eddies across the telescope aperture. The time constant of the atmosphere τ_0 is the ratio of Fried's coherence length to the wind speed in the dominant layer. Therefore, for times greater than τ_0 the two speckle patterns are not correlated and are correlated for times less than τ_0. The DIRSIG LADAR/LIDAR model does not currently test to make sure independent speckle patterns

should be generated. The capability to test these conditions and to produce correlated speckle patterns should be added to the model.

Once these improvements are made to the model additional phenomenology can be added. The model currently assumes that a significant number of photons are making it back to the detector. When there is significant atmospheric attenuation only a few photons may make it back to the detector. Therefore, the ability to model photon-counting detectors should be added to the model. One possible implementation is to add a Poisson statical distribution model on top of the photon map query to test each photon to see whether or not it is detected before adding it into the return. Raman scattering could be then be added to the model with a moderate amount of effort and lay the groundwork for the incorporation of Doppler and fluorescence models.

Works Cited

Andrews, L. C. and R. L. Phillips. *Laser Beam Propagation through Random Media*. SPIE Optical Engineering Press, 1998.

Bosenberg, J. "Ground-based Differential Absorption Lidar for Water-Vapor and Temperature Profiling: Methodology." *Applied Optics* 37 (1998): 3845–3860.

Dainty, J.C. *Laser Speckle and Related Phenomena*. Volume 9 of Topics in Applied Physics. Springer-Verlag, 1984.

Davis, C.A. and D.L. Walters. "Atmospheric inner-scale effects on normalized irradiance variance." *Applied Optics* 33 (December 1994): 8406–8411.

Douard, M., P. Rambaldi, and J.P. Wolf. "A Fourier Transform Lidar." *Advances in Atmospheric Remote Sensing with Lidar: Selected Papers of the 18th International Laser Radar Conference (ILRC)*. Ed. A. Ansmann Berlin: Springer, July 22-26 1996, 463–466.

Fastig, S., I. Paiss, and M. Kleinman. "Wide Bandwidth DIAL System - Analysis and Sensitivity Studies." *Advances in Atmospheric Remote Sensing with Lidar: Selected Papers of the 18th International Laser Radar Conference (ILRC)*. Ed. A. Ansmann Berlin: Springer, July 22-26 1996, 459–462.

Fiocco, G. and L. O. Smullin. "Detection of scattering layers in the upper atmosphere

(60-140 Km) by optical radaars." *Nature* 199 (1963): 1275.

Frehlich, R. "Simulation of laser propagation in a turbulent atmosphere." *Applied Optics* 39 (January 2000): 393–397.

Fried, D. "Optical resolution through a randomly inhomogeneous medium." *J. Opt. Soc. Am.* 56 (1966): 1372–1379.

Gardiner, T.D., M.J.T. Milton, F. Molero, and P.T. Woods. "Infrared DIAL Measurements with an Injection-Seeded OPO." *Advances in Atmospheric Remote Sensing with Lidar: Selected Papers of the 18th International Laser Radar Conference (ILRC).* Ed. A. Ansmann Berlin: Springer, July 22-26 1996, 451–454.

Gardner, C. and G. Papan. "Mesospheric Na wind/temperature lidar." *The Review of Laser Engineering* 23 (1995): 131–134.

Gmachl, C., D. Sivco, R. Colombelli, and F. Capasso. "Ultra-broadband semiconductor laser." *Nature* 415 (2002): 883–887.

Goodman, J.W. *Introduction to Fourier Optics.* 2 edition. McGraw-Hill, 1996.

Halldorsson, T. and J. Langerholc. "Geometrical Form Factors for the Lidar Function." *Applied Optics* 17 (1978): 240–244.

Harms, J. "Lidar Return Signals for Coaxial and Noncoaxial Systems with Central Obstruction." *Applied Optics* 18 (1978): 1559–1566.

Harms, J., W. Lahmann, and J.E.A. Selby. "Geometrical Compression of Lidar Return Signals (Remote Sensing of Atmosphere)." *Applied Optics* 17 (1978): 1131–1135.

Hummel, J.R., D.R. Longtin, N.L. DePiero, and R.J. Grasso. BACKSCAT Lidar Simulation Version 3.0: Technical Documentation and User's Guide. Technical Report AD-A267 296, Sparta, Inc., 24 Hartwell Avenue, Lexington, MA 02173, December

1992.

Hummel, J.R., D.R. Longtin, N.L. Paul, and J.R. Jones. BACKSCAT Lidar Backscatter Simulation User's Manual for Version 2.0. Technical Report AD-A243 949, Sparta, Inc., 24 Hartwell Avenue, Lexington, MA 02173, July 1991.

Knepp, D.L. "Multiple Phase-Screen Calculation of the Temporal Behavior of Stochastic Waves." *Proceedings of the IEEE* 71 (June 1983): 722–737.

Longtin, D.R., M.G. Cheifetz, J.R. Jones, and J.R. Hummel. BACKSCAT Lidar Simulation Version 4.0: Technical Documentation and User's Guide. Technical Report AD-A285 851, Sparta, Inc., 24 Hartwell Avenue, Lexington, MA 02173, June 1994.

Machol, J. "Comparison of the pseudorandom noise code and pulsed direct-detection lidars for atmospheric probing." *Applied Optics* 36 (1997): 6021–6023.

Martin, J.M. and S.M. Flatte. "Intensity image and statistics from numerical simulation of wave propagation in 3-D random media." *Applied Optics* 27 (June 1988): 2111–2126.

Measures, R.M. *Laser Remote Sensing: Fundamentals and Applications*. Wiley-Interscience, 1984.

Megie, G. "Measurement of the Atmospheric Pressure and Temperature by Lidar Differential Absorption: Influence of the Width of Laser Emission." *Applied Optics* 19 (1980): 34–43.

Milton, M., T. McIlveen, D. Hanna, and P. Woods. "A high-gain optical parametric amplifier tunable between 3.27 and 3.65 microns." *Optics Communications* 93 (1992): 186–190.

Nelson, D.H., D.L. Walters, E.P. MacKerrow, M.J. Schmitt, C.R. Quick, W.M. Porch,

and R.R. Petrin. "Wave optics simulation of atmospheric turbulence and reflective speckle effects in CO_2 lidar." *Applied Optics* 39 (2000): 1857–1871.

N.R. Guivens, Jr., S.E. Rafuse, J.R. Hummel, and M.G. Cheifetz. BACKSCAT Lidar Backscatter Simulation User's Manual for Version 1.0. Technical Report AD-A219 487, Sparta, Inc., 24 Hartwell Avenue, Lexington, MA 02173, December 1988.

Schmitt, M., B. McVey, B. Cooke, and G. Busch. "Comprehensive System Model for CO_2 DIAL." *Gas and Chemical Lasers*. Ed. R.C. Sze San Jose, CA: SPIE, January 1996, 95–103.

Schott, J.R., S.D. Brown, R.V. Raqueno, H.N. Gross, and G. Robinson. "An Advanced Synthetic Image Generation Model and its Application to Multi/Hyperspectral Algorithm Development." *Canadian Journal of Remote Sensing* 25 (1999): 99–111.

Streicher, J., I. Leike, and C. Werner. "ALIENS: Atmospheric Lidar end-to-end Simulator." *5th International Symposium on Atmospheric and Ocean Optics*. Ed. V. Zuev and G. Matvienko Tomsk, Russia: SPIE, June 15-17 1998, 380–386.

Thomas, M.E., D.D. Duncan, R.R. Beland, K.G. Gilbert, L. J. Otten III, W.C. Rose, and F.G. Gebhardt. *Atmospheric Propagation of Radiation*. Ed. F.G. Smith. Volume 2 of The Infrared and Electro-Optical Systems Handbook. Environmental Research Institute of Michigan and SPIE Optical Engineering Press, 1993.

Vechinski, D., M. Richards, J. Edwards, J. Touma, and M. Wellafre. Multi-Sensor Modeling and Analysis (MSMA) IRMA 5.0 User's Guide. Technical Report N-TR-00-073, Nichols Research, 1130 Eglin Parkway, Suite A, Shalimar, FL 32579, November 2000.

Verdeyen, J. *Laser Electronics*. Third edition. Prentice Hall, 1995.

Vezin, B., M. Douard, P. Rambaldi, and J.P. Wolf. "Development of Infrared Lidar Sys-

tems Based on 'Tracking-Free' Optical Parametric Oscillators." *Advances in Atmospheric Remote Sensing with Lidar: Selected Papers of the 18th International Laser Radar Conference (ILRC)*. Ed. A. Ansmann Berlin: Springer, July 22-26 1996, 455–458.

W. E. Wilcox, Jr. *Development and Experimental Verification of a High Resolution, Tunable Lidar Computer Simulation Model for Atmospheric Laser Remote Sensing*. , University of South Florida, , December 1995. .

Welch, G. and R. Phillips. "Simulation of enhanced backscatter by a phase screen." *J. Opt. Soc. Am. A* 7 (April 1990): 578–584.

Yariv, A. *Optical Electronics*. Saunders College Publishing, 1991.